Refining Earth's Ocean Oxygenation History using Molybdenum and Thallium Isotopes

by

Chadlin M. Ostrander

A Thesis Presented in Partial Fulfillment
of the Requirements for the Degree
Doctor of Philosophy

Approved April 2020 by the
Graduate Supervisory Committee:

Ariel D. Anbar, Chair
Christy B. Till
Meenakshi Wadhwa
Richard L. Hervig
Philip D. Mauskopf

ARIZONA STATE UNIVERSITY

May 2020

ABSTRACT

Isotope ratios of some trace metals have proven useful for tracking Earth's ocean oxygenation history. As the limitations of some of these isotope systems are realized, it becomes increasingly important to develop new and complementary systems. This dissertation examines the utility of molybdenum (δ^{98}Mo) and thallium (ε^{205}Tl) isotope compositions preserved in ancient marine shales to track past ocean oxygenation. My approach is as follows: (1) as an initial exercise, apply the well-established Mo isotope system to a set of ancient shales; (2) validate the use of the newly developed Tl isotope system; and finally (3) examine the potential of applying Mo and Tl isotopes in tandem.

Increasingly heavier δ^{98}Mo are found in shales deposited during the Neoarchean (2,800 to 2,500 million years ago, or Ma), which would be a predicted consequence of progressive ocean oxygenation across this timeframe. Increasingly heavier ε^{205}Tl across a well-documented Mesozoic Oceanic Anoxic Event (~94 Ma), on the other hand, would be a predicted consequence of progressive ocean *de*-oxygenation. An anti-correlation in the first combined application of Mo and Tl isotopes in ancient shales provides a strong fingerprint for previously unrecognized levels of ocean oxygenation at ~2,500 Ma. Lastly, neither δ^{98}Mo or ε^{205}Tl behave as predicted in shales deposited during three Ediacaran Ocean Oxygenation Events (~635 Ma, ~580 Ma, and ~560 Ma). These unexpected trends are due, at least in part, to local-scale overprints that must be taken into consideration when pairing together Mo and Tl isotopes in shales.

The ability of the Mo and Tl isotope systems to track changes in past ocean oxygenation is confirmed in this dissertation. Both isotope systems have the potential to

track these changes independently, but their combined utility is particularly powerful. Under ideal conditions, their combined application can provide an even more robust fingerprint for changes in past ocean oxygenation. Even under non-ideal conditions, their combined application makes it possible to decipher local-scale overprints from signals of past ocean oxygenation. It is therefore ideal, whenever possible, to measure both δ^{98}Mo and ε^{205}Tl in the same shale samples to assess past changes in ocean oxygenation.

ACKNOWLEDGMENTS

Pat Ward, my high school science teacher in Klamath Falls, Oregon, first got me excited about science. If our paths did not cross, there is absolutely zero chance that I would have chosen science as a career. Thank you, Pat, and the rest of the great science educators out there.

ASU was probably one of the few universities that would have accepted me in 2012. I was at the time six-years removed from a rural high school where I owned a 2.7 GPA. Five of those years were spent as an enlisted man in the Marines, where Muscles Are Required but Intelligence is Not Expected (M.A.R.I.N.E.). Thank you for giving someone like me a chance.

Ariel Anbar, my PhD advisor, probably allowed me to start working in his lab in 2012 because I looked like an ox. My arms and legs were big and capable of moving around heavy drill-cores. At the time, I was dang near as dumb as those rocks. Now, thanks to you and your team, I am smarter than the rocks. All jokes aside, I am truly grateful for the opportunity you provided. Most of all, thank you for giving me a long leash. I look forward to your continued mentorship.

Thank you to all of the folks at ASU. To Gwyn Gordon, my first mentor in the Anbar Lab, thank you for taking the time to hold my hand through the basics of isotopes and MC-ICPMS, and for not yelling at me when I repeatedly broke stuff in and around the lab in those early years. Most of all, thanks for laughing with me through it all. Steve Romaniello, thanks for your help with most of the science in this dissertation. Thanks also for dragging me and the others out of the lab on a consistent basis to see the sun. Thanks to Wang Zheng and Tyler Goepfert also for their help with MC-ICPMS, and to Geoff

Gilleaudeau for the lively discussions about everything isotopes, O_2, good music, and baseball. Thanks to Trevor (I hope you appreciate my directness). Thanks to Chris Mead for sharing coffee. Thanks to Liz McHugh for being part of the glue that holds the Anbar Lab together. Thanks to Mou Roy for leading the early efforts of the Agouron drill core curation. Thanks to my fellow graduate students, particularly Aleisha Johnson and Xinming Chen, for sharing their ideas and the experience. Thank you, Christy Till and the entire EPIC group, for holding my hand through my 2nd project. Zircons are beautiful, but just too darn small and hard to see for my liking. Finally, thanks to Meenakshi Wadhwa, Richard Hervig, and Philip Mauskopf for agreeing to serve on my dissertation committee. I hope I wasn't too much of a headache.

Thank you to the collaborators who made the science in this dissertation possible. First and foremost, thank you Sune Nielsen and Jeremy Owens for introducing me to thallium isotopes. Without thallium, this dissertation would just be a bunch of chapters about that boring molybdenum isotope system. Brian Kendall and Tim Lyons, thank you for commenting, at length, on crappy first drafts of manuscripts. I aim to hold myself to the same co-author standards that you two have set. Stephanie Olson, thank you for helping me solve the mysteries of the Jeerinah Formation. Well, at least we tried to solve them. To Ganqing Jiang, Swapan Sahoo, Noah Planavsky, David Johnston, and Erik Sperling, thank you for the introduction to the Ediacaran Period. To those same people, I apologize if I have added only more confusion to the debate. Jurek Blusztajn, thank you for your patience and for helping me generate Tl isotope data at WHOI. Finally, thanks to Chris Holmden for the hours-long conversations about science ethics. I look forward to stealing more of your time in the future.

Last and certainly not least, thank you to my family. To my wife Janet, thanks for carrying the family financially during my studies, and for being the perfect mother to our kids. You are my best friend and the ideal teammate. Why you chose me, I do not know, but I won’t complain. To my kids, Georgia and Benson, thanks for keeping my spry, and for forcing me to have better time management. That sounds somewhat like a joke, but I truly believe that becoming a father made me a better student. Your sticky fingerprints are all over this document.

TABLE OF CONTENTS

LIST OF TABLES

Table Page

LIST OF FIGURES

Figure Page

Figure Page

CHAPTER 1

EARTH'S OCEAN OXYGENATION HISTORY AND HOW MOLYBDENUM AND THALLIUM ISOTOPES CAN BE USED TO TRACK IT

1.1 Earth's ocean oxygenation history

The origin and subsequent evolution of life on Earth is tightly linked to the buildup of molecular oxygen (O_2) in Earth's oceans. In order for O_2 to first accumulate in the ocean, it needed to have been produced by early forms of biology (Lyons et al. 2014). Thereafter, in order to promote the rise of much larger marine animals, this O_2 accumulation needed to have been strong enough to meet their high energetic demands (Knoll 2011). Once animals did evolve, their presence in the ocean was sometimes diminished by transient episodes of ocean deoxygenation (in the form of mass-extinctions; Bond and Grasby 2017). This connection between O_2 and life will even play itself out in the not-so-distant future as Earth's oceans lose O_2 in response to anthropogenic climate forcing (Keeling et al. 2010). It is also plausible to assume that life on other habitable worlds regulates and gets regulated by O_2 accumulation in their respective aquatic environments (Schwieterman et al. 2018).

Oxygenation of Earth's oceans has generally mirrored that of Earth's atmosphere (Fig. 1.1). The initial rise of O_2 in Earth's atmosphere and oceans seems to have occurred sometime after ~2.50 billion-years-ago (Ga), during what is referred to as the Great Oxidation Event (GOE; Bekker et al. 2004, Luo et al. 2016, Philippot et al. 2018). The second rise, after which O_2 levels became comparable to those on Earth today, started sometime after ~635 million-years-ago (Ma) and is referred to as the Neoproterozoic Oxygenation Event (NOE; Scott et al. 2008, Sahoo et al. 2012).

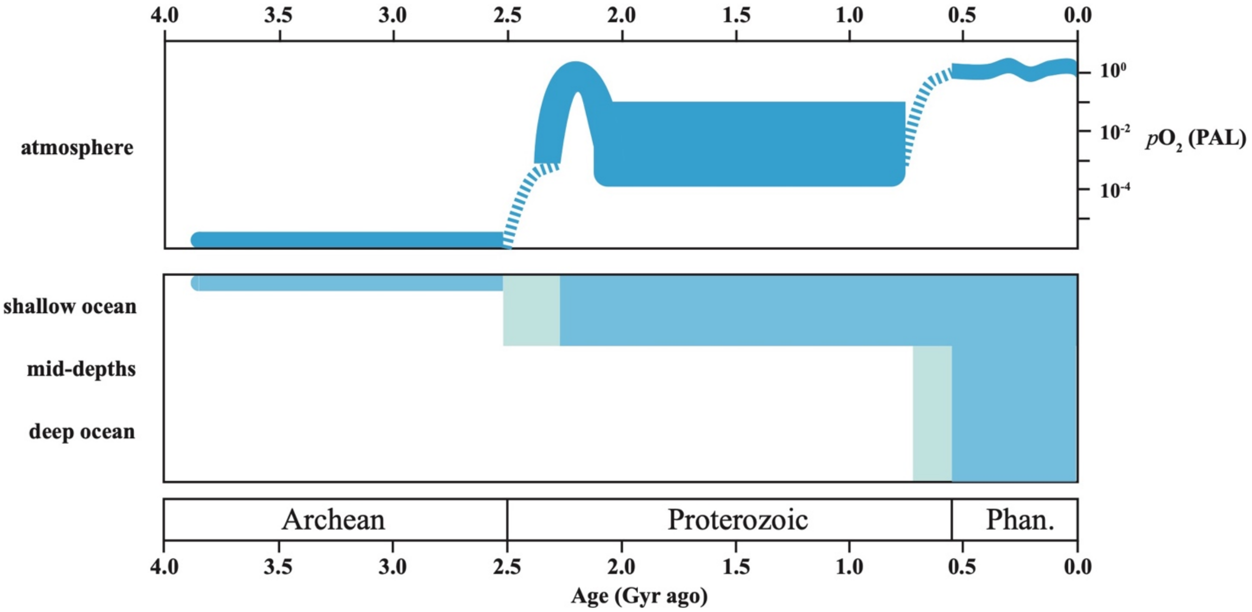

Fig. 1.1 Generalized oxygenation history of Earth's atmosphere (upper panel) and oceans (lower panel). O_2 is quantified in the upper panel in units of partial pressure of O_2 gas relative to the Present Atmospheric Level (PAL; panel modified after Lyons et al. 2014). The depth of O_2 penetration into the worldwide ocean is depicted in the lower panel (panel modified from Lowenstein et al. 2013). Phan. = Phanerozoic.

When viewed in greater detail, however, the oxygenation history of Earth's oceans is not quite so simple. For instance, Earth's two major oxygenation events seem to have been presaged by short-lived episodes of ocean oxygenation (e.g., Sahoo et al. 2012, Ostrander et al. 2019a). Earth's younger oceans seem to have also undergone multiple short-lived episodes of ocean *de*-oxygenation (e.g., Jenkyns 2010). It is therefore inadvisable to assume that Earth's oceans maintained a persistent redox state over large geologic timeframes (as perhaps may be assumed after glancing at Fig. 1.1). The timing and tempo of ocean oxygenation across these timeframes was much more complex, and these complexities merit continued investigation. Some of these complexities, as well as a few others, are expanded upon below.

1.1.1 Ocean oxygenation during the Archean Eon (4.0 Ga to 2.5 Ga)

Biology on Earth probably started producing O_2 sometime during the Archean Eon (4.0 Ga to 2.5 Ga; Lyons et al. 2014). An idea that has gained traction over the past few decades is that, similar to today, some of this early O_2 was probably produced by cyanobacteria in the photic zone of ancient oceans (Fischer 1965). It was posited in Fischer (1965) that O_2 may have even accumulated within patches of the surface ocean where production was especially strong, locations he referred to as "oxygen oases". Much more recently, in studies that resurrect this idea, modeling results suggest that O_2 accumulation in "oases" could have been fairly substantial, reaching up to ~ 10 μM to 25 μM O_2 (Kasting 1993, Olson et al. 2013). Apparently, surface oceans may have been one of the first locations of appreciable O_2 accumulation on Earth.

This idea is justified by Earth's geochemical record. Accumulation of O_2 in the surface ocean would have had a predictable consequence on the cycling of many redox-sensitive elements, and these predictions are at various times supported by the Archean rock record (e.g., Fe [Zerkle et al. 2012], Mo and Re [Kendall et al. 2010], Ce [Riding et al. 2014], and U [Satkoski et al. 2015]). This accumulation would also have had a predictable effect on the isotopic cycling of some elements in ancient oceans, and this prediction is also supported by the rock record (e.g., C [Eigenbrode and Freeman 2006], N

[Godfrey and Falkowski 2009, Garvin et al. 2009, Koehler et al. 2018], S [Kaufman et al. 2007, Eickmann et al. 2018], Se [Stüeken et al. 2015], Mo [Planavsky et al. 2014, Ossa Ossa et al. 2018a, Ostrander et al. 2019a, Thoby et al. 2019], Tl [Ostrander et al. 2020], and U [Kendall et al. 2013]).

1.1.2 Ocean oxygenation during the Proterozoic Eon (2.5 Ga to 542 Ma)

The Proterozoic Eon (2.5 Ga to 542 Ma) is intriguing for multiple reasons. First and foremost, this Eon is bracketed by Earth's two major oxygenation events (apparent in Fig. 1.1). Second, with the exception of these two major events, the Proterozoic is classically thought of as a time in Earth's history when O_2 levels were persistently low (leading to its designation as the "boring billion"; reviewed in Lyons et al. 2014). Scientists have recently flocked to the Proterozoic for these reasons; both to (a) constrain the timing and tempo of Earth's major oxygenation events, and to (b) assess exactly how "boring" – or not – was the oxygenation history of Proterozoic oceans.

Our understanding of the Proterozoic continues to evolve. It is no longer clear that the NOE was regulated to the Neoproterozoic. Instead, it is more likely that the widespread ocean oxygenation associated with the NOE was protracted well into the Phanerozoic Eon (e.g., Lu et al. 2018). It is also likely that the mid-Proterozoic was not as boring as once thought, with oceans perhaps experiencing transient oxygenation episodes (e.g., Zheng et al. 2016). These emerging uncertainties warrant even more research into the oxygenation history of Proterozoic oceans.

1.1.3 Ocean oxygenation during the Phanerozoic Eon (542 Ma to present)

A lot of Phanerozoic (542 Ma to present) research is dedicated to understanding ocean *de*-oxygenation. This de-oxygenation is especially important to understand because, right now, Earth's oceans are losing O_2 (Schmidtko et al. 2017). This is not the first time that Earth's geologically recent oceans lost O_2, however, with many Oceanic Anoxic Events (OAEs) taking place during the Mesozoic Era (~252 Ma to 65 Ma; Jenkyns 2010). By studying these OAEs, we can better understand the potential cause and effects of Earth's future ocean deoxygenation.

1.3 Using Mo isotopes to track past ocean oxygenation

The use of Mo isotopes as a tool for tracking changes in past ocean oxygenation is well-established. In brief, this utility stems from the idea that the Mo isotope composition of seawater (reported in delta notation as $\delta^{98}\mathrm{Mo} = \{({}^{98/95}\mathrm{Mo}_{\mathrm{sample}} \div {}^{98/95}\mathrm{Mo}_{\mathrm{NIST\ SRM\ 3134}} - 1) \times 10^3\} + 0.25‰$ (Nägler et al., 2014)) in Earth's past has been set by the global extent of ocean oxygenation, and that this seawater δ^{98}Mo can be reconstructed using ancient shales.

Today, seawater δ^{98}Mo is globally homogenous and heavier than that of the bulk upper continental crust ($\delta^{98}\mathrm{Mo}_{\mathrm{seawater}} = 2.34 \pm 0.10‰$ (Nägler et al. 2014), compared with $\delta^{98}\mathrm{Mo}_{\mathrm{bulk\text{-}crust}} = 0.47 \pm 0.12‰$ (Willbold and Elliot 2017)). Seawater δ^{98}Mo is homogenous today because the residence time of Mo (~440 kyr; Miller et al. 2011) is much greater than the ocean mixing time (~1.5 kyr). Today's heavy seawater δ^{98}Mo is thought to primarily be a consequence of the preferential removal of lighter-mass Mo isotopes from seawater by Mn oxide minerals in well-oxygenated marine sediments (Barling and Anbar 2004, Wasylenki et al. 2008). Both of the other prominent marine sinks for Mo also preferentially retain lighter-mass Mo isotopes, albeit not to the same extent (i.e., sediments deposited under anoxic and euxinic conditions; summarized in Kendall et al. 2017), and thus they also contribute to driving today's heavy seawater δ^{98}Mo. Little to no Mo isotope fractionation takes place from a mass-balance perspective during delivery of Mo to the ocean (Archer and Vance 2008, Neely et al. 2018, King and Pett-Ridge 2018), meaning this process does not contribute to today's heavy seawater δ^{98}Mo (see Fig. 1.2 for a summary of modern Mo isotope mass-balance).

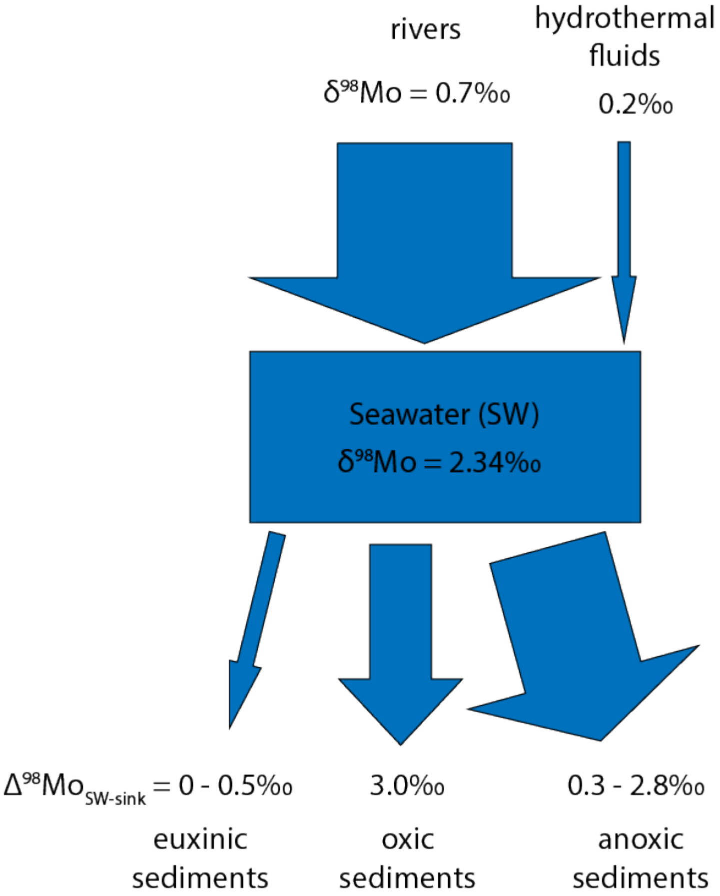

Fig. 1.2 Modern Mo isotope mass-balance. All values are from Kendall et al. 2017.

Also today, the globally homogenous seawater δ^{98}Mo can be transferred to some marine sediments that are deposited under euxinic conditions in restricted basins. In particular, seawater δ^{98}Mo is transferred to euxinic sediments deposited below the chemocline in the Black Sea (Barling et al. 2001, Arnold et al. 2004, Neubert et al. 2008), Kyllaren fjord (Noordmann et al. 2015), and Lake Rogoznica (Bura-Nakić et al. 2018). In these euxinic basins, transfer of seawater δ^{98}Mo to sediments occurs because of near-quantitative removal of Mo from bottom waters. This near-quantitative removal is driven by some combination of (a) the formation of particle-reactive tetrathiomolybdate (MoS_4^{2-}; Helz et al. 1996, Erickson and Helz 2000) and (b) saturation and subsequent precipitation of Fe-Mo-S minerals (Helz et al. 2011). Transfer of seawater δ^{98}Mo to sediments can be hindered in multiple ways, each of which is associated with the non-quantitative transfer of Mo from bottom waters to sediments and the preferential retention of lighter-mass Mo isotopes in sediments. This includes the formation and persistence of intermediate thiomolybdate complexes ($MoO_{4-X}S_4^{2-}$; Neubert et al. 2008), the formation of organic matter (King et al. 2018), or the formation and delivery of Fe oxide (Goldberg et al. 2009) and Mn oxide (Wasylenki et al. 2008) minerals. It is because of these many complicating factors that transfer of seawater δ^{98}Mo to sediments is a somewhat rare occurrence today, even in euxinic settings.

The Mo isotope paleoproxy has been applied to ancient shales for over a decade now, informing much of our current knowledge of Earth's ocean oxygenation history. The general assumption is that, provided the euxinic shales being studied faithfully track past seawater δ^{98}Mo (or nearly so), heavier δ^{98}Mo equate to a better oxygenated ocean, and vice-versa. This assumption is valid because a better oxygenated ocean would be more efficient at burying Mn oxide minerals enriched in lighter-mass Mo isotopes, leading to a complementary accumulation of the heavier-mass Mo isotopes in seawater. Shales deposited under euxinic conditions from the Neoarchean (2.8 Ga to 2.5 Ga) with δ^{98}Mo that are considerably heavier than that of the bulk upper continental crust may fingerprint the early oxygenation of Earth's surface oceans leading up to the GOE (Duan et al. 2010, Ostrander et al. 2019a, Ostrander et al. 2020). Shales deposited under euxinic conditions from the Proterozoic Eon also reveal δ^{98}Mo heavier than crustal values, but they never reach the modern seawater signature (Arnold et al. 2004, Dahl et al. 2010, Dahl et al. 2011, Kendall et al. 2011, Asael et al. 2013, Partin et al. 2015, Diamond et al. 2018, Planavsky et al. 2018, Asael et al. 2018). Most likely, these δ^{98}Mo in Proterozoic shales fingerprint the mildly oxygenated ocean that persisted over much of this Eon. δ^{98}Mo near that of modern seawater are not found until the end of the Proterozoic (Kendall et al. 2015, Ostrander et al. 2019b), pushing the appearance of near-modern levels of ocean oxygenation to around this timeframe. Finally, excursions to lighter δ^{98}Mo in euxinic shales from Mesozoic OAEs track the ocean deoxygenation associated with these events (Westermann et al. 2014, Dickson 2017).

1.2 Using Tl isotopes to track past ocean oxygenation

The use of Tl isotopes as a tool for tracking changes in past ocean oxygenation is fairly new. In brief, and similar to Mo isotopes, this utility stems from the idea that the Tl isotope composition of seawater (reported in epsilon notation as ε^{205}Tl =

($^{205/203}Tl_{sample}/^{205/203}Tl_{NIST\text{-}997} - 1) \times 10^4$) in Earth's past has been set by the global extent of ocean oxygenation, and that this seawater $\varepsilon^{205}Tl$ can be reconstructed using ancient shales.

Today, seawater $\varepsilon^{205}Tl$ is globally homogenous and much lighter than that of the bulk upper continental crust ($\varepsilon^{205}Tl_{seawater} = -6.0 \pm 0.3$ (Nielsen et al. 2006; Owens et al. 2017a), compared to $\varepsilon^{205}Tl_{bulk\text{-}crust} = -2.1 \pm 0.3$ (Nielsen et al. 2005)). Seawater $\varepsilon^{205}Tl$ is homogenous today because the residence time of Tl (~18.5 thousand years, or kyr; Nielsen et al. 2017) is much greater than the ocean mixing time (~1.5 kyr). Today's light seawater $\varepsilon^{205}Tl$ is primarily a consequence of the preferential removal of the heavier-mass Tl isotope from seawater by Mn oxide minerals in well-oxygenated marine sediments (Rehkämper et al. 2002, Nielsen et al. 2013). Neither of the other two prominent marine sinks for Tl preferentially retain the heavier-mass Tl isotope (i.e., low-temperature alteration of oceanic crust [Nielsen et al. 2006] and sediments deposited under anoxic conditions [Owens et al. 2017a, Fan et al. 2020]), and thus they cannot explain today's light seawater $\varepsilon^{205}Tl$. Furthermore, little to no Tl isotope fractionation takes place from a mass-balance perspective during delivery of Tl to the ocean (Nielsen et al. 2005, Baker et al. 2009), meaning this process also cannot account for today's light seawater $\varepsilon^{205}Tl$ (see Fig. 1.3 for a summary of modern Tl isotope mass-balance).

Also today, the globally homogenous seawater $\varepsilon^{205}Tl$ can be transferred to marine sediments deposited under anoxic conditions in basins well-connected to the open ocean. In particular, seawater $\varepsilon^{205}Tl$ is transferred to sediments deposited below the chemocline in Cariaco Basin (Venezuela; Owens et al. 2017a) and Santa Barbara Basin (USA; Fan et al. 2020). In the anoxic and H_2S-rich ("euxinic") Cariaco Basin, it is likely that transfer of seawater ε^{205}Tl to sediments is due to near-quantitative removal of Tl from the bottom waters because Tl concentrations rapidly decline in waters below the chemocline. A similar scenario unfolds today in the euxinic Black Sea, although the seawater ε^{205}Tl that gets transferred to sediments in this strongly restricted basin is a local signature (Owens et al. 2017a). The only time transfer of seawater ε^{205}Tl to sediments seems to be hindered in anoxic basins today is when Mn oxide minerals, which retain isotopically heavy Tl (Nielsen et al. 2013), either form or are delivered to sediments (Rehkämper et al. 2002, Rehkämper et al. 2004, Nielsen et al. 2011).

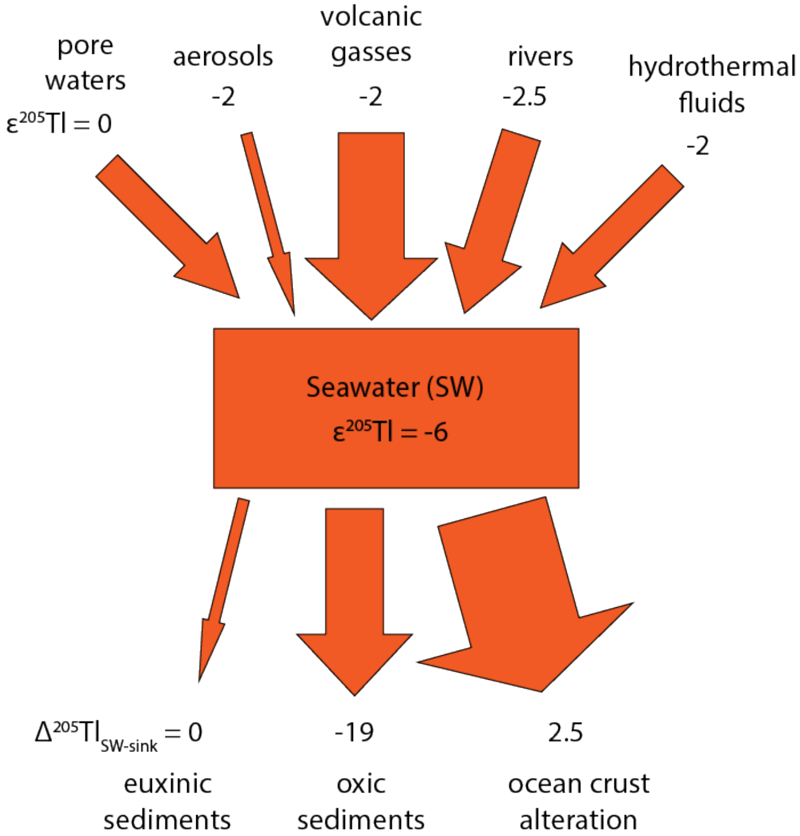

Fig. 1.3 Modern Tl isotope mass-balance. References are as follows: Nielsen et al. 2017, Owens et al. 2017a, Ostrander et al. 2017.

The Tl isotope paleoproxy is being rapidly applied to Earth's past. The general assumption is that, provided the anoxic shales being studied faithfully track past seawater ε^{205}Tl, lighter ε^{205}Tl equate to a better oxygenated ocean, and vice-versa. This assumption is valid because a better oxygenated ocean would be more efficient at burying Mn oxide minerals enriched in the heavier-mass Tl isotope, leading to a complementary accumulation of the lighter-mass Tl isotope in seawater. Shales deposited under anoxic conditions from the Ediacaran Period (635 Ma to 542 Ma) reveal a shift to lighter ε^{205}Tl around the time of the Shuram C-isotope excursion (see Grotzinger et al. 2011), and like the Shuram may fingerprint the widespread oxygenation of Earth's oceans. A heavy ε^{205}Tl excursion in anoxic shales from the late-Silurian Period (444 Ma to 419 Ma) fingerprints ocean deoxygenation during the Lau Kozlowskii Extinction Event (Bowman et al. 2019). Finally, heavy ε^{205}Tl excursions coincident with OAE-2 (Ostrander et al. 2017) and the Toarcian OAE (Them et al. 2018) also fingerprint the well-documented ocean deoxygenation associated with these events.

1.4 The combined utility of Tl and Mo isotopes

There exists some obvious overlap between the Tl and Mo isotope paleoproxies. Both the globally homogenous seawater ε^{205}Tl and δ^{98}Mo are governed in-part by the extent of global ocean oxygenation (but more specifically through associated Mn oxide burial), and both can also be transferred to marine shales deposited under euxinic conditions. It should therefore be possible to track changes in past ocean oxygenation more faithfully by using Tl and Mo isotopes together in the same euxinic shales. The predicted response to changes in ocean oxygenation (or deoxygenation) would be a Tl-Mo isotope anti-correlation because isotopic fractionation during Mn oxide sorption is in the opposing direction for the two isotope systems.

1.5 Dissertation outline

In this dissertation, I begin by applying the well-established Mo isotope proxy to shales deposited primarily under euxinic conditions in the runup to the GOE (~2.7 Ga to 2.5 Ga; Chapter 3). Next, I test the utility of the Tl isotope proxy in shales deposited under euxinic conditions during OAE-2 (~94 Ma; Chapter 2). Thereafter, I pair together for the first time the Mo and Tl isotope proxies in shales deposited under euxinic conditions during an early "whiff" of O_2 (~2.5 Ga; Chapter 4). Next, I apply independently the Mo (Chapter 5) and Tl (Chapter 6) isotope proxies to shales deposited during the rise of animals (~635 Ma to ~550 Ma), in the process learning important information about local-scale overprints for both systems. Finally, I conclude by providing a roadmap for the continued application of Tl and Mo isotopes as tools for tracking past ocean oxygenation.

CHAPTER 2

AN EXPANDED SHALE δ^{98}MO RECORD PERMITS RECURRENT SHALLOW MARINE OXYGENATION DURING THE NEOARCHEAN

The work presented in this chapter has been published as: Ostrander, C.M., Kendall, B., Olson, S.L., Lyons, T.W., Gordon, G.W., Romaniello, S.J., Zheng, W., Reinhard, C.T., Roy, M., Anbar, A.D. (2020) An expanded δ^{98}Mo record permits recurrent shallow marine oxygenation during the Neoarchean. *Chemical Geology* **532**, 119391.

Abstract

Multiple attempts have been made using the ancient shale record to track the molybdenum isotope composition (δ^{98}Mo) of seawater during the final two-hundred million years of the Archean Eon (2.7 to 2.5 billion-years-ago, or Ga). This seawater δ^{98}Mo value is important because it should have scaled with levels of ocean oxygenation during the runup to the Great Oxidation Event (GOE). Unfortunately, however, it is difficult to tell if the majority of the existing late-Archean shale δ^{98}Mo record tracks an ancient seawater value. Here, we further attempt to track pre-GOE seawater δ^{98}Mo using an expanded and well-characterized shale sample set from Western Australia (Jeerinah, Wittenoom, and Mt. Sylvia formations) and South Africa (Nauga and Klein Naute formations). Most importantly, and in contrast to most previous Mo isotope studies of similarly aged shales, local redox conditions for our shales have been independently constrained

using the iron (Fe) speciation proxy and bottom-water Mo contents at the time of deposition have been qualitatively estimated using Mo/TOC ratios. Local redox conditions and bottom water Mo availability are important parameters because transfer of the seawater δ^{98}Mo to sediments today is shown to be dependent on these conditions. According to our updated sedimentary δ^{98}Mo record, seawater δ^{98}Mo commonly exceeded 1.0‰ between ~2.69 Ga and 2.50 Ga. In order to drive such a heavy seawater δ^{98}Mo, there must have been a marine sink with a strong preference for lighter-mass Mo isotopes frequently present over this timeframe. The operation of some anaerobic processes in late-Archean marine settings could theoretically explain the heavier seawater δ^{98}Mo. Such processes are known to promote the preferential retention of lighter-mass Mo isotopes in marine sediments today (e.g., interactions between Mo and organic matter or the formation of thio-complexes). Alternatively, or in addition, adsorption of lighter-mass Mo isotopes to Fe and Mn oxide minerals formed in oxygenated marine environments can explain the heavier seawater δ^{98}Mo. A compilation of previous work suggests that oxygenated shallow marine environments were fairly common during the late-Archean, and thus Mo adsorption to Fe and Mn oxides formed in these settings probably played an important role in driving heavy seawater δ^{98}Mo over this timeframe.

2.1 Introduction

A clearer picture of Earth's initial oxygenation is emerging. Molecular oxygen (O_2) is still thought to have first accumulated in the atmosphere to appreciable levels between about 2.5 and 2.3 billion years ago (Ga), during what is referred to as the Great Oxidation Event (GOE; Bekker et al., 2004, Luo et al., 2016, Gumsley et al., 2017, Philippot et al., 2018). However, many recently discovered lines of evidence suggest that O_2 had accumulated at Earth's surface in small amounts well before the GOE, perhaps as early as ~3.8 Ga (summarized by Lyons et al., 2014). Most likely, this early accumulation took place within oxygen "oases" near the sites of O_2 production: on land within biological soil crusts (Konhauser et al., 2011, Lalonde and Konhauser, 2015), in lacustrine benthic mats (Sumner et al., 2015), or in productive portions of shallow marine environments (Kasting, 1992; Olson et al., 2013). Cyanobacteria in any of these locations could have produced O_2 with minimal impact on global atmospheric oxygenation, keeping O_2 levels in Earth's atmosphere very low until the GOE ($pO_2 < 10^{-5}$ to 10^{-7} the Present Atmospheric Level, or PAL (Farquhar et al., 2000; Pavlov and Kasting, 2002; Zahnle et al., 2006).

Multiple attempts have been made to track the oxygenation of Earth's shallow ocean during the runup to the GOE using molybdenum isotope compositions (reported in delta notation as $\delta^{98}Mo = \{(^{98/95}Mo_{sample} \div {}^{98/95}Mo_{NIST\ SRM\ 3134} - 1) \times 1000\} + 0.25‰$ (Nägler et al., 2014)) preserved in ancient marine shales (Wille et al., 2007; Duan et al., 2010; Eroglu et al., 2015; Kurzweil et al., 2015a; Ostrander et al., 2019a). The $\delta^{98}Mo$ of ancient seawater is generally thought to have scaled with levels of past ocean oxygenation (e.g., Arnold et al., 2004; Dahl et al., 2010; Chen et al., 2015). This idea arises from the fact that insoluble iron (Fe) and manganese (Mn) oxide minerals that can readily form in the presence of O_2

preferentially sorb lighter-mass Mo isotopes (Wasylenki et al., 2008; Goldberg et al., 2009). When O_2 initially accumulated in Earth's ocean, precipitation and deposition of these oxide minerals should have led to the preferential accumulation of heavier-mass Mo isotopes in seawater. This isotopically heavy seawater signature may be recorded as high δ^{98}Mo in certain marine sedimentary rocks. Indeed, a few late-Archean-aged shales and carbonates have significantly heavier δ^{98}Mo (up to δ^{98}Mo = 1.77 ± 0.15‰ (Wille et al., 2007; Duan et al., 2010; Eroglu et al., 2015; Kurzweil et al., 2015a; Ostrander et al., 2019a)) than bulk upper continental crust (δ^{98}Mo = ~ 0.30‰ to 0.40‰ (Greber et al., 2014; Voegelin et al., 2014; Willbold and Elliot, 2017)) and suggest at least sporadic oxygenation of Earth's ocean in the runup to the GOE.

Unfortunately, however, it is extremely difficult to tell whether or not much of the current pre-GOE shale δ^{98}Mo record tracks an ancient seawater signature. Transfer of the seawater δ^{98}Mo value to marine sediments today is shown to be dependent on local redox conditions and bottom water Mo availability (summarized in Kendall et al., 2017). In anoxic and H_2S-bearing ("euxinic") settings, the formation of particle-reactive thiomolybdate species ($MoO_{4-x}S_x^{2-}$) can result in efficient transfer of Mo from seawater into marine sediments (particularly when $H_2S[aq] \geqslant 11\ \mu M$ (Helz et al., 1996; Erickson and Helz, 2000)). When Mo removal from euxinic bottom waters to sediments in these environments is nearly quantitative, then the δ^{98}Mo of the euxinic sediments is equal to the global seawater value—or nearly so. Today, these conditions are met in redox-stratified restricted basins where local bottom water Mo availability is low. In such cases, Mo removal to the underlying euxinic sediments together with slow deep-water exchange with the open ocean hinders Mo recharge to the local bottom waters (the Black Sea (Neubert et al., 2008), Kyllaren fjord (Noordmann et al., 2015), and Lake Rogoznica (Bura-Nakić et al., 2018)). Evidence for locally euxinic depositional conditions has been provided for only a few Archean-aged shales targeted to date for Mo isotope analyses (the 2.7 Ga Carajás Formation from Brazil (Cabral et al., 2013) and the 2.5 Ga Mt. McRae Shale from Western Australia (Duan et al., 2010; Ostrander et al., 2019a)). Furthermore, little is often known about bottom water Mo availability during deposition of these shales (despite established methods for qualitatively estimating this parameter; e.g., Mo/TOC ratios (Algeo and Lyons, 2006)). Accordingly, it is difficult to tell whether or not much of the late-Archean shale δ^{98}Mo record may track ancient seawater δ^{98}Mo. By extension, it is then also difficult to track late-Archean ocean oxygenation using this record (a pitfall also elucidated by differences in the seawater δ^{98}Mo estimates inferred from carbonates and shales from the same late-Archean strata (Voegelin et al., 2010)).

Here, we further attempt to track pre-GOE ocean oxygenation by applying the Mo isotope paleoredox proxy to an expanded set of well-characterized late-Archean-aged shales. We have measured the Mo isotope compositions of 140 ancient shale samples from drill core from Western Australia (from the Jeerinah, Wittenoom, and Mt. Sylvia formations) and South Africa (from the Nauga and Klein Naute formations) deposited between ~2.69 Ga and 2.50 Ga. Critically, and unlike most previous Mo isotope studies of similarly-aged shales, local redox conditions for our shales have been independently constrained using the Fe speciation proxy. Moreover, bottom water Mo contents at the time of deposition for many of our shales have been qualitatively estimated using Mo/TOC ratios.

Iron speciation is an often-employed means for identifying ancient shales that were originally deposited under an euxinic water column (reviewed recently by Raiswell et al., 2018). In short, much of the Fe is present in marine settings in the water column or as species that are reactive toward H_2S on short, diagenetic timescales (e.g., dissolved Fe, carbonates, or oxides), and availability of this reactive Fe is typically elevated under anoxic depositional conditions. For a Precambrian shale to confidently qualify as being originally deposited under an anoxic water column, highly reactive Fe (Fe_{HR}) needs to comprise > 38% of its total Fe content ($Fe_{HR}/Fe_T > 0.38$ (Poulton and Canfield, 2011)). Furthermore, the extent to which these highly reactive Fe-bearing minerals have been converted to pyrite is dependent on the presence or absence of H_2S in the local water column (and perhaps also in sediment pore waters; see Hardisty et al., 2018). As such, Fe as pyrite (Fe_{PY}) needs to comprise at least 80% of the highly reactive Fe pool in an ancient shale for us to interpret the ancient depositional setting as euxinic ($Fe_{PY}/Fe_{HR} > 0.80$ (Poulton and Canfield, 2011)).

A classic method for constraining ancient bottom-water Mo contents is by comparing the relative abundances of Mo and TOC in marine sedimentary rocks (Algeo and Lyons, 2006). Ratios of Mo/TOC are high in sediments from modern euxinic basins that are well connected to the open ocean because Mo in the bottom waters of these basins is continually recharged (e.g., in the modern Cariaco Basin, where sedimentary Mo/TOC ratios average 25 ppm/wt% (Algeo and Lyons, 2006)). In comparison, Mo/TOC are lower in sediments from modern anoxic basins with a poor connection to the open ocean because Mo recharge is comparatively muted (e.g., in the modern Black Sea, where sedimentary

Mo/TOC ratios average 4.5 ppm/wt% (Algeo and Lyons, 2006)). Accordingly, the relative availability of Mo in bottom waters of these basins is fingerprinted by their sedimentary Mo/TOC ratios—that is, a high sedimentary Mo/TOC ratio fingerprints elevated Mo contents in bottom waters, and vice-versa.

By targeting shales of known local depositional redox, and by also qualitatively assessing bottom water Mo availability, we are well positioned to differentiate shales that may have captured the coeval seawater δ^{98}Mo signature during the late-Archean from those that probably did not. By extension, we are then also better prepared to track pre-GOE ocean oxygenation using the ancient shale record.

2.2 Shale Samples

Fig. 2.1 provides a generalized stratigraphy of the cores targeted in this study from the Pilbara Craton of Western Australia and the Kaapvaal Craton of South Africa, their approximate correlations, and highlights available age constraints. Neoarchean shales from these two locations are thought to have been deposited in the same marine basin along the active margin of a paleo-continent referred to as Vaalbara (de Kock et al., 2009). Our cores and their stratigraphy are described in detail in previous work (ABDP9: Anbar et al., 2007, AIDP2 and AIDP3: Koehler et al., 2018, GKP01 and GKF01: Schröder et al., 2006), and so we limit the details below to brief overviews.

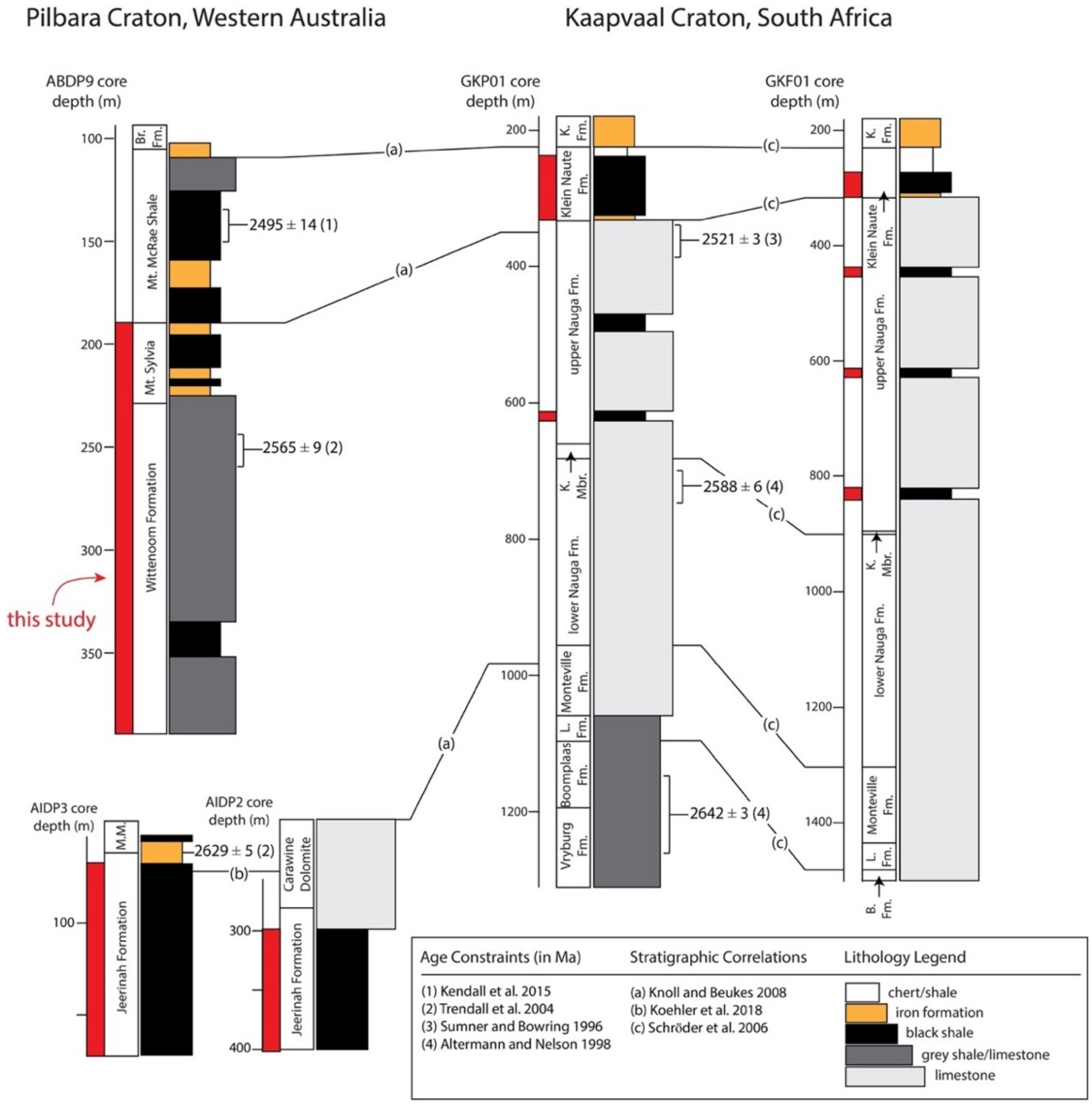

Fig. 2.1 Generalized stratigraphic columns of the drill cores targeted in this study. Intervals targeted in this section are signified by red rectangles to the left of the unit names. For more detailed stratigraphy of these cores, see subsequent figures or refer to Schröder et al., 2006 (GKP01 and GKF01), Anbar et al., 2007 (upper ABDP9), Kurzweil et al., 2015a (lower ABDP9), and Koehler et al., 2018 (AIDP2 and AIDP3). Available geochronological constraints and stratigraphic correlations have been included (see legend box for references). Some unit names have been abbreviated to conserve space: M.M. = Marra Mamba, Br. Fm. = Brockman Iron Formation, L. Fm. = Lokammona Formation, K. Mbr. = Kamden Member, K. Fm. = Kuruman Iron Formation, B. Fm. = Boomplaas Formation.

2.2.1 Western Australia Shales

2.2.1.1. The Jeerinah Formation (~2.69-2.63 Ga)

Organic-rich shales of the Jeerinah Formation, often referred to as the Roy Hill Shale, from two cores recently drilled in Western Australia comprise the oldest rocks targeted in this study. The cores were drilled in the Pilbara Craton in 2012 as part of the Agouron Institute Drilling Program (AIDP) and have been designated as AIDP2 and AIDP3. Sites were chosen based on low regional metamorphism, and special care was taken to avoid drill contamination, specifically for the purpose of testing highly contentious Archean hydrocarbon biomarkers (French et al., 2015). Both cores intersect nearly 100 m of continuous organic-rich and pyritic shale deposition. Shales in both cores are thought to have been deposited below storm wave base along a basinal depth gradient, with shales in AIDP2 being deposited closer to shore than those from AIDP3 (Koehler et al., 2018). The only precise time correlation between the two cores is an impact spherule bed, which occurs in AIDP2 near the bottom of the Carawine Dolomite and in AIDP3 during deposition of the upper Jeerinah Formation (Koehler et al., 2018). Age estimates derived from zircon U-Pb geochronology of volcanoclastics at the bottom and top of the Jeerinah Formation constrain deposition to a timeframe of about 2.690 ± 0.016 Ga (Arndt et al., 1991) to 2.629 ± 0.005 Ga (Trendall et al., 2004).

2.2.1.2. The Wittenoom and Mt. Sylvia Formations (~2.60-2.51 Ga)

Shales of the Wittenoom and Mt. Sylvia formations used in this study come from drill core ABDP9, which was retrieved in the summer of 2004 as a part of the Archean Biosphere Drilling Project (ABDP). Sedimentary rocks preserved in the ABDP9 core have experienced only mild regional metamorphism (prehnite-pumpellyite faces to < 300 °C) and minimal deformation (gentle folding dips <5°) (Brocks et al., 2003). The dominant lithologies in the Wittenoom Formation from ABDP9 are carbonates and gray shales, but black shales occur between 350 m and 330 m core depth and are also interbedded with gray shales between 270 m and 240 m. Sedimentary rocks of the younger Mt. Sylvia Formation oscillate between black shales and banded iron formation. All sedimentary rocks targeted here from drill core ABDP9 are thought to have been deposited below storm wave base in an outer-shelf setting (Morris and Horwitz, 1983). Zircon U-Pb ages of volcanoclastics from the underlying Marra Mamba Formation indicate that deposition of the Wittenoom Formation began after 2.597 ± 0.005 Ga (Trendall et al., 1998), and zircon U-Pb ages for volcanoclastics within the Wittenoom Formation indicate that deposition ended sometime after 2.565 ± 0.009 Ga (Trendall et al., 2004). Shales of the younger Mt. Sylvia Formation were deposited after 2.565 ± 0.009 Ga but before 2.495 ± 0.014 Ga based on a Re-Os age constraint for deposition of the overlying Mt. McRae Shale (Kendall et al., 2015).

2.2.2. South Africa Shales

2.2.2.1. The Nauga and Klein Naute Formations (>2.59-2.50 Ga)

Shale samples from the Nauga and Klein Naute Formations come from two well-preserved and extensive drill cores from South Africa referred to as GKP01 and GKF01. Both cores were drilled as a part of the Agouron Drilling Project, and similar to the recently drilled AIDP cores, water was used as a lubricant to avoid organic contamination (Schröder et al., 2006). Post-depositional alteration is minimal in both cores and limited to gentle tectonic warping due to sub-greenschist facies metamorphism (Miyano and Beukes, 1984).

The dominant lithology in both cores is dolostone and microbialites, but organic-rich shales are present in intervals of both cores (Schröder et al., 2006). These shales include multiple discrete beds within the Nauga Formation (referred to, in order of decreasing age, as N1, N2, and N3 (Kendall et al., 2010)) and a comparatively more extensive occurrence in the Klein Naute Formation. Sedimentary rocks from drill core GKP01 are thought to have been deposited further from shore than those in GKF01 (slope-basin transi- tion versus slope of the carbonate platform, respectively (Schröder et al., 2006)). The transition in both cores from carbonate-dominated deposition of the Nauga Formation to shale-dominated deposition re- corded in the Klein Naute Formation was likely due to drowning of the carbonate platform in response to sea level rise (Schröder et al., 2006). Deposition of the Nauga Formation started earlier than 2.588 ± 0.006 Ga (Altermann and Nelson, 1998) and ended sometime after 2.521 ± 0.003 Ga (Sumner and Bowring, 1996) based on zircon U-Pb ages derived from volcanoclastics in the middle and upper parts of the formation, respectively. A lower age-limit for the Klein Naute Formation is 2.480 ± 0.006 Ga based on a U-Pb age derived from a zircon in the overlying Kuruman Iron Formation (Nelson et al., 1999). A case has also been made that shales from the Klein Naute Formation may be coeval to shales of the Mt. McRae Shale from Western Australia (Kendall et al., 2010 and references therein). If this is correct, deposition of the Klein Naute Formation extended until at least 2.495 ± 0.014 Ga (Kendall et al., 2015).

2.3. Analytical Methods

2.3.1. Fe speciation methods

Iron speciation data was obtained at the Department of Earth and Planetary Sciences at the University of California-Riverside using a calibrated sequential extraction protocol (Reinhard et al., 2009; Kendall et al., 2010). First, about 100 mg of shale sample powder were treated with a buffered sodium acetate solution (pH = 4.5) to extract carbonate-associated Fe (Fe_{carb}: siderite, ferroan calcite, or dolomite-ankerite solid solution series). Next, samples were treated with a buffered sodium dithionite solution (pH = 4.8) to extract "reducible" Fe oxide phases that are reactive to hydrogen sulfide on early diagenetic time- scales (Fe_{OX}: goethite and hematite). Samples were then treated with a 0.2 M ammonium oxalate and 0.17 M oxalic acid solution (pH = 3.2) to extract magnetite (Fe_{mag}). These sequential extractions were diluted 100× in trace metal grade 2% nitric acid and analyzed using an Agilent 7500 cc ICP-MS. Replicate reproducibility was typically better than ~4%. Pyrite iron (Fe_{PY}) was calculated (assuming a stoichiometry of FeS_2) based on the wt% sulfur extracted during a two-hour hot chromous chloride distillation followed by iodometric titration. Replicate reproducibility for this step was typically below ~3%. Highly reactive iron (Fe_{HR}) is defined as the sum of $Fe_{carb} + Fe_{OX} + Fe_{mag} + Fe_{PY}$.

In this study, new Fe speciation data are reported only for shales of the Wittenoom and Mt. Sylvia Formations. Iron speciation data were already published for the other shale units: the Jeerinah Formation in AIDP2 and AIDP3 (Olson et al., 2019) and the Nauga and Klein Naute Formations in GKP01 and GKF01 (Kendall et al., 2010).

2.3.2. Trace metal concentration methods

Trace metal concentration data were generated at the W.M. Keck Foundation Laboratory for Environmental Biogeochemistry, School of Earth and Space Exploration, Arizona State University (ASU). Whole-rock samples were powdered, ashed, and dissolved, and the resulting concentrations were analyzed using the methods outlined in Anbar et al. (2007). In short, powdered samples were ashed overnight in a muffled furnace at 550 °C to help rid samples of organic material. Then, each sample was transferred to a trace metal clean lab and subjected to multiple rounds of concentrated acid digestion using trace metal grade hydrofluoric, hydrochloric, and nitric acid. Once completely dissolved, samples were diluted in 2% nitric acid and a few drops of HF in preparation for concentration analysis on a Thermo Scientific X-series quadrupole ICP-MS.

Trace metal concentrations were measured against multi-element calibration standards. Signal intensities for each analyte were at least three times greater than the blank and were bracketed by the least and most concentrated of these calibration standards. To correct for signal drift, an internal standard solution containing Ge, In, Y, and Bi was introduced in parallel with all samples and standards. Reproducibility for the analyte concentrations was better than 5% except for low Re samples (when Re concentrations are ~1.5 ng/g, the reproducibility drops to ~8%). USGS Geochemical Reference Materials SDO-1 (Devonian Shale) and SCO-1 (Cody Shale) were processed and measured alongside each set of samples to verify accuracy and were reproducible within error of published values.

New trace metal data is reported here only for shales of the Wittenoom and Mt. Sylvia Formations. Trace metal data were already published for the other shales: the

Jeerinah Formation in AIDP2 and AIDP3 (Olson et al., 2019) and the Nauga and Klein Naute Formations in GKP01 and GKF01 (Kendall et al., 2010).

2.3.3. Mo isotope methods

Isotope purification and analysis was also conducted at the W.M. Keck Foundation Laboratory at ASU following procedures outlined in previous work (Ostrander et al., 2019a, and references therein). In brief, enough sample was taken from stock solutions to provide 125 ng of Mo, followed by double-spiking with synthetic Mo (^{97}Mo and ^{100}Mo) prior to purification via ion exchange chromatography (Barling et al., 2001). After the sample matrix was removed, isotope ratio measurements were performed on a Thermo Neptune multi-collector ICPMS (MC-ICPMS) in low-resolution mode utilizing sample-standard bracketing and double spike analysis to correct for instrumental mass bias. Both samples and standards were analyzed at a concentration of 25 ng/ g Mo, which yielded typically around three volts of signal on mass 98. Individual sample solutions were analyzed in duplicate at least, but the overwhelming majority were analyzed in triplicate.

Average 2SD sample reproducibility was 0.05‰, and the maximum was 0.17‰. All measurements were made relative to the Johnson Matthey Specpure Mo plasma standard (Lot #802309E; RochMo2) and then recalculated relative to the international NIST SRM 3134 standard set to +0.25‰ (Nägler et al., 2014). In brief, the measured value for NIST SRM 3134 during our analytical sessions was 0.33 ± 0.03‰ (2SD) relative to RochMo2 (Table 2.1). Accordingly, 0.08‰ was subtracted from each sample measured relative to RochMo2 to yield the sample isotope composition relative to NIST SRM 3134 = +0.25‰. USGS rock reference material SDO-1 was simultaneously processed with each batch of samples to monitor accuracy and showed good reproducibility (1.01 ± 0.10‰ [2SD, n = 21] compared to a multi-laboratory average of 1.05 ± 0.14‰ [2SD] from Goldberg et al., 2013), as did various sample solutions (Table 2.1). Reported errors for our samples are always in 2SD and either equal to the 2SD reproducibility of the SDO-1 powder processed alongside our samples (0.10‰; noted above) or the individual sample's reproducibility, whichever is greater. For each analytical run, we measured a series of standards with varying spike-sample ratios. All samples were within the validated spike-sample range for accurate and precise δ^{98}Mo measurements.

Table 2.1 Mo isotope data from standard reference material solutions

Standard	δ^{98}Mo[a]	N	Normalized to NIST + 0.25‰	Goldberg et al. (2013)
ICL-Mo	0.16 ± 0.03‰	36	0.08 ± 0.03‰	0.09 ± 0.05‰
Kyoto-Mo	-0.05 ± 0.05‰	36	-0.13 ± 0.05‰	-0.12 ± 0.06‰
NIST SRM 3134	0.33 ± 0.03‰	41	0.25‰	0.25‰
SDO-1	1.13 ± 0.05‰	41	1.05 ± 0.05‰	1.05 ± 0.14‰

a. measured relative to Roch-Mo2

*all reported errors are 2SD of the standard reproducibility

2.4 Results

In addition to highlighting the results of our study, we also recap in this section pertinent Fe speciation and elemental concentration data reported in previous studies of the same shale samples.

2.4.1 Data from shales of the Jeerinah Formation

Iron speciation data from the Jeerinah Formation in drill cores AIDP2 and AIDP3 were recently reported by Olson et al., 2019 (Fig. 2.2). Instances of elevated Fe_{HR}/Fe_T and Fe_{Py}/Fe_{HR} ratios are present in both drill cores. For example, $Fe_{HR}/Fe_T \geq 0.38$ and $Fe_{Py}/Fe_{HR} \geq 0.80$ (ratios that can be ascribed confidently to local euxinia (Poulton and Canfield, 2011)) are found in most Jeerinah shales from AIDP2 between 374.67 m and 342.74 m. Similar ratios are found in all shales from the AIDP3 drill core between 101.77 m and 78.56 m. Outside of these intervals, the majority of shale samples from both drill cores have lower Fe_{HR}/Fe_T and Fe_{Py}/Fe_{HR} ratios suggestive of ferruginous conditions.

Molybdenum concentration data were also recently reported for these shales, ranging from as low as 1 μg/g to as high as 10 μg/g (Olson et al., 2019; Fig. 2.2). In general, Mo abundances were found to be greater in the AIDP2 drill core when Fe_{HR}/Fe_T and Fe_{Py}/Fe_{HR} ratios were elevated (between 374.67 m and 342.74 m). This observation was not the case in AIDP3, however, as Mo abundances in this drill core were generally higher when $Fe_{Py}/Fe_{HR} < 0.80$.

Bulk-rock δ^{98}Mo compositions measured by us in shales from the Jeerinah Formation range from −0.25 ± 0.10‰ to 1.02 ± 0.10‰ (Fig. 2.2). The heaviest shale δ^{98}Mo in both drill cores are within error of one another (0.98 ± 0.10‰ in AIDP2 and 1.02 ± 0.10‰ in AIDP3), and both occur when Fe_{HR}/Fe_T is $\geq$0.38 and Fe_{Py}/Fe_{HR} is $\geq$0.80. Overall, δ^{98}Mo in shales from AIDP2 are heavier when Fe speciation ratios are elevated (between 374.67 m and 342.74 m, where the average δ^{98}Mo = 0.85 ± 0.31‰). Molybdenum isotope compositions are comparatively lighter outside of this interval, peaking at 0.69 ± 0.10‰ at 377.89 m and averaging 0.53 ± 0.25‰. In comparison, the relationship between δ^{98}Mo and

Fe speciation data in shales from AIDP3 is less obvious. For example, heavy δ^{98}Mo values are found in AIDP3 shales with elevated Fe speciation ratios (e.g., 1.02 ± 0.10‰ at 68.22 m) as well in shales with lower Fe speciation ratios (e.g., 0.82 ± 0.10‰ at 130.17 m). Relatively light δ^{98}Mo are also found in AIDP3 when Fe_{HR}/Fe_T and Fe_{Py}/Fe_{HR} are elevated (e.g., 0.25 ± 0.10‰ at 101.77 m) as well as when they are low (e.g., −0.25 ± 0.10‰ at 74.10 m).

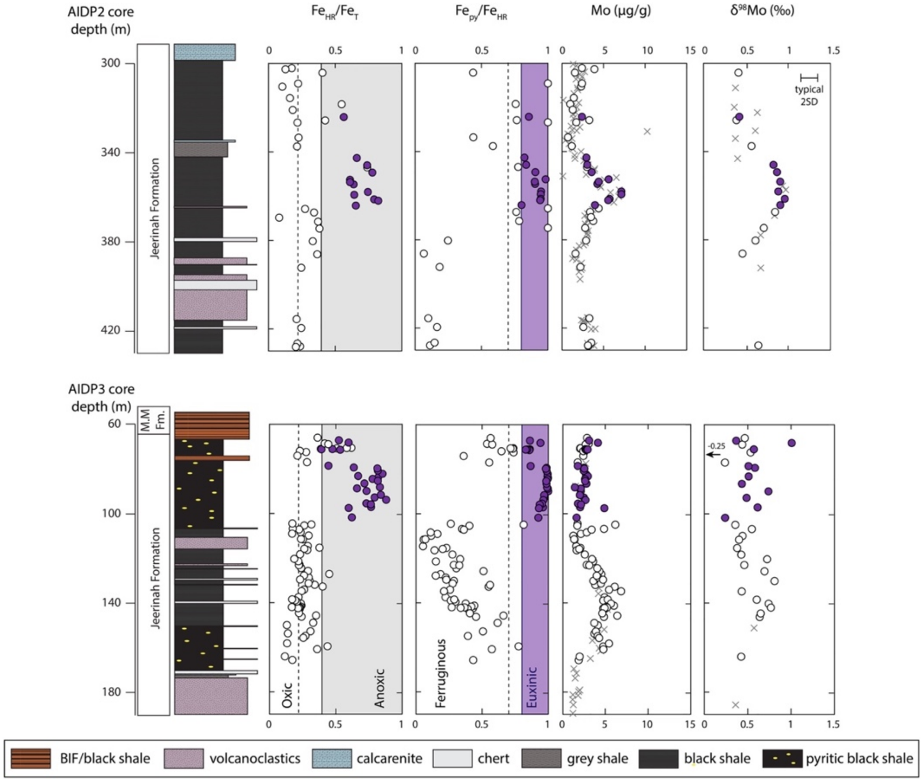

Fig. 2.2 Geochemistry of shales from the Jeerinah Formation preserved in drill cores AIDP2 (top) and AIDP3 (bottom). Stratigraphy is modified from Koehler et al. (2018) and iron speciation and Mo concentration data are from Olson et al., 2019. Purple circles signify shale samples deposited, according to Fe speciation, under euxinic conditions ($Fe_{HR}/Fe_T \geq 0.38$ and $Fe_{Py}/Fe_{HR} \geq 0.80$ (Poulton and Canfield, 2011)). Dashed lines signify relaxed thresholds for anoxic and euxinic conditions ($Fe_{HR}/Fe_T \geq 0.22$ and $Fe_{Py}/Fe_{HR} \geq 0.70$ (Poulton and Canfield, 2011)). White circles signify shale samples deposited under non-euxinic conditions. Shale samples represented with an “x” have no accompanying Fe speciation data. All δ^{98}Mo are bulk-rock values

2.4.2 Data from shales of the Wittenoom and Mt. Sylvia Formations

Our Fe speciation ratios generated for shales of the Wittenoom and Mt. Sylvia Formations from drill core ABDP9 are generally low (Fig. 2.3). Only one shale sample from these formations has Fe_{HR}/Fe_T of ≥0.38 and Fe_{Py}/Fe_{HR} of ≥0.80 (at 209.67 m in the Mt. Sylvia Formation). There is a slight increase in Fe_{HR}/Fe_T and Fe_{Py}/Fe_{HR} ratios toward the top of the Wittenoom Formation, starting at 235.71 m core depth. Above this depth and throughout the Mt. Sylvia Formation, Fe_{HR}/Fe_T is commonly > 0.38. No samples below 235.71 m possess Fe_{HR}/Fe_T ratios of ≥0.38.

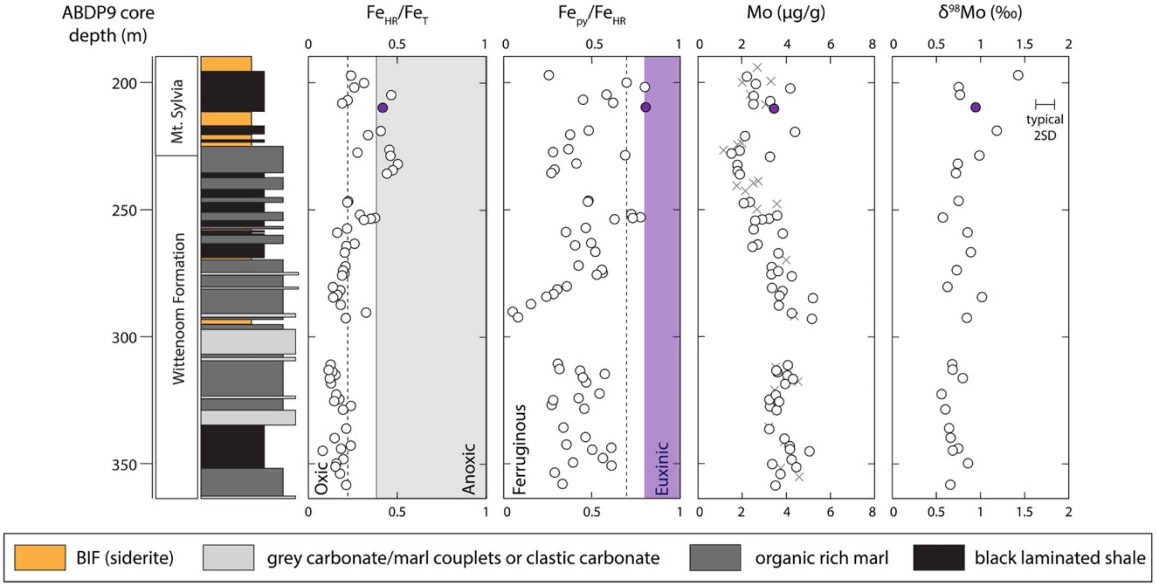

Fig. 2.3 Geochemistry of shales from the Wittenoom and Mt. Sylvia Formations preserved in drill core ABDP9. The lone purple circle signifies the only shale sample deposited, according to Fe speciation, under euxinic conditions ($Fe_{HR}/Fe_T \geq 0.38$ and $Fe_{Py}/Fe_{HR} \geq 0.80$ (Poulton and Canfield, 2011)). Dashed lines signify relaxed thresholds for anoxic and euxinic conditions ($Fe_{HR}/Fe_T \geq 0.22$ and $Fe_{Py}/Fe_{HR} \geq 0.70$ (Poulton and Canfield, 2011)). White circles signify shale samples deposited under non-euxinic conditions. Shale samples represented with an “x” have no accompanying Fe speciation data. All δ^{98}Mo are bulk-rock values.

Our Mo concentrations range from 1 μg/g to 5 μg/g in shales from the Wittenoom and Mt. Sylvia formations (Fig. 2.3). The only stratigraphic trend in Mo abundances occurs at 253.99 m core depth, where Fe_{HR}/Fe_T and Fe_{Py}/Fe_{HR} both increase slightly. Above this depth, Mo abundances dip to as low as 1 μg/g. Such low Mo abundances are not seen lower in the section.

Molybdenum isotope compositions range from 0.57 ± 0.10‰ to 1.44 ± 0.10‰ in shales from the Wittenoom and Mt. Sylvia formations (Fig. 2.3). The two heaviest δ^{98}Mo values occur in shales from the younger Mt. Sylvia Formation (1.20 ± 0.10‰ at 218.91 m and 1.44 ± 0.10‰ at 197.00 m), with the heavier of these two coming from our uppermost shale sample in ABDP9. For comparison, the heaviest δ^{98}Mo from the Wittenoom Formation is 1.03 ± 0.10‰ at 284.57 m. Outside of these few heavy isotope compositions, the remainder of the δ^{98}Mo in both formations are isotopically lighter and fairly invariant (average δ^{98}Mo = 0.75 ± 0.22‰).

2.4.3. Data from shales of the Nauga Formation

Kendall et al. (2010) and Zerkle et al. (2012) previously reported Fe speciation data for the shales in the Nauga Formation from drill cores GKP01 and GKF01 (Figs. 2.4 and 2.5). Between the two drill cores, only a single shale sample from GKP01 in the lowermost N1 interval of the Nauga Formation showed Fe_{HR}/Fe_T of ≥0.38 and Fe_{Py}/Fe_{HR} of ≥0.80 (639.20 m core depth).

Molybdenum abundances in Nauga shales from GKP01 and GKF01 are persistently low in all sampling intervals, peaking at 3 μg/g (Figs. 2.4 and 2.5). The lowest Mo concentrations from any shale units targeted in this study come from N1 in the Nauga

Formation, with values as low as 0.2 μg/g in GKF01. Molybdenum abundances increase slightly in the younger shales, eclipsing 2 μg/g for the first time in the N2 and N3 intervals of both cores.

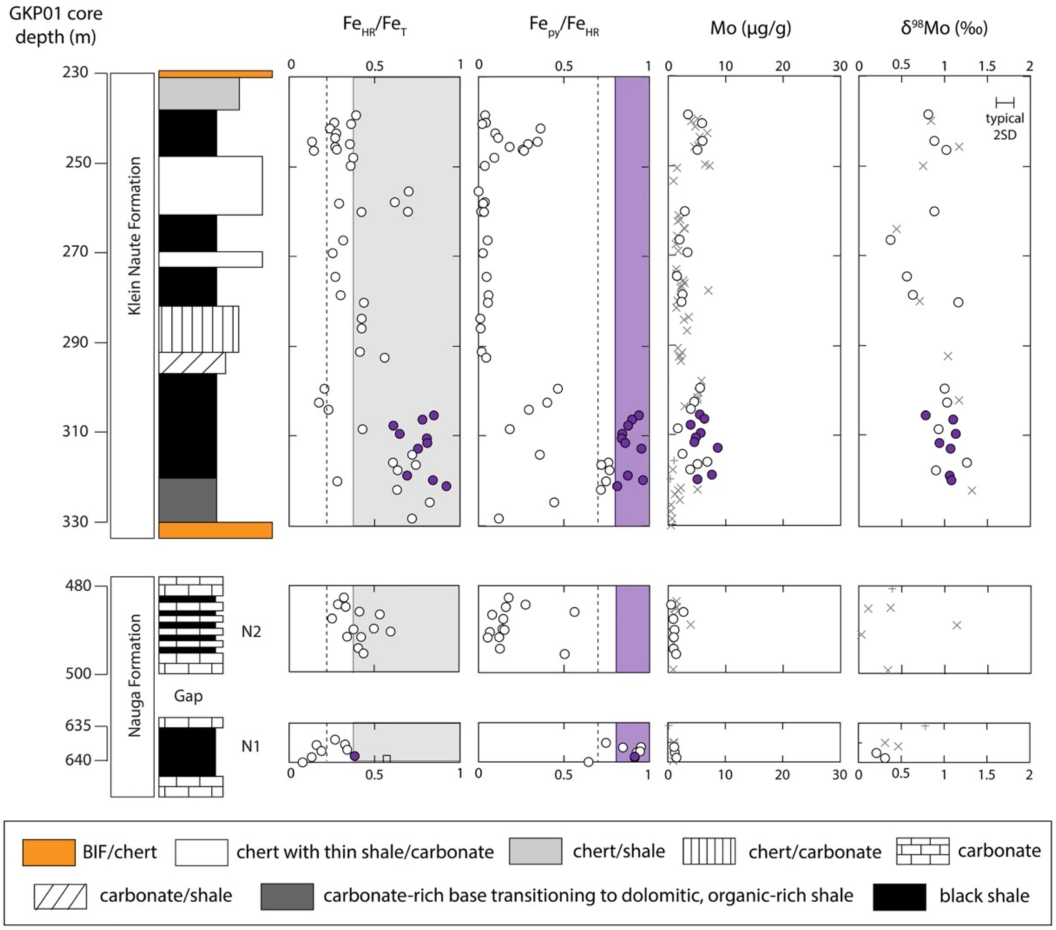

Fig. 2.4 Geochemistry of shales from the Klein Naute and Nauga Formations preserved in drill core GKP01. Stratigraphy, iron speciation, and the bulk of the Mo concentration data is from Kendall et al. (2010). Purple circles signify shale samples deposited, according to Fe speciation, under euxinic conditions ($Fe_{HR}/Fe_T \geq 0.38$ and $Fe_{Py}/Fe_{HR} \geq 0.80$ (Poulton and Canfield, 2011)). Dashed lines signify relaxed thresholds for anoxic and euxinic conditions ($Fe_{HR}/Fe_T \geq 0.22$ and $Fe_{Py}/Fe_{HR} \geq 0.70$ (Poulton and Canfield, 2011)). White circles signify shale samples deposited under non-euxinic conditions. Shale samples represented by "x" have no accompanying Fe speciation data and, in some cases, are from Wille et al. (2007). Samples represented by "+" are carbonates measured in Voegelin et al. (2010). All δ^{98}Mo are bulk-rock values.

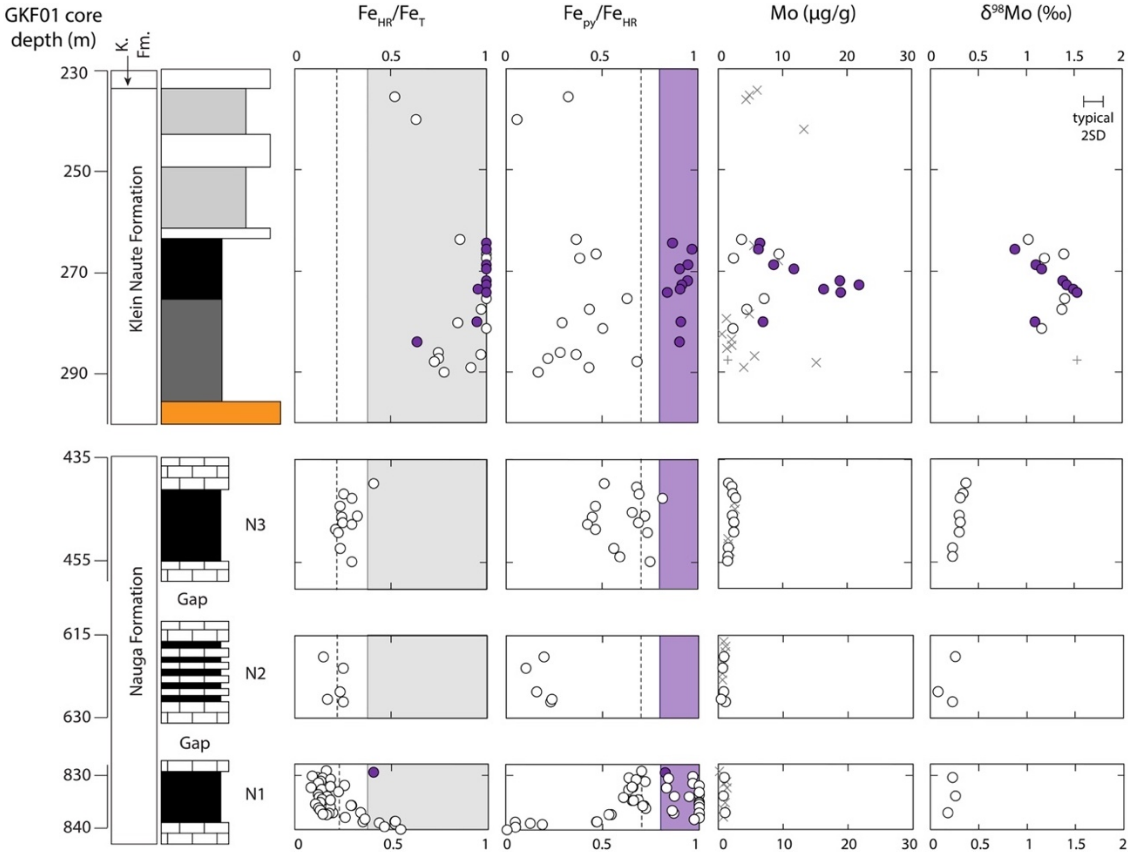

Fig. 2.5 Geochemistry of shales from the Klein Naute and Nauga Formations preserved in drill core GKF01. Stratigraphy, iron speciation, and the bulk of the Mo concentration data is from Kendall et al. (2010). Purple circles signify shale samples deposited, according to Fe speciation, under euxinic conditions ($Fe_{HR}/Fe_T \geq 0.38$ and $Fe_{Py}/Fe_{HR} \geq 0.80$ (Poulton and Canfield, 2011)). Dashed lines signify relaxed thresholds for anoxic and euxinic conditions ($Fe_{HR}/Fe_T \geq 0.22$ and $Fe_{Py}/Fe_{HR} \geq 0.70$ (Poulton and Canfield, 2011)). White circles signify shale samples deposited under non-euxinic conditions. Shale samples represented by "x" have no accompanying Fe speciation data. Samples represented by "+" are carbonates measured in Voegelin et al. (2010). See Fig. 2.4 for a stratigraphic legend. All δ^{98}Mo are bulk-rock values.

Molybdenum isotope compositions in Nauga shales reported here are also persistently low in both drill cores, spanning a restricted range from 0.10 ± 0.10‰ to 0.38 ± 0.10‰ (Figs. 2.4 and 2.5). The lowest δ^{98}Mo value comes from the N2 interval of GKF01 (625.18 m). The heaviest δ^{98}Mo comes from the N3 interval of GKF01 (439.64 m). Of the seven total shale samples in the Nauga Formation with δ^{98}Mo between 0.30‰ and 0.38‰, six are from this N3 interval in GKF01.

2.4.4. Data from shales of the Klein Naute Formation

Iron speciation and trace metal data were also reported by Kendall et al. (2010) for the Klein Naute Formation shales targeted here from drill cores GKP01 and GKF01 (Figs. 2.4 and 2.5). Both drill cores have extended intervals of Klein Naute shale deposition where Fe_{HR}/Fe_{T} is ≥0.38 and Fe_{Py}/Fe_{HR} is ≥0.80. In GKP01, these elevated Fe speciation ratios are found in many samples between 321.10 m and 305.34 m. In GKF01, similarly elevated Fe speciation ratios are found in many samples between 284.00 m and 264.43 m. Outside of these depth ranges in both cores, Fe_{HR}/Fe_{T} ratios often eclipse 0.38, but Fe_{Py}/Fe_{HR} never again exceeds 0.80. Fe_{Py}/Fe_{HR} are especially low in GKP01 between 292.50 m and 248.00 m, never exceeding 0.10.

Molybdenum abundances are highest in shales from the Klein Naute Formation compared to any of the other shale units we targeted, reaching values as high as 22 µg/g in GKF01 (at 272.71 m as reported in Kendall et al., 2010; Figs. 2.4 and 2.5). In GKF01, high Mo abundances are found primarily in shales with elevated Fe speciation ratios (i.e., between 284.00 m and 264.43 m). The highest Mo abundances in GKP01 are also found primarily in shales with elevated Fe speciation ratios (i.e., between 321.10 m and 305.34 m). However, Mo abundances in GKP01 are not as high as those in GKF01, reaching only 8.6 µg/g (312.73 m).

Molybdenum isotope compositions in shales from the Klein Naute Formation span a wide range, from as low as 0.38 ± 0.10‰ to as high as 1.54 ± 0.11‰ (Figs. 2.4 and 2.5).

Values for δ^{98}Mo are generally heavier in GKF01 compared to GKP01. For example, the heaviest observed δ^{98}Mo from both drill cores is from GKF01 (1.54 ± 0.11‰ at 274.23 m core depth). In GKP01, the heaviest δ^{98}Mo value is 1.27 ± 0.10‰ (at 315.85 m core depth). Furthermore, only one shale sample of the fourteen we measured for the Klein Naute Formation in GKF01 has a δ^{98}Mo lower than 1.0‰ (0.89 ± 0.12‰ at 265.67 m core depth). In GKP01, half of the shale samples we measured (10 out of 20) have δ^{98}Mo values lower than 1.0‰. Of note, the heaviest δ^{98}Mo value for GKF01 comes from a shale sample with a Fe_{HR}/Fe_T ratio of $\geq$0.38 and $Fe_{Py}/Fe_{HR} \geq 0.80$. In GKP01, the heaviest δ^{98}Mo is not found in a shale sample with Fe speciation ratios that meet or exceed these thresholds. However, this sample is located within the interval of shales in GKP01 where Fe_{HR}/Fe_T and Fe_{Py}/Fe_{HR} often exceed 0.38 and 0.80, respectively (between 321.10 m and 305.34 m). The three lightest δ^{98}Mo values in the Klein Naute Formation (0.38‰ to 0.64‰) are from shales in GKP01 with especially low Fe_{HR}/Fe_T and Fe_{Py}/Fe_{HR} ratios (< 0.38 and < 0.10, respectively, between 292.50 m and 248.00 m).

2.5 Discussion

In the following section we begin by discussing the influence of detrital contamination (Section 5.1.) and local redox conditions (Section 5.2.) on our shale δ^{98}Mo data. Guided by our new data, we then estimate the seawater δ^{98}Mo values between ~2.69 Ga and 2.50 Ga (Section 5.3.). This text is followed by a discussion of the links connecting our seawater δ^{98}Mo estimates to pre-GOE ocean oxygenation (Section 5.4.).

2.5.1 Impact of detrital contamination on δ^{98}Mo

It is evident that the extent of detrital Mo contamination played a key role in governing the δ^{98}Mo of our late Archean shales. When shale δ^{98}Mo are cross-plotted against Mo/Al for the same samples, a general logarithmic correlation is revealed (R^2 = 0.65; Fig. 2.6). This correlation most likely fingerprints binary mixing in our samples between two distinct Mo sources. One of these sources had a low Mo/Al ratio and a light δ^{98}Mo, each comparable to recent estimates for the modern upper continental crust (Mo/Al = 0.13 ppm/wt% (Rudnick and Gao, 2003) and δ^{98}Mo = ~ 0.30‰ to 0.40‰ (Greber et al., 2014; Voegelin et al., 2014; Willbold and Elliot, 2017)). Because Earth's upper continental crust is what eventually becomes detrital material, this first source was probably detritus. The other source had a much higher Mo/Al ratio and a heavier δ^{98}Mo and was most likely seawater-derived (authigenic) Mo. It is reasonable to assume, since this correlation is found in shales deposited over ~200 million years, that the δ^{98}Mo of both of these Mo sources was fairly constant over this timeframe. Thus, our measured bulk-shale δ^{98}Mo was probably set primarily by the relative contribution from each (and to some extent also local depositional redox; see Section 5.2.).

For the remainder of the text, we will discuss calculated authigenic δ^{98}Mo contributions to our shale samples and not the detritally contaminated bulk-rock δ^{98}Mo. The fraction of Mo derived from detrital material ($f_{detrital}$) for any shale sample can be estimated by:

$$f_{detrital} = (Al_{shale} \times Mo/Al_{detrital})/Mo_{shale},$$

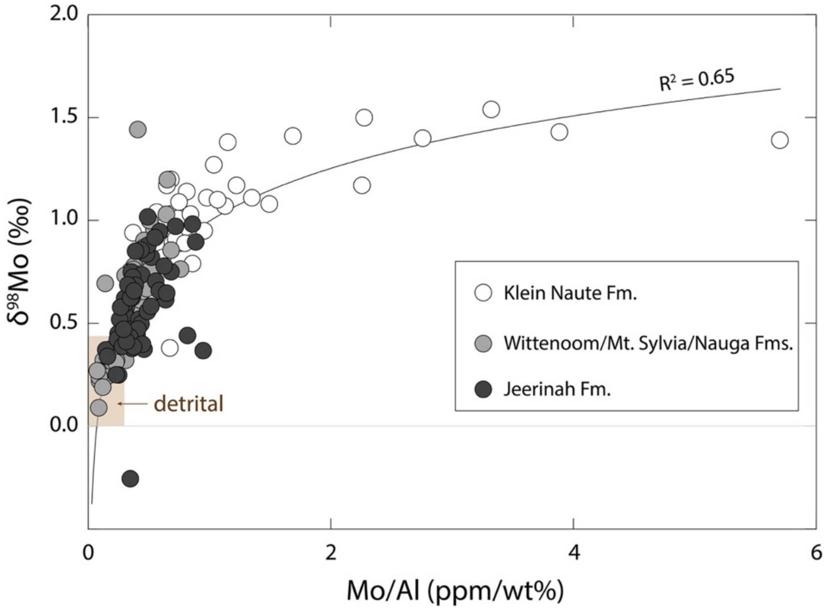

Fig. 2.6 A cross-plot of δ^{98}Mo versus Mo/Al for all shales in our sample set. The black line is a logarithmic trendline through the data ($R^2 = 0.65$). This general trend may signify binary mixing between a light δ^{98}Mo and low Mo/Al component (perhaps continental detritus) and a comparatively heavy δ^{98}Mo and high Mo/Al component (perhaps a seawater-derived authigenic component). All δ^{98}Mo are bulk-rock values.

where Mo_{shale} signifies the Mo abundances measured in our bulk-shale samples, and $Mo/Al_{detrital}$ represents the Mo/Al ratio of detrital material (assumed here to be equal to that of the upper continental crust: 0.13 ppm/wt% (Rudnick and Gao, 2003)). Then, the authigenic δ^{98}Mo contribution ($\delta^{98}Mo_{authigenic}$) can be estimated by;

$$\delta^{98}Mo_{authigenic} = [\delta^{98}Mo_{shale} - \delta^{98}Mo_{detrital} \times f_{detrital}]/1 - f_{detrital},$$

where $\delta^{98}Mo_{shale}$ and $\delta^{98}Mo_{detrital}$ signify the bulk-shale and detrital Mo isotope compositions, respectively. Here, we assume $\delta^{98}Mo_{detrital}$ was 0.25‰ because this is the value extrapolated from our shale dataset in Fig. 2.6 when Mo/Al is assumed to be 0.13 (the most recent estimate for the bulk upper continental crust (Rudnick and Gao, 2003)).

Although our detrital δ^{98}Mo estimate is slightly lighter than recent estimates for the modern upper continental crust (δ^{98}Mo = ~ 0.30‰ to 0.40‰ (Greber et al., 2014; Voegelin et al., 2014; Willbold and Elliot, 2017)), it is in general agreement with a value extrapolated from detrital-rich late Archean shales from drill cores GKP01 and GKF01 analyzed in another study (0.20‰ (Wille et al., 2007)). Furthermore, it is reasonable to assume that Archean continental crust had a greater proportion of mafic and ultramafic rocks with comparatively light δ^{98}Mo (δ^{98}Mo = ~ 0.05‰ (Greber et al., 2015; McCoy-West et al., 2019)).

Notably, we do not calculate $\delta^{98}Mo_{authigenic}$ values for shales with $f_{detrital} \geq 0.60$. We choose to impose this "detrital cutoff" because calculated $\delta^{98}Mo_{authigenic}$ values for shales with such high $f_{detrital}$ become particularly dependent on $\delta^{98}Mo_{detrital}$ and $Mo/Al_{detrital}$. This dependence is illustrated in Fig. 2.7 and expanded upon below. It is reasonable to assume that detrital source rocks during the Archean possessed δ^{98}Mo between that of komatiites (~ 0.05‰ (Greber et al., 2015; McCoy-West et al., 2019]) and the maximum estimated value for upper continental crust (~0.40‰ (Greber et al., 2014; Voegelin et al., 2014; Willbold and Elliot, 2017)). When $\delta^{98}Mo_{authigenic}$ is calculated for each of our shale samples using these endmember $\delta^{98}Mo_{detrital}$, the correction applied to our shales (that is, the difference between the calculated authigenic value and the measured shale value, or $\Delta^{98}Mo_{authigenic-shale}$) becomes especially variable above $f_{detrital}$ ~ 0.80 (differences in $\Delta^{98}Mo_{authigenic-shale}$ > 3.0‰ between the separate $\delta^{98}Mo_{detrital}$; Fig. 2.7, upper panel). Likewise, detrital source rocks during the Archean probably possessed Mo/Al (in ppm/wt%) between that of the upper continental crust (0.09 (Wedepohl, 1995) to 0.13 (Rudnick and Gao, 2003)) and komatiites (~0.18, based on a recent study of Archean komatiites from multiple cratons (Sossi et al., 2016)). When $\delta^{98}Mo_{authigenic}$ are calculated

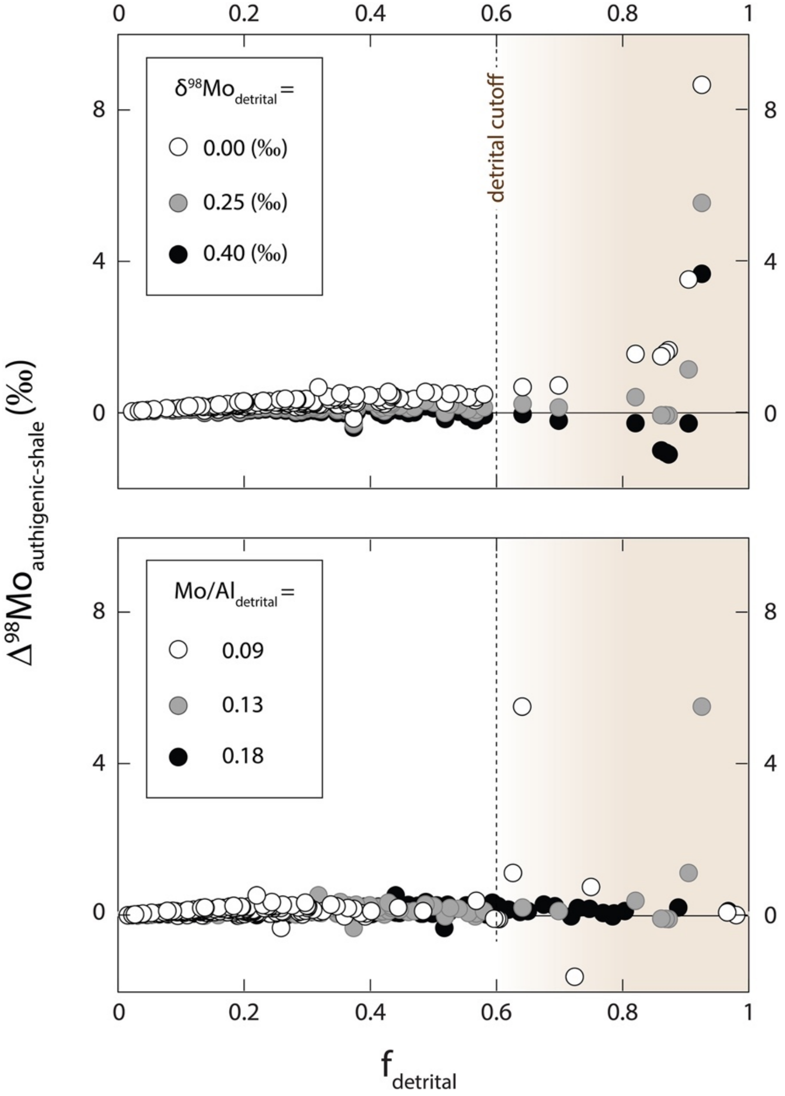

Fig. 2.7 Cross-plots illustrating the magnitude of authigenic correction that is applied to our shale samples for a given detrital δ^{98}Mo and Mo/Al value. (upper panel) Magnitude of δ^{98}Mo correction (signified by $\Delta^{98}Mo_{authigenic-shale}$) that is applied to our measured bulk-rock shale values assuming Mo/Al = 0.13, but with variable $\delta^{98}Mo_{detrital}$. (lower panel). Magnitude of correction that is applied to our measured bulk-rock shale values assuming $\delta^{98}Mo_{detrital}$ = 0.25, but with variable $Mo/Al_{detrital}$. Because the authigenic corrections become highly dependent on $\delta^{98}Mo_{detrital}$ and/or $Mo/Al_{detrital}$ above $f_{detrital}$ ~0.6, we have chosen to not utilize for interpretation $\delta^{98}Mo_{authigenic}$ from shales with $f_{detrital} \geq 0.6$.

using the plausible $Mo/Al_{detrital}$ endmembers, the corrections become especially variable above $f_{detrital}$ ~0.60 (differences in $\Delta^{98}Mo_{authigenic-shale}$ > 6.0‰ between the separate

$Mo/Al_{detrital}$; Fig. 2.7, lower panel). The only scenario that results in highly variable $\Delta^{98}Mo_{authigenic\text{-}shale}$ with $f_{detrital} < 0.60$ is one in which $\delta^{98}Mo_{detrital}$ was equal to komatiites (0.00‰) and $Mo/Al_{detrital}$ was equal to a lower-limit estimate for the modern upper continental crust (0.09) (scenario not plotted in Fig. 2.7). Because this pairing is unlikely, we think our $f_{detrital} < 0.60$ cutoff is reasonable.

2.5.2 Impact of local redox conditions on shale δ^{98}Mo

2.5.2.1 Shales deposited under locally euxinic conditions

Shales of the Jeerinah and Klein Naute formations were at times deposited under at least locally euxinic conditions (signified by $Fe_{HR}/Fe_T \geq 0.38$ and $Fe_{Py}/Fe_{HR} \geq 0.80$ (Poulton and Canfield, 2011)). Hence, by analogy with modern settings (Barling et al., 2001; Neubert et al., 2008; Noordmann et al., 2015; Bura-Nakić et al., 2018), these shales are our best candidates to have captured ancient seawater δ^{98}Mo values. Just because Fe speciation data in these late-Archean shales suggests local deposition was euxinic, however, does not necessarily mean that transfer of the seawater δ^{98}Mo to sediments definitely took place. For various reasons in euxinic settings today (e.g., insufficient H_2S and/or an overabundance of Mo in local bottom waters), quantitative transfer of Mo to sediments does not occur, along with incomplete conversion to thio-complexes. The result is sedimentary δ^{98}Mo that are isotopically lighter than the seawater value (e.g., $\Delta^{98}Mo_{seawater\text{-}sediment} \leq 0.5$‰ in strongly euxinic settings (Nägler et al., 2011; Bura-Nakić et al., 2018) and $\Delta^{98}Mo_{seawater\text{-}sediment} = 0.5$–3.0‰ in weakly euxinic settings (Arnold et al., 2004; Neubert et al., 2008)). In this subsection, we discuss some reasons to be optimistic about the capture of ancient seawater δ^{98}Mo in these shales and some others that are less encouraging.

There is reason to think that bottom-water Mo contents were low when deposition of shales from the Jeerinah and Klein Naute formations occurred under a euxinic water column, and this scenario would have helped promote transfer of seawater δ^{98}Mo to sediments. Ratios of Mo/TOC in shales from the Jeerinah (up to 1.1 ppm/wt%) and Klein Naute (up to 3.3 ppm/wt%) formations deposited under euxinic conditions are lower than those found in sediments from the modern Black Sea (4.5 ppm/wt% (Algeo and Lyons, 2006)). Thus, it is possible that bottom-water Mo concentrations at the original depositional sites for our euxinic shale samples from the Jeerinah and Klein Naute formations – and perhaps even in the worldwide ocean (Scott et al., 2008) – were predominantly very low, perhaps lower than those found in bottom waters of the modern Black Sea (< 10 nM (Nägler et al., 2011)). If so, transfer of the seawater δ^{98}Mo to these sediments was plausible, particularly if bottom-water sulfide concentrations were high.

On the other hand, there is also reason to imagine that only weakly or unstable euxinic conditions developed during deposition of some shales from the Jeerinah Formation, a scenario that could have hindered transfer of the seawater δ^{98}Mo to these shales. A case was made in Olson et al., 2019, based on a general correlation between Mo and S abundances in shales from the Jeerinah Formation in drill core AIDP2, that Mo delivery to the original sediments was limited by low or unstable sulfide availability. In modern marine settings where localized euxinia is weak or unstable, quantitative transfer of Mo from seawater to sediments does not occur and leads to sedimentary δ^{98}Mo that are always lighter than the seawater value (e.g., Neubert et al., 2008; Nägler et al., 2011;

Noordmann et al., 2015). More specifically, the formation and persistence of intermediate thiomolybdates ($MoO_{4-x}S_x^{2-}$)) in modern settings with low or variable H_2S contents drives sedimentary δ^{98}Mo lighter than the value of overlying waters because these intermediates have δ^{98}Mo that are lighter than the seawater value (Tossel, 2005). Ancient bottom-water H_2S contents cannot be quantified using the Fe speciation proxy, nor can H_2S stability. Therefore, by analogy with modern settings, δ^{98}Mo in some of our shale samples from the Jeerinah Formation may be isotopically lighter than the ancient seawater δ^{98}Mo despite Fe speciation ratios indicating euxinic deposition. It is also worth noting, however, that capture of seawater δ^{98}Mo by some sediments deposited under weakly or unstable euxinic conditions was nonetheless still plausible in an Archean ocean with low Mo availability (an idea expanded upon in the Section 5.2.2.).

Some geochemical trends in shales from the Klein Naute Formation may also suggest that seawater δ^{98}Mo was not transferred to these shales. For example, Mo abundances in shales from the Klein Naute Formation are the highest of any shale unit we studied (up to 22 µg/g; Kendall et al., 2010). In at least some modern marine settings where sedimentary Mo abundances are very high (e.g., reaching 200 µg/g in sediments from the Cariaco Basin (Lyons et al., 2003)), transfer of the seawater δ^{98}Mo to sediments does not occur (Arnold et al., 2004). Sedimentary Mo abundances are extremely high in these settings today because they maintain a strong connection with the Mo-replete open ocean—a connection that provides a continuous supply of Mo (Algeo and Lyons, 2006). This continuous supply of Mo, however, also hinders quantitative transfer of Mo from bottom waters to sediments in these settings. Consequently, sedimentary δ^{98}Mo in sediments from these settings are always isotopically lighter than seawater δ^{98}Mo (for example, because of the formation and persistence of intermediate thiomolybdates (Nägler et al., 2011)). By analogy, shales from the Klein Naute Formation that were deposited beneath a euxinic water column and have comparatively elevated Mo abundances may also possess δ^{98}Mo that are isotopically lighter than contemporaneous seawater if they were deposited in a setting that received a steady and appreciable supply of Mo from the open ocean.

2.5.2.2. Shales deposited under locally non-euxinic conditions

Shales we studied that were deposited beneath a non-euxinic water column are less likely to have captured the seawater δ^{98}Mo value. The overwhelming majority of our shale samples analyzed for Mo isotopes from the Wittenoom, Mt. Sylvia, and Nauga Formations possess Fe_{HR}/ Fe_T and Fe_{Py}/Fe_{HR} ratios indicative of non-euxinic depositional conditions (that is, $Fe_{HR}/Fe_T < 0.38$ and/or $Fe_{Py}/Fe_{HR} < 0.80$ (Poulton and Canfield, 2011)). Although not as prevalent, similar Fe speciation data are also found in many of our shale samples analyzed for Mo isotopes from the Jeerinah and Klein Naute Formations.

Before continuing, it is worth noting here that the formation of pyrrhotite in ancient sedimentary rocks can lead to the misidentification of ferruginous local redox conditions (Slotznick et al., 2018). Pyrrhotite is HCl-soluble and would thus be dissolved during the Fe_{carb} extraction, in turn driving Fe_{HR}/Fe_T and Fe_{Py}/Fe_{HR} ratios higher and lower, respectively (toward the ranges for ferruginous ratios: Fe_{HR}/ $Fe_T \geq 0.38$ and Fe_{Py}/FeHR < 0.8 (Poulton and Canfield, 2011)). Because we did not use mineralogical, petrographic, or geochemical techniques to identify shales from our sample set that contained pyrrhotite, it is therefore theoretically possible that some of our shales with Fe speciation ratios indicative of ferruginous depositional conditions were actually deposited in an oxic or euxinic setting. Importantly, to help differentiate oxic from ferruginous local redox conditions in this subsection, we rely not only on Fe speciation data but also on accompanying trace metal data. Similarly, to account for the possibility of locally euxinic conditions during deposition of our "ferruginous" (at least according to Fe speciation data) shales, we do not rule out the idea of these shale samples capturing past seawater δ^{98}Mo (as can happen in euxinic settings; discussed at length in the previous subsection).

Today, incomplete transfer of Mo from marine bottom-waters to sediments in non-euxinic marine settings results in sedimentary δ^{98}Mo that are highly variable but always isotopically lighter than coeval seawater (Δ^{98}Mo$_{\text{seawater-sediments}}$ = 0–3‰; summarized in Kendall et al. (2017)). This high degree of variability stems from the many processes shown to promote retention of lighter-mass Mo isotopes in marine sediments. For example, various combinations of complexation of Mo with Fe oxide minerals (Goldberg et al., 2009), Mn oxide minerals (Wasylenki et al., 2008), organic matter (King et al., 2018), and the formation of intermediate thiomolybdate species in sediment pore fluids and the water column (Neubert et al., 2008) can result in varying magnitudes of sedimentary enrichment in lighter-mass Mo isotopes in these settings. By analogy, the majority of our measured δ^{98}Mo from late-Archean shales with Fe$_{\text{HR}}$/Fe$_{\text{T}}$ values of < 0.38 and/or Fe$_{\text{Py}}$/Fe$_{\text{HR}}$ ratios of <0.80 may be isotopically lighter than contemporaneous seawater. It is difficult to estimate precisely how much lower than contemporaneous seawater δ^{98}Mo our measured δ^{98}Mo values are.

Shales from the Nauga Formation in GKP01 and GKF01 would be expected to have especially light δ^{98}Mo because these samples are thought to have been deposited in an environment where O_2 penetrated into marine sediments (Kendall et al., 2010). In modern marine settings where O_2 penetrates into sediment pore waters, in-situ formation of Fe and Mn oxide minerals results in sedimentary δ^{98}Mo considerably lighter than the contemporaneous seawater signature ($\Delta^{98}\text{Mo}_{\text{seawater-sediments}}$ = 0.3 to 2.8‰ when Fe oxides are present and $\Delta^{98}\text{Mo}_{\text{seawater- sediments}}$ = 1.9 to 3.3‰ when Mn oxides are present (Goldberg et al., 2012)). In support of this hypothesis, shales from the Nauga Formation have the lightest $\delta^{98}\text{Mo}_{\text{authigenic}}$ of all the Archean shale units we studied (average $\delta^{98}\text{Mo}_{\text{authigenic}}$ = 0.33‰).

Shales from the Wittenoom and Mt. Sylvia Formations were most likely deposited in a locally anoxic marine environment—that is, not under the same oxidizing conditions inferred for shales from the Nauga Formation. In modern marine settings where O_2 penetrates mildly into marine sediments (i.e., up to ~1 cm), Re is shown to accumulate more efficiently than does Mo (Morford et al., 2005). This geochemical pattern was found in shales from the Nauga Formation (N2 and N3) and was interpreted as evidence for mild water-column oxygenation and O_2 penetration into the original marine sediments (Kendall et al., 2010). Shales from the Wittenoom and Mt. Sylvia formations, however, are not enriched in Re relative to Mo (Fig. 2.8). One possible interpretation of these muted Re enrichments is that the original deposition environment was well-oxygenated, thereby permitting the penetration of O_2 into marine sediments to depths > 1 cm (conditions today that are not conducive to sedimentary Re retention (Morford et al., 2005)). However, δ^{98}Mo in shales from the Wittenoom and Mt. Sylvia Formations (average $\delta^{98}\text{Mo}_{\text{authigenic}}$ = 1.01‰) are considerably heavier than those from the roughly coeval Nauga Formation (average $\delta^{98}\text{Mo}_{\text{authigenic}}$ = 0.33‰). Thus, these shales were probably deposited in an anoxic environment less affected by lighter-mass Mo delivery by Fe and/or Mn oxide minerals.

Just because Fe speciation ratios in these shales suggest that deposition occurred under non-euxinic conditions does not mean there was no transfer of seawater Mo and even δ^{98}Mo to the sediments. As an example, some sediments deposited today in open-ocean continental margin settings contain H_2S strictly in shallow pore fluids but are nonetheless still fairly efficient at removing Mo from overlying waters (e.g., sediments from the Peru Margin (Poulson Brucker et al., 2009; Scholz et al., 2017)). Today, in the Mo-replete ocean, quantitative transfer of Mo is not achieved in these settings and results in a systematic isotopic offset between these sediments and seawater ($\Delta^{98}\mathrm{Mo}_{\mathrm{seawater\text{-}sediments}}$ = ~0.7‰, an effect governed by the formation and persistence of intermediate thiomolybdate species (Siebert et al., 2006; Poulson et al., 2006; Poulson Brucker et al., 2009; Nägler et al., 2011)). During the Archean, however, when dissolved Mo is thought to have been much less abundant in seawater than it is today (by at least an order of magnitude (Scott et al., 2008)), the Mo removal efficiency of these settings may have been sufficient enough in some instances to promote quantitative transfer to sediments. If correct, seawater δ^{98}Mo would have been transferred to sediments in these settings. Most importantly, it would be extremely difficult to identify such settings using Fe speciation data because sedimentary Fe speciation ratios are highly variable in modern marine settings where H_2S is restricted to sediment pore fluids ($\mathrm{Fe}_{\mathrm{HR}}/\mathrm{Fe}_{\mathrm{T}}$, in particular; see Hardisty et al. (2018)).

Shales with relatively heavy δ^{98}Mo, even if Fe speciation data suggests deposition was non-euxinic, are especially difficult to explain if the isotope data are not representative of seawater (or nearly so). For instance, two of our heaviest $\delta^{98}\mathrm{Mo}_{\mathrm{authigenic}}$ come from shales of the Mt. Sylvia Formation ($\delta^{98}\mathrm{Mo}_{\mathrm{authigenic}}$ = 1.44‰ at 218.91 m and 2.00‰ at 197.00 m core depth). If these ancient shales did not capture the coeval seawater δ^{98}Mo, then it implies that seawater at that time possessed an even heavier δ^{98}Mo (because all sediments today either capture the seawater δ^{98}Mo value or an isotopically lighter value; summarized in Kendall et al. (2017)). Although an even heavier seawater δ^{98}Mo cannot be ruled-out, it is worth considering that the heavier of these δ^{98}Mo$_{\text{authigenic}}$ already exceeds the heaviest Archean seawater δ^{98}Mo estimates made to date (up to δ^{98}Mo = ~1.8‰ (Duan et al., 2010; Cabral et al., 2013)). Alternatively, these shales from the Mt. Sylvia Formation may have captured the seawater δ^{98}Mo value.

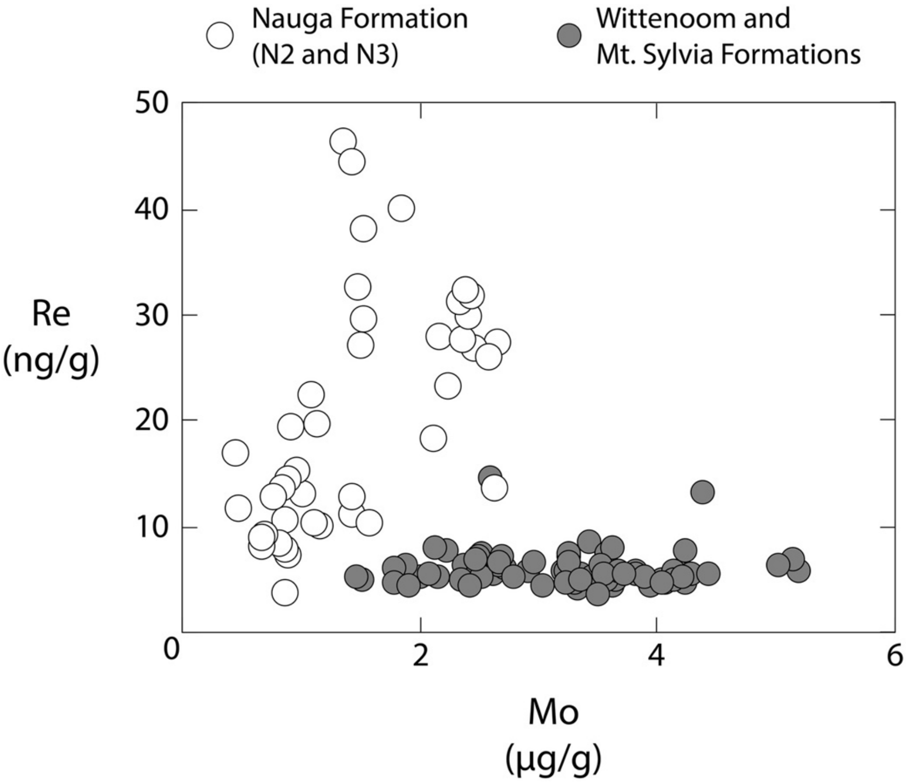

Fig. 2.8 Shale Re and Mo abundance cross plot from the roughly coeval Nauga (Kaapvaal Craton) and Wittenoom/Mt. Sylvia (Pilbara Craton) Formations. Trace metal abundance data from the Nauga Formation is from Kendall et al. (2010) and is interpreted as evidence for locally suboxic conditions during original deposition. Our new data from the Wittenoom and Mt. Sylvia Formations does not possess the same trend and therefore was probably not deposited under the same local redox conditions.

2.5.3 Evolution of the seawater δ^{98}Mo between ~2.69 Ga and 2.50 Ga

Before we attempt to constrain the δ^{98}Mo of late Archean seawater, it is important to first discuss some key characteristics of this signature. Namely, would our seawater δ^{98}Mo estimates be indicative of a local or global signature, and how variable was the δ^{98}Mo signature?

It is possible that our seawater δ^{98}Mo estimates are representative of a well-mixed and globally homogenous open-ocean value. The paleo-basin where sedimentary rocks from the Pilbara and Kaapvaal Cratons were originally deposited is thought to have had significant water exchange with the open-ocean (Morris and Horwitz, 1983; Beukes, 1987; de Kock et al., 2009). Therefore, shales from both cratons were likely in contact with open-ocean seawater during original deposition. If these shales captured the coeval seawater δ^{98}Mo value, then it was likely an open-ocean value. Moreover, previous calculations show that, even under the projected low dissolved seawater Mo abundances in the Archean (< 5 nM; Scott et al., 2008), the residence time of Mo (τMo) in Archean oceans would have still been much longer than the ocean mixing time (~ 1.5 kyr today). Kendall et al. (2011) estimated an Archean τMo of 35 kyr assuming a modern ocean Mo input flux. A model of the Proterozoic ocean estimated a comparable τMo of > 30 kyr (with some more unlikely scenarios still yielding τMo estimates > 3 kyr; Dahl et al. (2011)).

Our seawater δ^{98}Mo estimates are likely, at the minimum, to be representative of a regionally homogenous value. We argue this because we base our seawater δ^{98}Mo estimates on Mo isotope data from sedimentary rocks from both the Pilbara and Kaapvaal Cratons (discussed in the remainder of the Section). Sedimentary rocks from these two locations are thought to have been deposited ~1000 km apart (de Kock et al., 2009), so any agreement in seawater δ^{98}Mo estimates using rocks from these two locations likely signifies an at least regional seawater signature. A regional (localized) seawater δ^{98}Mo during the Neoarchean is theoretically possible if the residence time of Mo in the ocean was lower than that of the ocean mixing time, despite suggestions otherwise (outlined in the previous paragraph). For example, if the size of the Archean seawater Mo reservoir has been overestimated and/or if the ocean mixing time during the Archean was longer than it is today (for example, because of limited upwelling on a faster rotating early-Earth; Olson et al., 2020), then seawater δ^{98}Mo in an ancient basin may have been different from the δ^{98}Mo of open-ocean seawater. One implication of a regional seawater δ^{98}Mo is that it may have been particularly sensitive to changes in the δ^{98}Mo of local riverine inputs. This is because individual rivers can have highly variable, non-crustal δ^{98}Mo (Archer and Vance, 2008), even though the overwhelming majority of Mo delivered to the global ocean by rivers today is isotopically un- fractionated relative to bulk upper continental crust (King and Pett- Ridge, 2018).

Finally, at various times in Earth's history the seawater δ^{98}Mo signature may have fluctuated on relatively short timescales in response to changes in ocean oxygenation (over hundreds of thousands of years during Mesozoic Oceanic Anoxic Events (e.g., Dickson, 2017) to a few million years during Ediacaran Oceanic Oxygenation Events (Ostrander et al., 2019b)). Such fluctuations were possible during deposition of our shale samples and would be difficult to identify—that is, to distinguish from local controls on the δ^{98}Mo of local sediments. Hence, we do not focus on identifying possible, relatively short-term events.

2.5.3.1. Seawater δ^{98}Mo between ~2.69 Ga and 2.63 Ga

During deposition of the Jeerinah Formation, seawater δ^{98}Mo reached a value at least as heavy as 1.29‰ (see Fig. 2.9). This estimate comes from the heaviest authigenic-corrected shale δ^{98}Mo during euxinic deposition (at 68.22 m core depth in AIDP3). Again, as stated earlier (Section 5.2.1.), there is reason to think that shales from the Jeerinah Formation may not have captured the seawater δ^{98}Mo value. In general support of this idea, carbonates from the broadly time-equivalent Lokammona and Monteville formations (Beukes and Gutzmer, 2008) in GKF01 and GKP01 may have at times also captured seawater δ^{98}Mo and reveal slightly heavier δ^{98}Mo: bulk-rock $\delta^{98}\text{Mo}_{\text{NIST+0.25‰}}$ up to 1.58 ± 0.07‰; 2SE in GKF01 and authigenic $\delta^{98}\text{Mo}_{\text{NIST+0.25‰}}$ up to 1.95‰ in GKP01.

During deposition of the Wittenoom and Nauga Formations, seawater δ^{98}Mo seems to have commonly exceeded ~1.0‰ (see Fig. 2.9). Shales from the Wittenoom Formation are not strong candidates to have captured seawater δ^{98}Mo (Section 5.2.2.). Nonetheless, calculated authigenic δ^{98}Mo sometimes exceed 1.0‰ in these shales (9/21 samples) with the likelihood of an even heavier seawater δ^{98}Mo during their deposition. Authigenic δ^{98}Mo from the Nauga Formation never exceed this value, reaching only 0.61‰, but this is not surprising because shales from the Nauga Formation were likely deposited in oxic settings known in modern oceans to possess a strong preference for lighter-mass Mo isotopes (e.g., Poulson Brucker et al., 2009; Goldberg et al., 2012). Previously reported δ^{98}Mo in time-equivalent bulk-shale and carbonate samples from the Campbellrand-Malmani carbonate platform also sometimes exceed 1.0‰, peaking at values as high as 1.40 ± 0.11‰; 2SE (Eroglu et al., 2015).

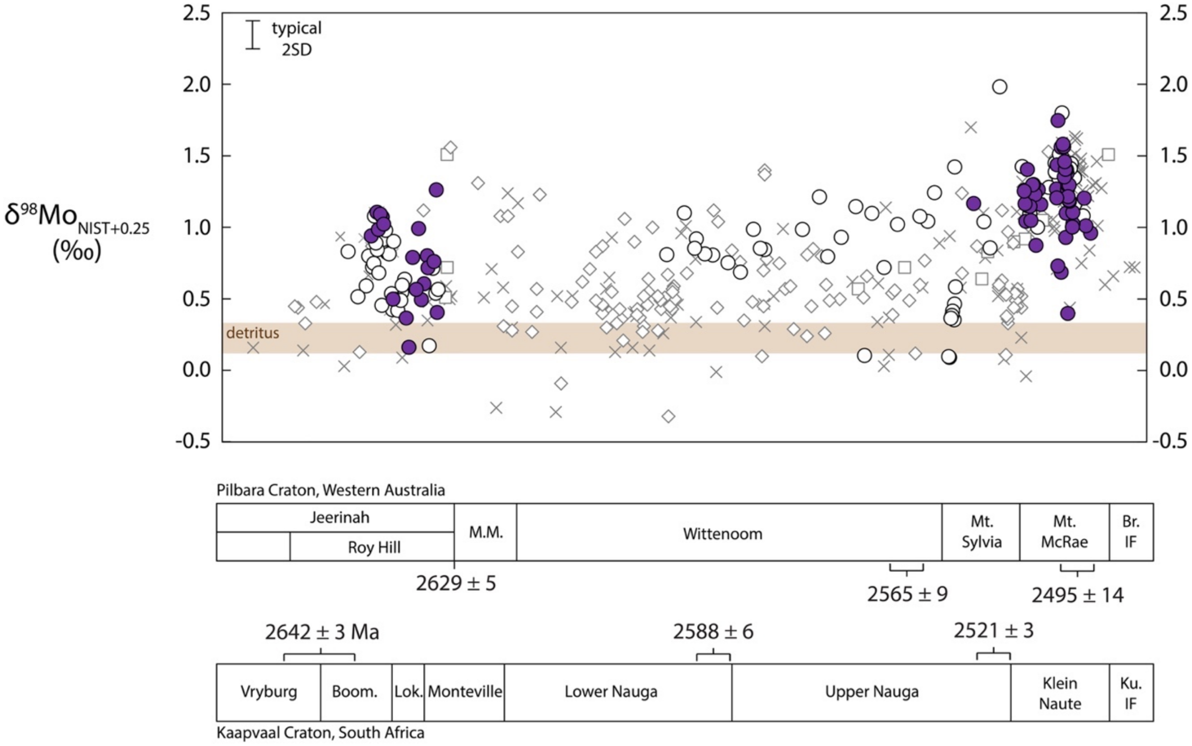

Fig. 2.9 Updated late-Archean (~2.70 Ga to 2.50 Ga) sedimentary Mo isotope record. See Fig. 2.1 for geochronological references. An authigenic correction has been applied to the majority of data from this study (see Section 5.1.). Purple circles signify shale samples deposited, according to Fe speciation, under euxinic conditions ($\mathrm{Fe_{HR}/Fe_{T}} \geq 0.38$ and $\mathrm{Fe_{Py}/Fe_{HR}} \geq 0.80$ (Poulton and Canfield, 2011)). White circles signify shale samples deposited under non-euxinic conditions. Shale samples represented by "x" have no accompanying Fe speciation data. Samples represented by diamonds are carbonates, and squares signify Mo isotope data from iron formations. The brown rectangle signifies our estimated late-Archean detrital δ^{98}Mo value (~0.25‰; see Section 5.1.). Data sources are as follows: Wille et al. (2007), Voegelin et al. (2010), Duan et al. (2010), Kurzweil et al. (2015a), Eroglu et al. (2015), Ostrander et al., 2019a, and this study.

2.5.3.2. Seawater δ^{98}Mo between ~2.60 Ga and 2.51 Ga

Seawater δ^{98}Mo may have been especially heavy during deposition of the Mt. Sylvia and uppermost Nauga formations. One of our shale samples from the Mt. Sylvia Formation has an extremely heavy calculated authigenic δ^{98}Mo value of 2.00‰ (at 197 m core depth in ABDP9). An exceptionally heavy bulk-rock δ^{98}Mo of 1.70 ± 0.02‰; 2SE was also found previously in a shale sample from the uppermost Nauga Formation in GKP01 (Wille et al., 2007).

2.5.3.2. Seawater δ^{98}Mo at 2.50 Ga

During deposition of the Klein Naute Formation, seawater δ^{98}Mo reached a composition of at least 1.59‰ (see Fig. 2.9). This value is equal to the heaviest of our authigenic-corrected δ^{98}Mo for a shale in the Klein Naute Formation (at 274.23 m core depth in GKF01). These shales are plausible candidates for having at times captured and preserved seawater δ^{98}Mo (Section 5.2.1.). Shales from the time-equivalent Mt. McRae Shale in Western Australia that were also deposited under euxinic conditions (Reinhard et al., 2009), and therefore possibly captured seawater δ^{98}Mo, possess a similar maximum authigenic-corrected δ^{98}Mo (1.64‰ (Ostrander et al., 2019a)), as do bulk rock δ^{98}Mo from carbonates in the Klein Naute Formation ($\delta^{98}Mo_{NIST+0.25‰}$ = 1.53 ± 0.02‰; 2SE, also in GKF01 (Voegelin et al., 2010)). This agreement, despite differences in geographic location (South Africa versus Western Australia) and lithology (carbonates versus shales), bolsters support for our 2.50 Ga seawater δ^{98}Mo signature estimate.

2.5.4. Marine oxygenation during the runup to the GOE

It is now evident from our updated shale dataset that seawater δ^{98}Mo between ~2.69 Ga and 2.50 Ga was commonly > 1.0‰ (and also apparent in Fig. 2.9), much more so than was previously recognized. In Wille et al. (2007), δ^{98}Mo in shales from South Africa > 1.0‰ were found exclusively in the uppermost Lower Nauga Formation and its overlying strata. In Voegelin et al. (2010), authigenic δ^{98}Mo exceeding 1.0‰ were found sporadically throughout the GKP01 drill core (in the Boomplaas and Monteville Formations, the Upper and Lower Nauga Formations, and the Klein Naute Formation). Molybdenum isotope compositions also sporadically exceed 1.0‰ in the coeval but more proximal carbonates and shales from the Campbellrand-Malmani carbonate platform (Eroglu et al., 2015). In studies of rocks from Western Australia, δ^{98}Mo > 1.0‰ were found previously in one iron formation sample from the Marra Mamba Formation, one shale sample from the Mt. Sylvia Formation, and many samples from the Mt. McRae Shale (Kurzweil et al., 2015a; Duan et al., 2010; Ostrander et al., 2019a). In most cases, and beyond the lower sample resolution of these earlier studies, the relative lack of heavy sedimentary δ^{98}Mo values was probably a consequence of detrital dilution and local redox conditions, effects that also skewed some of our shale δ^{98}Mo to isotopically lighter values (see Section 5.1. and Section 5.2.).

Such heavy seawater δ^{98}Mo values during the late-Archean require a marine sink for Mo with a strong preference for lighter-mass isotopes (assuming no measurable Mo isotope fractionation is expressed during delivery of Mo to the ocean; see King and Pett-Ridge (2018)). Today, there are some anaerobic processes shown to promote the preferential retention of lighter-mass Mo isotopes in marine sediments. Organic matter (OM), for example, can preferentially retain lighter-mass isotopes during Mo adsorption ($\Delta^{98}\mathrm{Mo}_{\mathrm{solution\text{-}OM}}$ = 0.63‰ – 1.79‰ (King et al., 2018)) and could have been produced during anoxygenic photosynthesis in shallow waters of the late-Archean ocean (for example, by photoferrotrophs (Konhauser et al., 2002)). Also, the presence of intermediate thiomolybdate species in marine bottom waters or sediments is shown to promote the retention of lighter-mass Mo isotopes in sediments (up to $\Delta^{98}\mathrm{Mo}_{\mathrm{solution\text{-}sediment}}$ = ~3.0‰ (Neubert et al., 2008)) and require only a low or unstable local H_2S inventory (Helz et al., 1996; Erickson and Helz, 2000). Lastly, Fe oxide minerals preferentially remove lighter-mass Mo isotopes from seawater ($\Delta^{98}Mo_{solution\text{-}oxide}$ = 0.83‰ − 2.19‰ (Goldberg et al., 2009)). They possess multiple anaerobic formation pathways (photo-oxidation (Cairns-Smith, 1978) and photoferrotrophy (Widdel et al., 1993)) fully independent of O_2 availability, and they readily formed in late-Archean marine settings (Konhauser et al., 2017).

All or some of the anaerobic processes noted above probably operated during the late-Archean and were thus at least partly responsible for driving the heavy seawater $\delta^{98}Mo$ inferred here. Unfortunately, it is impossible using only the Mo isotope paleoredox proxy to differentiate the effects of these anaerobic Mo isotope fractionation pathways from those that would have required O_2. For example, Fe oxides are also formed in the presence of O_2, and it is currently impossible using Mo isotopes to differentiate this formation pathway from an anaerobic one. Furthermore, although Mn oxide mineral formation is more intimately linked to O_2 (e.g., Calvert and Pedersen, 1996), the observed isotope fractionation effect imparted during adsorption of Mo to Mn oxides ($\Delta^{98}Mo_{solution\text{-}oxide}$ = 2.7 ± 0.1‰ (Wasylenki et al., 2008)) is very similar to that observed during the formation and persistence of intermediates among the thiomolybdate complexes under weakly euxinic conditions (up to $\Delta^{98}Mo_{solution\text{-}sediment}$ = ~3.0‰ in shallower-water sediments situated not far below the chemocline in the Black Sea (Neubert et al., 2008)). These overlaps make identification of ancient Mo isotope fractionation pathways nearly impossible.

Despite the many alternatives, it is plausible, if not likely, that Fe and Mn oxide minerals formed in O_2-bearing waters of late-Archean oceans were at least partly responsible for a heavy seawater $\delta^{98}Mo$. Many independent lines of geochemical evidence, some from the same sedimentary rocks targeted in our study, suggest that O_2-bearing waters were fairly common in at least local portions of the shallow ocean within the Hamersley and Griqualand West basins during the final two- hundred million years of the Archean (described below).

2.5.4.1. Marine oxygenation between ~2.69 Ga and 2.63 Ga

Geochemical trends found in organic-rich shales from the Jeerinah Formation suggest that O_2 was produced and accumulated at least transiently in Earth's ocean during its deposition. In Scott et al. (2011), a case was made based on Fe speciation data that the high abundance of TOC in shales from the Jeerinah Formation was not a product of anoxygenic photosynthesis in the ancient overlying water column. Thus, by elimination, oxygenic photosynthesis was the most likely culprit for driving these high sedimentary TOC abundances (also see Lyons et al., 2014). Heavy nitrogen (N) isotope compositions found in shales from the Jeerinah Formation support this suggestion because they are thought to require the operation of an aerobic N cycle in oxygenated shallow waters (Koehler et al., 2018).

Evidence for ancient ocean oxygenation is also present in stratum coeval to the Jeerinah Formation. Low Fe speciation ratios indicative of local oxic depositional conditions (i.e., $Fe_{HR}/Fe_T < 0.22$ and $Fe_{PY}/ Fe_{HR} < 0.70$ (Poulton and Canfield, 2011)) are found in some shale samples from the Lokamonna and Monteville formations from South Africa (Zerkle et al., 2012). As in the Jeerinah Formation, heavy N isotope compositions that require a local aerobic N cycle are also found in the Monteville Formation (Godfrey and Falkowski, 2009). Lastly, a surface-to-deep carbon (C) isotope gradient inferred from bulk rock and kerogen in shallow-water carbonates from South Africa, Zimbabwe, Canada, and Western Australia (including in the Jeerinah Formation) is interpreted as evidence for the accumulation of O_2 in shallow waters above large areas of global continental margins after about 2.7 Ga (Eigenbrode and Freeman, 2006).

2.5.4.2. Marine oxygenation between ~2.60 Ga and 2.51 Ga

Geochemical trends in the Nauga Formation from South Africa also point to at least transient marine oxygenation during their deposition. In discrete shale beds from the Nauga Formation, elevated rhenium (Re) abundances are accompanied by near-crustal Mo abundances (Kendall et al., 2010). This geochemical fingerprint is found today in marine sediments when O_2 is present in local marine bottom waters and also penetrates into sediment pore fluids (up to 1 cm below the sediment-water interface (Morford et al., 2005)). Heavy N isotope compositions requiring oxygenated surface waters are also found in kerogen from sedimentary rocks in the Nauga Formation (Godfrey and Falkowski, 2009).

2.5.4.3. Marine oxygenation at 2.50 Ga

Late-Archean marine oxygenation seems to have reached an apex at 2.50 Ga, evident by the many geochemical trends found in sedimentary rocks from this age that suggest a “whiff” of atmospheric and marine O_2 occurred at that time (Anbar et al., 2007; Kaufman et al., 2007; Garvin et al., 2009; Reinhard et al., 2009; Duan et al., 2010; Kendall et al., 2013, 2015; Stüeken et al., 2015; Gregory et al., 2015; Ostrander et al., 2019a). In Kaufman et al. (2007), the case was made for an oxidative marine S cycle at 2.50 Ga on the basis of large magnitudes of negative MDF-S preserved in the upper member of the Mt. McRae Shale from Western Australia and one of its South African equivalents (the Gamohaan Formation). Heavy N isotope compositions are also found in the upper member of the Mt. McRae Shale, suggesting the presence of O_2 in ancient shallow waters (Garvin et al., 2009). Positive selenium (Se; Stüeken et al. (2015)), Mo (Duan et al., 2010), and uranium (U; Kendall et al. (2013)) isotope compositions found in the upper Mt. McRae Shale may also fingerprint the presence of marine O_2 at 2.50 Ga. Finally, an anti-correlation between Mo and thallium (Tl) isotopes in the upper Mt. McRae Shale suggests that Mn oxide burial in oxygenated marine sediments beneath fully oxygenated water columns at 2.50 Ga was widespread on at least a regional scale (Ostrander et al., 2019a). For such widespread Mn oxide burial to have occurred, dissolved O_2 may have accumulated at depth over a potentially large area of global continental margins.

A noticeable δ^{98}Mo increase is still present within the sedimentary record at around 2.50 Ga and corroborates the "whiff" hypothesis (Fig. 2.9; and also see Wille et al. (2007) and Kurzweil et al. (2015a)). In light of our updated dataset, however, it is worth noting the comparable increase in sedimentary δ^{98}Mo found in a few shale samples deposited just before 2.50 Ga— in the Mt. Sylvia Formation (this study) and the uppermost Nagua Formation (Wille et al., 2007) (see Fig. 2.9). At face value, these heavier δ^{98}Mo could suggest that Earth's pre-GOE oceans became more well-oxygenated (at least transiently) earlier than was previously recognized. This suggestion may gain merit from the kerogen N isotope record because it shows suggestions of a coeval shift to positive values within the uppermost Nauga Formation that are not seen in similar magnitude within older strata (Godfrey and Falkowski, 2009). Further investigation is needed to test this hypothesis.

2.6 Conclusions

We presented new δ^{98}Mo data from 140 shale samples deposited between ~2.69 Ga and 2.50 Ga, on the eve of the GOE. Critically, and unlike most previous investigations, the local redox conditions during deposition of our shales were independently constrained using the Fe speciation proxy. These depositional redox constraints are extremely important because transfer of the seawater δ^{98}Mo to sediments is shown today to be linked to local redox. Our new dataset therefore provides us with a unique opportunity to estimate the evolution of seawater δ^{98}Mo during the final two hundred million years of the Archean Eon.

As is the case today, most of the shales we targeted that were deposited under non-euxinic conditions are unlikely to have captured and preserved contemporaneous seawater δ^{98}Mo. Instead, δ^{98}Mo preserved in these shales are probably skewed toward values lighter than those of ancient seawater. Today, lighter-mass Mo isotopes preferentially accumulate in non-euxinic marine sediments during complexation with Fe and Mn oxide minerals, organic matter, and in the presence of intermediate thio-complexes. Some combination of these processes probably also governed the δ^{98}Mo of our ancient shales deposited under analogous conditions.

Also akin to today, some of the shales we targeted that were deposited under euxinic conditions may have captured seawater δ^{98}Mo. Guided by the δ^{98}Mo data primarily from these shales, we infer a late-Archean seawater δ^{98}Mo that commonly exceeded 1.0‰. Such a heavy seawater δ^{98}Mo could be explained by the preferential retention of lighter-mass Mo isotopes in marine sediments during strictly anaerobic processes in the late-Archean ocean (e.g., during the formation of organic matter, photoferrotrophic Fe oxides, or intermediate thio-complexes). It is also highly plausible, however, that lighter-mass Mo isotopes were preferentially retained by Fe and Mn oxide minerals formed in oxygenated shallow waters of the pre-GOE ocean. In fact, many independent lines of geochemical evidence suggest that Earth's shallow oceans were commonly oxygenated during the final two-hundred million years of the Archean Eon, lending support to this idea.

One strategy moving forward would be to pair the Mo isotope palerodox proxy with other proxies to better differentiate anaerobic from aerobic processes. Thallium isotopes may prove useful because the Tl isotope composition of seawater is also thought to be set in-part by global ocean oxygenation and was shown recently to be transferred to sediments in modern euxinic marine settings (Owens et al., 2017). Accordingly, the same shale sample sets targeted here for Mo isotopes could also be targeted for complementary Tl isotope analyses. An additional benefit of pairing together Tl and Mo isotopes is that, unlike Mo, Tl isotopes would not be expected to fractionate during the anaerobic processes that complicate Mo isotope interpretations (e.g., during adsorption to Fe oxides or during formation of thio-complex intermediates [discussed in Ostrander et al., 2019a]). The uranium (U) isotope paleoredox proxy may also be useful because the U isotope composition of seawater is shown to be set in part by ocean oxygenation and can be inferred from carbonates (which typically have minor isotopic offset from the seawater value (Romaniello et al., 2013; Chen et al., 2018; Tissot et al., 2018)). Measuring U isotope ratios in carbonates deposited between ~2.7 Ga and 2.5 Ga would be a useful way to cross check the sometimes heavy δ^{98}Mo found in the late-Archean carbonate record (which may also have at times captured seawater δ^{98}Mo (Voegelin et al., 2010)). If shallow ocean oxygenation was indeed recurrent during the Neoarchean, as we posit here based on an expanded shale δ^{98}Mo record, then this oxygenation should also be fingerprinted in the contemporaneous sedimentary Tl and U isotope records.

CHAPTER 3

CONSTRAINING THE RATE OF OCEANIC DEOXYGENATION LEADING UP TO A CRETACEOUS OCEANIC ANOXIC EVENT (OAE-2: ~94 MA)

The work presented in this chapter has been published as: Ostrander, C.M., Owens, J.D., Nielsen, S.G. (2017) Constraining the rate of oceanic deoxygenation leading up to a Cretaceous Oceanic Anoxic Event. *Science Advances* **3**, e1701020.

Abstract

The rates of marine deoxygenation leading to Cretaceous Oceanic Anoxic Events are poorly recognized and constrained. If increases in primary productivity are the primary driver of these episodes, progressive oxygen loss from global waters should predate enhanced carbon burial in underlying sediments—the diagnostic Oceanic Anoxic Event relic. Thallium isotope analysis of organic-rich black shales from Demerara Rise across Oceanic Anoxic Event 2 reveals evidence of expanded sediment-water interface deoxygenation ~43 ± 11 thousand years before the globally recognized carbon cycle perturbation. This evidence for rapid oxygen loss leading to an extreme ancient climatic event has timely implications for the modern ocean, which is already experiencing large-scale deoxygenation.

3.1 Introduction

Anthropogenic forcing of the ocean-atmosphere system necessitates an understanding of Oceanic Anoxic Events (OAEs) and the associated time scales and mechanisms of initiation to predict potential future marine deoxygenation (Keeling et al. 2010). The cause of OAE-2, which occurred at the Cenomanian-Turonian boundary (~94 Ma (million years ago)), has been attributed to various combinations of increased surface temperatures (Schlanger and Jenkyns 1976), sea level rise (Arthur et al. 1987), nutrient trapping (Alexandre et al. 2010), and pulses of magmatic activity (Leckie et al. 2002; Adams et al. 2010; Owens et al. 2012)—all of which are likely to increase primary productivity (Owens et al. 2012). In the modern predominantly oxic ocean, primary productivity in the euphotic zone produces excess organic carbon that subsequently sinks and is remineralized to CO_2 by heterotrophic bacteria, in the process consuming free oxygen. Thus, increases in primary productivity are accompanied by increases in oxygen consumption and should lead to a progressive expansion in anoxic portions of the ocean (Meyer and Kump 2008). Recent advances place coarse temporal constraints on select OAE-2 trigger mechanisms (Turgeon and Creaser 2008; Du Vivier et al. 2014; Du Vivier et al. 2015) and provide evidence for this gradual marine de- oxygenation (Mort et al. 2007; Lue et al. 2010; Owens et al. 2013; Owens et al. 2016; Dickson et al. 2016), but the timing of the transition from widespread ocean oxygenation before OAE-2 to the peak of ocean deoxygenation remains effectively unconstrained. Uncertainty surrounding the exact duration of OAE-2—and thus also surrounding the timing of what is going on before and during the event—adds further complications, with recent estimates ranging from ~450 to 700 ky (thousand years) (Sageman et al. 2006; Meyers et al. 2012; Eldrett et al. 2015).

The massive burial of organic carbon during OAE-2 (perhaps 1.4 to 1.6 times that of the steady-state modern ocean [Owens et al. 2013; Kump and Arthur 1999]), which caused the observed carbon isotope excursion (Schlanger and Jenkyns 1976; Leckie et al. 2002), must be linked to changes in redox conditions even when considering caveats from sedimentation rate changes (Canfield 1994; Hartnett et al. 1998). Manganese (Mn) oxides are ubiquitous in sediments deposited below an oxygenated water column but are absent under anoxic or euxinic conditions, because quantitative chemical reduction of insoluble Mn (IV) to more soluble Mn (II) and Mn (III) occurs when oxygen is essentially removed from the water in contact with the sediment (Rue et al. 1997). Attempts to directly track perturbations in both local and global Mn oxide burial have been proven difficult because of numerous factors, but primarily because Mn budgets in ancient marine sediments are often perturbed by postdepositional processes (Burdige 1993).

Thallium (Tl) strongly adsorbs to Mn oxides during their precipitation with a large positive isotope fractionation factor, rendering seawater isotopically light (Rehkämper et al. 2002; Nielsen et al. 2013). Global Mn oxide precipitation is the primary control of the marine Tl isotope composition on time scales shorter than ~5 million years (Nielsen et al. 2009), and the modern marine residence time of Tl is ~18.5 ky (Nielsen et al. 2017). Therefore, reconstructions of the Tl isotope composition of seawater for short-term events, such as OAEs, should provide evidence of perturbations in Mn oxide precipitation. Recent work shows that, because Tl is quantitatively removed from seawater under euxinic conditions, sediments underlying these environments faithfully record the Tl isotope composition of overlying waters (Owens et al. 2017a). As long as the euxinic setting is well connected to the open ocean (for example, Cariaco Basin, Venezuela), sediments in these locations record the global seawater value. Thus, ancient euxinic sediments are an archive capable of tracking changes in the global Mn oxide burial flux in cases where the overlying water column was well connected to open ocean seawater.

Here, we present Tl isotope compositions of organic-rich euxinic black shales before, during, and after OAE-2 that were recovered from ODP (Ocean Drilling Program) Site 1258 located on Demerara Rise in the Atlantic Ocean (Table C.1) (Shipboard Scientific Party 2004). The stratigraphy and temporal framework of cores from Site 1258 sampled for this study are well constrained (see the Supplementary Materials for more details). The macroscopic view of the entire section has been shown to record local euxinic conditions based on Fe speciation (Owens et al. 2016) while, at the same time, being relatively well connected with the open ocean because of its paleogeographic location (Fig. C.1) (Shipboard Scientific Party 2004). These observations show that samples from ODP Site 1258 are ideal for reconstructing changes in Mn oxide burial before, during, and after OAE-2 using Tl isotopes.

3.2 Results

Before the event, Tl isotope compositions are slightly heavier than modern seawater values ($\varepsilon^{205}\text{Tl} = -6$) (Nielsen et al. 2004; Nielsen et al. 2006), averaging $\varepsilon^{205}\text{Tl} \sim -4.5$ and believed to represent connection to well-oxygenated global ocean (Fig. 3.1A; implications for this value are discussed in the Supplementary Materials). Most markedly, a distinct positive shift to $\varepsilon^{205}\text{Tl} \sim -2.5$ occurs before the onset of OAE-2 and is maintained until slightly before the termination of the event, where Tl isotopes start recovering toward lighter values of $\varepsilon^{205}\text{Tl} \sim -3$. Low-resolution black shale analysis before and during OAE-

2 from a second basin (Furlo, Marche-Umbria, Italy) reveals nearly identical values to Site 1258 both before and during enhanced organic carbon burial (Fig. C.2), suggesting that these two records faithfully record the global ocean Tl isotope composition with little or no significant basinal heterogeneity or restriction affecting Tl isotopes in these two locations.

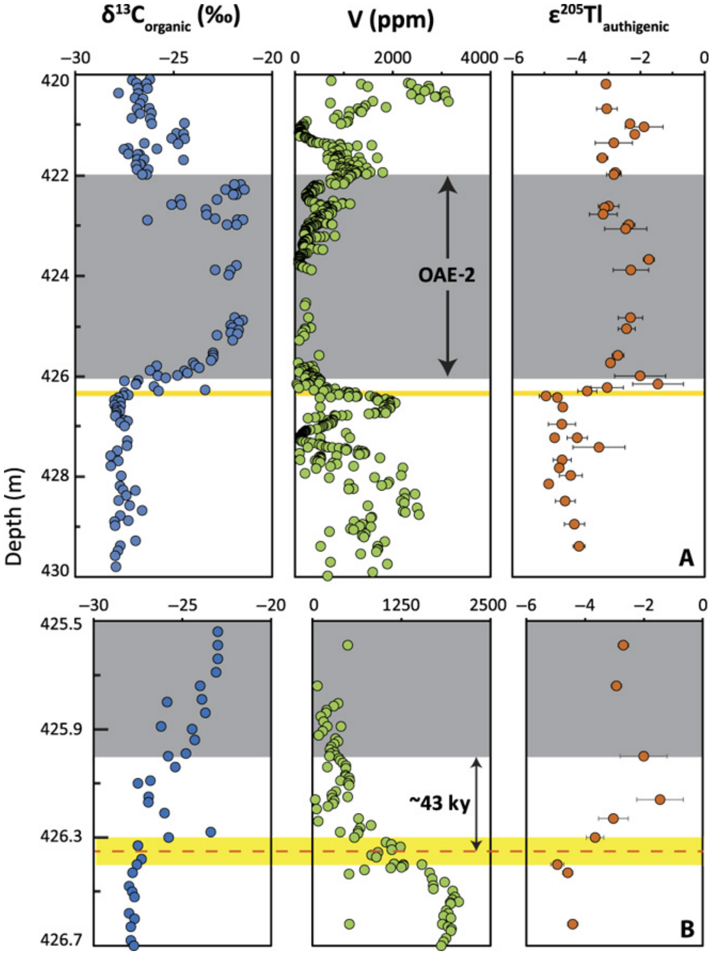

Fig. 3.1 Geochemical profile of ODP Site 1258 from Demerara Rise. (A) Spliced section analyzed for this study. OAE-2 is identified by the area in gray, as delineated by the carbon isotope excursion (Erbacher et al. 2005), and the shaded yellow region represents the onset of the Tl isotope shift. Vanadium concentrations are from previous studies (Hetzel et al. 2009; Owens et al. 2016). (B) Zoomed-in view of the profile immediately preceding OAE-2, highlighting the timing between the Tl isotope shift and disturbance of the global C cycle. Error bars represent 2-SD uncertainty of multiple sample analyses or the long-term reproducibility of SCO-1, whichever is greater.

3.3 Discussion

We conclude that the positive Tl isotope excursion reflects diminished global Tl scavenging by Mn oxides due to an expansion of areas in the ocean with minimal to no oxygen at the sediment-water interface. The Tl isotope excursion commences significantly before the carbon isotope excursion at Site 1258 (Fig. 3.1B) (Erbacher et al. 2005). Using a linear sedimentation rate extrapolated from the OAE, and assuming that the duration of OAE-2 was 600 ky, we calculate a time lag of ~43 ± 11 ky between the initiation of the Tl and C isotope excursion (see the Supplementary Materials). Therefore, our data imply that deoxygenation of the sediment-water interface (as indicated by Tl isotopes) was initiated ~43 ± 11 ky before expansion of global euxinia, as indicated by C and S isotope systematics (Owens et al. 2013). The 600 ky duration for OAE-2 used here is also the value used in recent attempts to constrain the timing of possible OAE-2 trigger mechanisms (Du Vivier et al. 2014; Du Vivier et al. 2015), guided by the GSSP (Global Boundary Stratotype Section and Point) time scale and estimates from multiple sites (Sageman et al. 2006; Meyers et al. 2012). If the duration of OAE-2 was actually shorter or longer than the 600 ky assumed here, then our estimate of ~43 ± 11 ky is too long or too short, respectively.

The decrease in Mn oxide burial before OAE-2 can be modeled using a previously used isotope mass balance model (Nielsen et al. 2009). Although euxinic sediments accumulate significant Tl concentrations and, therefore, may constitute a significant Tl sink when marine euxinia expands, anoxic sediments deposited underneath oxygen minimum zones (OMZs) appear to have essentially little to no Tl enrichment (Nielsen et al. 2011). Therefore, we can treat the initial deoxygenation before OAE-2 where marine euxinia was yet to expand in terms of the same inputs and outputs that govern the modern marine Tl isotope reservoir. The shift from ε^{205}Tl = −4.5 to −2.5 before OAE-2 can be accounted for if Mn oxide output fluxes decreased by ~40 to 80%, depending on the Tl isotope fractionation factor between seawater and Mn oxides (see Fig. 3.2 and the Supplementary Materials for further details).

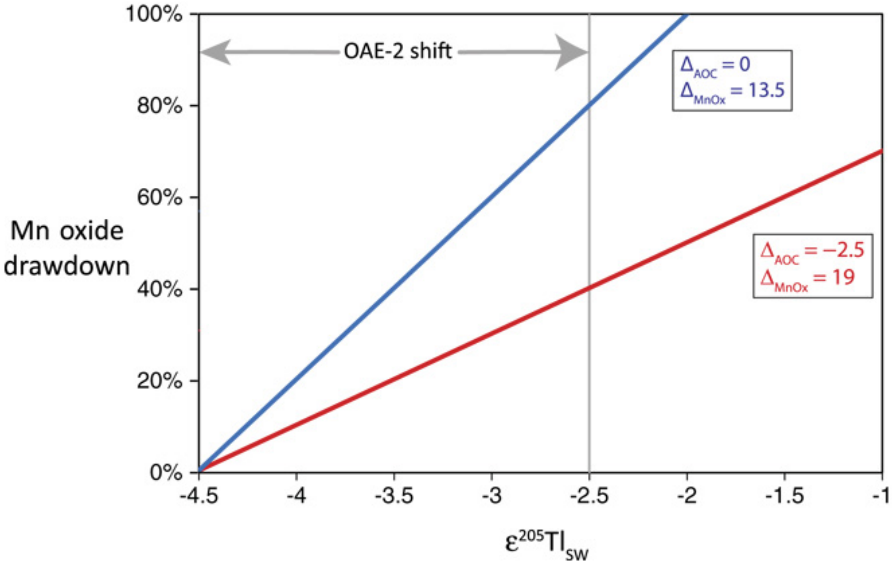

Fig. 3.2 The modeled decrease in Mn oxide burial associated with the Tl isotope shift from this study. Percentage of Mn oxide drawdown is calculated using the range of reported values for Tl isotope fractionation during incorporation into altered oceanic crust (AOC) and Mn oxides (MnOx) (inset boxes) (Nielsen et al. 2017). This yields a range of drawdown between 40 and 80% during OAE-2 (see the Supplementary Materials).

To our knowledge, this is the first study to track global perturbations in Mn oxide burial leading to a major climatic event. We can use these changes in Mn oxide burial as a direct measure of the seafloor area affected by anoxia. For this study, we refer to sediments being deposited beneath a sediment-water interface with oxygen concentrations close to 0, at least long enough to prevent Mn oxide burial, as anoxic. Thus, we can convert the ~40 to 80% change in Mn oxide burial flux into the area of anoxic seafloor by assuming that the areal extent of Mn oxide deposition was the primary control of Mn oxide burial fluxes over short time scales. Therefore, our model suggests that over a period of ~43 ± 11 ky, the area of anoxic seafloor expanded by 40 to 80%, or at a rate of ~2.2×10^3 to 7.5×10^3 km^2/year, substituting for previously oxygenated portions of the sediment-water interface (see the Supplementary Materials). If these oxygen depletions primarily manifested themselves via expansion of areas similar to modern OMZs, then more than the entire continental shelf and upper slope [~16% of the modern seafloor area (Menard and Smith 1966), although this area was likely larger during OAE-2 because of higher sea levels (Arthur et al. 1987)] would have been affected by periodic oxygen depletion. However, deoxygenation over large areas of the deep ocean (that is, abyssal, oligotrophic regions) is very difficult to maintain under a well-oxygenated atmosphere (Jenkyns 2010). Therefore, it is more likely that anoxic expansion was closer to our lower estimate of 40% (see the Supplementary Materials for further discussion).

By combining our results with previously published time constraints for possible OAE-2 trigger mechanisms and subsequent marine response, a clearer picture of pre–OAE-2 conditions materializes (Fig. 3.3). We assume that these conditions occurred over a backdrop of elevated surface temperatures (Schlanger and Jenkyns 1976) and paleocontinental arrangement (Alexandre et al. 2010) during the mid-Cretaceous that were conducive to enhanced nutrient delivery and sequestration, respectively. The initial trigger mechanism of changes in oceanic (de)oxygenation was likely the onset of large igneous province (LIP) activity, which occurred ~200 ky before OAE-2 (Du Vivier et al. 2014). The initiation of LIP activity likely enhanced nutrient delivery to the ocean even further and could have primed Cretaceous oceans for oxygen loss. Global oxygen loss from the water column becomes evident at ODP Site 1258 ~59 ky before OAE-2, when global drawdown of the oceanic vanadium reservoir begins (see the Supplementary Materials) (15, 37). Vanadium drawdown from the water column is probably linked to the V^{5+}–V^{4+} redox couple because of the more efficient incorporation of reduced V into organic matter (Lewan and Maynard 1982). Reduction of V^{5+} to V^{4+} does not require complete removal of oxygen from seawater (Rue et al. 1997), and therefore, V drawdown is expected to precede significant reduction in Mn oxide burial, consistent with the Tl isotopic shift postdating V drawdown by ~16 ky (Fig. 3.1). The difference in timing between V concentrations and Tl isotopes is unlikely to be due to different marine reservoir effects because Tl has a shorter residence time than V [~18.5 ky (Nielsen et al. 2017) versus ~100 ky (Morford and Emerson 1999)], and thus, global perturbation of marine Tl would precede that of V should this be the case. It was not until unradiogenic Os isotope values were delivered to sediments worldwide, ~50 ky before OAE-2, likely because of the onset of the main LIP activity (Du Vivier et al. 2014; Du Vivier et al. 2015), that deoxygenation became severe enough to greatly affect global Mn oxide burial, as delineated by the observed Tl isotope excursion (Fig. 3.1). It is likely that the dissolution of Mn oxides at this time liberated not only Mn from the oxic sediments (Jenkyns et al. 2017) but also many adsorbed trace metals including Tl and Mo, which is recorded in euxinic Demerara Rise sediments, as Mo concentrations briefly exceeded 600 parts per million (Hetzel et al. 2009; Owens et al. 2016) and the Tl isotope excursion reached values heavier than oceanic inputs [$\varepsilon^{205}Tl = -1.5 \pm 0.8$ at 426.16 mcd (meters composite depth)]. It was not until a significant area of productive, marginal portions of the ocean was affected by oxygen depletion that enhanced global pyrite and carbon burial commenced in earnest, marking the onset of OAE-2 (Owens et al. 2013). The outlined sequence of events is in agreement with models that invoke enhanced primary productivity as the main mechanism responsible for inducing the OAE (Schlanger and Jenkyns 1976; Meyer and Kump 2008; Jenkyns 2010; Du Vivier et al. 2014; Du Vivier et al. 2015).

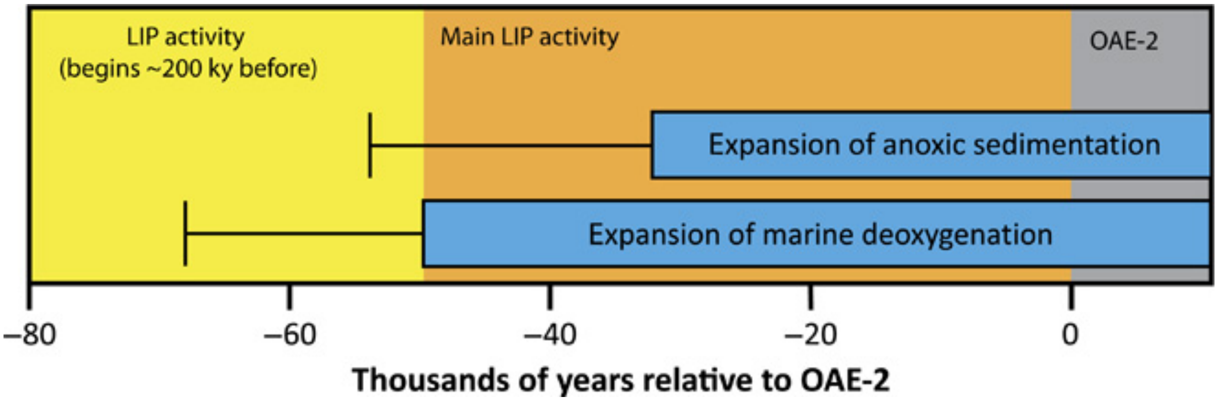

Fig. 3.3 Temporal constraints for pre–OAE-2 trigger mechanisms and changes in oceanic redox. All estimates are derived from constant sedimentation rates for ODP Site 1258 and depend on an estimate for the duration of OAE-2 of 600 ky (see the Supplementary Materials). LIP activity time constraints are from Os isotope data (Du Vivier et al. 2014; Du Vivier et al. 2015). The expanded marine deoxygenation estimate is based on the drawdown of the oceanic V reservoir (Hetzel et al. 2009; Owens et al. 2016), and the expansion of anoxic sedimentation estimate comes from this study (see the Supplementary Materials for more information). Error bars represent the difference between upper and lower time estimates, as explained in the Supplementary Materials.

In addition to the pre-OAE lag between the Tl and C isotope excursions, it is also significant that the recovery of Tl isotopes appears to be significantly slower than that of C isotopes (Fig. 3.1). In principle, this implies that Mn oxide burial, and thereby the global extent of anoxia, did not recover significantly even after organic carbon burial had largely diminished to pre-OAE levels. This post-OAE decoupling of the two isotope systems could imply that although overall organic matter burial declined, productivity was still sufficiently high to maintain the consumption of any oxygen that might have been subducted into the deep ocean through ocean circulation. Such a conclusion is supported by the fact that Os isotope values do not return to pre-event radiogenic values in most of the studied sites (Du Vivier et al. 2014; Du Vivier et al. 2015), which may indicate that significant LIP activity continued even after the recovery of C isotopes. In this case, the nutrient supply that fueled the initial increase in primary productivity could have remained relatively high and possibly maintained the expanded state of global anoxia. Alternatively, it has been hypothesized that the termination of increased carbon burial during OAE-2 was due to the drawdown of bioessential trace metals from seawater (Owens et al. 2016), which might have inhibited some parts of the carbon cycle and, therefore, reduced carbon burial even in the face of enhanced nutrient supply from LIP activity. Additionally, after the main OAE-2 event, a second positive C isotope excursion [between 421.19 and 420.98 mcd (Fig. 3.1)] and coeval drop in V concentrations are accompanied by a sudden positive Tl isotope excursion. These geochemical shifts are identical to those associated with the main OAE event, but the magnitudes are much smaller. Although this conclusion is speculative, this feature may imply a shorter-lived spike of deoxygenation and enhanced carbon burial that occurred shortly after OAE-2.

On the basis of our interpreted sequence of events leading up to OAE-2, the general marine response to increased nutrient supply, global warming, and sea level rise is expansion of oceanic anoxia without simultaneous expansion of ocean euxinia. Increased ocean deoxygenation is already apparent in the modern ocean, because marine O_2 has decreased by 2% over roughly the last half century (Schmidtko et al. 2017), and recent models predict a continued loss of 0.5 to 3.5% over the next half century (Keeling et al.

2010; Long et al. 2016), which would result in huge expansions of ocean anoxia within the next few thousand years. Should anthropogenically induced oxygen loss occur at similar rates as in the period leading up to OAE-2, then the current area of seafloor hypoxia [currently ~764,000 km^2 (Holly and Levin 2004)] would double in the next ~102 to 344 years, equivalent to an increase of ~2.2×10^4 to 7.5×10^4 km^2 of seafloor every decade—an easily detectable value. Localized oxygen loss is already apparent in the modern ocean (Keeling et al. 2010; Long et al. 2016; Schmidtko et al. 2017), and the ability to observe more widespread perturbation seems realistic under currently projected carbon emissions. Without positive human intervention, ancient OAE studies are destined to become uncomfortably applicable in the not-so-distant future.

CHAPTER 4

FULLY OXYGENATED WATER COLUMNS OVER CONTINENTAL SHELVES BEFORE THE GREAT OXIDATION EVENT

The work presented in this chapter has been published as: Ostrander, C.M., Nielsen, S.G., Owens, J.D., Kendall, B., Gordon, G.W., Romaniello, S.J., Anbar, A.D. (2019) Fully oxygenated water columns over continental shelves before the Great Oxidation Event. *Nature Geoscience* **12**, 186-191.

Abstract

Late Archaean sedimentary rocks contain compelling geochemical evidence for episodic accumulation of dissolved oxygen in the oceans along continental margins before the Great Oxidation Event. However, the extent of this oxygenation remains poorly constrained. Here we present thallium and molybdenum isotope compositions for anoxic organic-rich shales of the 2.5-billion-year-old Mount McRae Shale from Western Australia, which previously yielded geochemical evidence of a transient oxygenation event. During this event, we observe an anticorrelation between thallium and molybdenum isotope data, including two shifts to higher molybdenum and lower thallium isotope compositions. Our data indicate pronounced burial of manganese oxides in sediments elsewhere in the ocean at these times, which requires that the water columns above portions of the ocean floor were fully oxygenated—all the way from the air–sea interface to well below the sediment–water interface. Well-oxygenated continental shelves were probably

the most important sites of manganese oxide burial and mass-balance modelling results suggest that fully oxygenated water columns were at least a regional-scale feature of early Earth’s oceans 2.5 billion years ago.

4.1. Introduction

The extent of dissolved O_2 accumulation in Earth's oceans before the Great Oxidation Event (GOE, ~2.4 to 2.3 billion years ago (Ga); Lyons et al. 2014) remains poorly understood. Multiple lines of geochemical evidence indicate that O_2 was produced by cyanobacteria in the surface ocean well before accumulating in the atmosphere during and after the GOE (Eigenbrode and Freeman 2006; Kendall et al. 2010; Czaja et al. 2012; Kendall et al. 2013; Stüeken et al. 2015; Eickmann et al. 2018; Koehler et al. 2018). Models indicate that cyanobacteria in the surface ocean were capable of promoting mild accumulation of dissolved O_2 (up to 25 µM; Kasting et al. 1992) in shallow waters under a predominantly anoxic atmosphere, perhaps extending across large areas of the ocean (Olson et al. 2013). However, it is difficult to test these models because existing geochemical proxies cannot easily be used to assess the breadth and depth of ocean oxygenation.

A case has been made for widespread oxygenation of shallow waters before the GOE in continental margin environments on the basis of carbon isotopes in bulk rock and kerogen from 2.7 Ga carbonate sedimentary rocks (Eigenbrode and Freeman 2008). However, this earlier work could not determine whether O_2 accumulation was restricted to surface waters or extended deeper in the water column, let alone whether oxygenation reached bottom waters and sediments (that is, a fully oxygenated water column).

A fully oxygenated water column at 2.6–2.5 Ga was inferred from black shales (upper Nauga Formation, Ghaap Group, South Africa) enriched in Re but not Mo relative to average crustal abundances (Kendall et al. 2010). This geochemical signature occurs when O_2 is present in pore waters at a depth of up to around 1 cm below the sediment–

water interface, when Fe(III) becomes the dominant electron acceptor during oxidation of organic matter and sulfide accumulation is low (Morford et al. 2005; Morford et al. 2012) (Fig. 4.1a). However, this evidence was restricted to a single continental margin (Griqualand West Basin) and could not be extrapolated to the wider oceans.

If fully oxygenated water columns on continental margins were a widespread feature of pre-GOE oceans, then Mn oxide burial in sediments beneath these settings would also have been widespread. In the modern ocean, O_2 in marine bottom waters and sediments readily oxidizes dissolved Mn(II) and Mn(III) to insoluble Mn(IV)-bearing minerals that precipitate out of solution (Burdige 1993; Calvert and Pedersen 1996). In contrast, Mn oxides do not form under anoxic conditions, nor are they buried in anoxic marine sediments. Even if formed under O_2-rich conditions, Mn oxides undergo reductive dissolution shortly after being exposed to anoxic conditions within the water column or sediments (Burdige 1993; Calvert and Pedersen 1996; Kristensen et al. 2003). Manganese oxides are highly unstable when O_2 is absent because in such conditions they are an efficient electron acceptor (Froelich et al. 1979). Therefore, appreciable Mn oxide burial today only occurs where water columns are fully oxygenated and O_2 persistently penetrates sediment pore waters (Calvert and Pedersen 1996). In Earth's past, Mn oxides should have also been buried where O_2 penetrated deeply into marine sediments. This could have occurred under more oxidizing conditions than those identified by Kendall et al. (2010) in the Nauga Formation shales, where Re abundances are elevated but Mo abundances are negligible. Specifically, Mn oxide burial requires the penetration of O_2 well beyond 1cm below the sediment–water interface and occurs before Fe(III) becomes the primary electron acceptor during organic carbon oxidation (Froelich et al. 1979; Calvert and Pedersen 1996) (for example, Fig. 4.1b).

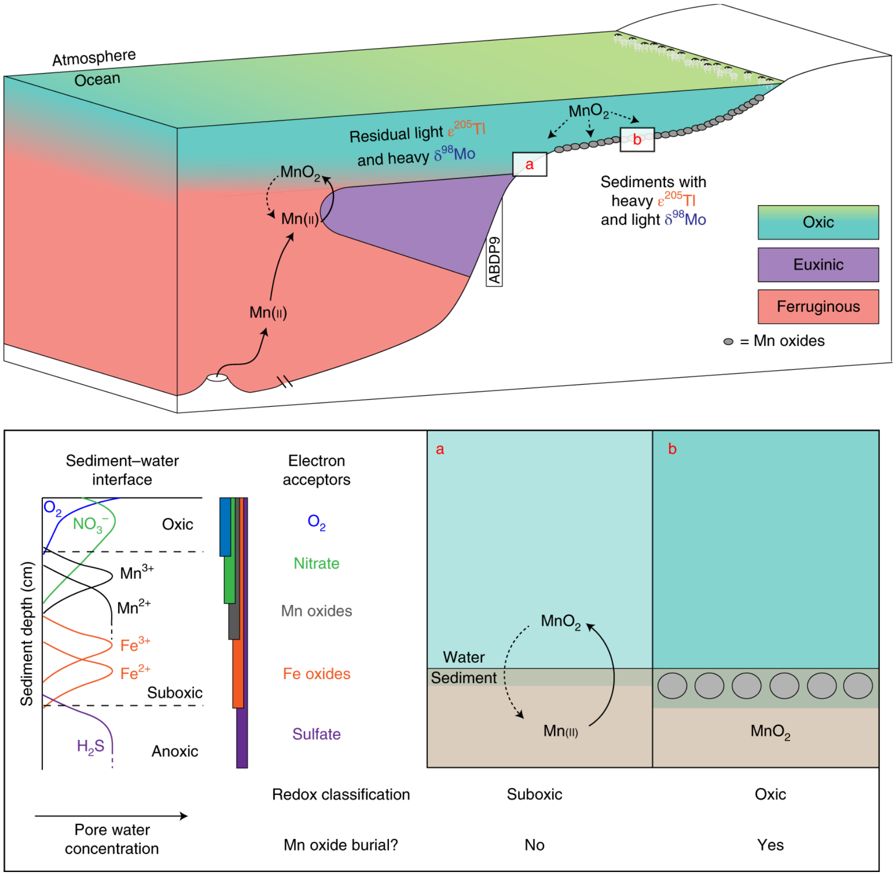

Fig. 4.1 Illustration of a possible well-oxygenated marine margin before the GOE. The top diagram depicts a possible marine margin in the Hamersley Basin during deposition of the 2.5 Ga Mount McRae Shale. Evidence exists for sufficient O_2 accumulation in an ancient water column between 2.6 and 2.5 Ga to weakly oxygenate underlying sediments (Kendall et al. 2010) (suboxic, depicted in a). However, O_2 penetration into these sediments was not sufficient to promote Mn oxide burial (Morford et al. 2005; Morford et al. 2012). If settings capable of burying Mn oxides were present in ancient oceans over a large seafloor area (oxic, depicted in b), then seawater Tl and Mo isotope compositions would have decreased and increased, respectively. The Mount McRae Shale was deposited under locally euxinic conditions (Reinhard et al. 2009) and should therefore have captured these changes in seawater isotope signatures (Neubert et al. 2008; Owens et al. 2017a). Sedimentary redox structure in the lower left-hand corner of the figure summarizes current understanding of the possible electron acceptors present under each redox condition (Froelich et al. 1979; Madison et al. 2013).

Here, we pair Tl and Mo isotope data from the late Archaean (~2.5 Ga) black shales of the Mount McRae Shale (Hamersley Basin, Western Australia) to track the extent of marine Mn oxide burial before the GOE. The isotopic cycling of both Tl and Mo in the ocean is directly linked to global Mn oxide burial fluxes (Nielsen et al. 2011, Owens et al. 2017a). Therefore, their paired application is a powerful way to infer the extent of fully oxygenated water columns at a regional-to-global scale, in contrast to other proxies (such as Re versus Mo enrichments (Morford et al. 2005) and sedimentary Fe speciation (Raiswell et al. 2018)) that focus only on redox conditions in the local water column.

4.2. Pairing Tl and Mo isotopes to track paleoredox conditions

The use of Tl isotopes as a palaeoredox proxy is relatively new (Nielsen et al. 2011; Ostrander et al. 2017; Them et al. 2018), but builds on extensive earlier study of Tl isotope systematics. The Tl isotope composition of modern seawater (reported in epsilon notation: ε^{205}Tl, where $\varepsilon^{205}\mathrm{Tl} = ({}^{205/203}\mathrm{Tl}_{\mathrm{sample}}/{}^{205/203}\mathrm{Tl}_{\mathrm{NIST\text{-}997}} - 1) \times 10^4$) is homogenous and lighter than that of bulk continental crust ($\varepsilon^{205}\mathrm{Tl}_{\mathrm{seawater}} = -6.0 \pm 0.3$ (Nielsen et al. 2006; Owens et al. 2017a), compared to $\varepsilon^{205}\mathrm{Tl}_{\mathrm{bulk\text{-}crust}} = -2.1 \pm 0.3$ (Nielsen et al. 2005)). The light ε^{205}Tl in modern seawater is a result of the preferential removal of isotopically heavy Tl from seawater by Mn oxides in well-oxygenated marine sediments (Nielsen et al. 2013). Importantly, the contemporaneous seawater ε^{205}Tl signature is captured and preserved in sediments from anoxic and sulfidic (that is, euxinic) basins (Owens et al. 2017a). Tl isotope studies of sedimentary rocks deposited under euxinic conditions therefore provide a means to track ancient seawater ε^{205}Tl signatures, which should vary in response to changes in Mn oxide burial fluxes. In support of this application, two recent studies used Tl isotope compositions in Mesozoic shales deposited in locally euxinic conditions to track changes in Mn oxide burial fluxes before, during and after oceanic anoxic events, documenting episodes of substantial marine deoxygenation (Ostrander et al. 2017; Them et al. 2018).

Molybdenum isotopes are a more established proxy that has also been shown to be sensitive to marine Mn oxide burial (Wasylenki et al. 2011). The modern seawater Mo isotope composition (reported in delta notation: δ^{98}Mo, where $\delta^{98}\text{Mo} = ({}^{98/95}\text{Mo}_{\text{sample}}/{}^{98/95}\text{Mo}_{\text{NIST-SRM-3134}} - 1) + 0.25‰$; Nägler et al. 2014) is heavier than that of bulk continental crust ($\delta^{98}\text{Mo}_{\text{seawater}} = 2.34 \pm 0.10‰$ (Nägler et al. 2014), compared with $\delta^{98}\text{Mo}_{\text{bulk-crust}} = 0.47 \pm 0.12‰$ (Willbold and Elliot 2017)). This heavy seawater δ^{98}Mo composition is due largely to the preferential removal of lighter-mass Mo isotopes by adsorption to Mn oxides in well-oxygenated marine sediments (Wasylenki et al. 2011). In a similar way to Tl, this heavy seawater δ^{98}Mo value is captured in strongly euxinic settings where Mo removal from bottom waters is quantitative (Neubert et al. 2008).

It is useful to measure Tl isotopes in addition to Mo isotopes because Mo isotope interpretation is complicated by alternative fractionation pathways that do not affect Tl isotopes. For example, processes that occur during continental weathering (Siebert et al. 2015) and riverine transport (Archer and Vance 2008) can remove isotopically light Mo (but see King et al. 2018), yet do not cause measurable Tl isotope fractionation (Nielsen et al. 2005). Weakly sulfidic marine sediments also incorporate lighter-mass Mo isotopes (Neubert et al. 2008) but impart no known isotopic effect on Tl (Owens et al. 2017a). Iron oxides can remove isotopically light Mo and drive seawater to heavy δ^{98}Mo values (Goldberg et al. 2009), but are unlikely to fractionate Tl isotopes because Fe oxides lack the ability to oxidize Tl(I) to Tl(III), which is what drives isotopic fractionation during sorption to Mn oxides (Peacock and Moon 2012; Nielsen et al. 2013).

4.3. Anticorrelation of Mo and Tl isotopes in 2.5 Ga shales

We focus on the 2.5 Ga Mount McRae Shale from Western Australia in drill core ABDP9 because black shales from the upper part of this formation host convincing evidence for a widespread oxygenation episode predating the GOE (Anbar et al. 2007; Kaufman et al. 2007; Garvin et al. 2009; Reinhard et al. 2009; Duan et al. 2010; Kendall et al. 2013, Kendall et al. 2015; Stüeken et al. 2015; Gregory et al. 2015). These rocks are an ideal archive for tracking fluctuations in seawater Tl and Mo isotope compositions at 2.5 Ga because they were deposited in locally euxinic conditions (Reinhard et al. 2009) that favour preservation of seawater δ^{98}Mo and ε^{205}Tl values (Fig. 4.1; see Supplementary Information for more details about the Mount McRae Shale).

Molybdenum isotope signatures much heavier than those of igneous crustal rocks were previously found in the Mount McRae Shale (and in coeval shales from South Africa; Wille et al. 2007) but could not be definitively ascribed to Mn oxide burial elsewhere in the ocean (Duan et al. 2010). If Mn oxides were being buried at this time, ε^{205}Tl should also be fractionated relative to bulk continental crust. An anticorrelation between ε^{205}Tl and δ^{98}Mo is expected because fractionation incurred during Mn oxide adsorption occurs in opposing directions for the two isotope systems (Nielsen et al. 2011; Owens et al. 2017a).

We find that ε^{205}Tl is systematically lighter during two distinct intervals of the euxinic upper shale (US) member in the Mount McRae Shale: 153.30–144.36m (US1) and

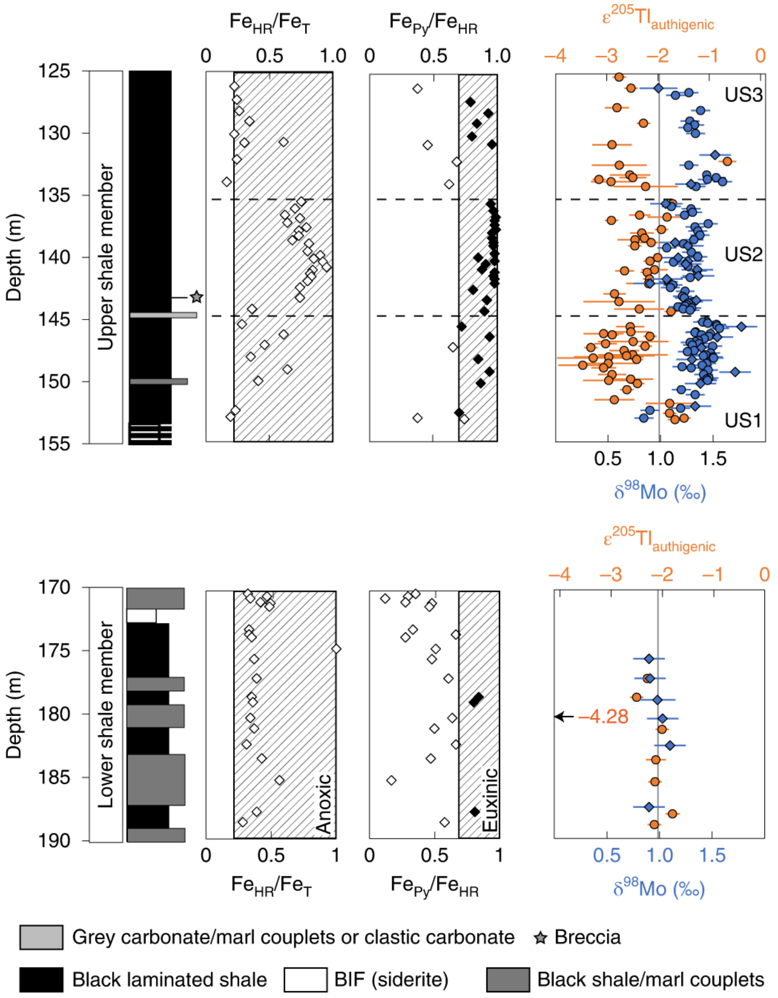

Fig. 4.2 Geochemical profiles in organic-rich shales from the Mount McRae Shale. Left: stratigraphic columns for the upper shale member (top) and lower shale member (bottom). Right: geochemical profiles. The hatched boxes represent values indicative of anoxic ($Fe_{HR}/Fe_T > 0.22$, where the HR and T subscripts signify highly reactive and total Fe, respectively) and euxinic ($Fe_{Py}/Fe_{HR} > 0.7$, where the Py subscript signifies Fe in the form of pyrite) deposition (Raiswell et al. 2018). Data that exceed both criteria are in black. Diamonds reflect data from previous work (Reinhard et al. 2009; Duan et al. 2010) and circles are data from this study. The grey vertical line in the isotope plots represents average isotope compositions from the lower shale member, with the exception of one anomalous Tl isotope value ($\varepsilon^{205}Tl = -4.28 \pm 0.13$ at 180.33 m). All error bars represent the 2 s.d. reproducibility of that sample or the external long-term reproducibility of natural reference materials, whichever is greater.

134.17–126.15m (US3) (average $\varepsilon^{205}Tl = -2.65$) (Fig. 4.2 and Fig. 4.3). δ^{98}Mo exhibits heavier values in these same intervals (average $\delta^{98}Mo = 1.37‰$), revealing the predicted anti-correlation with ε^{205}Tl. Compared with these intervals, Tl and Mo isotope compositions for 144.26-135.58m (US2) are heavier (average $\varepsilon^{205}\mathrm{Tl} = -2.39$, $P = 0.05$, two-tailed unpaired t-test) and lighter (average $\delta^{98}\mathrm{Mo} = 1.23‰$, $P \ll 0.05$), respectively. A cross-plot of shale samples with both isotope measurements from the upper shale reveals a statistically significant anti-correlation ($P = 0.01$). In contrast to the euxinic upper shale, isotope compositions are invariant in the non-euxinic lower shale member (170–190 m core depth, see the Supplementary Information for discussion of this interval, and interpretation of concentration data).

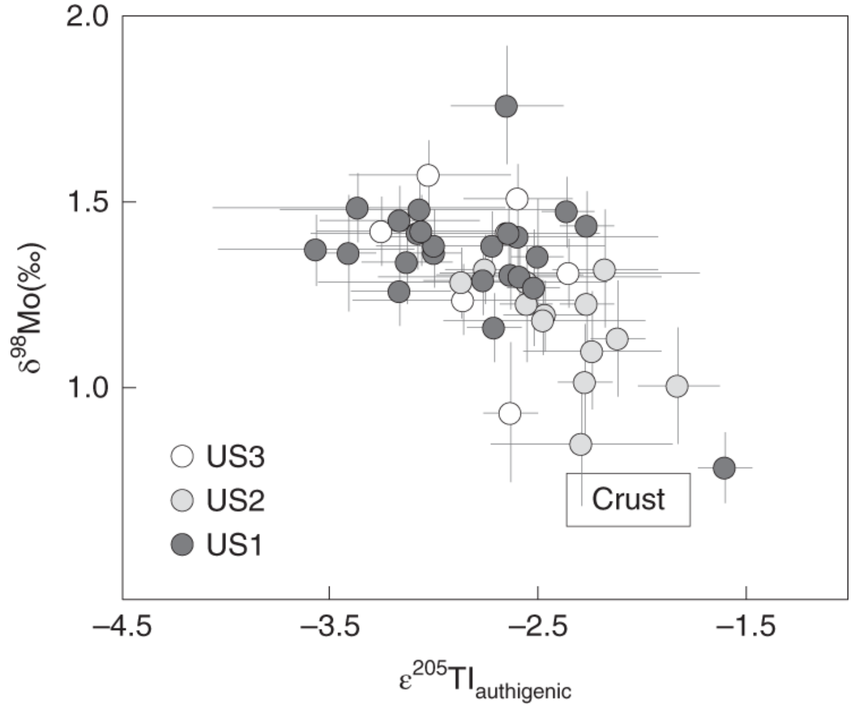

Fig. 4.3 Mo and Tl isotope cross-plot from the upper shale member. The anticorrelation trend in this plot, which is also apparent in Fig. 4.2, is statistically significant ($P = 0.01$). The box indicates current estimates for the isotope compositions of bulk continental crust (Nielsen et al. 2005; Willbold and Elliot 2017). All error bars represent the 2 s.d. reproducibility of that sample or the external long-term reproducibility of natural reference materials, whichever is greater.

4.4. Fully oxygenated water columns on continental shelves

Light ε^{205}Tl and heavy δ^{98}Mo in US1 and US3 provide strong evidence for the formation and subsequent burial of Mn oxides elsewhere in the ocean at these times. To drive the observed isotopic trends, water columns must have been fully oxygenated over portions of the ocean floor. It is most likely that Mn oxide burial at 2.5 Ga occurred in shallow oxygenated shelf environments where O_2 produced within the surface ocean by cyanobacteria was capable of being continuously transferred to underlying waters and marine sediments (for example, the environment illustrated in Fig. 4.1b).

Alternative local basin controls or processes in the sedimentary environment where the Mount McRae Shale was deposited cannot explain the observed isotope trends in the upper shale member. In a modern euxinic basin that is not well connected to the open ocean (that is, the Black Sea), Tl isotopes in the local water column and underlying sediments are heavier than the open-ocean signature (Owens et al. 2017a). If the Hamersley Basin was also not well connected to the open ocean, then the ε^{205}Tl value of the Mount McRae Shale may have been higher than the open-ocean signature. This would require even lighter seawater ε^{205}Tl compositions during deposition of US1 and US3, which would then imply an even greater extent of sediment Mn oxide burial elsewhere in the oceans. Furthermore, in modern euxinic settings where Mo is not quantitatively transferred from seawater to sediments, sedimentary δ^{98}Mo compositions are always lighter than the coeval seawater signature (Neubert et al. 2008). Hence, if Mo removal from euxinic bottom waters in the Hamersley Basin was not quantitative, then seawater δ^{98}Mo would be even heavier than observed in the Mount McRae Shale, again implying even more significant sediment Mn oxide burial elsewhere in the ocean.

In theory, the observed Tl and Mo isotope shifts might be alternatively explained by ‘shuttling’ of Tl and Mo bound to oxide minerals formed in oxic surface waters to underlying anoxic waters and/or sediments on Late Archaean continental margins, where these elements could then be captured in euxinic sediments. If so, fully oxygenated water columns would not be required to explain the antithetic shifts in Tl and Mo isotopes recorded in the Mount McRae Shale. However, this notion is not supported by observations in the modern Cariaco Basin, a modern analogue environment where Mn oxides are formed in oxygenated surface waters and subsequently transported to euxinic bottom waters and sediments deeper in the basin (Algeo and Tribovillard 2009). An oxide shuttle should cause ε^{205}Tl in euxinic sediments to be heavier than in surface oxic seawater (Nielsen et al. 2013). This is not observed, however. Euxinic sediment ε^{205}Tl in the Cariaco Basin is instead indistinguishable from overlying seawater (average $\varepsilon^{205}\text{Tl}_{\text{euxinic}} = -5.1 \pm 1.3$ (2 s.d.) versus $\varepsilon^{205}\text{Tl}_{\text{seawater}}$ -5.5 ± 0.7 (2 s.d.); Owens et al. 2017a). One possible explanation for this lack of Tl isotope fractionation is that Tl released by Mn oxide dissolution in sulfidic deep waters is first remixed and rehomogenized with the dissolved Tl pool before Tl capture in pyrite. Regardless, as anoxic sediments in the modern Cariaco Basin do not preserve the Tl isotope effects of oxide adsorption (Owens et al. 2017a) despite evidence that oxide minerals are delivered at least transiently to these sediments (Algeo and Tribovillard 2009), a Mn oxide shuttle in redox-stratified marine basins probably had a minimal impact on the Late Archaean seawater Tl isotope mass-balance.

Although there are proposed pathways of Mn oxide formation that do not require O_2, they would not be likely to cause the observed isotopic effects in the upper shale member. Oxidation of reduced Mn in the upper water column by hypothesized Mn-oxidizing phototrophs (Johnson et al. 2013) or by ultraviolet light (Anbar and Holland 1992) cannot account for burial at the seafloor because underlying anoxic waters and sediments would recycle Mn back into solution (as Mn(II); Burdige 1993; Calvert and Pedersen 1996). The high abundance of Fe(II) in deep ferruginous waters of the Archaean oceans (Lyons et al. 2014), for example, would readily promote reduction of Mn oxides in anoxic waters. If the water column or sediment pore waters were anoxic, even seasonally (Kristensen et al. 2003), reductive dissolution of Mn oxides would release sorbed Tl and Mo. Invoking an O_2-free explanation for the observed isotopic trends also requires neglecting the many independent lines of evidence for a 'whiff ' of O2 at 2.5 Ga (Anbar et al. 2007; Kaufman et al. 2007; Garvin et al. 2009; Reinhard et al. 2009; Duan et al. 2010; Kendall et al. 2013, Kendall et al. 2015; Stüeken et al. 2015; Gregory et al. 2015).

Palaeoseawater ε^{205}Tl and δ^{98}Mo values can be estimated directly from the Mount McRae Shale data and used to reconstruct ocean redox conditions. Measured ε^{205}Tl values serve as a direct estimate for the coeval seawater signature (as low as −3.57 ± 0.48) because euxinic sediments capture the overlying seawater Tl isotope value (Owens et al. 2017a). The δ^{98}Mo value recorded in euxinic marine sediments is always equal to or lighter than seawater (Neubert et al. 2008), and thus represents a lower limit for the coeval seawater signature (as heavy as 1.56 ± 0.10‰). It is possible, or even likely, that the Tl and Mo isotope compositions of seawater fluctuated during deposition of the upper shale member of the Mount McRae Shale. Deposition of this interval is estimated (Anbar et al. 2007) to have occurred over ~11 Myr and the whiff of O_2 was probably a transient episode of even shorter duration (Kendall et al. 2015). To estimate ocean redox conditions during peak Mn oxide burial, we use the lightest ε^{205}Tl and heaviest δ^{98}Mo values from the upper shale member. During peak Mn oxide burial, the retention of heavier-mass Tl and lighter-mass Mo isotopes would have been maximized, resulting in the lightest ε^{205}Tl and heaviest δ^{98}Mo seawater signatures. Unsurprisingly, the lightest ε^{205}Tl (−3.57 ± 0.48 at 148.75 m) and heaviest δ^{98}Mo (1.56 ± 0.10‰ at 145.74m) occur during US1, an interval that hosts multiple lines of geochemical evidence for an oxygenation episode (Anbar et al. 2007; Reinhard et al. 2009; Duan et al. 2010; Kendall et al. 2013, Kendall et al. 2015; Stüeken et al. 2015).

Using the estimated seawater ε^{205}Tl and δ^{98}Mo values, ocean redox conditions can be inferred using isotope mass-balance equations as follows:

$$\varepsilon^{205}\mathrm{Tl}_{\mathrm{inputs}} = \varepsilon^{205}\mathrm{Tl}_{\mathrm{AOC}}(f_{\mathrm{AOC}}) + \varepsilon^{205}\mathrm{Tl}_{\mathrm{oxic}}(f_{\mathrm{Tl\text{-}oxic}}) + \varepsilon^{205}\mathrm{Tl}_{\mathrm{other}}(f_{\mathrm{other}})$$

and

$$\delta^{98}\mathrm{Mo}_{\mathrm{inputs}} = \delta^{98}\mathrm{Mo}_{\mathrm{euxinic}}(f_{\mathrm{euxinic}}) + \delta^{98}\mathrm{Mo}_{\mathrm{SAD}}(f_{\mathrm{SAD}}) + \delta^{98}\mathrm{Mo}_{\mathrm{oxic}}(f_{\mathrm{Mo\text{-}oxic}})$$

where $\varepsilon^{205}\mathrm{Tl}_x$ and $\delta^{98}\mathrm{Mo}_x$ represent the isotopic composition of average oceanic inputs and outputs, and f_x denotes the relative removal flux for each output. For Tl, we designate low-T alteration of oceanic crust (f_{AOC}), well-oxygenated Mn oxide-rich sediments ($f_{\mathrm{Tl\text{-}oxic}}$), and other ($f_{\mathrm{other}}$) as the three dominant marine outputs. The other output signifies Tl removal with no associated isotopic fractionation (for example, euxinic basins; Owens et al. 2017a). For Mo, similar to recent work, we use euxinic sediments (f_{euxinic}), sediments that are sulfidic at depth (f_{SAD}; where sulfide is limited to sediment pore waters), and well-oxygenated Mn oxide-rich sediments ($f_{\text{Mo-oxic}}$) as the three outputs (Kendall et al. 2017) (see the Supplementary Information for more detailed information about modelling, including key assumptions).

The mass-balance model results indicate that well-oxygenated Mn oxide-rich sediments were an important sink for both Tl ($f_{\text{Tl-oxic}}$ = 6–21%) and Mo ($f_{\text{Mo-oxic}}$ = 20–34%) at 2.5 Ga. Together, these results suggest that fully oxygenated shelf environments were a common feature on continental margins, at least regionally, at 2.5 Ga.

We make no attempt here to convert these fluxes into the areal extent of seafloor because the flux per areal unit into these marine outputs was probably much different in the Archaean compared with today. Burial rates of Tl and Mo in modern oxic marine environments that bury Mn oxides are very low, much lower than their burial rates in other modern marine outputs (for example, the burial of Tl during low-T alteration of oceanic crust (Nielsen et al. 2017) and burial of Mo under strong euxinic conditions (Kendall et al. 2017)). For this reason, seafloor area calculations using modern Tl and Mo burial rates and our ancient seawater isotope signature estimates would require the majority of the seafloor at 2.5 Ga to have been oxic. Expansive oxic conditions before the GOE are unlikely because many independent lines of evidence support a predominately anoxic global ocean at this time (Lyons et al. 2024). It is most likely that burial rates of Tl and Mo in 2.5 Ga oxic environments were much higher than today. For example, dissolved Mn concentrations in Archaean seawater may have been four orders of magnitude higher than today (Holland 1984), providing a strong potential for high Mn oxide burial rates in oxic environments, and therefore a stronger potential for Tl and Mo adsorption. Furthermore, the burial rate of Mo (and potentially also of Tl) into euxinic environments could have been much lower than today because sulfate concentrations in Archaean oceans were very low (Habicht et al. 2002). Euxinic conditions in a low-sulfate ocean could have been much weaker than today, lowering the potential for sedimentary retention of Mo. In summary, a smaller area of 2.5 Ga seafloor burying Mn oxides could conceivably drive a more pronounced seawater Tl and Mo isotope signature effect than today, but is difficult to estimate precisely.

Our findings provide a new perspective on marine oxygenation at 2.5 Ga, on the cusp of the GOE. Multiple lines of geochemical evidence provide strong support for O_2 in shallow waters of the Hamersley Basin at 2.5 Ga (Anbar et al. 2007; Kendall et al. 2013; Stüeken et al. 2015) and the adjoining Griqualand West Basin (Wille et al. 2007; Czaja et al. 2012) (which may have bordered the same ocean basin; De Kock et al. 2009). However, because Mn oxide burial requires fully oxygenated water columns at 2.5 Ga, our multi-isotope data supports more oxygenated continental shelves over a greater area than previously recognized using other geochemical datasets. Specifically, the inferred seawater ε^{205}Tl and δ^{98}Mo composition requires fully oxygenated water columns in shelf environments within the Hamersley Basin and adjoining basins(s), and potentially even large portions of the continental margins worldwide. Our results highlight the important and expanding role of cyanobacteria as engineers of the Archaean biosphere, particularly in the run-up to the GOE.

CHAPTER 5

MULTIPLE NEGATIVE MOLYBDENUM ISOTOPE EXCURSIONS IN THE DOUSHANTUO FORMATION (SOUTH CHINA) FINGERPRINT COMPLEX REDOX-RELATED PROCESSES IN THE EDIACARAN NANHUA BASIN

The work presented in this chapter has been published as: Ostrander, C.M., Sahoo, S.K., Kendall, B., Jiang, G., Planavsky, N.J., Lyons, T.W., Nielsen, S.G., Owens, J.D., Gordon, G.W., Romaniello, S.J., Anbar, A.D. (2019) Multiple negative molybdenum isotope excursions in the Doushantuo Formation (South China) fingerprint complex redox-related processes in the Ediacaran Nanhua Basin. *Geochimica et Cosmochimica Acta* **261**, 191-209.

Abstract

The Ediacaran Doushantuo Formation offers one of the most complete and extensively studied records of end- Neoproterozoic biotic and environmental change. Here, we report multiple coeval negative molybdenum (Mo) isotope excursions (to as low as $\delta^{98}Mo_{NIST+0.25}$ = -2.24 ± 0.10‰; 2SD) in shales from four separate sites in South China (Rongxi, Taoying, Wuhe, and Yuanjia) that preserve the Doushantuo Formation. The negative δ^{98}Mo excursions appear coincident with previously discovered and seemingly peculiar redox-sensitive element (RSE) patterns in the same sedimentary rocks. We propose that these geochemical trends can be explained by some combination of (a)

enhanced local marine oxygenation in the sedimentary basin where the Doushantuo Formation was originally deposited (the Nanhua Basin) and (b) changes in the degree of connectivity between this paleo basin and the open ocean. Enhanced local marine oxygenation, by exposing more sediments in the Nanhua basin to H_2S-poor conditions, could have hindered quantitative tetrathiomolybdate formation within these sediments. Local marine oxygenation could have also stimulated the operation of a Mn oxide shuttle. Today, both of these processes are shown to promote the retention of lighter-mass Mo isotopes in sediments and also govern RSE enrichment pat- terns. Alternatively, or in addition, the Nanhua Basin may not have maintained an uninterrupted connection with the open ocean during the entirety of the Ediacaran Period. The negative δ^{98}Mo excursions occur coincident with sea level highstands that could have also exposed more sediments in the basin to H_2S poor conditions and/or catalyzed the operation of a local Mn oxide shuttle. When trying to infer temporal changes in ancient global ocean redox, it is important to consider the influence of sea level changes and associated variations in local depositional conditions on stratigraphic trends in RSE enrichments and isotope compositions.

5.1 Introduction

The tempo of marine oxygenation during the Ediacaran Period (635–542 million years ago, or Ma) is debated. It is generally accepted that the shallow ocean was oxygenated throughout the Ediacaran (Lowenstein et al., 2013, and references therein). However, two predominant viewpoints exist for the O_2 contents of the deeper waters: (1) always anoxic (Johnston et al., 2013; Sperling et al., 2015) or (2) subject to episodic ocean oxygenation events (OOEs [Fike et al., 2006; McFadden et al., 2008; Kendall et al., 2015; Sahoo et al., 2012, 2016]). Resolution of this debate is important to understanding what role – if any – O_2 levels in Ediacaran oceans played in controlling the dynamics of early animal evolution (Knoll, 2011; Lenton et al., 2014).

The most commonly invoked evidence for Ediacaran OOEs comes in the form of redox-sensitive element (RSE; e.g., V, Mo, Re, and U) enrichments in shales – foremost from the Doushantuo Formation of South China (Sahoo et al., 2012, 2016). In the modern ocean, widespread oxygenation supports large seawater reservoirs of RSE, which enables strong sedimentary RSE accumulation in the anoxic organic-rich marine sediments that cover a small percentage of the ocean floor (e.g., Scott et al., 2008; Sahoo et al., 2012; Partin et al., 2013; Sheen et al., 2018). Intuitively, ancient black shales deposited in the primarily anoxic Precambrian global ocean (Reinhard et al., 2013) and also during episodes of extensive global ocean anoxia during the Cambrian (Gill et al., 2011; Owens et al., 2016) have much lower RSE abundances because widespread burial in anoxic sediments depleted RSE seawater reservoirs. The transition away from a predominantly anoxic Precambrian ocean and toward a well-oxygenated one more similar to today's is expected to have led to first-order increases in RSE seawater reservoirs and sedimentary RSE accumulation. The geochemical fingerprints of at least the initial, likely transient phases of this transition seem to have been captured in black shales from the Ediacaran Doushantuo Formation (Scott et al., 2008; Sahoo et al., 2012, 2016).

Some RSE trends in the Doushantuo Formation are peculiar, causing some researchers to question their straightforward link to Ediacaran ocean oxygenation (e.g., Miller et al., 2017). For example, some RSEs are enriched in Doushantuo shales to levels comparable to those found in only the most RSE-enriched Phanerozoic shales (V in particular, which reaches wt. % abundances [Sahoo et al., 2016]). Furthermore, during the ca. 580 Ma OOE recorded in Doushantuo shales, some RSEs are not enriched at all (e.g., Mo [Sahoo et al., 2016], although pyrite from these shales is enriched in Mo [Gregory et al., 2017]). Lastly, the widespread ocean oxygenation implied by the episodes of RSE enrichment in the Doushantuo Formation does not seem to be supported by some geochemical compilations (e.g., a recent compilation of the Fe speciation record [Sperling et al., 2015]).

Using the Mo isotope paleoredox proxy, we provide new perspective on the sedimentary RSE record from South China. The Mo isotope composition of organic-rich marine shales can be an effective way to track redox changes in Earth's ancient oceans (see a recent review by Kendall et al., 2017). For example, sedimentary rocks deposited under anoxic and sulfidic (hereafter referred to as euxinic) conditions in restricted basins can sometimes capture the coeval seawater δ^{98}Mo (e.g., in deep portions of the Black Sea [Neubert et al., 2008], Kyllaren fjord [Noordmann et al., 2015], and Lake Rogoznica [Bura-Nakić et al., 2018]). Transfer of the seawater δ^{98}Mo to marine sediments is possible in these settings because nearly all Mo in marine bottom waters can be transferred to underlying sediments. The Mo isotope composition of seawater is a useful parameter because it is thought to be a direct consequence of the relative distribution of oxic versus euxinic conditions on the seafloor (Barling et al., 2001; Arnold et al., 2004). For these reasons, the primary application of the Mo isotope paleoredox proxy to date has been as a tool for estimating global marine redox conditions using ancient sedimentary rocks originally deposited under euxinic conditions (Kendall et al., 2017).

In the majority of modern marine settings, however, including some that are defined as euxinic, near-quantitative transfer of Mo from deep water to sediments does not occur and results in sedimentary δ^{98}Mo that are isotopically lighter than the coeval seawater value (e.g., Arnold et al., 2004; Poulson et al., 2006; Poulson-Brucker et al., 2009; Nägler et al., 2011; Noordmann et al., 2015). In these settings, incomplete transfer of Mo from seawater to sediments and the complexation of Mo with Fe oxide minerals (Goldberg et al., 2009, 2012), Mn oxide minerals (Wasylenki et al., 2008), and organic matter (King et al., 2018) – as well as the persistence of intermediate thiomolybdate species (Neubert et al., 2008) – results in the preferential retention of lighter-mass Mo isotopes in these sediments. Therefore, a case can be made that an important utility of the Mo isotope paleoproxy rests with tracking these processes – rather than, or in addition to, its value as a proxy tracking global seawater δ^{98}Mo.

We have measured the Mo isotope compositions of the same shale samples from the Doushantuo Formation from South China that yielded the RSE evidence for OOEs (i.e., those analyzed in Sahoo et al., 2012, 2016). Redox-sensitive elements, in addition to their sensitivity to global marine redox conditions, are also sensitive to the complexation processes that affect sedimentary δ^{98}Mo (e.g., Morford et al., 1999, 2005; Tribovillard et al., 2006; Scholz et al., 2011, 2013, 2018). Therefore, by identifying these complexation processes using Mo isotopes, we can assess their possible contribution to the RSE patterns in the Doushantuo Formation.

5.2 Material and Methods

5.2.1 The Doushantuo Formation from South China

We targeted shales of the Ediacaran Doushantuo Formation ($635–560 Ma [Condon et al., 2005; An et al., 2015]) in multiple sections from the Yangtze platform in South China, a paleo-location referred to as the Nanhua Basin (Jiang et al., 2011) (Fig. 5.1). In order of increasing distance from the paleo-shoreline, we measured Mo isotope compositions of shales originally deposited on the continental slope of the Nanhua Basin from sites at Rongxi, Taoying, and Wuhe and of shales deposited deeper within the basin from the Yuanjia site. A case has been made previously that sedimentary rocks deposited in the slope and basin environments of the Nanhua Basin were connected with the open ocean during deposition of the Doushantuo Formation (Jiang et al., 2011; Sahoo et al., 2012).

We targeted shales from the entire Wuhe site (Members II through IV) and shales deposited during the purported OOEs from lowermost Member II (Rongxi, Taoying, and Yuanji), Member III (Taoying), and Member IV (Rongxi, Taoying) of the other sections

(Fig. 5.2). All of these sections are described in detail in previous work (Jiang et al., 2011; Sahoo et al., 2012, 2016); only a very brief overview is provided here.

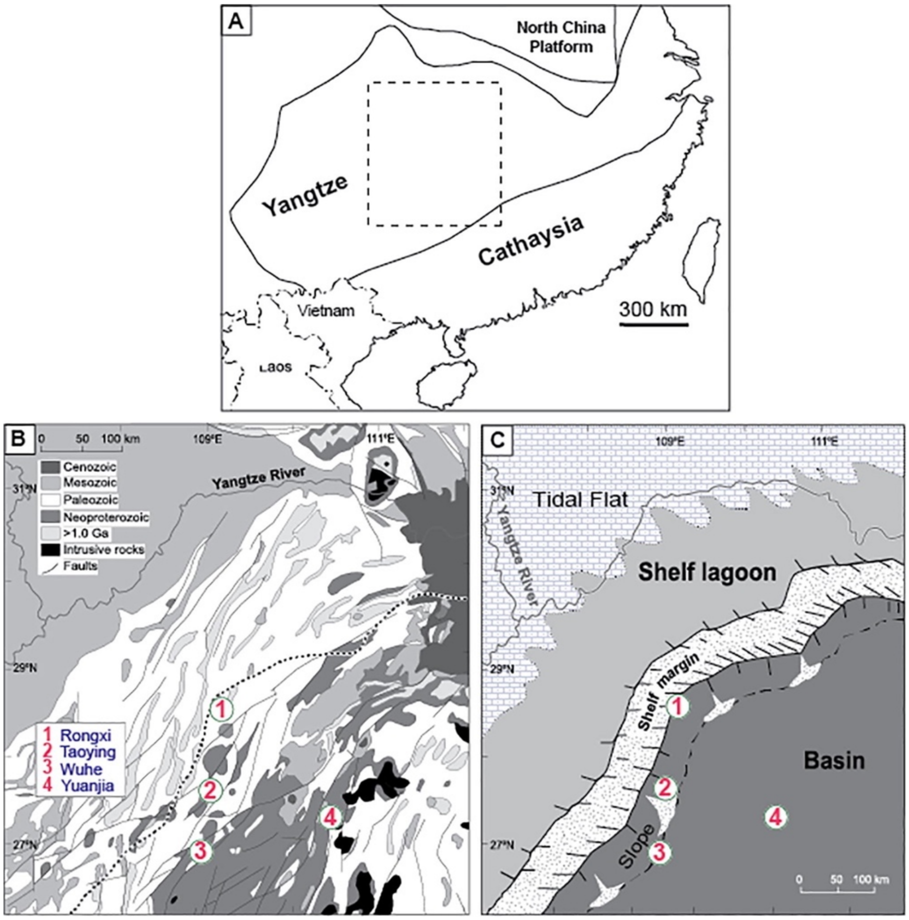

Fig. 5.1 Tectonic, geological, and paleogeographic maps for the Yangtze platform of South China. (a) Tectonic map showing the Yangtze and Cathaysia blocks in China, with the dashed rectangle corresponding to the area depicted in B and C. (b) Simplified geological map showing exposures of strata in the central Yangtze platform of South China. The dotted line signifies the position of the platform margin during the late Neoproterozoic, and each number represents a site from which shales used in this study were originally collected. (c) Paleogeographic reconstruction of the Nanhua Basin during the Ediacaran Period. Figures modified from Jiang et al. (2011).

Much effort has been dedicated to stratigraphically correlating the many sections from South China that preserve the Doushantuo shales. For ease of correlation, the

Doushantuo Formation is split into four distinct members based primarily on lithology (Fig. 5.2). The cap carbonates overlying the glacial diamictites of the Marinoan glaciation are assigned to Member I (635.2 ± 0.6 Ma [Condon et al., 2005]). Cap carbonates of Member I are overlain by mixed carbonate-siliciclastics, with the onset of Member II in slope sections typically signified by a transition to shale-dominated units. In the shelf and upper slope sections, including the Rongxi section, Member III is dominated by carbonates, but equivalent strata in the lower slope and basin sections are shale-dominated, with carbonate beds unevenly distributed in the lower and upper parts. Black shales of Member IV are widespread across the entire Nanhua Basin and are seen in all measured sections.

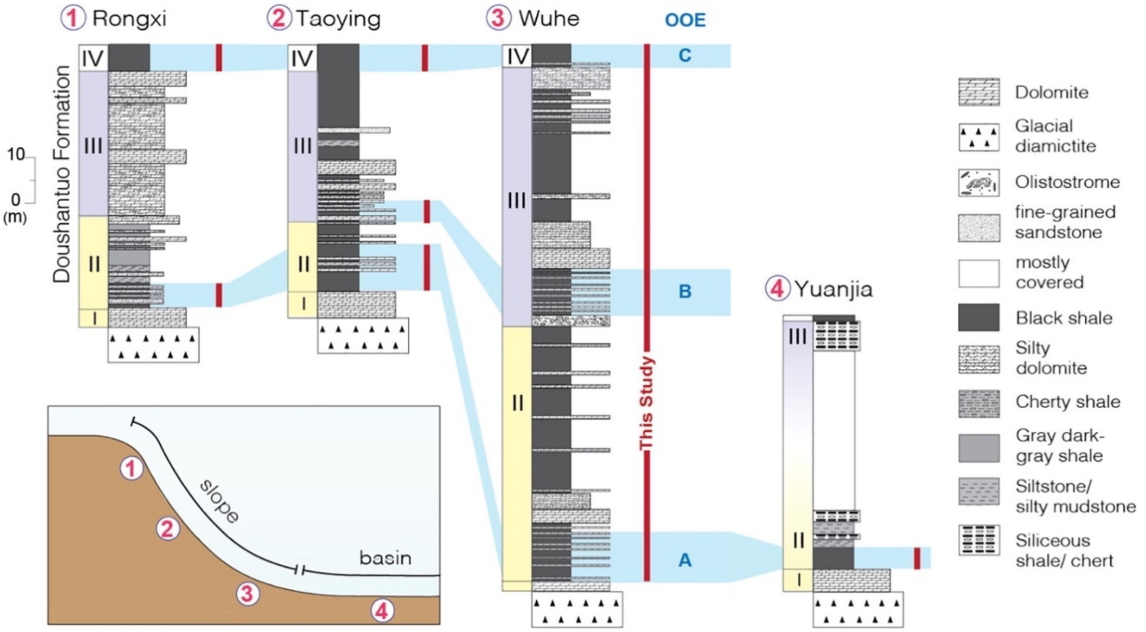

Fig. 5.2 Sections analyzed in this study. For a detailed description of lithology, see Jiang et al., 2011, Sahoo et al., 2012. Section intervals targeted here are signified by the vertical red bar. Previously identified Ediacaran ocean oxygenation events (OOEs) are identified by blue boxes (A, B, and C [Sahoo et al., 2012, Sahoo et al., 2016]). Stratigraphic columns, slope reconstruction, and legend are modified from Jiang et al., 2011, Sahoo et al., 2016.

5.2.2 Mo isotope methods

All sample digestion, chromatography, and instrumental analysis was completed at the W. M. Keck Foundation Laboratory for Environmental Biogeochemistry at Arizona State University. Whole-rock powders were ashed and digested and concentrations were analyzed via quadrupole Inductively Coupled Plasma Mass Spectrometry (ICPMS) using techniques outlined in previous work (Olson et al., 2019). Subsequently, enough sample was taken from each digested stock solution to provide 125 ng of Mo, and thereafter spiked with an optimal amount of calibrated synthetic Mo isotope double spike (^{97}Mo and ^{100}Mo) to correct for isotopic fractionation during chromatography and for instrumental mass bias (Siebert et al., 2001). Molybdenum purification involved the typical two-step anion and cation column procedure (e.g., Duan et al., 2010).

Table 5.1 Mo isotope data from standard reference material solutions

Standard	δ^{98}Mo (2SD)^{a,*}	N	Normalized to NIST + 0.25‰	Goldberg et al. (2013)
ICL-Mo	0.18 (0.04)	21	0.10 (0.04)	0.09 (0.05)
Kyoto-Mo	-0.03 (0.06)	5	-0.11 (0.06)	-0.12 (0.06)
NIST SRM 3134	0.33 (0.04)	42	0.25	0.25
SDO-1	1.14 (0.05)	35	1.06 (0.05)	1.05 (0.14)

a. measured relative to Roch-Mo2

*all reported errors are 2SD of the standard reproducibility

Isotope ratio measurements were performed on a Thermo Neptune multi-collector ICPMS (MC-ICPMS) in low-resolution mode with an Elemental Scientific Inc. Apex inlet system and using sample-standard bracketing. All measurements were made using the Johnson Matthey Specpure Mo plasma standard (Lot #802309E; RochMo2) as the bracketing standard and then re-calculated relative to the new international NIST SRM

3134 standard = +0.25‰ (Nägler et al., 2014). In brief, the measured value for NIST SRM 3134 was 0.33 ± 0.04‰; 2SD relative to RochMo2 during our analytical sessions (Table 5.1). Accordingly, 0.08‰ was subtracted from each sample Mo isotope composition measured relative to RochMo2. Samples and standards were analyzed at a concentration of 25 ng/g Mo, which yielded about three volts of signal on mass 98. Samples were analyzed in duplicate (at least), with the average 2SD sample reproducibility being 0.05‰ and the maximum being 0.22‰. Over the period of Mo isotope analysis for this study, USGS rock reference material SDO-1 (Devonian Ohio Shale) was simultaneously processed with each batch of samples to monitor accuracy and showed good reproducibility (δ^{98}Mo = 1.07 ± 0.05‰; 2SD; compared to 1.05 ± 0.14‰; 2SD; in previous work [Goldberg et al., 2013]) as did multiple secondary standard solutions (Table 5.1). Lastly, for each analytical run, a series of standards with varying spike-sample ratios was measured. All samples were within the validated spike-sample range for accurate and precise δ^{98}Mo values.

5.3 Results

Molybdenum isotope compositions in shales of the Doushantuo Formation from all slope and basin sections across the purported OOEs (i.e., in Doushantuo Members II, III, and IV) are predominantly negative (as low as -2.24 ± 0.10‰; 2SD; in Member II of the Taoying section) (Figs. 5.3 and 5.4). The heaviest measured shale δ^{98}Mo during the OOEs is 1.32 ± 0.15‰ (2SD) and comes from Member IV of the Rongxi section. Maximum δ^{98}Mo in shales deposited during the older OOEs are isotopically lighter: 0.76 ± 0.10‰

during the OOE in lower Member II (again from the Rongxi section) and 0.78 ± 0.10‰ during the OOE in lower Member III (from the Taoying section).

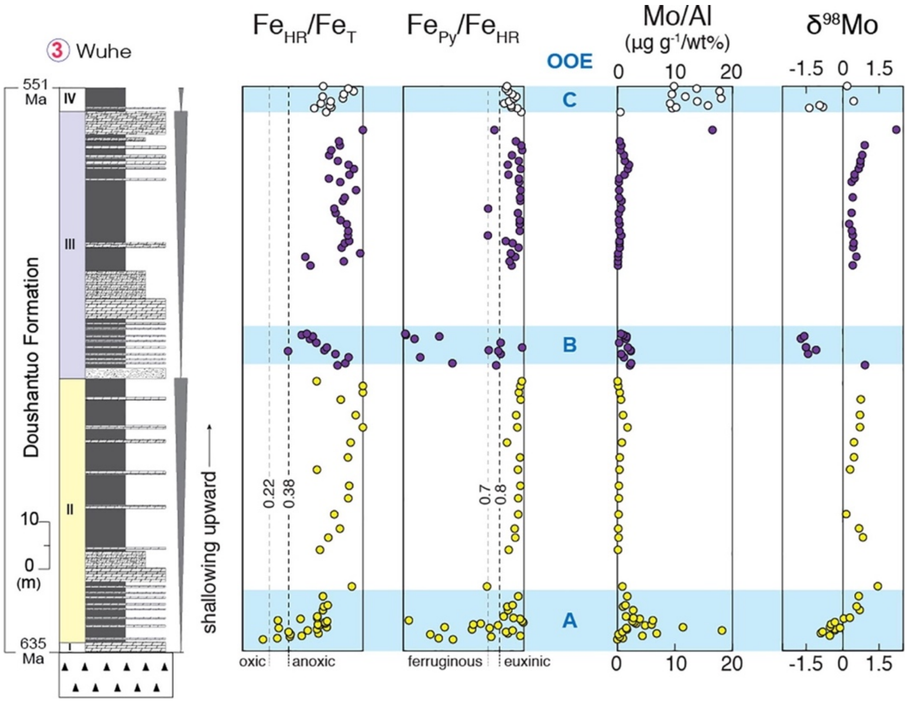

Fig. 5.3 Geochemistry of the Wuhe section. Iron speciation and trace metal data is from Sahoo et al., 2012, Sahoo et al., 2016. Thresholds for anoxic and euxinic deposition are adapted from Raiswell et al. (2018). Again, blue boxes signify purported OOEs. Data points are color-coded according to Doushantuo Member. See Fig. 5.1 for a lithology key. All error bars represent the 2SD reproducibility of that sample or the external long-term reproducibility of natural reference materials, whichever is greater. In most cases, error bars are smaller than the data points. Figure modified from Sahoo et al. (2016).

In contrast, δ^{98}Mo in shales from the Wuhe section between the OOEs are always positive (Fig. 5.3). One sample from uppermost Member III from this section (110.7 m) is especially heavy (2.24 ± 0.10‰; 2SD). Other than this one sample, δ^{98}Mo values are much lighter, exceeding 1.0‰ only one other time (1.47 ± 0.10‰; 2SD; in lowermost Member

II immediately above the oldest OOE) and remain fairly invariant otherwise (δ^{98}Mo = 0.57 ± 0.21‰; 2SD).

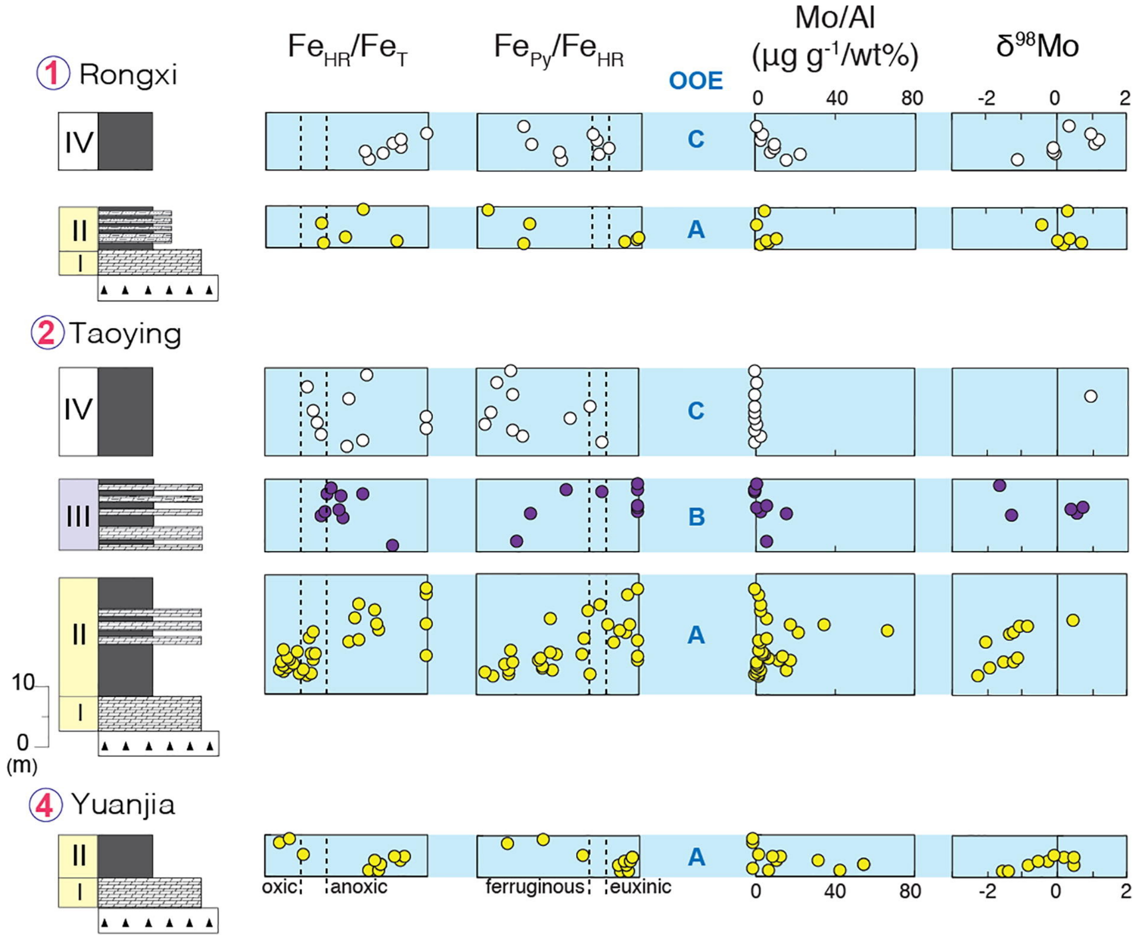

Fig. 5.4 Geochemistry of the Rongxi, Taoying, and Yuanjia sections. Iron speciation and trace metal data is from Sahoo et al., 2012, Sahoo et al., 2016, Sahoo, 2015. Thresholds for anoxic and euxinic deposition are adapted from Raiswell et al. (2018). Again, blue boxes signify purported OOEs and data points are color-coded according to Doushantuo Member. See Fig. 5.1 for a lithology key. All error bars represent the 2SD reproducibility of that sample or the external long-term reproducibility of natural reference materials, whichever is greater. In most cases, error bars are smaller than the data points. Figure modified from Sahoo et al. (2012).

5.4 Discussion

In the following section, we begin by first discussing local processes in the Ediacaran Nanhua Basin that most likely played a role in driving the observed negative Mo isotope compositions in the Doushantuo Formation (Section 4.1). We then discuss how these local processes likely also played some role in governing the RSE patterns found in shales of the Doushantuo Formation (Section 4.2). Lastly, we finish this section by discussing a combination of plausible scenarios that may account for the transient nature of the geochemical excursions found in the Doushantuo Formation (Sections 4.3 and 4.4).

5.4.1 Negative δ^{98}Mo in Doushantuo shales

Negative δ^{98}Mo that are well below crustal estimates cannot represent Ediacaran global open-ocean seawater. The estimated average δ^{98}Mo of upper crustal rocks covers a restricted range between about 0.35‰ and 0.60‰ (Willbold and Elliot, 2017). Because the vast majority of Mo delivered to the ocean is sourced from crustal rocks (Miller et al., 2011; Greaney et al., 2018) and because all processes that operate during Mo delivery to and removal from the ocean preferentially retain lighter-mass Mo isotopes, the seawater δ^{98}Mo at any time in Earth's history was probably never lighter than this crustal composition (reviewed in Kendall et al., 2017).

Only two processes in modern marine settings are capable of driving the large negative Mo isotope fractionation effects observed in the Doushantuo Formation: delivery of lighter-mass Mo isotopes to sediments by (1) Mn oxide minerals (i.e., a Mo shuttle [Scholz et al., 2013, 2018]) and (2) thiomolybdates (Tossell, 2005; Neubert et al., 2008).

The operation of one or both of these processes in the Ediacaran Nanhua Basin must have led to the preservation of a sedimentary δ^{98}Mo much lighter than the ancient seawater composition.

5.4.1.1. "Shuttling" by Mn oxide minerals

The transient development of a Mn oxide "shuttle" in the Ediacaran Nanhua Basin could help explain the negative δ^{98}Mo excursions in shales from the Doushantuo Formation. Today, the most well-studied marine basin hosting a Mn oxide shuttle is the Baltic Sea (e.g., Scholz et al., 2013, 2018; Hardisty et al., 2016). In the Baltic Sea, during transient introduction of well-oxygenated waters into the semi-restricted basin, insoluble Mn oxides form high in the water column and sink to the seafloor (Huckriede and Meischner, 1996). Upon being introduced to the anoxic and euxinic conditions deeper in the water column or underlying sulfidic sediments, these same Mn oxides are solubilized during reductive dissolution, typically evading burial in marine sediments if O_2 is not present in bottom waters (Calvert and Pedersen, 1996; Häusler et al., 2018). Some RSEs bound to Mn oxides are retained in sediments after reductive dissolution, however, because they are less soluble under the reducing conditions present in bottom waters and sediments (e.g., Mo and V [Morford et al., 2005; Scholz et al., 2011, 2013]). In the case of Mo, the presence of appreciable hydrogen sulfide is required to promote sedimentary retention (Crusius et al., 1996; Morford et al., 2005). When Mo is shuttled by Mn oxides from oxic surface waters of the Baltic Sea to underlying sulfidic sediments, these sediments have δ^{98}Mo nearly 3.0‰ lighter than the overlying seawater value (Scholz et al., 2013, 2018), similar to the equilibrium isotope effect imparted during Mo sorption to Mn oxides (Δ^{98}Mo = 2.7 ± 0.1‰ [Wasylenki et al., 2008]).

In comparison, sediments that receive lighter-mass Mo isotopes via an Fe oxide shuttle have an authigenic δ^{98}Mo only $1.0‰ lighter than the overlying seawater value (e.g., those from the geologically recent Peruvian continental margin [Scholz et al., 2017]). This smaller isotopic offset is similar to that imparted during Mo sorption to ferrihydrite and goethite (Δ^{98}Mo = 1.11 ± 0.15‰ and Δ^{98}Mo = 1.40 ± 0.48‰, respectively [Goldberg et al., 2009]), Fe oxide minerals shown to be abundant in particulate matter of the modern Peruvian margin oxygen minimum zone (Scholz et al., 2017). Given the magnitude of the δ^{98}Mo excursions found here in shales of the Doushantuo Formation (to as low as $\delta^{98}\mathrm{Mo}_{\mathrm{NIST+0.25}}$ = -2.24 ±0.10‰; 2SD), it is unlikely that the sediments were strongly affected by an Fe oxide shuttle. More likely, the extremely light δ^{98}Mo require the larger Mo isotope fractionation effects associated with adsorption to Mn oxides (Δ^{98}Mo = 2.7 ± 0.1‰ [Wasylenki et al., 2008]).

Large V enrichments in shales from the Doushantuo Formation support the operation of an oxide shuttle in the Nanhua Basin. These shales are dramatically enriched in V (up to ~3 wt% [Sahoo et al., 2016]), more so than any modern marine sediments (all <0.05 wt% [Nameroff et al., 2002; Scholz et al., 2011]). In fact, the exceptional enrichments have been cited as challenging the original interpretation linking RSE enrichments to OOEs (Miller et al., 2017) and attributed instead to poorly understood secondary enrichment processes. Notably, V possesses a particularly strong affinity for oxide minerals and is consequently highly enriched in ferromanganese crusts (up to 0.08

wt% [Hein and Koschinsky, 2014]) relative to its abundance in seawater (35 nmol/L [Collier, 1984]), much more so than most other RSEs (Fig. 5.5). Modern anoxic marine sediments that receive RSE-laden oxides from overlying oxic waters, or those that form oxides in-situ during seasonal inflow of oxygenated waters, also become enriched in V (up to 0.04 wt% [e.g., Morford et al., 2005; Scholz et al., 2011]). A general negative correlation between V_{EF} and δ^{98}Mo ($R^2 = 0.59$; Fig. 5.6) is consistent with co-delivery of V and lighter-mass Mo isotopes via a Mn-oxide shuttle. This relationship is not as apparent between δ^{98}Mo and EFs for RSEs with a relatively lower affinity for oxide minerals (Mo_{EF} [$R^2 = 0.12$] and U_{EF} [$R^2 = 0.19$]; Fig. 5.6).

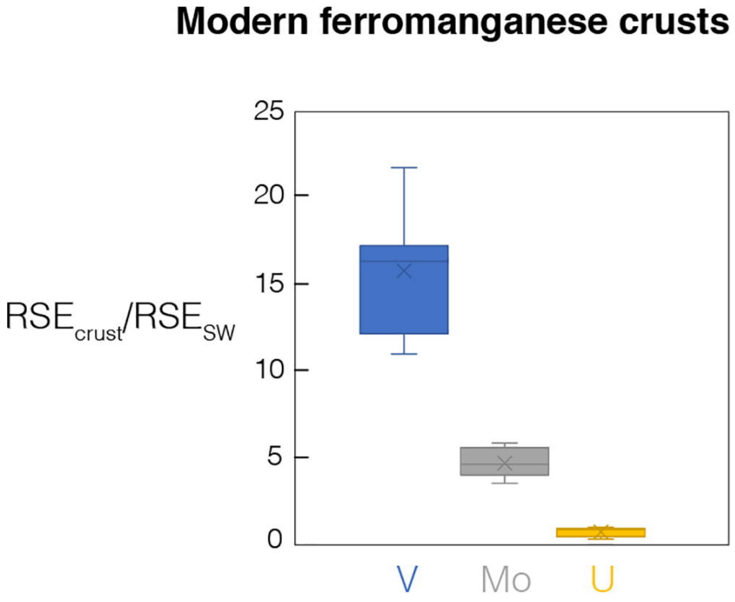

Fig. 5.5 Whisker plots showing relative abundance of redox-sensitive elements (RSEs) in modern seawater and ferromanganese crusts. Seawater RSE concentrations (in nmol/kg [Morris, 1975, Collier, 1984, and Chen et al., 1986]) and ferromanganese crust RSE abundances (in µg/g [Hein and Koschinsky, 2014]) come from previous work. Whisker plots represent the range of values when dividing the average RSE abundances from ferromanganese crusts from different sites (Table 1, Hein and Koschinsky [2014]) by the average seawater concentration of that RSE.

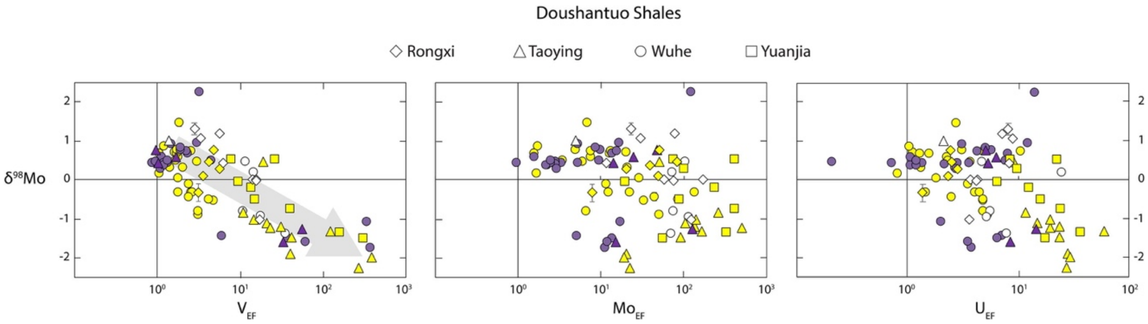

Fig. 5.6 Cross-plots of Mo isotope compositions and RSE enrichment factors (EF) in Doushantuo Shales. Mo isotope data is from this study and elemental abundances come from previous work (Sahoo et al., 2012, Sahoo et al., 2016). Enrichment Factors were calculated relative to upper continental crust as follows: $RSE_{EF} = (RSE/Al)_{shale} \div (RSE/Al)_{upper\ crust}$ (RSE abundances in μg/g and Al in wt%). Upper continental crust elemental abundances used in our calculations come from Rudnick and Gao (2003). Data point shapes coincide with the different sites from South China, and colors signify the different Doushantuo Members (II = yellow, III = purple, and IV = white).

An alternate means of promoting V hyper-enrichment, recently proposed by Scott et al. (2017), is unlikely to have driven the strong V enrichments in the Doushantuo Formation. Scott et al. (2017) attribute strong V enrichments (up to 0.25 wt%) in organic-rich shales from the Late Devonian-Early Mississippian Bakken Formation to extremely high levels of H_2S (to >10 mM) in the original bottom waters or sediments. This hypothesis is supported by strong enrichment of Mo in the same shale samples (up to 0.18 wt%) because sedimentary Mo accumulation today is enhanced in H_2S-rich settings (Crusius et al., 1996; Morford et al., 2005). In the Doushantuo Formation, however, the most V-enriched shales (up to single wt% during OOE ‘‘B” in the Wuhe section; see Fig. 5.3) have very low Mo abundances (reaching only 15 ug/g). Furthermore, Fe speciation ratios in these shales, as well as those deposited during OOE ‘‘A” where V abundances are also very high (up to 0.4–0.6 wt% at the Taoying, Wuhe, and Yuanji sites), often dip below the thresholds for euxinic deposition (see Figs. 5.3 and 5.4). These geochemical fingerprints are inconsistent with the H_2S-replete conditions required by the Scott et al. (2017) hypothesis. Therefore, although this mechanism of V hyper-enrichments may explain the Bakken Formation data, it is not supported by the geochemical trends in the Doushantuo Formation.

Operation of an oxide shuttle during the OOEs is also suggested when viewed using a more classical method of identification – that is, preferential sedimentary accumulation of Mo over U under sulfidic conditions (Algeo and Tribovillard, 2009). During the operation of a local oxide shuttle, Mo can accumulate in sulfidic marine sediments much more efficiently than U because scavenging of Mo by oxide minerals is stronger than scavenging of U by oxide minerals (apparent in Fig. 5.5). Consistent with this model, Mo enrichments in Doushantuo shales during the OOEs are sometimes much greater than U when δ^{98}Mo are very negative (Fig. 5.7). Some shale samples with very negative δ^{98}Mo do not exhibit this Mo-U enrichment pattern, however, requiring an alternative explanation (see Section 4.1.2).

Importantly, muted Mn contents in bulk shale samples throughout the Doushantuo Formation from all sections studied here do not preclude the shuttle hypothesis (never above 0.24 wt% Mn relative to the average upper continental crust value of 0.08 wt% [Rudnick and Gao, 2003]; see Supplementary Data Table). Although sedimentary RSE enrichments are an expected consequence of an oxide shuttle, sedimentary Mn accumulation is not. Manganese is highly soluble after reductive dissolution under anoxic or euxinic conditions (as Mn^{2+}) and does not readily form sulfide minerals (Burdige, 1993). A persistent presence of free O_2 in marine bottom waters is required to promote appreciable

Mn accumulation in marine sediments (Calvert and Pedersen, 1996; Häusler et al., 2018). Previous attempts to constrain local marine redox conditions on the slope of and within the deeper portions of the Nanhua Basin found evidence for either euxinic, anoxic, or suboxic conditions (e.g., Wang et al., 2012; Sahoo et al., 2012, 2016; Jin et al., 2018), all of which do not favor Mn accumulation. Even under the most oxidizing of these conditions (i.e., sub-oxic), O_2 may not sufficiently penetrate marine sediments to support Mn retention (Morford et al., 2005). Thus, there is no reason to expect Mn enrichments in shales of the Doushantuo Formation despite the likely delivery of Mo via Mn oxides. Notably, individual pyrite grains from shales of the Doushantuo Formation deposited during OOEs are slightly enriched in Mn (but <1.0 wt% [Gregory et al., 2017]). These slightly elevated abundances might fingerprint the intense (re)cycling of Mn that took place in the original bottom waters or sediments, especially given the low affinity of Mn for sulfide (Burdige, 1993).

5.4.1.2. Incomplete tetrathiomolybdate formation

When transfer of Mo from seawater into sediments is non-quantitative, a large isotopic offset can result from the formation of thiomolybdate ions (i.e., $MoO_XS_{4-X}^{2-}$), an offset that can leave sediments dramatically enriched in lighter-mass Mo isotopes (Tossell, 2005; Neubert et al., 2008; Nägler et al., 2011). Thiomolybdate ions form in the presence of hydrogen sulfide. In marine settings where hydrogen sulfide is abundant in marine bottom waters and sediments (>11 uM H_2S(aq)), the predominant thiomolybdate formed is tetrathiomolybdate (MoS_4^{2-} [Erickson and Helz, 2000]). In marine settings where sulfide availability is low and/or unstable (i.e., where local marine bottom waters are only weakly or transiently euxinic, anoxic and non-sulfidic, or weakly oxygenated), however, conversion of molybdate to tetrathiomolybdate is incomplete and leads to the formation of thiomolybdate intermediates with very different Mo isotope compositions (mono- ($MoO_3S_1^{2-}$), di- ($MoO_2S_2^{2-}$), and tri- ($MoO_1S_3^{2-}$) thiomolybdates [Tossell, 2005]). In the most extreme case found to date, sedimentary δ^{98}Mo thought to be a product of incomplete tetrathiomolybdate formation are up to ~3‰ lighter than the seawater composition (immediately below the chemocline of the Black Sea [Neubert et al., 2008; Nägler et al., 2011]).

Similar to the identification of an oxide shuttle, variations in sedimentary Mo-U patterns may also be used to identify conditions unfavorable for quantitative tetrathiomolybdate transformation (e.g., Azrieli-Tal et al., 2014). Fluctuations in ancient localized hydrogen sulfide contents are thought to be fingerprinted in shales by progressive increases (more sulfidic) and decreases (less sulfidic) in the enrichments of both Mo and U (Algeo and Tribovillard, 2009). This pattern results from the shared affinity of both RSEs for reducing conditions, affinities that strengthen steadily as conditions become more reducing in marine bottom waters and sediments. Indeed, many of the Doushantuo shales with very negative δ^{98}Mo plot along a line of increasing Mo and U (Fig. 5.7). This relationship is an expected consequence of an ancient, relatively open- marine environment where redox conditions fluctuated between suboxic, anoxic, and euxinic deposition. Iron speciation ratios reported in previous work corroborate this suggestion (Sahoo et al., 2012, 2016). At times during the purported OOEs, Fe_{HR}/Fe_T and Fe_{Py}/Fe_{HR} ratios in all sections show variations consistent with deposition from oxic, anoxic, and euxinic bottom waters

(Figs. 5.3 and 5.4). These variations in local redox conditions, particularly away from euxinia, would have promoted incomplete tetrathiomolybdate formation in the original sediments, resulting in the preferential retention of lighter-mass Mo isotopes.

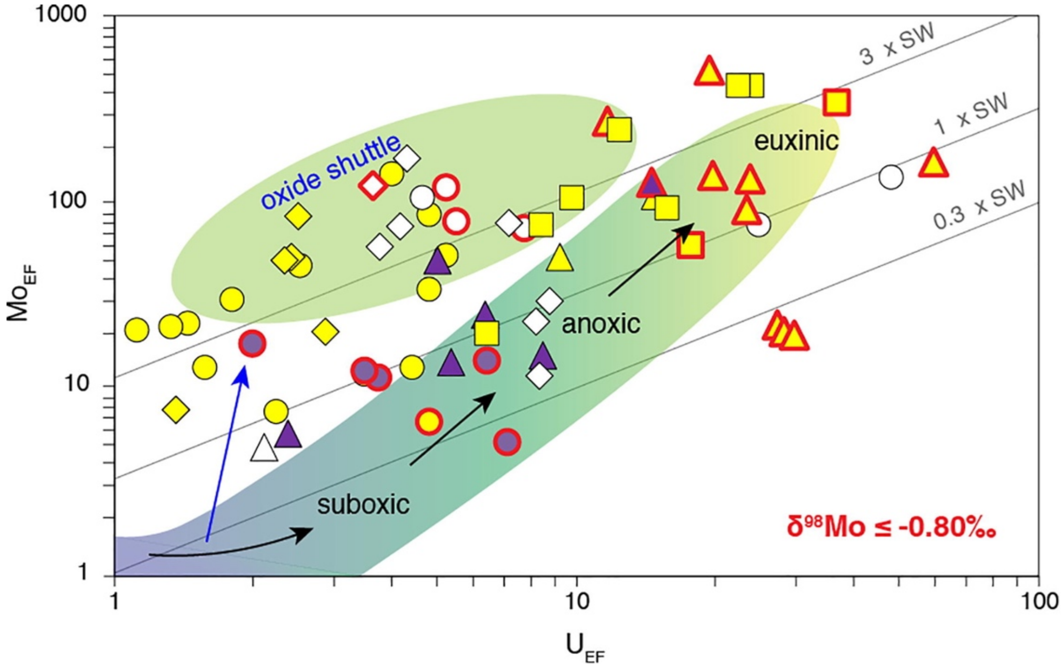

Fig. 5.7 Cross-plot of Mo and U enrichment Factors (EF) in Doushantuo Shales during OOEs. Trace metal data in this plot comes from Sahoo et al., 2012, Sahoo et al., 2016, Sahoo, 2015. Enrichment Factors were calculated relative to upper continental crust as follows: $RSE_{EF} = (RSE/Al)_{shale} \div (RSE/Al)_{upper\ crust}$ (RSE abundances in µg/g and Al in wt%). Upper continental crust elemental abundances used in our calculations come from Rudnick and Gao (2003). Data point shapes coincide with the different sites from South China (diamonds = Rongxi, triangles = Taoying, circles = Wuhe, and squares = Yuanjia) and colors signify the different Doushantuo Members (II = yellow, III = purple, and IV = white). Shale samples with $\delta^{98}Mo \leq -0.80‰$ are outlined in red. Figure and fields are modified from Algeo and Tribovillard, 2009, Jin et al., 2018.

Notably, some Doushantuo shale samples still plot outside of the suboxic-anoxic-euxinic and oxide shuttle fields in Fig. 5.7. Shales that plot between these two fields may be explained by some combination of fluctuations in local redox conditions (i.e., between suboxic, anoxic, and euxinic) and the operation of an oxide shuttle. The four shale samples from the Taoying site that plot to the right of the suboxic-anoxic-euxinic field (i.e., those with much higher U_{EF} relative to Mo_{EF}; Fig. 5.7), however, may still require an alternative explanation. Nonetheless, with the exception of these four samples, all other Doushantuo shales plot within or between the suboxic-anoxic-euxinic and oxide shuttle fields. Therefore, the local processes these Mo_{EF}-UEF patterns signify likely played the most significant role in driving the geochemical trends found in Doushantuo shales deposited during the purported OOEs.

5.4.2. A reappraisal of RSE trends in the Doushantuo Formation during OOES

The processes outlined in the preceding section, in addition to driving light sedimentary δ^{98}Mo, are known to have a profound effect on sedimentary RSE abundances. In this light, the RSE patterns in the Doushantuo Formation during the purported OOEs need to be re-assessed.

5.4.2.1. Links to other local processes in the Nanhua Basin

Sedimentary RSE enrichments today, in addition to being affected by oxide shuttling, are heavily dependent on local redox conditions. This dependency must have also been present in ancient marine sedimentary environments (summarized in Tribovillard et al., 2006). Of the RSEs highlighted here, V, Re, and U are all preferentially retained in sediments under anoxic conditions. Molybdenum, however, is not retained in sediments unless dissolved sulfide contents in marine bottom waters or sediment pore waters are comparatively high (Crusius et al., 1996; Morford et al., 2005). This well-documented link between Mo and sulfide is supported by the RSE data from the Doushantuo Formation during the OOEs. Specifically, Doushantuo shale samples with Fe_{HR}/Fe_T and Fe_{Py}/Fe_{HR} ratios indicative of euxinic deposition (i.e., $Fe_{HR}/Fe_T > 0.22$ and $Fe_{Py}/Fe_{HR} > 0.80$ [Raiswell et al., 2018]) have more pronounced Mo enrichments (in particular, shales from OOEs A and C; Fig. 5.8). These differences in the abundance of Mo between shales deposited under euxinic versus non-euxinic conditions (p-value = 0.000004 for a two-tailed and unpaired t-test) are greater than those observed for the other RSEs (p-value = 0.04 for U, 0.08 for V, and 0.12 for Re using the same test). Furthermore, Mo abundances are elevated in spheroidal pyrite grains throughout the Wuhe section, particularly during OOEs (Gregory et al., 2017). Together, these relationships support the idea that sedimentary Mo retention in the Doushantuo Formation was coupled to sulfide in the water column and sediments.

While, in general, shale Mo abundances during OOEs are greater when Fe speciation indicates deposition occurred under at least locally euxinic conditions, there are still clear exceptions to this rule. For example, a few shale samples deposited under euxinic conditions according to the Fe data possess very low Mo abundances (e.g., as low as 2 μg/g in the Wuhe section during OOE ‘‘B”), while some deposited under predominantly non-euxinic conditions based on the Fe data possess much higher Mo abundances (e.g., as high as 81 μg/g in the Rongxi section during OOE ‘‘C”). There are multiple possible explanations for these outliers. For example, local depositional controls in the paleo-basin, such as the availability and type of organic matter (Algeo and Lyons, 2006), sedimentary carbonate content, and sedimentation rates (Hardisty et al., 2018), would have influenced the sedimentary Mo abundances (as well as the other RSE abundances). Furthermore, each

OOE represents roughly a duration of 5–10 million years (Sahoo et al., 2016). As such, fluctuations in global marine redox conditions within and especially between these events are possible, indeed likely, and could have played an important role in regulating sedimentary Mo abundances. Changes in the degree of connection between the Nanhua Basin and the open ocean, if this occurred over million-year timescales, would have also played a strong role in regulating the abundance of Mo in seawater and sediments of the basin (Algeo and Lyons, 2006).

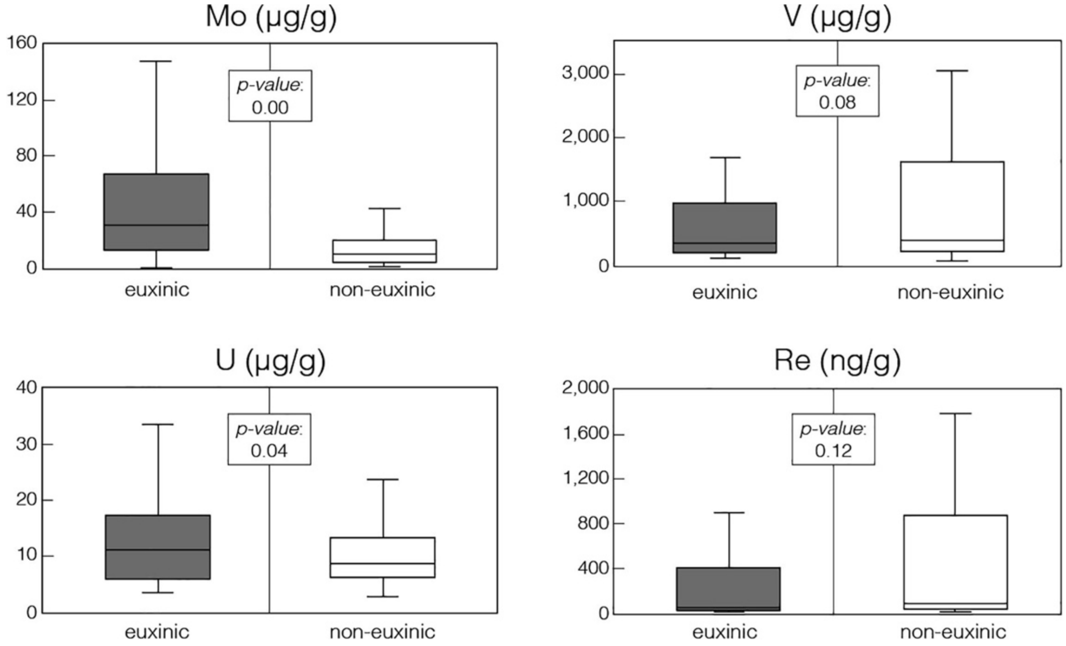

Fig. 5.8 Whisker plots showing RSE concentrations in Doushantuo shales during OOEs according to local redox conditions. Local redox conditions are determined by Fe speciation data (e.g., shale samples with $Fe_{HR}/Fe_T > 0.22$ and $Fe_{Py}/Fe_{HR} > 0.8$ are deemed euxinic in these plots). Data from all sections targeted in this study are included in the plots (i.e., Rongxi, Taoying, Wuhe, and Yuanjia). Iron speciation and RSE data is from Sahoo et al., 2012, Sahoo et al., 2016.

5.4.2.2. Links to global ocean oxygenation

In modern marine sediments, Re and U, unlike Mo and V, are largely unaffected by oxide shuttling (Morford et al., 2005; Algeo and Tribovillard, 2009), and therefore their high abundances in black shales from the Doushantuo Formation are probably linked to extensive global ocean oxygenation. The only known way to enhance sedimentary Re and U abundances to Phanerozoic levels, such as is found during Ediacaran OOEs in the Doushantuo Formation, is by increasing ocean oxygenation and in turn expanding the size of their global seawater reservoirs (Partin et al., 2013; Sheen et al., 2018). This general relationship is evident in the ancient shale record, where both Re and U abundances are predominantly low in shales from the Precambrian but show a first-order increase across the Ediacaran-Cambrian boundary in response to an overall trend towards higher ocean O^2 levels in the Phanerozoic Eon (Partin et al., 2013; Sheen et al., 2018).

The combined effects of a local Mn oxide shuttle and global-scale OOEs may explain why sedimentary RSE enrichments in the Doushantuo Formation are so high, sometimes exceeding those found in modern marine sediments. Large-scale OOEs during the Ediacaran Period would have increased RSE reservoirs, while at the same time also stimulating RSE delivery to sedimentary environments hosting an oxide shuttle. These combined effects are apparent when shale V and Re abundances from the Doushantuo Formation during OOEs are plotted against one another and reveal a general correlation ($R^2 = 0.38$; Fig. 5.9). High sedimentary Re abundances in the Doushantuo Formation require global ocean oxygenation (Sheen et al., 2018), while high sedimentary V abundances may be best explained by supplementation via a local oxide shuttle (see Section

4.1.1). Therefore, the correlation between these two elements is an indication that both processes may have been operating in unison.

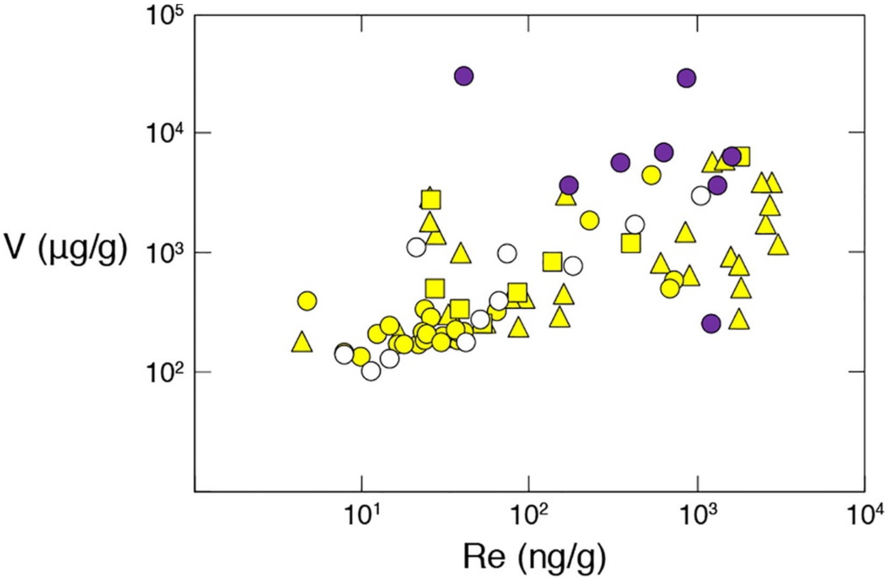

Fig. 5.9 Cross-plot of V and Re concentrations in Doushantuo Shales during OOEs. V and Re concentration data is from Sahoo et al., 2012, Sahoo et al., 2016. Data point shapes coincide with the different sites from South China (triangles = Taoying, circles = Wuhe, and squares = Yuanjia; similar to Fig. 5.6) and colors signify the different Doushantuo Members (II = yellow, III = purple, and IV = white).

Molybdenum isotope compositions reported in this study for the Doushantuo Formation during the purported OOEs, despite the described complications and the exceptionally light values, could still be evidence for a better-oxygenated Neoproterozoic ocean. At multiple times during the Phanerozoic Eon, such as during some Mesozoic Oceanic Anoxic Events (OAEs), the seawater δ^{98}Mo is estimated to have been much lower than that of the modern ocean ($\delta^{98}Mo_{SW}$ = ~1.45‰ during both the Toarcian OAE and Cenomanian-Turonian OAE-2 [summarized in Dickson, 2017]). Paleoproxy evidence suggests that Earth's deep open ocean remained mostly oxygenated during these OAEs, with deoxygenation taking place primarily in shallow shelf and margin environments (<10% of the global seafloor [Owens et al., 2013; Dickson et al., 2016; Clarkson et al., 2018]). Large RSE enrichments are preserved in sedimentary rocks deposited during these events despite the large scale of marine deoxygenation and accompanying decline in seawater δ^{98}Mo (e.g., Mo concentrations in the hundreds of μg/g and V in the thousands [Hetzel et al., 2009; Owens et al., 2012; Owens et al., 2016]). In short, a seawater δ^{98}Mo during Ediacaran OOEs lower than that of the modern ocean is not inconsistent with the OOE hypothesis. Ocean oxygenation during the Ediacaran OOEs could have been greater than those present during most of the Proterozoic Eon – and perhaps comparable to ocean oxygenation levels during Mesozoic OAEs.

General agreement between the levels of predicted ocean oxygenation during Ediacaran OOEs and the Mesozoic OAEs could even be supported by the worldwide Neoproterozoic Fe speciation record (Sperling et al., 2015). When originally presented, these Fe data were interpreted in the opposite way – as being contradictory to the OOE hypothesis. Sperling et al. (2015) argued for predominantly anoxic global marine margins throughout the Neoproterozoic. These authors were limited to predictions for marine margin settings because Neoproterozoic shales on or near Earth's surface today were deposited predominantly in these proximal and relatively shallow settings (that is, a preservational bias leads to a sampling bias). During Mesozoic OAEs, pronounced ocean deoxygenation was most prevalent in marginal environments because of the higher biological production in these regions (Dickson et al., 2016; Owens et al., 2013; Owens et al., 2018). Therefore, in an ocean with redox conditions similar to those Mesozoic OAEs, margin settings may very well have been predominantly anoxic, despite increasing oxygenation away from those margins. If correct, this model would allow for the persistence of anoxia suggested in the Sperling et al. (2015) data along the margins, while still allowing for a well-oxygenated deep open ocean.

5.4.3. Transiency of negative δ^{98}Mo and strong RSE enrichments

Equally impressive as the magnitude of negative δ^{98}Mo and RSE enrichments in shales of the Doushantuo Formation is their transient and seemingly episodic appearance. The short-lived nature of these excursions (<5–10 million years [Sahoo et al., 2016]) may fingerprint major changes that occurred to the Nanhua Basin if not the global ocean during the Ediacaran.

We present two hypotheses: the transient nature of the geochemical trends found in the Doushantuo Formation may have been a result of some combination of (1) changes in the position of the local chemocline and/or (2) dramatic changes in global sea level. Critically, neither of these hypotheses can at present be ruled out as a contributing factor to the episodic geochemical trends. Furthermore, these hypotheses are not mutually exclusive; changes in the position of the local chemocline can be modulated by global sea level changes. For these reasons, we highlight here the evidence in support of each hypothesis and discuss some of the associated implications.

5.4.3.1. Links to chemocline fluctuations

A deepening of the chemocline in the Nanhua Basin during OOEs could help explain the geochemical trends found in the Doushantuo Formation. Deepening of the chemocline would have exposed more sediments on at least the slope of the Nanhua Basin, and potentially sediments deposited deeper within the basin (i.e., at the Yuanjia site), to oxic or suboxic bottom waters (e.g., Han and Fan, 2015). Manganese oxide minerals formed in these bottom waters, as well as higher in the water column, could then have shuttled RSEs to the marine sediments. Again, because Mn contents are muted in all shale samples analyzed here, O_2 in marine bottom waters at the studied localities probably did not penetrate deep enough into underlying sediments to promote Mn retention in these settings (i.e., conditions in sedimentary pore waters probably only reached suboxic; see Section 4.1.1). An additional consequence of more oxidizing marine bottom waters above the original Nanhua Basin sediments would be a decrease in the availability of labile organic matter, which would have suppressed accumulation of sulfide in pore waters. By association, incomplete sedimentary tetrathiomolybdate formation could also have been promoted by deepening of the chemocline. The coupled effects from a local Mn oxide shuttle and incomplete tetrathiomolybdate formation, as a result of a deepening chemocline in the Nanhua Basin, could have promoted retention of lighter-mass Mo isotopes in the original sediments.

Deepening of the chemocline during OOEs need not have been restricted to the Nanhua Basin, and instead this phenomenon may have occurred over large areas of Ediacaran global oceans. In fact, the original OOE hypothesis predicts this based on the requirement of enhanced global ocean oxygenation to drive the dramatic increase in each seawater RSE reservoir (Sahoo et al., 2012, 2016). Proterozoic oceans are thought to have been predominantly anoxic, with oxic conditions restricted primarily to shallow settings (e.g., Reinhard et al., 2013, 2016). In comparison, Ediacaran oceans during OOEs are thought to have been better oxygenated, with oxic conditions being commonly present also in much deeper settings.

If the local chemocline did deepen in the Ediacaran Nanhua Basin during the purported OOEs, then this phenomenon may have been linked to localized physical processes. For example, strengthened wind speeds can drive deeper local pycnoclines, and by extension also deeper chemoclines. Likewise, the formation of local bottom waters could have driven the same effect because, since these waters would have been very dense and O_2-rich, they would have introduced O_2 to greater depths in the water column (as has happened multiple times over the past few decades in areas of the Mediterranean Sea [Schneider et al., 2014]). The transient development of one or both of these localized physical processes in the Ediacaran Nanhua Basin may therefore have been a major factor in driving the negative δ^{98}Mo excursions and coeval RSE patterns found in the Doushantuo Formation.

5.4.3.2. Links to changes in global sea level

The episodic geochemical trends found in the Doushantuo Formation could also have been stimulated by global sea level change during the Ediacaran. Marine regressions and transgressions show a strong link to the geochemical trends in the Doushantuo Formation (apparent in Fig. 5.3), and these dramatic changes in sea level have been invoked in previous work to explain other geochemical patterns in the Doushantuo Formation (Och et al., 2016).

Some of the geochemical trends found between the purported OOEs in Doushantuo shales from the Wuhe section, although not originally interpreted in this manner (Sahoo et al., 2016), could be linked to a loss in connection between the Nanhua Basin and the open ocean. A prevalence of the clay mineral saponite in sedimentary rocks from the Jiulongwan section from South China was interpreted as evidence for a shelf lagoon in the Nanhua Basin (see Fig. 5.1) that was strongly restricted during deposition of Members I and II of the Doushantuo Formation (Bristow et al., 2009; but also see Huang et al., 2013 for an alternative explanation of this data). Anomalously low RSE concentrations in sedimentary rocks of the Jiulongwan section (Mo and U abundances of ~2 μg/g) were interpreted as corroborative evidence for a restricted setting with limited RSE input from open ocean seawater (Bristow et al., 2009). Similar to the findings of Bristow et al. (2009), RSE abundances in the Wuhe section outside of the purported OOEs are also extremely low (Mo and U, for example, are often <2 μg/g [Sahoo et al., 2016]) and may thus be interpreted in the same way. Importantly, the degree of restriction on the slope and in the deeper basin need not have been as severe as that experienced by the shelf lagoon. Isolation of the shelf lagoon during deposition of Members I and II of the Doushantuo Formation is postulated to have been sufficiently strong to promote a lacustrine environment (Bristow et al., 2009; but also see Huang et al., 2013), but coeval sections at this time deposited in the basin probably maintained some connection to the open ocean (Bristow et al., 2009).

Evidence for a semi-restricted Nanhua Basin between the purported OOEs is not limited to low RSE abundances. For instance, local reservoir effects in highly restricted euxinic environments today with very low seawater sulfate concentrations prevent transfer of the large negative S isotope fractionation effects induced during microbial sulfate reduction to sediments of those basins (Gomez and Hurtgen, 2015). Positive pyrite S isotope compositions between OOEs in the Wuhe section (Sahoo et al., 2016) could therefore also be explained by the development of basinal restriction. Basinal restriction may also help explain why sediments from the Wuhe site were deposited under a persistently euxinic water column between the OOEs (according to Fe speciation data; Fig. 5.3). Modern restricted basins where inflow of nutrient- and O_2-rich marine bottom waters is limited are also often euxinic (Meyer and Kump, 2008). It is worth noting, however, that modern restricted basins are probably more susceptible to the development of euxinic conditions than were restricted basins during the Ediacaran because of the higher abundance of sulfate in modern seawater. Furthermore, a strong surface-to-deep carbon (C) isotope gradient in the Ediacaran Nanhua Basin between the OOEs has been inferred from systematic differences in the carbonate and organic C isotope profiles from various sections in South China (e.g., Jiang et al., 2007; Wang et al., 2016). Strong surface-to-deep C isotope gradients are found today in restricted redox-stratified basins (e.g., the Black Sea and Framvaren Fjord [Volkov, 2000]). Finally, independent evidence for regression and development of sea level lowstands (e.g., the appearance of cross-laminations in carbonates from South China [McFadden et al., 2008]) coincides with the periods between OOEs (apparent in Fig. 5.3) and may have favored basin restriction. Many basins are likely to lose at least some connectivity with the open ocean during sea level lowstands.

Like the correlation between marine regressions and the intervals between the OOEs, the correlation between marine transgressions and the OOEs themselves may also not be coincidental. In fact, marine transgression, by improving connection between the Ediacaran Nanhua Basin and the open ocean, provides a means of catalyzing a vigorous Mn oxide shuttle and bringing metals into the basin. In the modern Baltic Sea, the operation of a Mn oxide shuttle is catalyzed in a similar manner – that is, by the transient introduction of well-oxygenated waters into the semi-restricted basin (Huckriede and Meischner, 1996). We propose that times of transient inflow of well-oxygenated Ediacaran ocean surface waters to a Nanhua Basin that was better connected to the open ocean stimulated a Mn oxide shuttle similar to that observed in the modern Baltic Sea. During these inflow events, rapid accumulation of isotopically light Mo, as well as many other RSEs, would have occurred in euxinic sediments of the basin.

Some key differences do exist between the geochemistry of sediments from the recent Baltic Sea and that preserved in the Doushantuo Formation. For example, Mn contents reach much higher values in geologically recent Baltic Sea sediments compared to those of the Doushantuo Formation (~15 wt% [Hardisty et al., 2016] versus <1.0 wt% [Sahoo et al., 2016], respectively). We could explain this disparity by inflow events into the Ediacaran Nanhua Basin that were sporadic or of weaker intensity relative to those occurring recently in the Baltic Sea. The presence of O_2 in marine bottom waters and its ability to catalyze Mn oxide formation in underlying sediments is likely a prerequisite for sedimentary Mn accumulation (Calvert and Pedersen, 1996). In support of this assumption, sedimentary Mn accumulation in the Baltic Sea is limited during inflow events that occur sporadically over extremely short timescales (e.g., a single year) because penetration of O_2

into marine bottom waters occurs over correspondingly short timescales and leads to only limited Mn oxide formation (Heiser et al., 2001; Lenz et al., 2015). By analogy, Ediacaran sediments are not expected to have accumulated Mn if O_2 penetration into deep marine waters of the local sedimentary basin was sporadic or if O_2 failed to penetrate into the deep waters of the basin.

5.4.4. Implications of basinal restriction between the OOEs

A weakened connection between the Nanhua Basin and the open ocean during the intervals between the purported OOEs would have had profound consequences on the geochemistry of the basin. Today, a poor connection between the Black Sea and the open ocean inhibits delivery of Mo to this basin (Eckert et al., 2013). Consequently, the availability of Mo in bottom waters and also its burial flux in organic-rich sediments of the modern Black Sea are not as pronounced as those observed in anoxic basins better connected to the open ocean (e.g., the Cariaco Basin [Algeo and Lyons, 2006]). Knowing this, it becomes apparent that shale Mo abundances between the purported OOEs may undersell the true size of the coeval global seawater Mo inventory if the basin was poorly connected to the open ocean at these times. Additionally, it has been shown that organic-rich marine sediments from modern restricted basins such as the Black Sea (Neubert et al., 2008) are ideal candidates for capturing the contemporaneous seawater δ^{98}Mo (as well as Kyllaren fjord [Noordmann et al., 2015] and Lake Rogoznica [Bura-Nakić et al., 2018]). This is so because minimized recharge of Mo from the open ocean into these settings strengthens the possibility of near-quantitative Mo transfer from marine bottom waters to sediments. Therefore, although these sedimentary enrichments may undersell the true size of the coeval global seawater Mo reservoir, shales deposited at these times may be ideal candidates for capturing the coeval global seawater δ^{98}Mo.

If shales deposited between the purported OOEs from the Wuhe site did faithfully capture the coeval seawater δ^{98}Mo, then that composition was generally very light ($\delta^{98}Mo_{SW}$ 0.94 ± 0.10‰; 2SD). We indicate ‘‘generally” because our low-resolution study of shales at the Wuhe site (one sample about every two meters) is very likely to leave large expanses of Ediacaran time unaccounted for – millions of years in some cases, based on sample age estimates from Sahoo et al. (2016). Furthermore, two shale samples from the Wuhe site that may have been deposited outside of the OOEs have heavier δ^{98}Mo (1.47 ± 0.10‰; 2SD at 13.7 m and 2.24 ± 0.10‰; 2SD at 110.7 m) and may signify short-lived increases to the coeval seawater δ^{98}Mo. Alternatively, these heavier δ^{98}Mo may actually be from shale samples deposited near the termination or shortly after the onset of the OOEs. This scenario is possible because the two shale samples from Wuhe with comparatively heavy δ^{98}Mo are located immediately before or after the purported OOEs (according the OOE locations proposed in Sahoo et al. [2016]; Fig. 5.3). Nevertheless, generally lighter seawater δ^{98}Mo estimates inferred from the vast majority of shales deposited outside of the OOEs may indicate generally lower global ocean O_2 contents at these times.

5.5. Conclusions

Our new Mo isotope data help us argue that local controls in the Ediacaran Nanhua Basin played important roles in driving some of the geochemical trends in black shales of the Doushantuo Formation from South China. In particular, the transient development of an Mn oxide shuttle and changes in the extent of tetrathiomolybdate formation linked to sulfide availability are both supported by the extremely negative shale δ^{98}Mo excursions reported here. Coeval RSE patterns and accompanying Fe speciation data from the same sedimentary rocks, although not originally interpreted in this manner (Sahoo et al., 2012, 2016), are also consistent with this hypothesis.

Importantly, enhanced oceanic oxygenation during the Ediacaran is still required to explain some of the geochemical patterns in the Doushantuo Formation (i.e., those found in Sahoo et al., 2012, 2016), despite the local redox-related complications identified here. Elevated Re and U abundances are particularly difficult to explain without invoking global-scale oceanic oxygenation because oxide shuttling and changes in local sulfide availability are not adequate to enrich these two metals to the levels found in the Doushantuo Formation.

In light of our new data, it is worth reconsidering whether the Nanhua Basin maintained an uninterrupted connection with the open ocean during the entirety of the Ediacaran Period. If the Nanhua Basin was well-connected to the open ocean throughout the Ediacaran (as is assumed in previous work [Sahoo et al., 2012, 2016]), then:

1. Redox-sensitive element abundances in organic-rich shales from the Doushantuo Formation should scale with coeval levels of global ocean oxygenation. Elevated RSE abundances would signify a better oxygenated global ocean, while muted RSE abundances would be indicative of a relatively less oxygenated one (i.e., the original hypothesis of Sahoo et al. [2016]);

2. Negative δ^{98}Mo excursions are likely a consequence of chemocline deepening in the basin (Section 4.3.1.; and also see the leftmost panels in Fig. 5.10). When the chemocline deepened, more sediments on the slope of the basin would have been exposed to oxic or suboxic conditions. Shuttling of Mo to sediments by Mn oxides would be more likely under these conditions. Sedimentary sulfide contents may also have diminished under these conditions, in turn promoting incomplete tetrathiomolybdate formation. Both of these processes are known to stimulate retention of lighter-mass Mo isotopes in marine sediments and may thus explain the negative δ^{98}Mo.
3. Positive δ^{98}Mo found in organic-rich euxinic shales deposited between the OOEs are likely a consequence of chemocline shallowing. When the chemocline shallowed, more sediments on the slope of the basin would have been exposed to euxinic conditions. Shuttling of Mo to sediments by Mn oxides would have been less likely under these conditions. An associated increase in local sulfide availability would have also favored more complete tetrathiomolybdate formation. Neither of these processes would have favored the retention of lighter-mass Mo isotopes in marine sediments. The positive δ^{98}Mo in these shales are most likely closer to matching the coeval ancient seawater composition. Unfortunately, it is difficult to tell if the true seawater δ^{98}Mo is recorded. Modern marine basins that maintain a strong connection with the open ocean never capture the coeval seawater δ^{98}Mo and instead capture a large range of isotopically lighter values (summarized

by Kendall et al., 2017). By analogy, the organic-rich shales of the Doushantuo may also capture fractionated Mo isotope values.

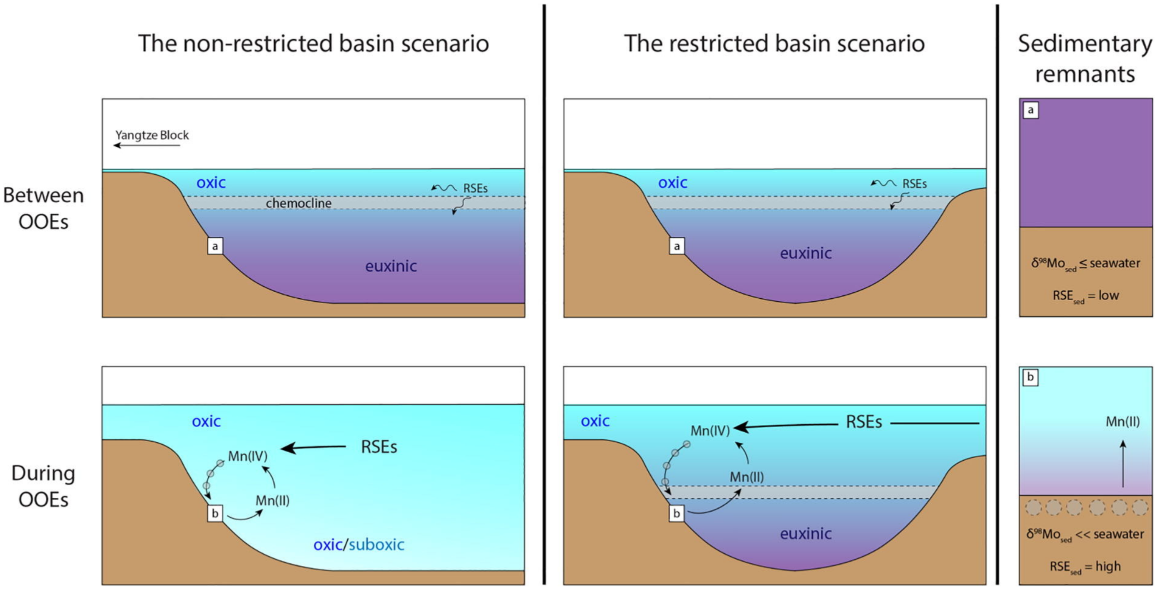

Fig. 5.10 Possible evolution of seawater in the Ediacaran Nanhua Basin depending on the degree of connection between this basin and the open ocean. The leftmost panels outline the possible evolution of seawater if the Nanhua Basin maintained an uninterrupted connection with the open ocean throughout the Ediacaran. The center panels outline this possible evolution if the Nanhua Basin was at times a restricted basin. Panels at the far right labeled "a" and "b" outline the associated sedimentary remnants on the slope of the paleo basin for each scenario (a = between OOEs and b = during OOEs). Grey circles represent insoluble Mn oxide minerals.

Alternatively, if the connection between this basin and the open-ocean was not always strong during the Ediacaran (Section 4.3.2.; and also see the center panels in Fig. 5.10), then:

1. Organic-rich shales of the Doushantuo Formation deposited during sea level highstands would be the best candidates to preserve the remnants of open-ocean chemistry, as viewed from the perspective of RSE enrichments. This likelihood is

because the Nanhua Basin would have been most strongly connected to the open ocean at these times. By contrast, muted RSE enrichments in shales deposited during sea level lowstands would not be as likely to preserve information about the RSE reservoir of the open-ocean. This possibility is especially true if the Nanhua Basin was at times strongly restricted and exchanged little or no seawater with the open ocean.

2. Negative δ^{98}Mo excursions are likely a consequence of open-ocean seawater inflow events into an otherwise restricted basin – similar to what happens today in the Baltic Sea (Scholz et al., 2018). During transgressions, inflow of oxic open-ocean surface waters to the basin could have stimulated the operation of a local Mn oxide shuttle, while also exposing more sediments on the slope to oxic or suboxic conditions. Again, lighter-mass Mo isotopes would be preferentially retained in sediments due to these processes.
3. Positive δ^{98}Mo found in organic-rich shales during marine regressions are, again, primarily a result of the termination of the processes driving the extremely negative δ^{98}Mo excursions. However, if these shales were deposited in a strongly restricted basin, then they are strong candidates to preserve the coeval seawater δ^{98}Mo because restricted euxinic basins are shown to sometimes capture the coeval seawater δ^{98}Mo today (Neubert et al., 2008; Noordmann et al., 2015; Bura-Nakić et al., 2018).The majority of seawater δ^{98}Mo inferred from these shales ($\delta^{98}Mo_{SW} \leq 0.94 \pm 0.10$‰; 2SD) are much lighter than that of the modern ocean ($\delta^{98}Mo_{SW} = 2.34 \pm 0.10$‰ [Nägler et al., 2014]). Accordingly, these lighter δ^{98}Mo may

fingerprint a comparatively less oxygenated global ocean at that time compared to the modern ocean.

Some combination of both scenarios could also explain the data.

Moving forward, it will be important to unmix or at least account for these local and global complications and their links to geochemical trends in Ediacaran-aged sedimentary rocks. Constraining the degree of restriction between the Ediacaran Nanhua Basin and the open ocean during the time intervals between the purported OOEs is of particular importance. To date, inferences about the state of global marine redox conditions during the Ediacaran are based mostly on geochemical trends found in shales of the Doushantuo Formation and their relationship to coeval open-ocean chemistry. Well-documented contemporaneous shales from the multiple sections of Northwestern Canada (e.g., Johnston et al., 2013; Miller et al., 2017) are another potentially attractive target for future paleoredox studies. However, the Ediacaran-aged shales from Northwestern Canada offer their own challenges because they are thought to have been deposited under primarily ferruginous conditions (based on Fe speciation data [Johnston et al., 2013; Miller et al., 2017]), which limits the utility of paleoredox proxies such as Mo.

CHAPTER 6

THALLIUM ISOTOPE INSIGHTS INTO OCEAN OXYGENATION DURING THE EDIACARAN PERIOD

The work presented in this chapter is in preparation to submit to Chemical Geology: Ostrander, C.M., Owens, J.D., Nielsen, S.G., Lyons, T.W., Sperling, E.A., Shu, Y., Chen, X., Johnston, D.T., Sahoo, S.K., Anbar, A.D. Thallium isotope insights into ocean oxygenation during the Ediacaran Period

Abstract

The tempo of Ediacaran ocean oxygenation is debated. We attempt to reconstruct some of this oxygenation history by measuring thallium isotope ratios (reported as ε^{205}Tl) in shales from South China (Wuhe section) and Northwestern Canada (Wernecke and Mackenzie Mountains sections). At face value, our ε^{205}Tl records from these two locations are very different. South China shales reveal two pronounced and extremely negative Tl isotope excursions (in mid-members II and III of the Doushantuo Formation, to as low as $\varepsilon^{205}Tl_{authigenic}$ = - 10.4 ± 0.2), while Northwestern Canada shales reveal comparatively invariant values (average $\varepsilon^{205}Tl_{authigenic}$ = -2.1 ± 1.6; 2SD, n = 73). These disparate records are in much better agreement, however, if we filter from our dataset shales that are inferred in previous work to have been deposited in a restricted setting. By analogy with modern settings (cf., the Black Sea), ε^{205}Tl in these shales most likely fingerprint local-scale processes. On the other hand, and also by analogy with modern equivalents (cf., Cariaco

and Santa Barbara basins), shales deposited in an open ocean setting probably captured a globally homogenous seawater ε^{205}Tl (ε^{205}Tl$_{SW}$). Moving forward with this assumption, we find that open ocean ε^{205}Tl$_{SW}$ was often comparable to the ε^{205}Tl of bulk upper continental crust—even at times during previously purported Ediacaran Ocean Oxygenation Events (OOEs). Widespread ocean oxygenation for the duration of these events is not supported by the occurrence of near-crustal ε^{205}Tl$_{SW}$. Notwithstanding, we do find evidence for brief periods of enhanced ocean oxygenation in both shale records during some OOEs in the form of considerably negative inferred ε^{205}Tl$_{SW}$ (e.g., ε^{205}Tl$_{authigenic}$ as low as -5.3 ± 0.3 in lowermost Doushantuo Member III). Thus, although some original details of the OOE hypothesis are not supported by our dataset, some of its general ideas are supported by the new Tl isotope data. When interpreting geochemical data, it is important to make global-scale inferences only after identifying and accounting for local-scale overprints.

6.1 Introduction

It has proven difficult to constrain the history of ocean oxygenation during the Ediacaran Period (635 to 542 million-years-ago, or Ma). Some of this difficulty stems from the fact that fingerprints of widespread ocean oxygenation are found in some sedimentary rocks deposited during the Ediacaran, but not in others deposited at roughly the same time. For instance, redox-sensitive elements (RSEs; e.g., V, Cr, Mo, Re, and U) are at times highly enriched in shales from South China and inferred as evidence for widespread Ocean Oxygenation Events ("OOEs"; at ~635 Ma, ~580 Ma, and ~560 Ma [Scott et al. 2008, Sahoo et al. 2012, 2016]). Strong shale RSE enrichments can fingerprint widespread ocean oxygenation because accumulation of RSEs in seawater, and by extension also in worldwide marine sediments, should scale to first order with levels of global ocean oxygenation (Scott et al. 2008, Partin et al. 2013, Reinhard et al. 2013, Sahoo et al. 2016, Sheen et al. 2018). The OOE hypothesis, however, is complicated by the roughly coeval shale record from Northwestern Canada, which hosts no pronounced RSE enrichments (Johnston et al. 2013, Sperling et al. 2016, Miller et al. 2017). Reconciling the differences in these records is crucial if we are to understand what role – if any – marine oxygenation played in promoting the rise of complex life during the Ediacaran (Knoll 2011, Lenton et al. 2014).

Some disparities between these two shale RSE records must be due to local-scale differences at the time of their deposition. First, shales from both locations are thought to have been deposited almost exclusively under a locally anoxic water column. However, South China shales were deposited primarily under H_2S-bearing ("euxinic") conditions (e.g., Li et al. 2010, Sahoo et al. 2016) and Northwestern Canada shales under Fe^{2+}-rich (“ferruginous”) conditions (e.g., Johnston et al. 2013, Sperling et al. 2016). Whether a shale was deposited under euxinic or ferruginous conditions plays a key role in its ability to accumulate RSEs (summarized in Tribovillard et al. [2006]). Second, it was recently proposed that RSE delivery to the South China shales was supplemented by the operation of a local manganese (Mn) oxide “shuttle” (Ostrander et al. 2019a). The operation of such a shuttle has not been proposed during deposition of shales from Northwestern Canada. Third, it was also suggested in Ostrander et al. (2019a) that the transient nature of the RSE enrichments in South China shales was due at least in part to changes in the open ocean connection of the paleo-Basin. Changes in basin connectivity have not been invoked during deposition of the shales from Northwestern Canada. Finally, Ediacaran-aged shales from South China are highly condensed compared to their Northwestern Canada counterparts. The condensed nature of South China sections must accentuate to some degree their RSE enrichments (discussed also in Miller et al. [2017]). In sum, there are multiple local-scale overprints that need to be accounted for when interpreting global-scale trends in these Ediacaran shales.

Using thallium (Tl) isotopes, we attempt in this study to read through these local-scale overprints and, when possible, infer the tempo of Ediacaran global ocean oxygenation. We have generated Tl isotope data for 60 shale samples from South China (Wuhe section) and 75 shale samples from Northwestern Canada (Wernecke and Mackenzie Mountains sections). We have purposely targeted the same shale samples that host the disparate RSE records discussed above (that is, shales investigated previously in Johnston et al. [2013], Sperling et al. [2016], and Sahoo et al. [2016]).

Thallium isotopes are emerging as a powerful tool for tracking Earth's ocean oxygenation history (Nielsen et al. 2011, Ostrander et al. 2017, 2019b, Them et al. 2018, Bowman et al. 2019, Fan et al. 2020). Thallium possesses an affinity for Mn oxide minerals, and once sorbed to their surface and subsequently oxidized from Tl(I) to Tl(III) will undergo substantial positive isotope fractionation (specifically, after sorption to hexagonal birnessite [Peacock and Moon 2012, Nielsen et al. 2013]). Manganese oxides are ubiquitous on the seafloor today because their formation and subsequent preservation is dependent on O_2, and O_2 is readily abundant in marine bottom waters around the globe. The widespread occurrence of Mn oxides today, and consequently also the pronounced preferential removal of the heavier-mass Tl isotope from seawater, drives the globally homogenous seawater Tl isotope composition ($\varepsilon^{205}Tl_{SW}$) to a lighter value than oceanic inputs ($\varepsilon^{205}Tl_{SW} = -6.0 \pm 0.3$; 2SD [Nielsen et al. 2006, Owens et al. 2017a] compared to $\varepsilon^{205}Tl_{IN} = \sim -1.8$ [Nielsen et al. 2017]; summarized in Fig. 6.1). This $\varepsilon^{205}Tl_{SW}$ gets transferred to siliciclastic marine sediments today that are deposited under anoxic bottom waters, presumably because of quantitative Tl removal from marine bottom waters in these settings (Owens et al. 2017a). Importantly for this study, transfer of $\varepsilon^{205}Tl_{SW}$ in anoxic settings seems to occur irrespective of H_2S availability (under H_2S-rich conditions in Cariaco Basin [Owens et al. 2017a] and under H_2S-poor conditions in Santa Barbara Basin [Fan et al. 2020]). In sum, by analogy with today, past $\varepsilon^{205}Tl_{SW}$ should have been governed by the extent of ocean oxygenation (but more directly, through associated Mn oxide burial) and transferred to sediments deposited under anoxic conditions. In support of this utility, Tl isotopes in shales deposited under anoxic conditions have successfully been used to track ocean oxygenation (Ostrander et al. 2019, Fan et al. 2020) and ocean deoxygenation

(Nielsen et al. 2011, Ostrander et al. 2017, Them et al. 2018, Bowman et al. 2019) at various times in Earth’s past.

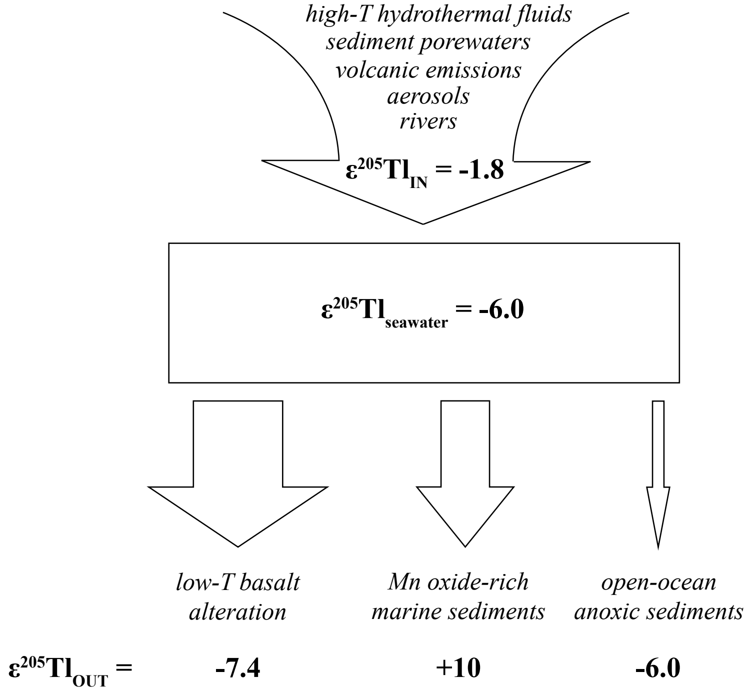

Fig. 6.1 Modern seawater Tl isotope mass-balance. See Table 6.2 for accompanying references and notes.

Critically, open ocean $\varepsilon^{205}\mathrm{Tl}_{SW}$ is only shown to be transferred to sediments in anoxic settings today that are well-connected to the open ocean. Seawater ε^{205}Tl is still transferred to marine sediments in the only restricted basin investigated to date using Tl isotopes (the Black Sea [Owens et al. 2017a]). However, this $\varepsilon^{205}\mathrm{Tl}_{SW}$ is strictly a local signal and noticeably different from that of the open ocean ($\varepsilon^{205}\mathrm{Tl}_{SW}$ = ~2.2 ± 0.3; 2SD in oxic surface waters). As we will see, it is imperative when using Tl isotopes as a global proxy to target shales deposited in non-restricted settings.

6.2 Ediacaran shale samples

6.2.1 South China shales

Shales from the Doushantuo Formation used in this study come from the Wuhe section in Guizhou Province, South China (Fig. 6.2). Shale sample slabs were originally collected from outcrops for the purposes of bulk and trace element analyses, iron (Fe) speciation, and sulfur (S) isotopes (Sahoo et al. 2012, 2016). Throughout South China, the Doushantuo Formation has been split into four distinct members (summarized in Jiang et al. [2011]). As is the case throughout the rest of the Yangtze platform, Member I at the Wuhe site is comprised of cap carbonates that overly diamictites associated with the Marinoan Glaciation. Throughout the rest of the Doushantuo at Wuhe, organic-rich black shales are the dominant lithology (extending over 10s of meters in mid-Members II and III), but these shales are frequently interrupted by intervals of carbonate deposition. Carbonate beds are most frequent at the base of Members II and III, and also at the top of Member III. Zircon U – Pb ages from volcanic ash beds in Member I (635.2 ± 0.6 Ma) and uppermost Member IV (551.1 ± 0.7 Ma) of the Doushantuo Formation constrain its duration to ~ 84 million years (myr) into the Ediacaran Period (Condon et al. 2005). It has also been suggested, however, based on alternative inferences of stratigraphic correlations in South China, that the Doushantuo Formation does not quite extend this far into the Ediacaran, and perhaps only extended to ≥560 Ma (An et al. 2015). In either scenario, the Doushantuo Formation is highly condensed for how much geologic time it is inferred to represent (≥75 to 85 myr preserved in ~120 m of stratigraphy; see Fig. 6.2).

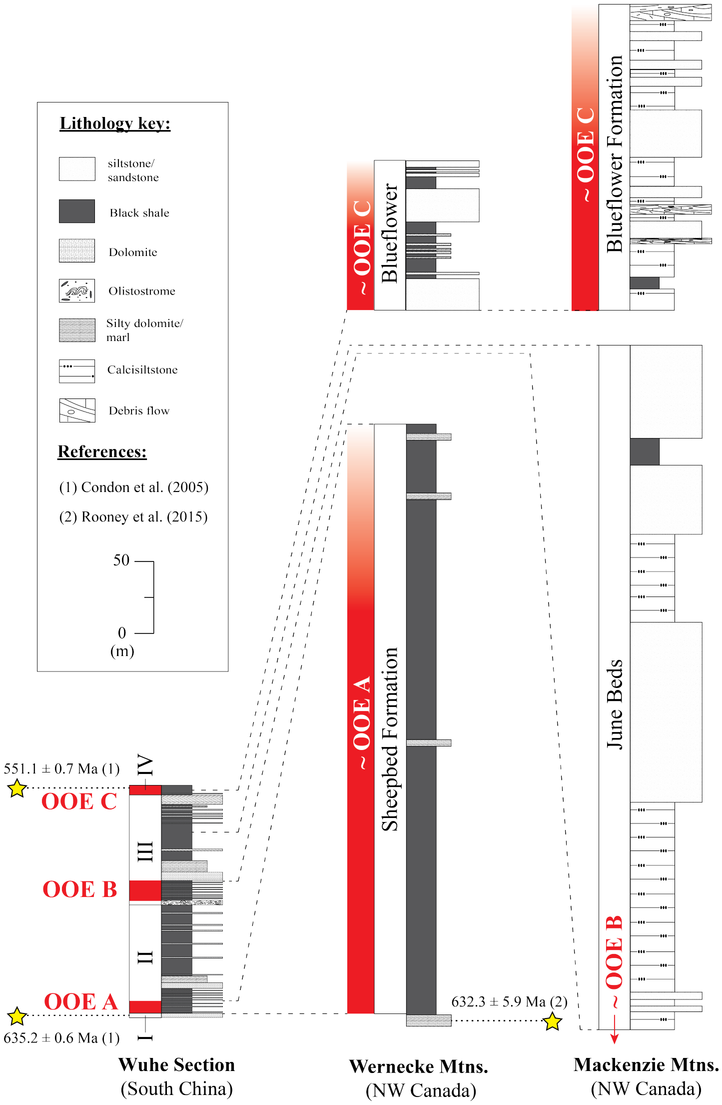

Fig. 6.2 Stratigraphic columns for the sections targeted in this study. Stratigraphy for the Wuhe section is modifed from Jiang et al. (2011), for the Wernecke Mountains section is modified from Johnston et al. (2013), and for the Mackenzie Mountains section is modified from Sperling et al. (2015). Available geochronological constraints and stratigraphic correlations have been included (see the text and legend box for references).

The Wuhe site is thought to preserve sedimentary rocks that were deposited for the duration of the Ediacaran Period below wave base in a slope setting of a paleo-basin referred to as the Nanhua Basin (summarized in Jiang et al. [2011]). Classically, the paleo-slope is thought to have maintained a strong and uninterrupted connection with the open ocean (e.g., Sahoo et al. 2012, 2016). More recently, however, it has been suggested based on multiple independent lines of evidence that this slope perhaps did not maintain a strong connection with the open ocean (e.g., inferred changes in sea level and their correspondence with the appearance of some geochemical trends [Ostrander et al. 2019a]). Instead, it is posited in Ostrander et al. (2019a) that these shales may have been deposited for long periods of time during the Ediacaran in an at least semi-restricted marine basin. Such a scenario could explain why the Doushantuo Formation was originally deposited according to Fe speciation data under predominantly euxinic conditions (a common feature of restricted settings today [Meyer and Kump 2008]). These conclusions are in agreement with Och et al. (2016), who compiled geochemical data from many sedimentary sections in South China and posited that the Ediacaran Nanhua Basin was comprised of a series of successive restricted waterways. The conclusions reached in Ostrander et al. (2019a) are, therefore, simply a continuation of the ideas proposed in Och et al. (2016), extending these restricted waterways to include the depositional site of the Wuhe section. If correct, this theory has important implications for the application of some geochemical proxies to this sedimentary archive – Tl isotopes being one of them.

6.2.2 Northwestern Canada shales

Our shales from Northwestern Canada come from two different sites: the Wernecke Mountains and the Mackenzie Mountains (Fig. 6.2). Akin to the South China shales, these shale samples were collected from outcrops for the initial purposes of bulk and trace element analyses, Fe speciation, and S isotopes (see Johnston et al. [2013] and Sperling et al. [2016]). The oldest samples that we targeted from Northwestern Canada come from the

Sheepbed Formation (Wernecke Mountains), which was deposited beginning shortly after the end of the Marinoan Glaciation based on a shale Re – Os age near its base of 632.3 ± 5.9 Ma (Rooney et al. 2015). The Sheepbed Formation in the Wernecke Mountains consists overwhelmingly of shales but is also interbedded with thin limestones. Shale deposition is also common in the June Beds locality that we targeted from the Mackenzie Mountains, albeit less extensive and having a tendency toward calcisiltstone. The youngest shales that we targeted from Northwestern Canada come from the Blueflower Formation, which we have sampled at both sites. Shales occur in both locations, interbedded throughout with medium- to coarse-grained sandstone and breccias. Ediacaran strata from our two Northwestern Canada sites are much more extensive than their inferred coeval equivalents in South China, extending many more hundreds of meters despite preserving much shorter geologic timeframes (see Fig. 6.2 for a side-by-side comparison).

Shales from both of our investigated Northwestern Canada sites are generally thought to have been deposited during the Ediacaran below wave base in a slope environment, with shales from the Wernecke Mountains being deposited in a more distal setting than those from the Mackenzie Mountains (Macdonald et al. 2013). The lower one-hundred meters of the Sheepbed Formation in the Wernecke Mountains is interpreted to have been deposited in an especially deep marine setting, during glacio-eustatic marine transgression (Johnston et al. 2013). Unlike their coeval equivalents from South China, it has not been suggested that shales from Northwestern Canada were deposited over large periods of time during the Ediacaran Period in a restricted setting. Perhaps in support of this assumption, Fe speciation data in shales from Northwestern Canada indicate deposition under local ferruginous conditions, which are the conditions thought to typify margin settings throughout the period (Canfield et al. 2008, Sperling et al. 2015)

6.2.3 Stratigraphic correlations

For our investigation, we adopt the Ediacaran stratigraphic correlations proposed in Macdonald et al. (2013) (see Fig. 6.2). The strongest temporal link between our study sites is formed by geochronological constraints that are within error from zircon in Doushantuo Formation Member I (a U – Pb age of 635.2 ± 0.6 Ma [Condon et al. 2005]) and shales in the lowermost Sheepbed Formation (a Re – Os age of 632.3 ± 5.9 Ma [Rooney et al. 2015]). Outside of this one strong tie-point, the remainder of the correlations have been guided primarily by changes in lithology and well-documented changes in the worldwide carbonate carbon (C) isotope record during the Ediacaran (again, see Macdonald et al. [2013]). In brief, adopting these correlations equates our Sheepbed Formation samples (Wernecke Mountains) to lowermost Member II of the Doushantuo Formation, and therefore roughly also to the oldest purported Ediacaran OOE (OOE A). Our June Beds samples (Mackenzie Mountains) are equated to mid-Member III, either near or after the end of the middle OOE (OOE B). Finally, both sets of Blueflower Formation samples are then roughly equivalent to lower- to mid-Member IV and extending shortly beyond its terminus. This final correlation suggests that the Blueflower Formation was deposited during much if not all of the youngest Ediacaran OOE (OOE C).

6.3 Tl isotope methods

All sample preparation and purification steps were performed in the NIRVANA Laboratory at Woods Hole Oceanographic Institution (WHOI) and Jeremy Owens' Laboratory at Florida State University (FSU) within the National High Magnetic Field Laboratory (NHMFL) following methods outlined in previous work (Rehkämper and Halliday 1999, Nielsen et al. 2004). Powdered samples were first transferred to Teflon reactors and treated with 2 M HNO_3 for 12 to 15 hours at 130°C, a treatment which is shown to effectively separate authigenic Tl bound to pyrite from detrital Tl (Nielsen et al. 2011). Following this partial dissolution, samples were centrifuged and their supernatants containing the authigenic fraction were transferred by pipette to new Teflon reactors. Special care was taken to not disturb the solid (detrital) residues during this step. If a residue was disturbed, samples were re-centrifuged before another transfer attempt. After centrifugation, all authigenic fractions, and some detrital fractions from the South China samples, were digested for 1.5 hours at ~300°C and 100 bars in a high-pressure asher to help dissolve organic compounds. After dissolution of the remaining silicate residues in 1:1 concentrated HNO_3 and HF, both fractions were then completely dissolved in 1 M HCl in preparation for Tl purification via ion exchange chromatography. Notably, because our authigenic fractions were never treated with HF, even if some detrital material had been incorrectly transferred during the leach step it would not be expected to dissolve. On that note, we did not see any solids in our Teflon reactors before chromatography. Similar to Ostrander et al. (2017), each authigenic fraction was passed through one micro-column. Because the Tl:matrix ratios were much lower for the South China detrital fractions, however, each of these was first passed through a large glass column and then a micro-column.

Thallium isotope analyses were conducted at the WHOI Plasma Mass Spectrometry Facility and at the NHMFL in Tallahassee. At both locations, a Thermo Neptune multi-collector inductively coupled plasma mass spectrometer (MC-ICPMS) was used with an Aridus II desolvating nebulizer sample introduction system. Measurements were made in low-resolution mode using sample-standard bracketing relative to NIST 997 Tl in epsilon notation. Similar to previous Tl isotope studies, instrumental mass bias was monitored using external normalization to NIST SRM 981 Pb. Because each sample was doped with a known quantity of NIST SRM 981 Pb, Tl concentrations could be calculating during MC-ICPMS analysis using the measured ^{205}Tl/^{208}Pb ratios. We report all Tl isotope values in epsilon notation relative to NIST 997 Tl metal:

$$\varepsilon^{205}\mathrm{Tl} = ({}^{205/203}\mathrm{Tl}/_{\mathrm{sample}}/{}^{205/203}\mathrm{Tl}_{\mathrm{NIST\text{-}997}} - 1) \times 10{,}000.$$

At least one USGS shale SCO-1 standard was leached, purified, and analyzed with each sample set to monitor accuracy (Table 6.1). Measured $\varepsilon^{205}\mathrm{Tl}_{\mathrm{authigenic}}$ for SCO-1 powders from vials housed at WHOI (ε^{205}Tl = - 3.0 ± 0.2; 2SD, n = 4) and FSU (ε^{205}Tl = - 3.1 ± 0.6; 2SD, n = 2) were within error of one another and reproduced values reported in a recent study (Ostrander et al. [2017], where the same WHOI SCO-1 vial yielded $\varepsilon^{205}\mathrm{Tl}_{\mathrm{authigenic}}$ = - 2.9 ± 0.1; 2SD, n = 9). Authigenic ε^{205}Tl for SCO-1 powders from a vial housed at Arizona State University, however, were slightly different (ε^{205}Tl = - 3.4 ± 0.2;

2SD, n = 9), even though these standards were prepared alongside those from the WHOI vial. Most likely, these slight differences are due to previously unrecognized heterogeneities in $\varepsilon^{205}Tl_{authigenic}$ between SCO-1 vials. In contrast, measured detrital $\varepsilon^{205}Tl$ between the SCO-1 vials from ASU ($\varepsilon^{205}Tl$ = - 2.6 ± 0.2; 2SD, n = 4) and WHOI ($\varepsilon^{205}Tl$ = - 2.5 ± 0.4; 2SD, n = 2) were within error of one another. These detrital $\varepsilon^{205}Tl$ also reproduced values reported in Ostrander et al. (2017) (where SCO-1 $\varepsilon^{205}Tl_{detrital}$ = - 2.5 ± 0.3; 2SD, n = 9). Guided by these SCO-1 data, all errors reported in this study for our shales represent the 2SD reproducibility of that sample or the 2SD reproducibility of the associated SCO-1 fraction processed alongside that sample, whichever is greater (summarized in Table 6.1).

Table 6.1 Tl isotope data for USGS shale SCO-1

	$\varepsilon^{205}Tl_{authigenic}{}^{a,*}$	N	$\varepsilon^{205}Tl_{detrital}{}^{a,*}$	N	processed alongside
This study					
ASU Vial	-3.4 ± 0.2	9	-2.6 ± 0.2	4	Wuhe section
WHOI Vial	-3.0 ± 0.2	4	-2.5 ± 0.4	2	Wuhe and Wernecke sections
FSU Vial	-3.1 ± 0.6	3	N/A		Mackenzie section
Ostrander et al. (2017)					
WHOI Vial	-2.9 ± 0.1	9	-2.5 ± 0.3	9	

a. measured relative to NIST 997 Tl

*all reported errors are 2SD of the standard reproducibility

6.4 Results

6.4.1 South China

The most striking feature of our dataset is two pronounced negative $\varepsilon^{205}Tl_{authigenic}$ excursions revealed in shales from the Doushantuo Formation, one in the middle of

Member II (to as low as $\varepsilon^{205}\text{Tl}_{\text{authigenic}}$ = - 10.4 ± 0.2 at 38.8m), and another in the middle of Member III (to as low as $\varepsilon^{205}\text{Tl}_{\text{authigenic}}$ = - 9.1 ± 0.2 at 97.3m) (Fig. 6.3). Measured $\varepsilon^{205}\text{Tl}_{\text{authigenic}}$ outside of these excursions, which includes shale samples deposited during the purported OOEs, are less negative and comparatively invariant. For instance, $\varepsilon^{205}\text{Tl}_{\text{authigenic}}$ in lowermost Member II (0.0m to 11.4m) are all between -4.2 ± 0.2 and -2.0 ± 0.5. In uppermost Member II and lowermost Member III (47.8m to 82.2m), $\varepsilon^{205}\text{Tl}_{\text{authigenic}}$ are all between -5.3 ± 0.3 and -2.2 ± 0.3. In Member IV (112.2m to 117.7m), $\varepsilon^{205}\text{Tl}_{\text{authigenic}}$ are all between -3.5 ± 0.2 and 0.4 ± 0.7. Authigenic shale Tl concentrations peak during the purported OOEs (approaching 3 µg/g).

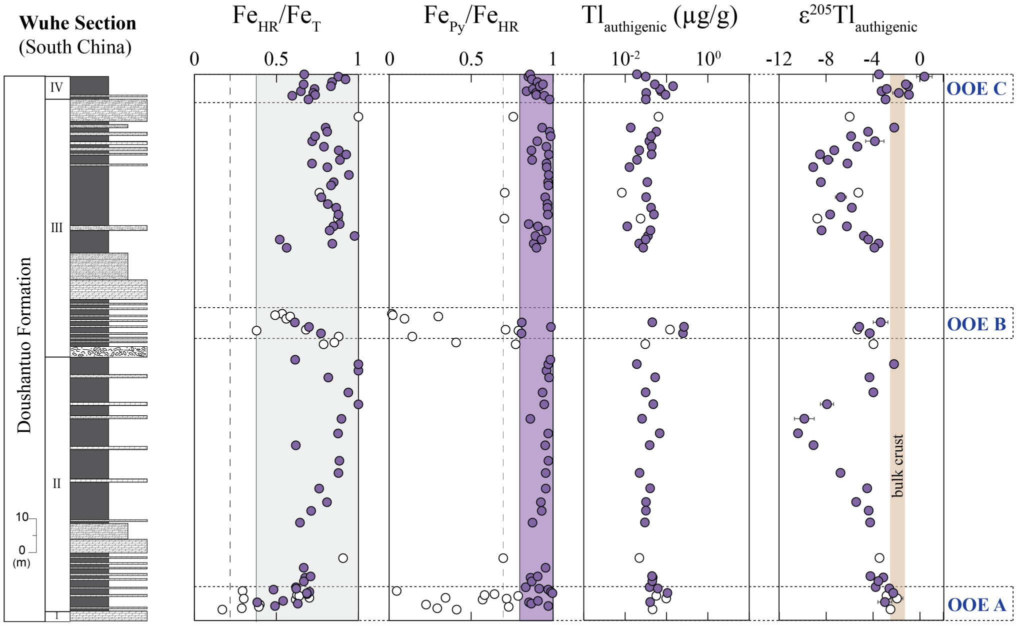

Fig. 6.3 Geochemistry of shales from the Wuhe section. Stratigraphy is modified from Jiang et al. (2011) and Fe speciation data and "OOE" intervals are from Sahoo et al. (2016). Purple circles signify samples deposited, according to Fe speciation data, under euxinic conditions ($Fe_{HR}/Fe_T \geq 0.38$ and $Fe_{Py}/Fe_{HR} \geq 0.80$ [Poulton and Canfield 2011]). Dashed lines signify relaxed thresholds for anoxic and euxinic conditions ($Fe_{HR}/Fe_T \geq 0.22$ and $Fe_{Py}/Fe_{HR} \geq 0.70$ [Poulton and Canfield, 2011]). White circles signify shale samples deposited under non-euxinic conditions. The brown shaded region in the Tl isotope plot signifies the range of values for the bulk upper continental crust ($\varepsilon^{205}Tl_{UCC} = -2.1 \pm 0.3$ [Nielsen et al. 2005]).

Comparable negative excursions are not revealed by the $\varepsilon^{205}\mathrm{Tl}_{\mathrm{detrital}}$ data, which are in comparison invariant (average $\varepsilon^{205}\mathrm{Tl}_{\mathrm{detrital}} = -3.6 \pm 1.9$; 2SD; Fig. 6.4). Notably, samples with lighter $\varepsilon^{205}\mathrm{Tl}_{\mathrm{detrital}}$ also possesses increasingly lighter $\varepsilon^{205}\mathrm{Tl}_{\mathrm{authigenic}}$ ($R^2 = 0.8$). Detrital Tl concentrations are also enriched in shales deposited during the OOEs, but the magnitude of enrichment is about an order of magnitude lower than authigenic counterparts (~0.4 μg/g).

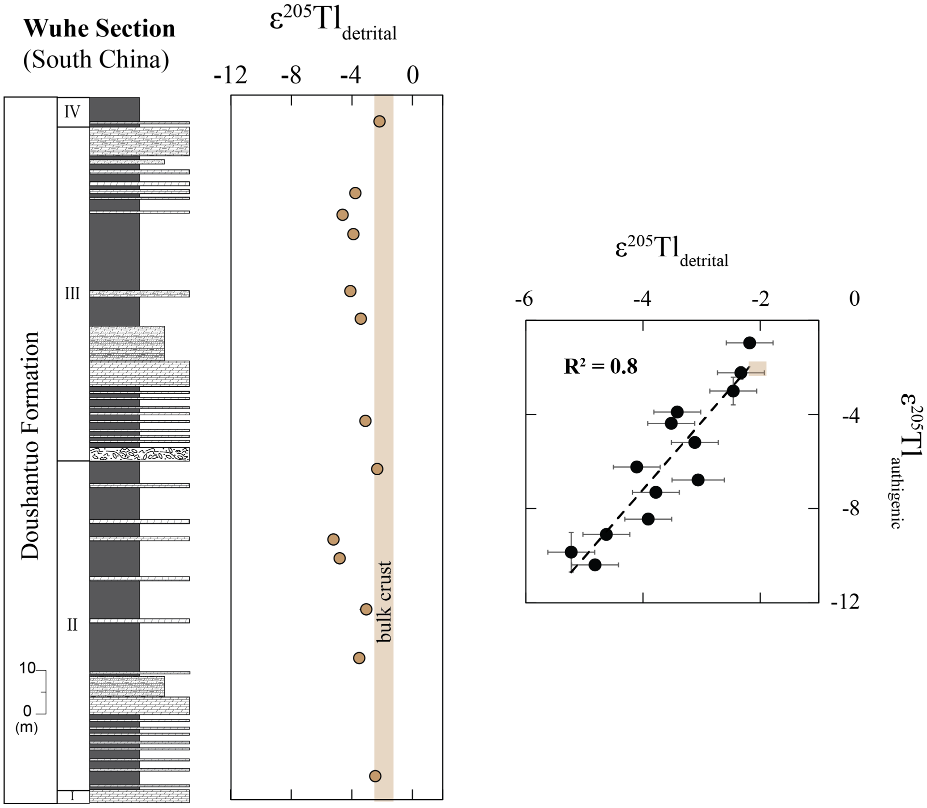

Fig. 6.4 Detrital Tl isotope data for shales from the Wuhe section. Stratigraphy is modified from Jiang et al. (2011) and "OOE" intervals are from Sahoo et al. (2016). Accompanying cross-plot shows the general correlation between our measured detrital and authigenic Tl isotope compositions. The brown shaded regions in both plots signify the range of values for the bulk upper continental crust ($\varepsilon^{205}\mathrm{Tl}_{\mathrm{UCC}} = -2.1 \pm 0.3$ [Nielsen et al. 2005]).

6.4.2 Northwestern Canada

Measured $\varepsilon^{205}\text{Tl}_{\text{authigenic}}$ in the overwhelming majority of shales from Northwestern Canada, from both the Wernecke Mountain (Fig. 6.5) and Mackenzie Mountain (Fig. 6.6) sections, are within error of bulk upper continental crust ($\varepsilon^{205}\text{Tl}_{\text{UCC}} = -2.1 \pm 0.3$ [Nielsen et al. 2005]). The only notable deviation away from bulk crust $\varepsilon^{205}\text{Tl}$ is a slight negative $\varepsilon^{205}\text{Tl}_{\text{authigenic}}$ excursion in the lower Sheepbed Formation (Wernecke Mountains) that reaches a nadir of $\varepsilon^{205}\text{Tl}_{\text{authigenic}} = -4.4 \pm 0.2$. Authigenic Tl concentrations are low and invariant in all shales from Northwestern Canada (maximum $\text{Tl}_{\text{authigenic}} = 0.3$ μg/g).

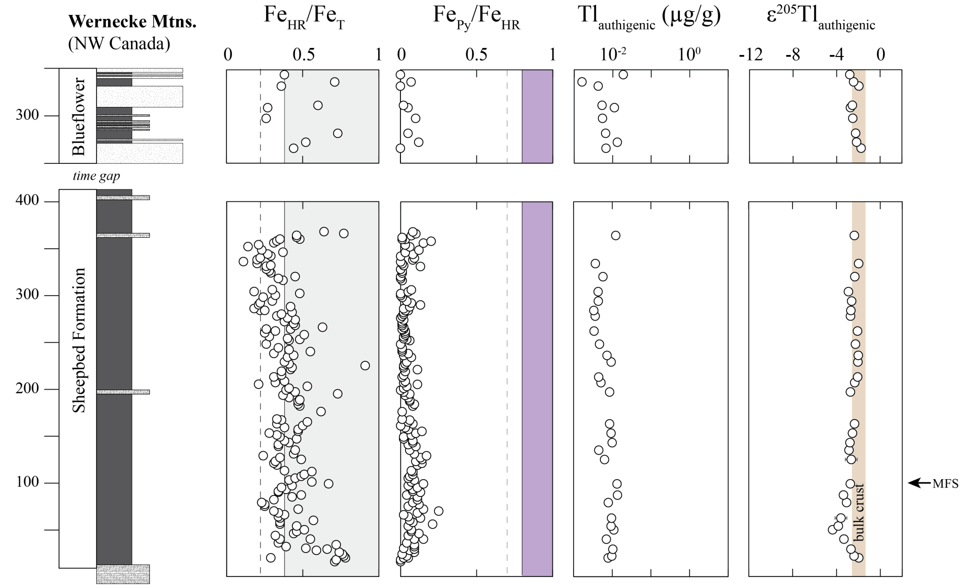

Fig. 6.5 Geochemistry of shales from the Wernecke Mountains. Stratigraphy is modified from Johnston et al. (2013) and Fe speciation data are from the same study. The grey and purple shaded areas signify the range of Fe speciation values indicative of anoxic ($\text{Fe}_{\text{HR}}/\text{Fe}_{\text{T}} \geq 0.38$) and euxinic ($\text{Fe}_{\text{Py}}/\text{Fe}_{\text{HR}} \geq 0.80$) local redox conditions, respectively (Poulton and Canfield 2011). Dashed lines signify relaxed thresholds ($\text{Fe}_{\text{HR}}/\text{Fe}_{\text{T}} \geq 0.22$ and $\text{Fe}_{\text{Py}}/\text{Fe}_{\text{HR}} \geq 0.70$ [Poulton and Canfield, 2011]). White circles signify shale samples deposited under non-euxinic conditions (in this case, all samples). The brown shaded region in the Tl isotope plot signifies the range of values for the bulk upper continental crust ($\varepsilon^{205}\text{Tl}_{\text{UCC}} = -2.1 \pm 0.3$ [Nielsen et al. 2005]). ”MFS” refers to a maximum flooding surface identified in Johnston et al. (2013).

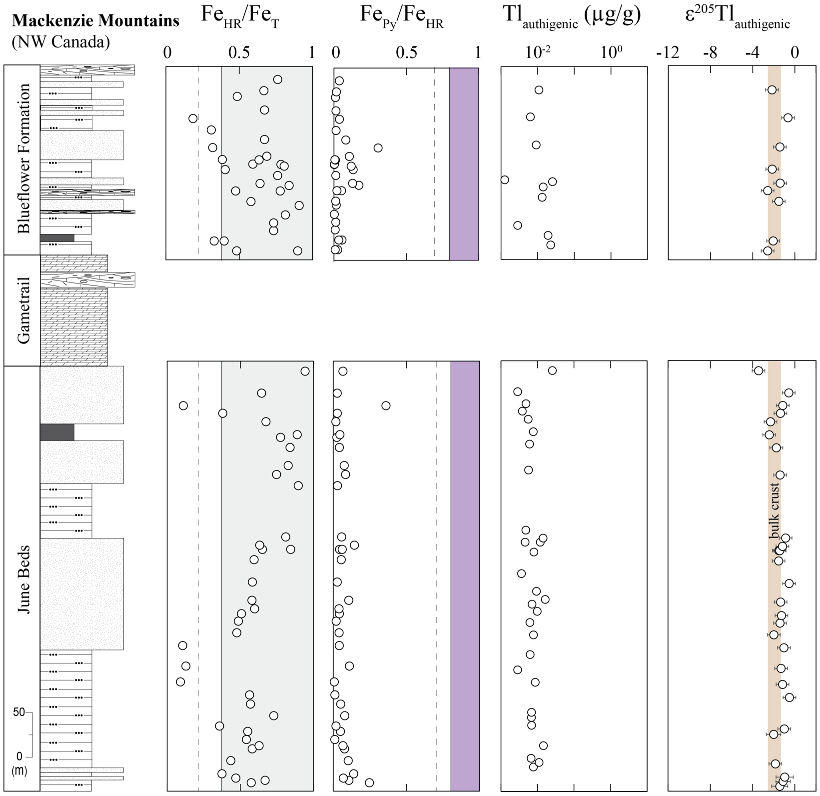

Fig. 6.6 Geochemistry of shales from the Mackenzie Mountains. Stratigraphy is modified from Sperling et al. (2015) and Fe speciation data are from the same study. The grey and purple shaded areas signify the range of Fe speciation values indicative of anoxic ($Fe_{HR}/Fe_T \geq 0.38$) and euxinic ($Fe_{Py}/Fe_{HR} \geq 0.80$) local redox conditions, respectively (Poulton and Canfield 2011). Dashed lines signify relaxed thresholds ($Fe_{HR}/Fe_T \geq 0.22$ and $Fe_{Py}/Fe_{HR} \geq 0.70$ [Poulton and Canfield, 2011]). White circles signify shale samples deposited under non-euxinic conditions (in this case, all samples). The brown shaded region in the Tl isotope plot signifies the range of values for the bulk upper continental crust ($\varepsilon^{205}Tl_{UCC} = -2.1 \pm 0.3$ [Nielsen et al. 2005]).

6.5 Discussion

We begin this section by first discussing the negative $\varepsilon^{205}Tl_{authigenic}$ excursions found in the Doushantuo Formation (South China) (**Section 5.1.**). This is then followed by discussion of our comparatively invariant Northwestern Canada shale $\varepsilon^{205}Tl_{authigenic}$ record (**Section 5.2.**). Lastly, we finish by discussing the potential connections between our new shale Tl isotope record and global ocean oxygenation during the Ediacaran Period (**Section 5.3.**).

6.5.1 Negative ε^{205}Tl excursions in the Doushantuo Formation

There appear to be two distinct Tl sources in our South China shales. The primary Tl source in our shales was released during the initial leach step (i.e., $\varepsilon^{205}\mathrm{Tl}_{\mathrm{authigenic}}$; Fig. 6.3) and is the culprit for our extremely negative isotope excursions. The subordinate Tl source in our shales was retained in our solid residues ($\varepsilon^{205}\mathrm{Tl}_{\mathrm{detrital}}$) and possesses a heavier, comparatively invariant Tl isotope composition (Fig. 6.4). A 100% successful leach should, in theory, result in a $\varepsilon^{205}\mathrm{Tl}_{\mathrm{detrital}}$ value comparable to the bulk upper continental crust ($\varepsilon^{205}\mathrm{Tl}_{\mathrm{UCC}} = -2.1 \pm 0.3$ [Nielsen et al. 2005]). Given the predominance of authigenic Tl in our shales that were measured for both $\varepsilon^{205}\mathrm{Tl}_{\mathrm{detrital}}$ and $\varepsilon^{205}\mathrm{Tl}_{\mathrm{authigenic}}$ ($f_{\mathrm{authigenic}}$ = 0.50 to 0.89), and the difficulties associated with transferring 100% of the authigenic Tl during the leach step, it is unlikely that all of our leaches successfully removed 100% of the authigenic Tl. A good correlation between our measured $\varepsilon^{205}\mathrm{Tl}_{\mathrm{detrital}}$ and $\varepsilon^{205}\mathrm{Tl}_{\mathrm{authigenic}}$ support this assumption ($R^2 = 0.8$; Fig. 6.4), fingerprinting the isotopically light excess authigenic Tl retained in some of our detrital fractions. This correlation could also suggest that isotopically heavy excess detrital Tl was retained in some of our authigenic fractions. We argue that this second scenario is less likely, however, because detrital phases are unlikely to be dissolved in dilute HNO_3 during the leach step. Furthermore, special care was taken to make sure no detrital residue was transferred during the leach step (discussed in **Section 3**).

6.5.1.2 Unlikely links to global-scale processes

The two prominent negative $\varepsilon^{205}Tl_{authigenic}$ excursions found in the Doushantuo Formation could fingerprint dramatic perturbations to the global Tl cycle. The shale samples from the Wuhe section that host these excursions are thought, based on Fe speciation data (Sahoo et al. [2016]; plotted in Fig. 6.3) and pyrite morphology (Wang et al. 2012), to have been deposited under a persistently euxinic water column. Accordingly, and by analogy with modern euxinic settings, these shales should have captured the overlying $\varepsilon^{205}Tl_{SW}$ during deposition (Owens et al. 2017a). If these shales were deposited in a basin that maintained a strong connection to the open ocean (cf., Cariaco Basin), then this $\varepsilon^{205}Tl_{SW}$ would have mirrored that of the open ocean. By extension, any variations to this $\varepsilon^{205}Tl_{SW}$ could then signify changes to past global Tl isotope mass-balance.

The only way to dramatically alter global Tl isotope mass-balance is to change the relative contribution of principal marine outputs for Tl (Baker et al. 2009). One reason for this requirement is that, although there is some isotopic heterogeneity in the Tl that gets delivered to the ocean today, the overwhelming majority of this Tl is isotopically indistinguishable from the bulk upper continental crust ($\varepsilon^{205}Tl_{IN} = \sim -1.8$; summarized in Nielsen et al. [2017], and also see Fig. 6.1). Second, two of the principal marine outputs for Tl are shown to impart significant isotope fractionation effects: low-temperature (low-T) alteration of oceanic crust (Nielsen et al. 2006) and highly oxidized Mn oxide-bearing marine sediments (Rehkämper et al. 2002, Nielsen et al. 2013). To further illustrate this concept, we employ the following isotope mass-balance equation:

$$\varepsilon^{205}Tl_{IN} = \varepsilon^{205}Tl_{OXIC}(f_{OXIC}) + \varepsilon^{205}Tl_{AOC}(f_{AOC}) + \varepsilon^{205}Tl_{ANOXIC}(f_{ANOXIC})$$

where $\varepsilon^{205}\mathrm{Tl}_X$ signify the Tl isotope compositions of marine inputs ("IN") and the three principal outputs ("OUT", but more specifically "OXIC" = Mn oxide-rich sediments deposited beneath oxygenated bottom waters; "AOC" = low-T alteration of oceanic crust; and "ANOXIC" = sediments deposited beneath anoxic bottom waters), and f_X their respective output flux contributions (summarized also in Fig. 6.1). Because the differences between $\varepsilon^{205}\mathrm{Tl}_{SW}$ and these outputs (that is, Δ_{OXIC}, Δ_{AOC}, and Δ_{ANOXIC}; values summarized in Table 6.2) have been constrained experimentally and in modern marine settings, ε^{205}Tl for each output can also be expressed as $\varepsilon^{205}\mathrm{Tl}_{SW} - \Delta_{OUT}$:

$$\varepsilon^{205}\mathrm{Tl}_{IN} = (\varepsilon^{205}\mathrm{Tl}_{SW} - \Delta_{OXIC})(f_{OXIC}) + (\varepsilon^{205}\mathrm{Tl}_{SW} - \Delta_{AOC})(f_{AOC}) + (\varepsilon^{205}\mathrm{Tl}_{SW} - \Delta_{ANOXIC})(f_{ANOXIC})$$

By performing these substitutions, ranges for f_x can be calculated for any given $\varepsilon^{205}\mathrm{Tl}_{SW}$ estimate. As a reference, open-ocean seawater today has a globally homogenous $\varepsilon^{205}\mathrm{Tl}_{SW}$ of -6.0 ± 0.3; 2SD (Nielsen et al. 2006, Owens et al. 2017a). This ε^{205}Tl has been set primary by Tl removal during oceanic crust alteration ($f_{AOC} = 0.64$) and by Tl delivery to marine sediments deposited beneath oxygenated bottom waters ($f_{OXIC} = 0.32$), and to a much lesser extent by Tl delivery to marine sediments deposited under anoxic bottom waters ($f_{ANOXIC} = 0.04$) (f_X are calculated from Nielsen et al. [2017] and Owens et al. [2017a]; see Fig. 6.7 for a graphical illustration).

If the extremely negative $\varepsilon^{205}\mathrm{Tl}_{\mathrm{authigenic}}$ from the Doushantuo Formation do fingerprint globally homogenous Ediacaran open ocean ε^{205}Tl values, then it implies f_{OXIC} was an even more prominent marine sink for Tl at these times than in the modern ocean (illustrated in Fig. 6.7). There are large ranges of f_{AOC} and f_{ANOXIC} values that can explain these negative $\varepsilon^{205}\mathrm{Tl}_{\mathrm{SW}}$ estimates, but all scenarios require a substantial f_{OXIC} contribution ($f_{\mathrm{OXIC}} \geq 0.44$). Put another way, f_{OXIC} would have needed to increase substantially at these times during the Ediacaran, at the expense of f_{AOC} and/or f_{ANOXIC}.

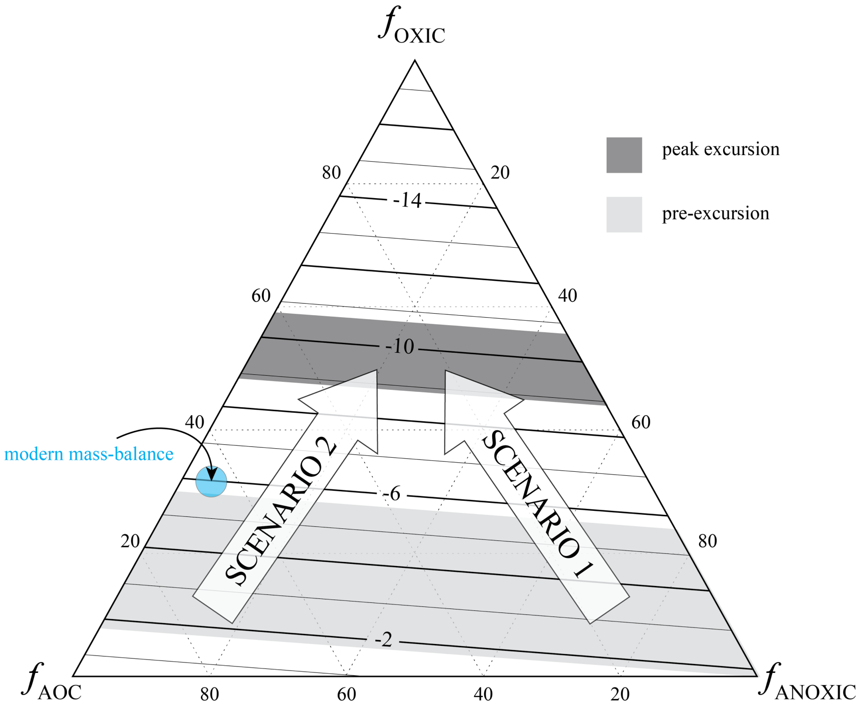

Fig. 6.7 Results of our Tl isotope mass-balance calculations polotted in a ternary diagram. Lines inside the diagram represent the open ocean $\varepsilon^{205}\mathrm{Tl}_{\mathrm{SW}}$ that results from the combination of f_{OXIC}, f_{AOC}, and f_{ANOXIC} at that point in the diagram. Modern Tl isotope mass-balance, and the resultant $\varepsilon^{205}\mathrm{Tl}_{\mathrm{SW}}$, is plotted in blue for reference. Our most negative $\varepsilon^{205}\mathrm{Tl}_{\mathrm{authigenic}}$ from the Doushantuo formation are plotted in dark grey, while those values immediately preceding the excursions are plotted in light grey. The white arrows signify theoretical scenarios that could drive the negative Tl isotope excursions found in the Doushantuo Formation. See **Section 5.1.1.** for more details.

We argue that one simplified scenario – an increase in f_{OXIC} primarily at the expense of f_{ANOXIC} ("Scenario 1" in Fig. 6.7) – is unlikely. In its most simple form, this scenario implies global Ediacaran oceans became better oxygenated during both negative $\varepsilon^{205}\mathrm{Tl}_{\mathrm{authigenic}}$ excursions. Many geochemical studies suggest that the global Ediacaran ocean was at times better oxygenated than the primarily anoxic Proterozoic ocean that preceded it (summarized in Lyons et al. 2014). Some of these studies infer enhanced ocean oxygenation concurrent with, or even as the driving force for, the Shuram C-isotope Excursion (e.g., Fike et al. [2006], McFadden et al. [2008], Zhang et al. [2019]; but also see Knauth and Kennedy [2009], Derry [2010], and Schrag et al. [2013] for alternative origin theories). Because the younger of the two negative $\varepsilon^{205}\mathrm{Tl}_{\mathrm{authigenic}}$ excursions revealed here occurs in the same Doushantuo Member that hosts the Shuram Excursion (Member III; Jiang et al. [2011]), this Tl isotope excursion could add credence to the ocean oxygenation hypothesis (e.g., Fan et al. [2020]). The older and greater magnitude negative $\varepsilon^{205}\mathrm{Tl}_{\mathrm{authigenic}}$ excursion revealed here (that is, the one that manifests in mid-Member II), however, does not align in-time, not even approximately, with any supporting evidence for enhanced global ocean oxygenation. An absence of corroborating evidence for widespread ocean oxygenation during deposition of mid-Member II does not rule-out the possibility, but it does not give us immediate confidence in invoking this simple explanation for both negative $\varepsilon^{205}\mathrm{Tl}_{\mathrm{authigenic}}$ excursions.

The alternate simplified scenario – an increase in f_{OXIC} primarily at the expense of f_{AOC} ("Scenario 2" in Fig. 6.7) – is at the moment highly skeptical. A reduction in f_{AOC} would imply that, at these times during the Ediacaran, low-T hydrothermal circulation worldwide was perturbed so that Tl removal into this output diminished. As an example, it is perhaps possible that at times in Earth's past when global sedimentation rates increased (e.g., as a result of enhanced terrestrial weathering), thick blankets of sediment could have prevented the percolation of fluids into some off-axis basalts. Alternatively, sluggish oceanic crust production rates at times in Earth's past could have reduced the areal extent of seafloor undergoing low-T alteration. Both of these hypothetical scenarios are admittedly highly simplified and do not take into consideration much of the complexity associated with hydrothermal circulation in ocean crust (for example, see Mottl 2003). Notwithstanding, either of these scenarios or any others that would have at times reduced the relative flux of Tl into altered oceanic crust would have diminished removal of the lighter-mass Tl isotope from seawater, in-turn facilitating its accumulation in seawater. It is worth noting that such scenarios would be expected to unfold over fairly long timescales, which agrees with the progressive nature of the negative $\varepsilon^{205}Tl_{authigenic}$ excursions, which occur over 10s of millions-of-years according to the age estimates of Sahoo et al. (2016). It is additionally worth noting that an increase in seawater $\delta^{238}U$ was recently inferred across the Ediacaran Shuram Excursion (Zhang et al. 2019), roughly coincident with the negative $\varepsilon^{205}Tl_{authigenic}$ excursion found here in upper-Member III and also in another study (Fan et al. 2020). A global increase in seawater $\delta^{238}U$ would also be an expected consequence of diminished low-T hydrothermal circulation of U, because this phenomenon would have diminished the preferential removal of heavier-mass U isotopes from seawater into this U output (Andersen et al. 2015). Still, despite some of the merits of this hypothesis, we would argue that caution is warranted, and these ideas should only be adopted in the future if supported by additional independent evidence. More importantly, there is a much simpler explanation for the negative $\varepsilon^{205}\mathrm{Tl}_{\mathrm{authigenic}}$ excursions (discussed below).

Table 6.2 Tl isotope mass-balance parameters used in this study

	$\varepsilon^{205}\mathrm{Tl}$	Δ_{OUT}	Ref.
Inputs	-1.8		1
Outputs			
OXIC	+10	-16	1
AOC	-7.4*	+1.4	
ANOXIC	-6	0	2, 3

References: 1. Nielsen et al. 2017; 2. Owens et al. 2017a; 3. Fan et al. 2020

*This value is adjusted slightly from Ref. 1 to achieve mass-balance. Ref. 1. did not include anoxic sediments as a principal output. We have added this anoxic output and estimate its *f* and Δ based on Ref. 2 (see their Figure 1).

6.5.1.2 More plausible links to local-scale processes

A simpler, and we argue more plausible, explanation for the negative $\varepsilon^{205}\mathrm{Tl}_{\mathrm{authigenic}}$ excursions is that they are a consequence of local basin-scale controls. This hypothesis gains support, first and foremost, from the many independent lines of evidence that suggest the Doushantuo Formation was deposited in an at least semi-restricted basin concurrent with both $\varepsilon^{205}\mathrm{Tl}_{\mathrm{authigenic}}$ excursions (between the purported OOEs; see Fig. 6.3 [Ostrander et al. 2019a]). By analogy with modern restricted settings (cf., the Black Sea [Owens et al. 2017a]), it is then plausible that $\varepsilon^{205}\mathrm{Tl}_{\mathrm{SW}}$ in the basin at these times was strictly a local signature, independent of the open ocean $\varepsilon^{205}\mathrm{Tl}_{\mathrm{SW}}$. If so, then this local $\varepsilon^{205}\mathrm{Tl}_{\mathrm{SW}}$ would have been set exclusively by Tl mass-balance in the local basin.

There are basin-scale controls that could conceivably drive a local $\varepsilon^{205}\mathrm{Tl}_{\mathrm{SW}}$ signature to be very negative. For example, although local-scale heterogeneity in ε^{205}Tl values of oceanic inputs is, from a mass-balance perspective, not likely to drive large variations in open-ocean $\varepsilon^{205}\mathrm{Tl}_{\mathrm{SW}}$ (Baker et al. 2009), this heterogeneity could have an effect on $\varepsilon^{205}\mathrm{Tl}_{\mathrm{SW}}$ in a restricted basin. River water in some locations today has a considerably lighter ε^{205}Tl than bulk continental crust (as low as $\varepsilon^{205}\mathrm{Tl} = -6.8 \pm 1.5$ in the Danube [Nielsen et al. 2005]), as do some volcanic emissions (as low as -16.7 ± 0.5 in Kilauea, HI [Baker et al. 2009]). If the principal Tl source(s) to the local Nanhua Basin approached or exceeded these modern ε^{205}Tl values, then mass-balance in the basin could have been skewed in that same direction – especially if this basin received little to no additional Tl from the open ocean.

A case could also be made that outputs of Tl in a restricted basin, namely Mn oxide-bearing sediments, would be very efficient in driving a negative $\varepsilon^{205}\mathrm{Tl}_{\mathrm{SW}}$. First, a basin that exchanges little to no Tl with the open ocean would be minimally affected, if at all, by altered oceanic crust. This is to say that, in a basin where very little or no seawater is circulated through oceanic crust, Tl isotope mass-balance in the basin would be controlled only by the relative distribution of oxic versus anoxic sediments in that basin. Going one step further, because Mn oxide-bearing oxic sediments would be the only Tl output that imparts an isotope fractionation effect in this scenario (and a substantial effect, at that [Rehkämper et al. 2002, Nielsen et al. 2013]), isotope mass-balance in the basin would be controlled almost exclusively by Mn oxides. In restricted euxinic basins, dissolved Fe^{2+} is efficiently removed from seawater during pyrite precipitation. As a consequence, marine sediments deposited beneath shallow oxygenated waters in euxinic basins can become particularly rich in Mn oxide minerals (relative to Fe oxide minerals, which would also readily form if Fe^{2+} were not efficiently removed from local waters [Force and Cannon 1988]). In sum, it seems reasonable to hypothesize that in some restricted redox-stratified basins, both today and in Earth's past, efficient burial of Mn oxides in sediments deposited beneath shallow oxygenated waters could drive a local $\varepsilon^{205}Tl_{SW}$ to very negative values.

It is worth also discussing here that the local operation of a Mn oxide "shuttle" in the Nanhua Basin during the purported OOEs, as is suggested by extremely negative $\delta^{98}Mo$ in the same samples (Ostrander et al. 2019a), cannot explain the shifts to more positive $\varepsilon^{205}Tl_{authigenic}$ values at these times. First, our heavier $\varepsilon^{205}Tl_{authigenic}$ values are not regulated to just the OOE intervals and instead persist over much longer stratigraphic distances (Fig. 6.3). Second, if the shuttle scenario is a viable explanation, we would predict a substantial increase in Tl/Mo ratios and $\varepsilon^{205}Tl_{authigenic}$ during the OOEs (illustrated in Fig. 6.8). This is because Tl/Mo ratios in Mn oxide-replete ferromanganese crusts and nodules today (Tl/Mo = ~0.3 [Hein and Koschinsky 2014]) are two orders of magnitude greater than those found in anoxic marine sediments from Cariaco Basin (Tl/Mo = ~0.007; calculated from Tl data reported in Owens et al. [2017a] and Mo data summarized in Algeo and Lyons [2006]). Additionally, $\varepsilon^{205}Tl$ in ferromanganese crusts and nodules today ($\varepsilon^{205}Tl = \sim +10$ [Rehkämper et al. 2002, Nielsen et al. 2013]) are substantially heavier than those found in sediments from Cariaco Basin ($\varepsilon^{205}Tl = -5.1 \pm 1.3$; 2SD [Owens et al. 2017a]). These Mn oxide fingerprints are not found in shales deposited during the OOEs (Fig. 6.8). To the contrary, our heaviest $\varepsilon^{205}Tl_{authigenic}$ are accompanied by the lowest Tl/Mo ratios (in shales from OOE C). These findings suggest that a Mn oxide shuttle had little to no effect on our measured $\varepsilon^{205}Tl_{authigenic}$ during the purported OOEs.

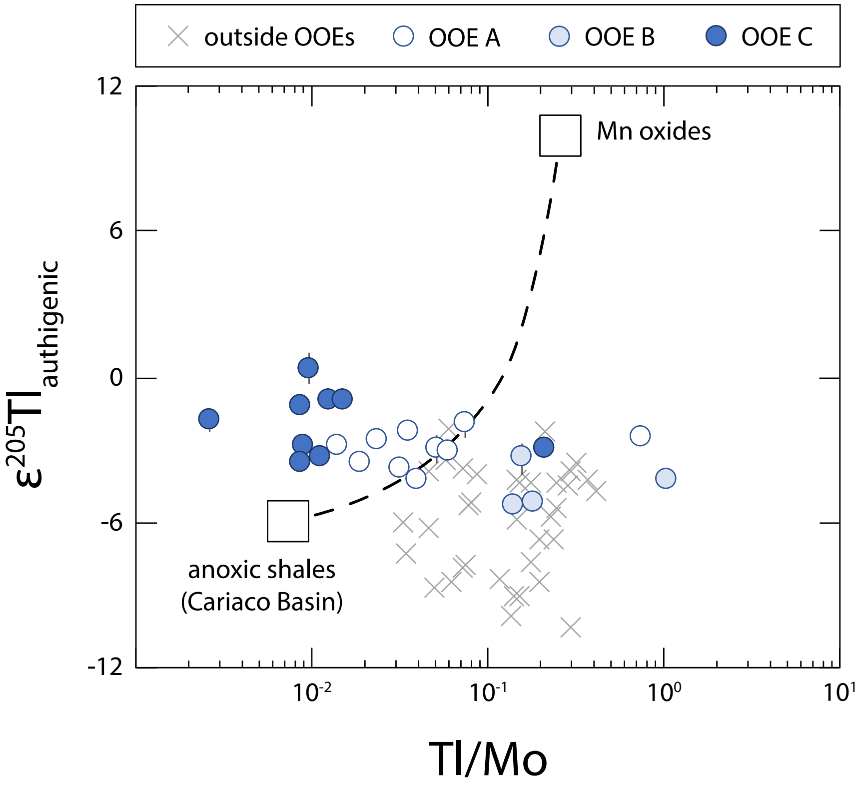

Fig. 6.8 Semi-log plot of our $\varepsilon^{205}Tl_{authigenic}$ and Tl/Mo ratios from Doushantuo shales. The dashed line signifies modern mixing between an anoxic shale component from the Cariaco Basin and Mn oxide minerals (see text for references). If Tl had been at times delivered to the shales of the Doushantuo Formation by Mn oxide minerals, this is the mixing trend we would predict.

The ability of a Mn oxide shuttle to alter sedimentary $\delta^{98}Mo$, but have little to no effect on sedimentary $\varepsilon^{205}Tl$, is also evident in the modern Cariaco Basin (discussed in Ostrander et al. [2019b]). The $\delta^{98}Mo$ fingerprint of an oxide shuttle is transferred to marine sediments today below the chemocline in the Cariaco Basin (specifically, $\delta^{98}Mo$ considerably lighter than seawater [Brüske et al. 2020]). In contrast, there is no obvious effect on sedimentary ε^{205}Tl below the chemocline, which instead match overlying seawater (ε^{205}Tl = -5.1 ± 1.3; 2SD [Owens et al. 2017a]). One possible explanation for this disparity is that, unlike Mo which is strongly retained in sulfidic sediments (Crusius et al. 1996), Tl may be released to the water column during Mn oxide dissolution in sulfidic settings. Once in the water column, this Tl can then remix and re-homogenize with the dissolved seawater Tl pool before complexation with pyrite. Future investigations of redox-stratified modern settings should test this hypothesis.

6.5.2 Invariant Northwest Canada shale ε^{205}Tl record

Our comparatively invariant Northwest Canada shale ε^{205}Tl record supports the idea of local-scale processes driving much of the ε^{205}Tl variability in South China shales. First, $\varepsilon^{205}\mathrm{Tl}_{\mathrm{authigenic}}$ in shales from the June Beds (Mackenzie Mountains), which are the inferred coeval equivalents of Doushantuo Formation Member III (Macdonald et al. [2013]; see also Fig. 6.2), do not possess the same extreme negative $\varepsilon^{205}\mathrm{Tl}_{\mathrm{authigenic}}$ excursions (Fig. 6.6). Instead, $\varepsilon^{205}\mathrm{Tl}_{\mathrm{authigenic}}$ in the June Beds are fairly invariant ($\varepsilon^{205}\mathrm{Tl}_{\mathrm{authigenic}}$ = -1.4 ± 1.2; 2SD). Shales from the June Beds are thought to have been deposited under predominantly ferruginous conditions (Sperling et al. 2016). No investigations have been conducted on Tl isotope cycling in modern ferruginous settings, but a recent study did investigate Tl isotopes in sediments deposited beneath modern anoxic and H_2S-poor waters (Santa Barbara Basin [Fan et al. 2020]). In Fan et al. (2020), it was shown that anoxic core-top sediments from the Santa Barbara Basin possessed $\varepsilon^{205}\mathrm{Tl}_{\mathrm{authigenic}}$ indistinguishable from globally homogenous $\varepsilon^{205}\mathrm{Tl}_{\mathrm{SW}}$ ($\varepsilon^{205}\mathrm{Tl}_{\mathrm{authigenic}}$ = -5.6 ± 0.2; 2SD [Fan et al. 2020] compared to $\varepsilon^{205}\mathrm{Tl}_{\mathrm{SW}}$ = -6.0 ± 0.3; 2SD [Nielsen et al. 2006, Owens et al. 2017a]). Though the analogy is not perfect, it is possible that shales from the June Beds also captured overlying $\varepsilon^{205}Tl_{SW}$ at the time of their deposition. Regardless of the absolute validity of the analogy, the mere fact that shales from the June Beds exhibit invariant $\varepsilon^{205}Tl$ is strong evidence against dramatic perturbation to global $\varepsilon^{205}Tl_{SW}$ at this time. The possibility of a heterogenous open ocean $\varepsilon^{205}Tl_{SW}$ at this time is also unlikely because the residence time of Tl in seawater would, if anything, be expected to increase in a poorly oxygenated Ediacaran environment. For example, delivery of Tl to the ocean and its stability once there is not strongly coupled to redox, and decreased uptake of Tl by Mn oxides in a poorly-oxygenated ocean would only increase seawater Tl concentrations (e.g., during Mesozoic OAEs [Nielsen et al. 2011]).

Additionally, and perhaps more substantially, there is broad agreement between both shale records if $\varepsilon^{205}Tl_{authigenic}$ from shales of the Doushantuo Formation that are thought to have been deposited in a restricted basin are omitted from our dataset (Fig. 6.9). Put another way, when shales from both locations are thought most likely to have been deposited under anoxic conditions in a basin well-connected to the open ocean (cf., the modern Cariaco and Santa Barbara basins), the $\varepsilon^{205}Tl$ records generally agree. This agreement is, we argue, strong evidence that a globally homogenous $\varepsilon^{205}Tl_{SW}$ was transcribed to both sedimentary records at these times, or nearly so.

A few of our shale samples from Northwestern Canada are thought to have been deposited under mildly oxidizing conditions, and as such may not have captured past $\varepsilon^{205}Tl_{SW}$. For example, in the Blueflower Formation from the Mackenzie Mountains, wider bilaterian burrows were interpreted by Sperling et al. (2016) as evidence for partial local oxygenation. If the in-situ formation or burial of Mn oxides during this time affected our measured $\varepsilon^{205}\mathrm{Tl}_{\mathrm{authigenic}}$, we would predict heavier values (Rehkämper et al. 2002, 2004). Indeed, measured $\varepsilon^{205}\mathrm{Tl}_{\mathrm{authigenic}}$ in these Blueflower Formation samples are sometimes slightly heavier than their equivalents in the Wernecke Mountains (apparent in Fig. 6.9). Notably, however, it is unlikely that the full positive Tl isotope fractionation effect between seawater and Mn oxides was imparted on the original sediments ($\Delta_{\mathrm{SW\text{-}OXIDE}} = \sim -19$ [Rehkämper et al. 2002, Nielsen et al. 2013]). If this was the case, then we would expect sedimentary $\varepsilon^{205}\mathrm{Tl}_{\mathrm{authigenic}}$ to be substantially heavier, more than only slightly heavier than bulk crustal values (only as heavy as $\varepsilon^{205}\mathrm{Tl}_{\mathrm{authigenic}} = -0.7 \pm 0.6$). We do not think that the encroachment of oxic surface waters concurrent with a maximum flooding surface (MFS) in the lower Sheepbed Formation (Johnston et al. 2013) affected transfer of $\varepsilon^{205}\mathrm{Tl}_{\mathrm{SW}}$ to these shales because there is no noticeable variation in our measured $\varepsilon^{205}\mathrm{Tl}_{\mathrm{authigenic}}$ across the MFS (Fig. 6.5). In sum, it is reasonable to assume that, with a few minor exceptions, most of our Northwestern Canada shales may have captured open ocean $\varepsilon^{205}\mathrm{Tl}_{\mathrm{SW}}$.

6.5.3 Ediacaran ocean oxygenation

We discuss in this final section what connections can be made between our Tl isotope dataset and Ediacaran global ocean oxygenation. We focus on previously purported Ediacaran OOEs at ~635 Ma, ~580 Ma, and ~560 Ma (Sahoo et al. 2016) because it is at these times that we think that both our shale records are most likely to have tracked changes in open ocean $\varepsilon^{205}\mathrm{Tl}_{\mathrm{SW}}$ (discussed in **Section 5.2.**; also see Fig. 6.9).

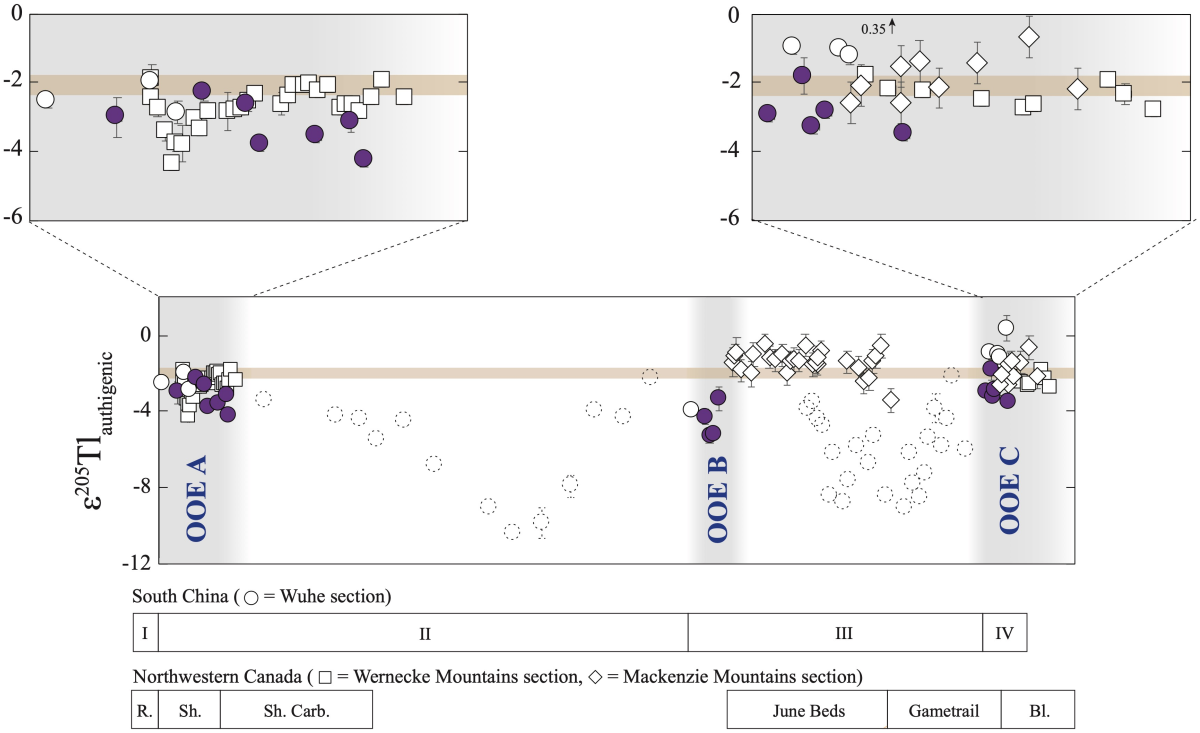

Fig. 6.9 Tl isotope data from shales deposited in a setting well-connected to the open ocean. Datapoint color schemes are the same as in Figs. 6.3-6.5. Tl isotope data from shales deposited in a restricted Nanhua Basin are also included, but with dashed outlines. OOE intervals again come from Sahoo et al. (2016). Some unit names have been abbreviated to conserve space: R. = Ravensthroat Formation, Sh. = Sheepbed Formation, Sh. Carb. = Sheepbed Carbonate, Bl. = Blueflower Formation. See Fig. 6.1 for stratigraphic correlations.

The original OOE hypothesis (Sahoo et al. 2016) leads to a few predictions for our Tl isotope dataset. First, this hypothesis predicts negative $\varepsilon^{205}\mathrm{Tl}_{\mathrm{authigenic}}$ excursions during each OOE. Again, this is because widespread ocean oxygenation would have been accompanied by concurrent increases in Mn oxide burial, in-turn driving a more negative open ocean $\varepsilon^{205}\mathrm{Tl}_{\mathrm{SW}}$. Second, if the magnitude of global ocean oxygenation during the OOEs were comparable to today, as was proposed, then $\varepsilon^{205}\mathrm{Tl}_{\mathrm{SW}}$ may have also been comparable to today ($\varepsilon^{205}\mathrm{Tl}_{\mathrm{SW}} = -6.0 \pm 0.3$; 2SD [Nielsen et al. 2006, Owens et al. 2017a]).

Finally, because it was originally suggested that the OOEs persisted over millions of years (<5 to 10 myr), the negative $\varepsilon^{205}Tl_{authigenic}$ excursions would not likely have been affected by non steady-state periods and, therefore, should have persisted throughout the duration of each OOE similarly to the extent of the RSE enrichments.

These OOE predictions are not met by our dataset. There are a few short-lived negative $\varepsilon^{205}Tl_{authigenic}$ excursions during the OOEs, the most prominent occurring in the lower Sheepbed Formation (OOE A) and in lowermost Doushantuo Member III (OOE B). However, only $\varepsilon^{205}Tl_{authigenic}$ during OOE B approach values comparable to modern open ocean $\varepsilon^{205}Tl_{SW}$ ($\varepsilon^{205}Tl_{authigenic} = -5.3 \pm 0.3$). Moreover, no negative $\varepsilon^{205}Tl_{authigenic}$ excursions persist over the million-year timescales of the OOEs. To the contrary, $\varepsilon^{205}Tl_{authigenic}$ within error of the bulk upper continental crust ($\varepsilon^{205}Tl_{UCC} = -2.1 \pm 0.3$ [Nielsen et al. 2005]) are found over large stratigraphic distances during the two OOEs for which we generated the most data (OOE A and OOE C; Fig. 6.9). These near-crustal value for $\varepsilon^{205}Tl_{authigenic}$, which are found in shales from both South China and Northwestern Canada, do not support persistent widespread ocean oxygenation for the duration of the OOEs.

This is not to say, however, that global ocean oxygenation levels did not increase at times during the purported OOEs, or even that global oxygenation levels could not generally have been higher during the OOEs. As mentioned above, there are some considerably negative $\varepsilon^{205}Tl_{authigenic}$ found during the events in shales from both South China and Northwestern Canada. Additionally, the only set of shales deposited outside of the OOEs that we posit captured open ocean $\varepsilon^{205}Tl_{SW}$ (the June Beds) reveal $\varepsilon^{205}Tl_{authigenic}$ indistinguishable from the $\varepsilon^{205}Tl$ of bulk upper continental crust (Fig. 6.9). The near-crustal open ocean $\varepsilon^{205}Tl_{SW}$ inferred from the June Beds shales is consistent with a comparatively anoxic global ocean outside of the surrounding OOEs. In sum, although some details of the OOE hypothesis are not supported by our dataset, some of the more general ideas of this hypothesis can still be supported.

6.6 Conclusions

When attempting to reconstruct Earth's past environments, it is inadvisable to rely on a single archive. This statement is intuitive and supported here by our new Ediacaran Tl isotope dataset. Shales from South China reveal two extremely negative $\varepsilon^{205}Tl_{authigenic}$ excursions, while $\varepsilon^{205}Tl_{authigenic}$ in their coeval equivalents from Northwestern Canada are generally invariant. Much of this geochemical disparity can be reconciled simply by invoking local-scale differences between the individual paleo-depositional sites. The most critical difference would have been the degree of open-ocean connection at each site, and how this connectivity changed during the Ediacaran Period.

We get much better agreement in our Tl isotope records if we look exclusively at shales deposited in settings that were well-connected to the open ocean (according to Ostrander et al. [2019a]). This finding is also intuitive because today's globally homogenous $\varepsilon^{205}Tl_{SW}$ gets transferred only to marine sediments deposited in basins that maintain a strong connection to the open ocean (cf., the Cariaco [Owens et al. 2017a] and Santa Barbara [Fan et al. 2020] basins). Performing this exercise regulates our most negative $\varepsilon^{205}Tl_{authigenic}$ excursions in South China to shales deposited in a restricted basin. In modern restricted basins (cf., the Black Sea [Owens et al. 2017a]), and by analogy also past restricted basins, Tl isotope mass-balance in the basin gets regulated exclusively by local controls (e.g., $\varepsilon^{205}Tl$ of local inputs and Mn oxide burial within the basin).

When we continue this exercise, some predictions of the original OOE hypothesis (Sahoo et al. 2016) are not met by our dataset. The original OOE hypothesis predicts negative $\varepsilon^{205}\mathrm{Tl}_{\mathrm{authigenic}}$ excursions for the duration of each OOE, which would be an expected consequence of widespread marine Mn oxide burial over ~5 to 10 myr timeframes. To the contrary, our $\varepsilon^{205}\mathrm{Tl}_{\mathrm{authigenic}}$ record across each OOE reveals values that are primarily indistinguishable from the bulk upper continental crust ($\varepsilon^{205}\mathrm{Tl}_{\mathrm{UCC}} = -2.1 \pm 0.3$ [Nielsen et al. 2005]). These near-crustal $\varepsilon^{205}\mathrm{Tl}_{\mathrm{authigenic}}$ suggest that widespread ocean oxygenation was not persistent for the duration of each OOE. However, there are a few considerably negative $\varepsilon^{205}\mathrm{Tl}_{\mathrm{authigenic}}$ values in shales from both South China and Northwestern Canada deposited during the OOEs (to as low as $\varepsilon^{205}\mathrm{Tl}_{\mathrm{SW}} = -5.3 \pm 0.3$). Therefore, although some details of the OOE hypothesis are not supported by our dataset, some of the general ideas are still consistent with the new Tl isotope data.

A logical next step would be to constrain open ocean $\varepsilon^{205}\mathrm{Tl}_{\mathrm{SW}}$ using additional Ediacaran sedimentary records. There are some timeframes during the Ediacaran Period for which our inferences of past $\varepsilon^{205}\mathrm{Tl}_{\mathrm{SW}}$ are based solely on one set of shales (e.g., the ~580 Ma OOE), and some timeframes during which we are unable to confidently estimate $\varepsilon^{205}\mathrm{Tl}_{\mathrm{SW}}$ whatsoever (e.g., most of the timeframe separating the ~635 Ma and ~580 Ma OOEs). A more robust and complete Ediacaran $\varepsilon^{205}\mathrm{Tl}_{\mathrm{SW}}$ curve could be constructed simply by targeting additional sets of shales for Tl isotope analyses. As was made clear in our study, it would be ideal for these prospective studies to target shales from multiple locations that were deposited under local anoxic conditions. Some plausible targets are early- to mid-Ediacaran shales from South Australia and East Greenland (Canfield et al. 2008), and mid- to late Ediacaran shales from Newfoundland (Canfield et al. 2007), Uruguay (Frei et al. 2013), and Czech Republic (Kurzweil et al. 2015b). As was also made clear in our study, it will be important to take into consideration processes that operated at each paleo-location on a local-scale before invoking changes to global-scale processes.

CHAPTER 7

SUMMARY AND FUTURE DIRECTIONS

7.1 Summary

The ability of the Mo and Tl isotope systems to track changes in past ocean oxygenation is confirmed in this dissertation. Heavy δ^{98}Mo in shales deposited during the Neoarchean (2,800 Ma to 2,500 Ma) track early ocean oxygenation on a young Earth (**Chapter 2**; Ostrander et al. 2020). Heavy ε^{205}Tl in shales deposited during Oceanic Anoxic Event 2 track a much younger episode of ocean *de*-oxygenation (**Chapter 3**; Ostrander et al. 2017). An anti-correlation between δ^{98}Mo and ε^{205}Tl in shales deposited at the end of the Archean Eon (~2,500 Ma) tracks especially strong ocean oxygenation on the eve of the Great Oxidation Event (**Chapter 4**; Ostrander et al. 2019a). Finally, δ^{98}Mo (**Chapter 5**; Ostrander et al. 2019b) and ε^{205}Tl (**Chapter 6**; Ostrander et al. *in prep*) in shales deposited during the Ediacaran track intermediate ocean oxygenation across the Proterozoic-Phanerozoic transition

As was also made clear in this dissertation, there are caveats to the paired application of Mo and Tl isotopes. For instance, seawater ε^{205}Tl in restricted basins can be a strictly local signature (e.g., the Black Sea; Owens et al. 2017a), whereas seawater δ^{98}Mo in these same basins is equal to the globally homogenous value (Neubert et al. 2008). It is therefore important, whenever possible, to target shales from basins that maintained a strong connection to the open ocean. At the same time, transfer of seawater δ^{98}Mo to euxinic sediments is hindered in open-ocean settings because quantitative Mo removal is difficult to achieve in these settings when the local Mo is continuously replenished (e.g., in the Cariaco Basin; Arnold et al. 2004, Brüske et al. 2020). It may therefore be more realistic to rely on δ^{98}Mo trends – and not absolute δ^{98}Mo values – when pairing Mo and Tl isotopes in shales from open-ocean settings. At the least, if seawater δ^{98}Mo and ε^{205}Tl cannot *both* be faithfully reconstructed from a single set of shales, it may be possible to decipher which one is more likely by measuring both isotope systems (for example, see **Chapters 5 and 6**). Finally, moving further back in time, it is also worth considering whether the conditions at that time would have been conducive to transfer of both seawater δ^{98}Mo and ε^{205}Tl. Such conditions may have been met on an early Earth, when low seawater Mo concentrations may have allowed for transfer of seawater δ^{98}Mo even in open-ocean settings (see **Chapter 4**).

7.2 Future Directions

There are still many questions yet to be answered when it comes to Mo and Tl isotopes. For example, although there have been many thorough investigations of Mo isotope cycling in modern marine settings (summarized in Kendall et al. 2017), only two comparatively cursory investigations have targeted Tl isotopes (Owens et al. 2017a, Fan et al. 2020). In Owens et al. (2017a), ε^{205}Tl were measured primarily in oxic surface waters and only in much deeper sediments below the chemocline in the Black Sea and Cariaco Basin. In Fan et al. (2020), ε^{205}Tl were measured only in sediments deposited below the chemocline in the Santa Barbara Basin. What would be extremely useful to know, however, is how do ε^{205}Tl behave in waters extending from the chemocline to the basin floor in these settings? At the same time, it would be extremely useful to also know how ε^{205}Tl behave in sediments deposited at all depths in the basin. We know that δ^{98}Mo are sometimes highly variable in waters and sediments in the Black Sea, particularly below the chemocline, and this variability helps us to understand what controls Mo removal in this location (namely, the formation of thiomolybdate complexes; Neubert et al. 2008). Perhaps more importantly, if there are sediments deposited below the chemocline in these basins that do not capture the ε^{205}Tl of oxic surface waters then we can assume that this was also the case for some of their ancient shale equivalents.

The current shale Tl isotope record is also quite sparse (Fig. 7.1), leaving many opportunities for future work. Essentially the entirety of the Archean and Proterozoic shale records are devoid of ε^{205}Tl data. By targeting more Archean shales for ε^{205}Tl analyses, we can better constrain the earliest stages of ocean oxygenation on Earth (Lyons et al. 2014). By targeting more Proterozoic shales for ε^{205}Tl analyses, we can better constrain ocean oxygenation across Earth's major oxygenation events (the GOE and NOE) and also during the supposed "Boring Billion" (summarized also in Lyons et al. 2014). There are also many interesting events in the Phanerozoic linked to changes in ocean oxygenation that also merit immediate investigation with Tl isotopes, such as the "explosion" of life during the Cambrian (Marshall 2006) and its widespread demise during the end-Permian (Wignall and Twitchett 1996).

Finally, a topic that also merits future consideration is mineral-specific Tl and Mo isotope fractionation. It has been demonstrated in laboratory settings, but not yet confirmed in natural environments, that Tl isotope fractionation during adsorption to Mn oxides is

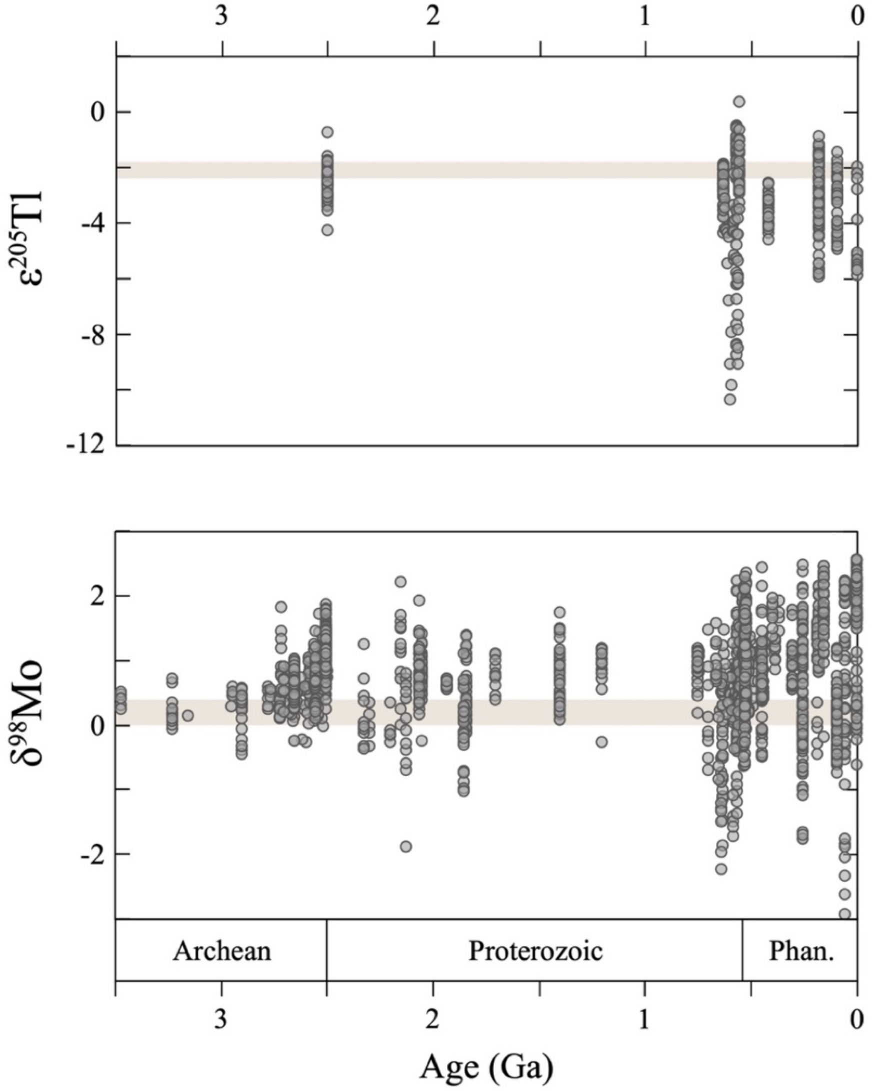

Fig. 7.1 Shale Tl and Mo isotope compilations. The shaded brown region in both plots signifies the range of values for bulk silicate Earth and upper continental crust (summarized in Nelson et al. 2017 and Kendall et al. 2017). Phan. = Phanerozoic. Data sources for Tl are Owens et al. (2017a), Ostrander et al. (2017, 2019, *in prep*), Them et al. (2018), Bowman et al. (2019), and Fan et al. (2020). Data sources for Mo are Arnold et al. (2004), Siebert et al. (2005), Wille et al. (2007, 2008, 2013), Lehmann et al. (2007), Pearce et al. (2008, 2010), Neubert et al. (2008), Gordon et al. (2009), Kendall et al. (2009, 2011, 2015), Dahl et al. (2010, 2011), Duan et al. (2010), Herrmann et al. (2012), Zhou et al. (2012), Dickson and Cohen (2012), Dickson et al. (2012), Xu et al. (2013), Proemse et al. (2013), Asael et al. (2013, 2018), Westermann et al. (2014), Partin et al. (2015), Eroglu et al. (2015), Noordmann et al. (2015), Cheng et al. (2016, 2017), Chen et al. (2015), Wen et al. (2015), Kurzweil et al. (2015a, 2015b), Lu et al. (2017), Scheller et al. (2018), Diamond et al. (2018), Ossa Ossa et al. (2018a, 2018b), Chen et al. (2019), Ostrander et al. (2019a, 2019b, 2020), and Gilleaudeau et al. (2020).

dependent on mineralogy. Specifically, large positive Tl isotope fractionation effects are only induced during adsorption of Tl to hexagonal birnessite (Nielsen et al. 2013). This is because the process thought to be responsible for this isotope fractionation effect – that is, oxidation of Tl^+ to Tl^{3+} – only occurs during adsorption of Tl at vacancies within hexagonal birnessite structure (Peacock and Moon 2012). In comparison, Tl^+ is not oxidized to Tl^{3+} during adsorption of Tl to triclinic birnessite and todorokite, and therefore no Tl isotope fractionation is predicted (Peacock and Moon 2012). Interestingly, todorokite-rich hydrothermal crusts appear to exhibit very little Tl isotope fractionation (Rehkämper et al. 2002) whereas similar samples are shown to impart a large fractionation effect on Mo isotopes (Goto et al. 2015). Thus, it seems possible that Tl and Mo isotopes could be used to not just identify Mn oxides, but more specifically differentiate between different Mn oxide minerals. One possible utility for this mineral-specific identification could be to constrain the primary minerals present during Mn ore formation—and by extension also their elusive formation mechanisms (summarized in Maynard 2010).

By addressing some or all of these outstanding questions, we can build a more reliable set of isotope paleoproxies. Addressing these questions would also expand the utility of the Mo and Tl isotope systems. As was made clear in this dissertation, these isotope systems are already fairly reliable, and they already possess strong utility. Nonetheless, there is always room for improvement.

REFERENCES

Adams, D.D., Hurtgen, M.T., Sageman, B.B. (2010) Volcanic triggering of a biogeochemical cascade during Oceanic Anoxic Event 2. *Nature Geoscience* 3, 201-204.

Alexandre, J.T., Tuenter, E., Henstra, G.A., van der Zwan, K.J., van de Wal, R.S.W., Dijkstra, H.A., de Boer, P.L. (2010) The mid-cretaceous North Atlantic nutrient trap: Black shales and OAEs. *Palaeoceanography* 25, PA4201.

Algeo, T.J., Lyons, T.W. (2006) Mo-total organic carbon covariation in modern anoxic marine environments: Implications for analysis of paleoredox and paleohydrographic conditions. *Paleoceanography* 21, PA1016.

Algeo, T.J., Tribovillard, N. (2009) Environmental analysis of paleoceanographic systems based on molybdenum-uranium covariation. *Chemical Geology* 268, 211–225.

Altermann, W., Nelson, D.R. (1998) Sedimentation rates, basin analysis and regional correlation of three Neoarchean and Paleoproterozoic sub-basins of the Kaapvaal craton as implied by precise SHRIMP U-Pb zircon ages from volcanic sediments. *Journal of Sedimentary Geology* 120, 225–256.

An, Z., Jiang, G., Tong, J., Tian, L., Ye, Q., Song, H., Song, H. (2015) Stratigraphic position of the Ediacaran Miaohe biota and its constrains on the age of the upper Doushantuo $\delta^{13}C$ anomaly in the Yangtze Gorges area, South China. *Precambrian Research* 271, 243–253.

Anbar, A.D., Holland, H.D. (1992) The photochemistry of manganese and the origin of banded iron formations. *Geochimica et Cosmochimica Acta* 56, 2595–2603.

Anbar, A.D., Duan, Y., Lyons, T.W., Arnold, G.L., Kendall, B., Creaser, R.A., Kaufman, A.J., Gordon, G.W., Scott, C., Garvin, J., Buick, R. (2007) A whiff of oxygen before the great oxidation event? *Science* 317, 1903–1906.

Andersen, M.B., Elliott, T., Freymuth, H., Sims, K.W.W., Niu, Y., Kelley, K.A. (2015) The terrestrial uranium isotope cycle. *Nature* 517, 356-359.

Archer, C., Vance, D. (2008) The isotopic signature of the global riverine molybdenum flux and anoxia in the ancient oceans. *Nature Geoscience* 1, 597–600.

Arndt, N.T., Nelson, D.R., Compston, W., Trendall, A.F., Thorne, A.M. (1991) The age of the Fortesque Group, Hamersley basin, Western Australia, from ion microprobe U-Pb zircon results. *Australian Journal of Earth Sciences* 38, 261–281.

Arnold, G.L., Anbar, A.D., Barling, J., Lyons, T.W. (2004) Molybdenum isotope evidence for widespread anoxia in Mid- Proterozoic oceans. *Science* 304, 87–90.

Arthur, M.A., Schlanger, S.O., Jenkyns, H.C. (1987) The Cenomanian/Turonian Oceanic Anoxic Event II: Paleaeoceanographic controls on organic matter production and preservation. *Geological Society, London, Special Publications* 26, 401-420.

Asael, D., Tissot, F.L.H., Reinhard, C.T., Rouxel, O., Dauphas, N., Lyons, T.W., Ponzevera, E., Liorzou, C., Chéron, S. (2013) Coupled molybdenum, iron and uranium stable isotopes as oceanic paleoredox proxies during the Paleoproterozoic Shunga Event. *Chemical Geology* 362, 193-210.

Asael, D., Rouxel, O., Poulton, S.W., Lyons, T.W., Bekker, A. (2018) Molybdenum record from black shales indicates oscillating atmospheric oxygen levels in the early Paleoproterozoic. *American Journal of Science* 318, 275-299.

Azrieli-Tal, I., Matthews, A., Bar-Matthews, M., Almogi-Labin, A., Vance, D., Archer, C., Teutsch, N. (2014) Evidence from molybdenum and iron isotopes and molybdenum-uranium covariation for sulphidic bottom waters during Eastern Mediterranean sapropel S1 formation. *Earth and Planetary Science Letters* 393, 231–242.

Baker, R.G.A., Rehkämper, M., Hinkley, T.K., Nielsen, S.G., Toutain, J.P. (2009) Investigation of thallium fluxes from subaerial volcanism—Implications for the present and past mass balance of thallium in the ocean. *Geochimica et Cosmochimica Acta* 73, 6340-6359.

Barling, J., Arnold, G.L., Anbar, A.D. (2001) Natural mass-dependent variations in the isotopic composition of molybdenum. *Earth and Planetary Science Letters* 193, 447–457.

Barling, J., Anbar, A.D. (2004) Molybdenum isotope fractionation during adsorption by manganese oxides. *Earth and Planetary Science Letters* 217, 315-329.

Bekker, A., Holland, H.D., Wang, P.-L., Rumble III, D., Stein, H.J., Hannah, J.L., Coetzee, L.L., Beukes, N.J. (2004) Dating the rise of atmospheric oxygen. *Nature* 427, 117–120.

Beukes, N.J. (1987) Facies relations, depositional environments and diagenesis in a major early Proterozoic stromatolitic carbonate platform to basinal sequence, Campbellrand Subgroup, Transvaal Supergroup, Southern Africa. *Sedimentary Geology* 54, 1–46.

Beukes, N.J., Gutzmer, J. (2008) Origin and paleoenvironmental significance of major iron formations at the Archean-Paleoproterozoic boundary. *Society of Economic Geologists Reviews* 15, 5–47.

Bond, D.P.G., Grasby, S.E. (2017) On the causes of mass extinctions. *Palaeogeography, Palaeoclimatology, Palaeoecology* 478, 3-29.

Bowman, C.N., Young, S.A., Kaljo, D., Eriksson, M.E., Them II, T.R., Hints, O., Martma, T., Owens, J.D. (2019) Linking the progressive expansion of reducing conditions to a stepwise mass extinction event in the late Silurian oceans. *Geology* 47, 968-972.

Breillat, N., Guerrot, C., Marcoux, E., Négrel, P. (2016) A new global database of δ^{98}Mo in molybdenites: a literature review and new data. *Journal of Geochemical Exploration* 161, 1-15.

Bristow, T.F., Kennedy, M.J., Derkowski, A., Droser, M.L., Jiang, G. Creaser, R.A. (2009) Mineralogical constraints on the paleoenvironments of the Ediacaran Doushantuo Formation. *Proceedings of the National Academy of Sciences USA* 106, 13190–13195.

Brocks, J.J., Buick, R., Logan, G.A., Summons, R.E. (2003) Composition and syngeneity of molecular fossils from the 2.78 to 2.45 billion-year-old Mount Bruce Supergroup, Pilbara Craton, Western Australia. *Geochimica et Cosmochimica Acta* 67, 4289–4319.

Brüske, A., Weyer, S., Zhao, M.-Y., Planavsky, N.J., Wegwerth, A., Neubert, N., Dellwig, O., Lau, K.V., Lyons, T.W. (2020) Correlated molybdenum and uranium isotope signatures in modern anoxic sediments: Implications for their use as paleo-redox proxy. *Geochimica et Cosmochimica Acta* 270, 449-474.

Bura-Nakić, E., Andersen, M.B., Archer, C., de Souza, G.F., Marguš, M., Vance, D. (2018) Coupled Mo-U abundances and isotopes in a small marine euxinic basin: constraints on processes in euxinic basins. *Geochimica et Cosmochimica Acta* 222, 212–229.

Burdige, D.J. (1993) The biogeochemistry of manganese and iron reduction in marine sediments. *Earth-Science Reviews* 35, 249–284.

Cabral, A.R., Creaser, R.A., Nägler, T., Lehmann, B., Voegelin, A.R., Belyatsky, B., Pašava, J., Seabra Gomes Jr., A.A., Galbiatti, H., Böttcher, M.E., Escher, P. (2013) Trace element and multi-isotope geochemistry of Late-Archean black shales in the Carajás iron-ore district, Brazil. *Chemical Geology* 362, 91–104.

Cairns-Smith, A.G. (1978) Precambrian solution photochemistry, inverse segregation, and banded iron formation. *Nature* 276, 807–808.

Calvert, S.E., Pedersen, T.F. (1996) Sedimentary geochemistry of manganese: Implications for the environment of formation of manganiferous black shales. *Economic Geology* 91, 36–47.

Canfield, D.E. (1994) Factors influencing organic carbon preservation in marine sediments. *Chemical Geology* 114, 315–329.

Canfield, D.E., Poulton, S.W., Narbonne, G.M. (2007) Late-Neoproterozoic deep-ocean oxygenation and the rise of animal life. *Science* 315, 92-95.

Canfield, D.E., Poulton, S.W., Knoll, A.H., Narbonne, G.M., Ross, G., Goldberg, T., Strauss, H. (2008) Ferruginous conditions dominated later Neoproterozoic deep-water chemistry. *Science* 321, 949-952.

Chen, J., Zhao, L., Algeo, T.J., Zhou, L., Zhang, L., Qiu, H. (2019) Evaluation of paleomarine redox conditions using Mo-isotope data in low-[Mo] sediments: A case study from the Lower Triassic of South China. *Palaeogeography, Palaeoclimatology, Palaeoecology* 519, 178-193.

Chen, J.H., Edwards, R.L., Wasserburg, G. J. (1986) 238-U, 234-U and 232-Th in seawater. *Earth and Planetary Science Letters* 80, 241–251.

Chen, X., Ling, H.-F., Vance, D., Shields-Zhou, G.A., Zhu, M., Poulton, S.W., Och, L.M., Jiang, S.-Y., Li, D., Cremonese, L., Archer, C. (2015) Rise to modern levels of ocean oxygenation coincided with the Cambrian radiation of animals. *Nature Communications* 6, 7142.

Chen, X., Romaniello, S.J., Herrmann, A.D., Hardisty, D., Gill, B.C., Anbar, A.D. (2018) Diagenetic effects on uranium isotope fractionation in carbonate sediments from the Bahamas. *Geochimica et Cosmochimica Acta* 237, 294–311.

Cheng, M., Li, C., Zhou, L., Algeo, T.J., Zhang, F., Romaniello, S., Jin, C., Lei, L., Feng, L., Jiang, S. (2016) Marine Mo biogeochemistry in the context of dynamically euxinic mid-depth waters: A case study of the lower Cambrian Niutitang shales, South China. *Geochimica et Cosmochimica Acta* 183, 79-93.

Cheng, M., Li, C., Zhou, L., Feng, L., Algeo, T.J., Zhang, F., Romaniello, S.J., Jin, C., Ling, H., Jiang, S. (2017) Transient deep-water oxygenation in the early Cambrian Nanhua Basin, South China. *Geochimica et Cosmochimica Acta* 210, 42-58.

Clarkson, M.O., Stirling, C.H., Jenkyns, H.C., Dickson, A.J., Porcelli, D., Moy, C.M., Pogge von Strandmann, P.A.E., Cooke, I.R., Lenton, T.M. (2018) Uranium isotope evidence for two episodes of deoxygenation during Oceanic Anoxic Event 2. *Proceedings of the National Academy of Sciences USA* 115, 2918–2923.

Collier, R.W. (1984) Particulate and dissolved vanadium in the North Pacific Ocean. *Nature* 309, 441–444.

Condon, D., Zhu, M., Bowring, S., Wang, W., Yang, A., Jin, Y. (2005) U-Pb ages from the Neoproterozoic Doushantuo Formation, China. *Science* 308, 95–98.

Crusius, J., Calvert, S., Pedersen, T., Sage, D. (1996) Rhenium and molybdenum enrichments in sediments as indicators of oxic, suboxic and sulfidic conditions of deposition. *Earth and Planetary Science Letters* 145, 65–78.

Czaja, A.D., Johnson, C.M., Roden, E.E., Beard, B.L., Voegelin, A.R., Nägler, T.F., Beukes, N.J., Wille, M. (2012) Evidence for free oxygen in the Neoarchean ocean based on coupled iron-molybdenum isotope fractionation. *Geochimica et Cosmochimica Acta* 86, 118-137.

Dahl, T.W., Hammarlund, E.U., Anbar, A.D., Bond, D.P.G., Gill, B.C., Gordon, G.W., Knoll, A.H., Nielsen, A.T., Schovsbo, N.H., Canfield, D.E. (2010) Devonian rise in atmospheric oxygen correlated to the radiations of terrestrial plants and large predatory fish. *Proceedings of the National Academy of Sciences USA* 107, 17911–17915.

Dahl, T.W., Canfield, D.E., Rosing, M.T., Frei, R.E., Gordon, G.W., Knoll, A.H., Anbar, A.D. (2011) Molybdenum evidence for expansive sulfidic water masses in ~750 Ma oceans. *Earth and Planetary Science Letters* 311, 264–274.

de Kock, M.O., Evans, D.A.D., Beukes, N.J. (2009) Validating the existence of Vaalbara in the Neoarchean. *Precambrian Research* 174, 145–154.

Derry, L.A. (2010) A burial diagenesis origin for the Ediacaran Shuram-Wonoka carbon isotope anomaly. *Earth and Planetary Science Letters* 294, 152-162.

Diamond, C.W., Planavsky, N.J., Wang, C., Lyons, T.W. (2018) What the ~1.4 Ga Xiamaling Formation can and cannot tell us about the mid-Proterozoic ocean. *Geobiolgy* 16, 219-236.

Dickson, A.J., Cohen, A.S. (2012) A molybdenum isotope record of Eocene Thermal Maximum 2: Implications for global ocean redox during the early Eocene. *Paleoceanography* 27, PA3230.

Dickson, A.J., Cohen, A.S., Coe, A.L. (2012) Seawater oxygenation during the Paleocene-Eocene Thermal Maximum. *Geology* 40, 639-642.

Dickson, A.J., Jenkyns, H.C., Porcelli, D., van den Boorn, S., Idiz, E. (2016) Basin-scale controls on the molybdenum-isotope composition of seawater during Oceanic Anoxic Event 2 (Late Cretaceous). *Geochimica et Cosmochimica Acta* 178, 291–306.

Dickson, A.J. (2017) A molybdenum-isotope perspective on Phanerozoic deoxygenation events. *Nature Geoscience* 10, 721–726.

Du Vivier, A.D.C., Selby, D., Sageman, B.B., Jarvis, I., Gröcke, D.R., Voigt, S. (2014) Marine ^{187}Os/^{188}Os isotope stratigraphy reveals interaction of volcanism and ocean circulation during Oceanic Anoxic Event 2. *Earth and Planetary Science Letters* 389, 23–33.

Du Vivier, A.D.C., Selby, D., Condon, D.J., Takashima, R., Nishi, H. (2015) Pacific ^{187}Os/^{188}Os isotope chemistry and U–Pb geochronology: Synchroneity of global Os isotope change across OAE 2. *Earth and Planetary Science Letters* 428, 204–216.

Duan, Y., Anbar, A.D., Arnold, G.L., Lyons, T.W., Gordon, G.W., Kendall, B. (2010) Molybdenum isotope evidence for mild environmental oxygenation before the Great Oxidation Event. *Geochimica et Cosmochimica Acta* 74, 6655–6668.

Eckert, S., Brumsack, H.J., Severmann, S., Schnetger, B., März, C., Fröllje, H. (2013) Establishment of euxinic conditions in the Holocene Black Sea. *Geology* 41, 431–434.

Eickmann, B., Hofmann, A., Wille, M., Bui, T.H., Wing, B.A., Schoenberg, R. (2018) Isotopic evidence for oxygenated Mesoarchaean shallow oceans. *Nature Geoscience* 11, 133-138.

Eigenbrode, J.L., Freeman, K.H. (2006) Late Archean rise of aerobic microbial ecosystems. *Proceedings of the National Academy of Sciences USA* 103, 15759–15764.

Eldrett, J.S., Ma, C., Bergman, S.C., Lutz, B., Gregory, F.J., Dodsworth, P., Phipps, M., Hardas, P., Minisini, D., Ozkan, A., Ramezani, J., Bowring, S.A., Kamo, S.L., Ferguson, K., Macaulay, C., Kelly, A.E. (2015) An astronomically calibrated stratigraphy of the Cenomanian-Turonian and earliest Coniacian from the Cretaceous Western Interior Seaway, USA: Implications for global chronostratigraphy. *Cretaceous Research* 56, 316–344.

Erbacher,J., Friedrich, O., Wilson, P.A., Birch, H., Mutterlose, J. (2005) Stable organic carbon isotope stratigraphy across Oceanic Anoxic Event 2 of Demerara Rise, western tropical Atlantic. *Geochemistry Geophysics Geosystems* 6, Q06010.

Erickson, B.E., Helz, G.R. (2000) Molybdenum(VI) speciation in sulfidic waters: stability and lability of thiomolybdates. *Geochimica et Cosmochimica Acta* 64, 1149–1158.

Eroglu, S., Schoenberg, R., Wille, M., Beukes, N., Taubald, H. (2015) Geochemical stratigraphy, sedimentology, and Mo isotope systematics of the ca. 2.58–2.50 Ga-old Transvaal Supergroup carbonate platform, South Africa. *Precambrian Research* 266, 27–46.

Fan, H., Nielsen, S.G., Owens, J.D., Auro, M., Shu, Y., Hardisty, D.S., Horner, T.J., Bowman, C.N., Young, S.A., Wen, H. (2020) Constraining oceanic oxygenation during the Shuram excursion in South China using thallium isotopes. *Geobiology*, 2020;00:1-17.

Farquhar, J., Bao, H., Thiemens, M. (2000) Atmospheric influence of Earth's earliest sulfur cycle. *Science* 289, 756–758.

Fike, D.A., Grotzinger, J.P., Pratt, L.M., Summons, R.E. (2006) Oxidation of the Ediacaran ocean. *Nature* 444, 744–747.

Fischer, A. (1965) Fossils, early life, and atmospheric history. *Proceedings of the National Academy of Sciences USA* 53, 1205-1215.

Force, E.R., Cannon, W.F. (1988) Depositional model for shallow-marine manganese deposits around black shale basins. Economic *Geology* 83, 93-117.

Frei, R., Gaucher, C., Stolper, D., Canfield, D.E. (2013) Fluctuations in late Neoproterozoic atmospheric oxidation – Cr isotope chemostratigraphy and iron speciation of the late Ediacaran lower Arroyo del Soldado Group (Uruguay). *Gondwana Research* 23, 797-811.

French, K.L., Hallmann, C., Hope, J.M., Schoon, P.L., Zumberge, J.A., Hoshino, Y., Peters, C.A., George, S.C., Love, G.D., Brocks, J.J., Buick, R., Summons, R.E. (2015) Reappraisal of hydrocarbon biomarkers in Archean rocks. *Proceedings of the National Academy of Sciences USA* 112, 5915–5920.

Froelich, P.N., Klinkhammer, G.P., Bender, M.L., Luedtke, N.A., Heath, G.R., Cullen, D., Dauphin, P., Hammond, D., Hartman, B., Maynard, V. (1979). Early oxidation of organic matter in pelagic sediments of the eastern equatorial Atlantic: suboxic diagenesis. *Geochimica et Cosmochimica Acta* 43, 1075–1090.

Garvin, J., Buick, R., Anbar, A.D., Arnold, G.L., Kaufman, A.J. (2009) Isotopic evidence for an aerobic nitrogen cycle in the latest Archean. *Science* 323, 1045–1048.

Gill, B.C., Lyons, T.W., Young, S.A., Kump, L.R., Knoll, A.H., Saltzman, M.R. (2011) Geochemical evidence for widespread euxinic in the Later Cambrian ocean. *Nature* 469, 80–83.

Gilleaudeau, G.J., Sahoo, S.K., Ostrander, C.M., Owens, J.D., Poulton, S.W., Lyons, T.W., Anbar, A.D. (2020) Molybdenum isotope and trace metal signals in an iron-rich Mesoproterozoic ocean: A snapshot from the Vindhyan Basin, India. *Precambrian Research* in press, 105718.

Godfrey, L.V., Falkowski, P.G. (2009) The cycling and redox state of nitrogen in the Archaean ocean. *Nature Geoscience* 2, 725–729.

Goldberg, T., Archer, C., Vance, D., Poulton, S.W. (2009) Mo isotope fractionation during adsorption to Fe (oxyhydr)oxides. *Geochimica et Cosmochimica Acta* 73, 6502–6516.

Goldberg, T., Archer, C., Vance, D., Thamdrup, B., McAnena, A., Poulton, S.W. (2012) Controls on Mo isotope fractionations in a Mn-rich anoxic marine sediment, Gullmar Fjord, Sweden. *Chemical Geology* 296–297, 73–82.

Goldberg, T., Gordon, G., Izon, G., Archer, C., Pearce, C.R., McManus, J., Anbar, A.D., Rehkämper, M. (2013) Resolution of inter-laboratory discrepancies in Mo isotope data: an intercalibration. *Journal of Analytical Atomic Spectrometry* 28, 724–735.

Gomez, M.L., Hurtgen, M.T. (2015) Sulfur isotope fractionation in modern euxinic systems: implications for paleoenvironmental reconstructions of paired sulfate-sulfide isotope records. *Geochimica et Cosmochimica Acta* 157, 39–55.

Gordon, G.W., Lyons, T.W., Arnold, G.L., Roe, J., Sageman, B.B., Anbar, A.D. (2009) When do black shales tell molybdenum isotope tales? *Geology* 37, 535-538.

Goto, K.T., Shimoda, G., Anbar, A.D., Gordon, G.W., Harigane, Y., Senda, R., Suzuki, K. (2015) Molybdenum isotopes in hydrothermal manganese crust from the Ryukyu arc system: Implications for the source of molybdenum. *Marine Geology* 369, 91-99.

Greaney, A.T., Rudnick, R.L., Gaschnig, R.M., Whalen, J.B., Luais, B., Clemens, J. D. (2018) Geochemistry of Molybdenum in the continental crust. *Geochimica et Cosmochimica Acta* 238, 36–54.

Greber, N.D., Pettke, T., Nägler, T.F. (2014) Magmatic-hydrothermal molybdenum isotope fractionation and its relevance to the igneous crustal signature. *Lithos* 190-191, 104–110.

Greber, N.D., Puchtel, I.S., Nägler, T.F., Mezger, K. (2015) Komatiites constrain molybdenum isotope composition of Earth's mantle. *Earth and Planetary Science Letters* 421, 129–138.

Gregory, D.D., Large, R.R., Halpin, J.A., Steadman, J.A., Hickman, A.H., Ireland, T.R., Holden, P. (2015) The chemical conditions of the late Archean Hamersley basin inferred from whole rock and pyrite geochemistry with $\Delta^{33}S$ and $\delta^{34}S$ isotope analyses. *Geochimica et Cosmochimica Acta* 149, 223–250.

Gregory, D.D., Lyons, T.W., Large, R.R., Jiang, G., Stepanov, A.S., Diamond, C.W., Figueroa, M.C., Olin, P. (2017) Whole rock and discrete pyrite geochemistry as complementary tracers of ancient ocean chemistry: an example from the Neoproterozoic Doushantuo Formation, China. *Geochimica et Cosmochimica Acta* 216, 201–220.

Grotzinger, J.P., Fike, D.A., Fischer, W.W. (2011) Enigmatic origin of the largest-known carbon isotope excursion in Earth's history. *Nature Geoscience* 4, 285-292.

Gumsley, A.P., Chamberlain, K.R., Bleeker, W., Söderlund, U., de Kock, M.O., Larsson, E.R., Bekker, A. (2017) Timing and tempo of the Great Oxidation Event. *Proceedings of the National Academy of Sciences USA* 114, 1811–1816.

Habicht, K.S., Gade, M., Thamdrup, B., Berg, P., Canfield, D.E. (2002) Calibration of sulfate levels in the Archean ocean. *Science* 298, 2372–2374.

Han, T., Fan, H. (2015) Dynamic evolution of the Ediacaran ocean across the Doushantuo Formation, South China. *Chemical Geology* 417, 261–272.

Hardisty, D.S., Riedinger, N., Planavsky, N.J., Asael, D., Andren, T., Jorgensen, B.B., Lyons, T.W. (2016) A Holocene history of dynamic water column redox conditions in the Landsort Deep, Baltic Sea. *American Journal of Science* 316, 713–745.

Hardisty, D.S., Lyons, T.W., Riedinger, N., Isson, T.T., Owens, J.D., Aller, R.C., Rye, D.M., Planavsky, N.J., Reinhard, C.T., Gill, B.C., Masterson, A.L., Asael, D., Johnston D. T. (2018) An evaluation of sedimentary molybdenum and iron as proxies for pore fluid paleoredox conditions. *American Journal of Science* 318, 527–556.

Hartnett, H.E., Keil, R.G., Hedges, J.I., Devol, A.H. (1998) Influence of oxygen exposure time on organic carbon preservation in continental margin sediments. *Nature* 391, 572–575.

Häusler, K., Dellwig, O., Schnetger, B., Feldens, P., Leipe, T., Moros, M., Pollehne, F., Schönke, M., Wegwerth, A., Arz, H.W. (2018) Massive Mn carbonate formation in the Landsort Deep (Baltic Sea): hydrographic conditions, temporal succession, and Mn budget calculations. *Marine Geology* 395, 260–270.

Hay, W.W., Sloan II, J.L., Wold, C.N. (1988) Mass age distribution and composition of sediments on the ocean floor and the global rate of sediment subduction. *Journal of Geophysical Research* 93, 14933–14940.

Hein, J., Koschinsky, A. (2014) Deep-ocean ferromanganese nodules and crusts. In Treatise on Geochemistry 2nd Edition (TGC2), New Volume on Geochemistry of Mineral Deposits, 2nd ed. (ed. S. Scott), pp. 273–291.

Heiser, U., Neumann, T., Scholten, J., Stüben, D. (2001) Recycling of manganese from anoxic sediments in stagnant basins by seawater inflow: a study of surface sediments from the Gotland Basin, Baltic Sea. *Marine Geology* 177, 151–166.

Helz, G.R., Miller, C.V., Charnock, J.M., Mosselmanns, J.F.W., Pattrick, R.A.D., Garner, C.D., Vaughan, D.J. (1996) Mechanism of molybdenum removal from the sea and its concentration in black shales: EXAFS evidence. *Geochimica et Cosmochimica Acta* 60, 3631–3642.

Helz, G.R., Bura-Nakić, E., Mikac, N., Ciglenečki, I. (2011) New model for molybdenum behavior in euxinic waters. *Chemical Geology* 284, 323-332.

Herrmann, A.D., Kendall, B., Algeo, T.J., Gordon, G.W., Wasylenki, L.E., Anbar, A.D. (2012) Anomalous molybdenum isotope trends in Upper Pennsylvanian euxinic facies: Significance for use of δ^{98}Mo as a global marine redox proxy. *Chemical Geology* 324-325, 87-98.

Hetzel, A., Böttcher, M.E., Wortmann, U.G., Brumsack, H.-J. (2009) Paleo-redox conditions during OAE 2 reflected in Demerara Rise sediment geochemistry (ODP Leg 207). *Palaeogeography Palaeoclimatology Palaeoecology* 273, 302–328.

Holland, H.D. (1984) The Chemical Evolution of the Atmosphere and Oceans (Princeton Univ. Press, Princeton).

Holly, J.J., Levin, L.A. (2004) Global distribution of naturally occurring marine hypoxia on continental margins. *Deep Sea Research Part I: Oceanographic Research Papers* 51, 1159–1168.

Huang, J., Chu, X., Lyons, T.W., Planavsky, N.J., Wen, H. (2013) A new look at saponite formation and its implications for early animal records in the Ediacaran of South China. *Geobiology* 11, 3–14.

Huckriede, H., Meischner, D. (1996) Origin and environment of manganese-rich sediments within black-shale basin. *Geochimica et Cosmochimica Acta* 60, 1399–1413.

Jenkyns, H.C. (2010) Geochemistry of oceanic anoxic events. *Geochemistry Geophysics Geosystems* 11, Q03004.

Jenkyns, H.C., Dickson, A.J., Ruhl, M., van den Boorn, S.H.J.M. (2017) Basalt-seawater interaction, the Plenus Cold Event, enhanced weathering and geochemical change: Deconstructing OAE 2 (Cenomanian-Turonian, Late Cretaceous). *Sedimentology* 64, 16–43.

Jiang, G., Kaufman, A.J., Christie-Blick, N., Zhang, S., Wu, H. (2007) Carbon isotope variability across the Ediacaran Yangtze platform in South China: implications for a large surface-to-deep ocean δ^{13}C gradient. *Earth and Planetary Science Letters* 261, 303–320.

Jiang, G., Shi, X., Zhang, S., Wang, Y., Xiao, S. (2011) Stratigraphy and paleogeography of the Ediacaran Doushantuo Formation (ca. 635–551 Ma) in South China. *Gondwana Research* 19, 831–849.

Jin, C., Li, C., Algeo, T.J., O'Connell, B., Cheng, M., Shi, W., Shen, J., Planavsky, N.J. (2018) Highly heterogeneous ''poikiloredox" conditions in the early Ediacaran Yangtze Sea. *Precambrian Research* 311, 157–166.

Johnson, J.E., Webb, S.M., Thomas, K., Ono, S., Kirschvink, J.L., Fischer, W.W. (2013) Manganese-oxidizing photosynthesis before the rise of cyanobacteria. *Proceedings of the National Academy of Sciences USA* 110, 11238–11243.

Johnston, D.T., Poulton, S.W., Tosca, N.J., O'Brien, T., Halverson, G.P., Schrag, D.P., Macdonald, F.A. (2013) Searching for an oxygenation event in the fossiliferous Ediacaran of northwestern Canada. *Chemical Geology* 362, 273–286.

Kasting, J.F. (1992) Models relating to Proterozoic atmospheric and ocean chemistry. In: Schopf, J., Klein, C. (Eds.), The Proterozoic Biosphere, a Multidisciplinary Study. Cambridge University Press, pp. 1185–1187.

Kaufman, A.J., Johnston, D.T., Farquhar, J., Masterson, A.L., Lyons, T.W., Bates, S., Anbar, A.D., Arnold, G.L., Garvin, J., Buick, R. (2007) Late Archean biospheric oxygenation and atmospheric evolution. *Science* 317, 1900–1903.

Keeling, R.F., Körtzinger, A., Gruber, N. (2010) Ocean deoxygenation in a warming world. *Annual Review of Marine Science* 2, 199-229.

Kendall, B., Creaser, R.A., Gordon, G.W., Anbar, A.D. (2009) Re-Os and Mo isotope systematics of black shales from the Middle Proterozioc Velkerri and Wollogorang formations, McArthur Basin, northern Australia. *Geochemica et Cosmochimica Acta* 73, 2534-2558.

Kendall, B., Reinhard, C.T., Lyons, T.W., Kaufman, A.J., Poulton, S.W., Anbar, A.D. (2010) Pervasive oxygenation along late Archaean ocean margins. *Nature Geoscience* 3, 647–652.

Kendall, B., Gordon, G.W., Poulton, S.W., Anbar, A.D. (2011) Molybdenum isotope constraints on the extent of late Paleoproterozoic ocean euxinia. *Earth and Planetary Science Letters* 307, 450–460.

Kendall, B., Brennecka, G.A., Weyer, S., Anbar, A.D. (2013) Uranium isotope fractionation suggests oxidative uranium mobilization at 2.50 Ga. *Chemical Geology* 362, 105–114.

Kendall, B., Creaser, R.A., Reinhard, C.T., Lyons, T.W., Anbar, A.D. (2015) Transient episodes of mild environmental oxygenation and oxidative continental weathering during the late Archean. *Science Advances* 1, e1500777.

Kendall, B., Komiya, T., Lyons, T.W., Bates, S.M., Gordon, G.W., Romaniello, S.J., Jiang, G., Creaser, R.A., Xiao, S., McFadden, K., Sawaki, Y., Tahata, M., Shu, D., Han, J., Li, Y., Chu, X., Anbar, A.D. (2015) Uranium and molybdenum isotope evidence for an episode of widespread ocean oxygenation during the late Ediacaran Period. *Geochimica et Cosmochimica Acta* 156, 173–193.

Kendall, B., Dahl, T.W., Anbar, A.D. (2017) Good golly, why Moly? The stable isotope geochemistry of molybdenum. *Reviews in Mineralogy and Geochemistry* 82, 682–732.

Kersten, M., Xiao, T., Kreissig, K., Brett, A., Coles, B.J., Rehkämper, M. (2014) Tracing anthropogenic thallium in soil using stable isotope compositions. *Environmental Science and Technology* 48, 9030–9036.

King, E.K., Pett-Ridge, J.C. (2018) Reassessing the dissolved molybdenum isotopic composition of ocean inputs: the effect of chemical weathering and groundwater. *Geology* 46, 955–958.

King, E.K., Perakis, S.S., Pett-Ridge, J.C. (2018) Molybdenum isotope fractionation during adsorption to organic matter. *Geochimica et Cosmochimica Acta* 222, 584–598.

Knauth, P., Kennedy, M.J. (2009) The late Precambrian greening of the Earth. *Nature* 460, 728-732.

Knoll, A.H. (2011) The multiple origins of complex multicellularity. *Annual Review of Earth and Planetary Sciences* 39, 217–239.

Koehler, M.C., Buick, R., Kipp, M.A., Stüeken, E.E., Zaloumis, J. (2018) Transient surface ocean oxygenation recorded in the ~2.66-Ga Jeerinah Formation, Australia. *Proceedings of the National Academy of Science USA* 115, 7711–7716.

Konhauser, K.O., Hamade, T., Raiswell, R., Morris, R.C., Ferris, F.G., Southam, G., Canfield, D.E. (2002) Could bacteria have formed Precambrian banded iron formations? *Geology* 30, 1079–1082.

Konhauser, K.O., Lalonde, S.V., Planavsky, N.J., Pecoits, E., Lyons, T.W., Mojzsis, S.J., Rouxel, O.J., Barley, M.E., Rosìere, C., Fralick, P.W., Kump, L.R., Bekker, A. (2011) Aerobic bacterial pyrite oxidation and acid rock drainage during the Great Oxidation Event. *Nature* 478, 369–373.

Konhauser, K.O., Planavsky, N.J., Hardisty, D.S., Robbins, L.J., Warchola, T.J., Haugaard, R., Lalonde, S.V., Partin, C.A., Oonk, P.B.H., Tsikos, H., Lyons, T.W., Bekker, A., Johnson, C.M. (2017) Iron formations: a global record of Neoarchaean to Palaeoproterozoic environmental history. *Earth-Science Reviews* 172, 140–177.

Krapež, B., Barley, M.E., Pickard, A.L. (2003) Hydrothermal and resedimented origins of the precursor sediments to banded iron formations: Sedimentological evidence from the early Palaeoproterozoic Brockman Supersequence of Western Australia. *Sedimentology* 50, 979−1011.

Kristensen, E., Kristiansen, K.D., Jensen, M.H. (2003) Temporal behavior of manganese and iron in a sandy coastal sediment exposed to water column anoxia. *Estuaries* 26, 690–699.

Kump, L.R., Arthur, M.A. (1999) Interpreting carbon-isotope excursions: Carbonates and organic matter. *Chemical Geology* 161, 181–198.

Kurzweil, F., Wille, M., Schoenberg, R., Taubald, H., Van Kranendonk, M.J. (2015a) Continuously increasing δ^{98}Mo values in Neoarchean black shales and iron formations from the Hamersley Basin. *Geochimica et Cosmochimica Acta* 164, 523–542.

Kurzweil, F., Drost, K., Pašava, J., Wille, M., Taubald, H., Schoeckle, D., Schoenberg, R. (2015b) Coupled sulfur, iron, and molybdenum isotope data from black shales of the Teplá-Barrandian unit argue against deep ocean oxygenation during the Ediacaran. *Geochimica et Cosmochimica Acta* 171, 121-142.

Lalonde, S.V., Konhauser, K.O. (2015) Benthic perspective on Earth's oldest evidence for oxygenic photosynthesis. *Proceedings of the National Academy of Science USA* 112, 995–1000.

Leckie, R.M., Bralower, T.J., Cashman, R. (2002) Oceanic anoxic events and plankton evolution: Biotic response to tectonic forcing during the mid-Cretaceous. *Palaeoceanography* 17, 13-1-13-29.

Lehmann, B., Nägler, T.F., Holland, H.D., Wille, M., Mao, J., Pan, J., Ma, D., Dulski, P. (2007) Highly metalliferous carbonaceous shale and Early Cambrian seawater. *Geology* 35, 403-406.

Lenton, T.M., Boyle, R.A., Poulton, S.W., Shields-Zhou, G.A., Butterfield, N.J. (2014) Co-evolution of eukaryotes and ocean oxygenation in the Neoproterozoic era. *Nature Geoscience* 7, 257.

Lenz, C., Jilbert, T., Conley, D.J., Wolthers, M., Slomp, C.P. (2015) Are recent changes in sediment manganese sequestration in the euxinic basins of the Baltic Sea linked to the expansion of hypoxia? *Biogeosciences* 12, 4875–4894.

Lewan, M.D., Maynard, J.B. (1982) Factors controlling enrichment of vanadium and nickel in the bitumen of organic sedimentary rocks. *Geochimica et Cosmochimica Acta* 46, 2547–2560.

Li, C., Love, G.D., Lyons, T.W., Fike, D.A., Sessions, A.L., Chu, D. (2010) A stratified redox model for the Ediacaran ocean. *Science* 328, 80-83.

Long, M.C., Deutsch, C., Ito, T. (2016) Finding forced trends in oceanic oxygen. Global Biogeochemical Cycles 30, 381–397.

Lowenstein, T.K., Kendall, B., Anbar, A.D. (2013) The geologic history of seawater. In Treatise on Geochemistry: Second Edition 8, 569–622. Elsevier Inc. https://doi.org/10.1016/B978- 0-08-095975-7.00621-5.

Lu, W., Ridgewell, A., Thomas, E., Hardisty, D.S., Luo, G., Algeo, T.J., Saltzman, M.R., Gill, B.C., Shen, Y., Ling, H., Edwards, C.T., Whalen, M.T., Zhou, X., Gutchess, K.M., Jin, L., Rickaby, R.E.M., Jenkyns, H.C., Lyons, T.W., Lenton, T.M., Kump, L.R., Lu, Z. (2018) Late inception of a resiliently oxygenated upper ocean. *Science* 361, 174-177.

Lu, X., Kendall, B., Stein, H.J., Li, C., Hannah, J.L., Gordon, G.W., Ebbestad, J.R. (2017) Marine redox conditions during deposition of Late Ordivician and Early Silurian organic-rich mudrocks in the Siljan ring district, central Sweden. *Chemical Geology* 457, 75-94.

Lue, Z., Jenkyns, H.C., Rickaby, R.E.M. (2010) Iodine to calcium ratios in marine carbonate as a paleo-redox proxy during oceanic anoxic events. *Geology* 38, 1107–1110.

Luo, G., Ono, S., Beukes, N.J., Wang, D.T., Xie, S., Summons, R.E. (2016) Rapid oxygenation of Earth's atmosphere 2.33 billion years ago. *Science Advances* 2, e1600134.

Lyons, T.W., Werne, J.P., Hollander, D.J., Murray, R.W. (2003) Contrasting sulfur geochemistry and Fe/Al and Mo/Al ratios across the last oxic-to-anoxic transition in the Cariaco Basin, Venezuela. *Chemical Geology* 195, 131–157.

Lyons, T.W., Reinhard, C.T., Planavsky, N.J. (2014) The rise of oxygen in Earth's early ocean and atmosphere. *Nature* 506, 307–315.

Macdonald, F.A., Strauss, J.V., Sperling, E.A., Halverson, G.P., Narbonne, G.M., Johnston, D.T., Kunzmann, M., Schrag, D.P., Higgins, J.A. (2013) The stratigraphic relationship between the Shuram carbon isotope excursion, the oxygenation of Neoproterozoic oceans, and the first appearance of the Ediacaran biota and bilaterian trace fossils in northwestern Canada. *Chemical Geology* 362, 250-272.

Madison, A.S., Tebo, B.M., Mucci, A., Sundby, B., Luther, G.W. III (2013) Abundant porewater Mn(III) is a major component of the sedimentary redox system. *Science* 341, 875–878.

Marshall, C.R. (2006) Explaining the Cambrian "explosion" of animals. *Annual Review of Earth and Planetary Sciences* 34, 355-384.

Maynard, J.B. (2010) The chemistry of manganese ores through time: a signal of increasing diversity of Earth-surface environments. *Economic Geology* 105, 535-552.

McCoy-West, A.J., Chowdhury, P., Burton, K.W., Sossi, P., Nowell, G.M., Fitton, J.G., Kerr, A.C., Cawood, P.A., Williams, H.M. (2019) Extensive crustal extraction in Earth's early history inferred from molybdenum isotopes. *Nature Geoscience* 12, 946–951.

McFadden, K.A., Huang, J., Chu, X., Jiang, G., Kaufman, A.J., Zhou, C., Yuan, X., Xiao, S. (2008) Pulsed oxidation and biological evolution in the Ediacaran Doushantuo Formation. *Proceedings of the National Academy of Sciences USA* 105, 3197–3202.

Menard, H.W., Smith, S.M. (1966) Hypsometry of ocean basin provinces. *Journal of Geophysical Research* 71, 4305–4325.

Meyer, K.M., Kump, L.R. (2008) Oceanic euxinia in earth history: Causes and consequences. *Annual Review of Earth and Planetary Sciences* 36, 251–288.

Meyers, S.R., Sageman, B.B., Arthur, M.A. (2012) Obliquity forcing of organic matter accumulation during Oceanic Anoxic Event 2. *Paleoceanography* 27, PA3212.

Miller, A.J., Strauss, J.V., Halverson, G.P., Macdonald, F.A., Johnston, D.T., Sperling, E.A. (2017) Tracking the onset of Phanerozoic-style redox-sensitive trace metal enrichments: new results from basal Ediacaran post-glacial strata in NW Canada. *Chemical Geology* 457, 24–37.

Miller, C.A., Peucker-Ehrenbrink, B., Walker, B.D., Marcantonio, F. (2011) Re-assessing the surface cycling of molybdenum and rhenium. *Geochimica et Cosmochimica Acta* 75, 7146–7179.

Milliman, J.D. (1993) Production and accumulation of calcium carbonate in the ocean: Budget of a nonsteady state. *Global Biogeochemical Cycles* 7, 927–957.

Miyano, T., Beukes, N.J. (1984) Phase relations of stilpnomelane, ferriannite, and riebekite in very low-grade metamorphosed iron formations. *Geological Society of South Africa Transactions* 87, 111–124.

Morford, J.L., Emerson, S. (1999) The geochemistry of redox sensitive trace metals in sediments. *Geochimica et Cosmochimica Acta* 63, 1735–1750.

Morford, J.L., Emerson, S.R., Breckel, E.J., Kim, S.H. (2005) Diagenesis of oxyanions (V, U, Re, and Mo) in pore waters and sediments from a continental margin. *Geochimica et Cosmochimica Acta* 69, 5021–5032.

Morford, J.L., Martin, W.R., Carney, C.M. (2012) Rhenium geochemical cycling: Insights from continental margins. *Chemical Geology* 324-325, 73-86.

Morris, A.W. (1975) Dissolved molybdenum and vanadium in the northeast Atlantic Ocean. *Deep-Sea Research* 22, 49–54.

Morris, R.C., Horwitz, R.C. (1983) The origin of the iron-formation-rich Hamersley group of Western Australia – deposition on a platform. *Precambrian Research* 21, 273–297.

Mort, H.P., Adatte, T., Föllmi, K.B., Keller, G., Steinmann, P., Matera, V., Berner, Z., Stüben, D. (2007) Phosphorus and the roles of productivity and nutrient recycling during oceanic anoxic event 2. *Geology* 35, 483–486.

Mottle, M.J. (2003) Partitioning of energy and mass fluxes between mid-ocean ridge axes and flanks at high and low temperature. *In* Halbach, P., et al., eds., Energy and mass transfer in marine hydrothermal systems: Berlin, Germany, Dahlem University Press, 271-286.

Nägler, T.F., Neubert, N., Böttcher, M.E., Dellwig, O., Schnetger, B. (2011) Molybdenum isotope fractionation in pelagic euxinia: evidence from the modern Black and Baltic Seas. *Chemical Geology* 289, 1–11.

Nägler, T.F., Anbar, A.D., Archer, C., Goldberg, T., Gordon, G.W., Greber, N.D., Siebert, C., Sohrin, Y., Vance, D. (2014) Proposal for an international molybdenum isotope measurement standard and data representation. *Geostandards and Geoanalytical Research* 38, 149–151.

Nameroff, T.J., Balistrieri, L.S., Murray, J.W. (2002) Suboxic trace metal geochemistry in the eastern tropical North Pacific. *Geochimica et Cosmochimica Acta* 66, 1139–1158.

Neely, R.A., Gislason, S.R., Ólafsson, M., McCoy-West, A.J., Pearce, C.R., Burton, KW. (2018) Molybdenum isotope behavior in groundwaters and terrestrial hydrothermal systems, Iceland. *Earth and Planetary Science Letters* 486, 108-118.

Nelson, D.R., Trendall, A.F., Alterman, W. (1999) Chronological correlation between the Pilbara and Kaapvaal cratons. *Precambrian Research* 97, 165–189.

Neubert, N., Nägler, T.F., Böttcher, M.E. (2008) Sulfidity controls molybdenum isotope fractionation into euxinic sediments: evidence from the modern Black Sea. *Geology* 36, 775–778.

Nielsen, S.G., Rehkämper, M., Baker, J.A., Halliday, A.N. (2004) The precise and accurate determination of thallium isotope compositions and concentrations for water samples by MC-ICPMS. *Chemical Geology* 204, 109–124.

Nielsen, S.G., Rehkämper, M., Porcelli, D., Andersson, P., Halliday, A.N., Swarzenski, P.W., Latkoczy, C., Günther, D. (2005) Thallium isotopic composition of the upper continental crust and rivers—an investigation of the continental sources of dissolved marine thallium. *Geochimica et Cosmochimica Acta* 19, 2007–2019.

Nielsen, S.G., Rehkämper, M., Teagle, D.A.H., Butterfield, D.A., Alt, J.C., Halliday, A.N. (2006) Hydrothermal fluid fluxes calculated from the isotopic mass balance of thallium in the ocean crust. *Earth and Planetary Science Letters* 251, 120–133.

Nielsen, S.G., Mar-Gerrison, S., Gannoun, A., LaRowe, D., Klemm, V., Halliday, A.N., Burton, K.W., Hein, J.R. (2009) Thallium isotope evidence for a permanent increase in marine organic carbon export in the early Eocene. *Earth and Planetary Science Letters* 278, 297–307.

Nielsen, S.G., Goff, M., Hesselbo, S.P., Jenkyns, H.C., LaRowe, D.E., Lee, C.T.A. (2011) Thallium isotopes in early diagenetic pyrite—A paleoredox proxy? *Geochimica et Cosmochimica Acta* 75, 6690–6704.

Nielsen, S.G., Rehkämper, M. (2011) Thallium isotopes and their application to problems in earth and environmental science, in Handbook of Environmental Isotope Geochemistry,M. Baskaran Ed. (Springer), 247–270.

Nielsen, S.G., Wasylenki, L.E., Rehkämper, M., Peacock, C.L., Xue, Z., Moon, E.M. (2013) Towards an understanding of thallium isotope fractionation during adsorption to manganese oxides. *Geochimica et Cosmochimica Acta* 117, 252–265.

Nielsen, S.G., Rehkämper, M., Prytulak, J. (2017) Investigation and application of thallium isotope fractionation. *Reviews in Mineralogy and Geochemistry* 82, 759–798.

Noordmann, J., Weyer, S., Montoya-Pino, C., Dellwig, O., Neubert, N., Eckert, S., Paetzel, M., Böttcher, M.E. (2015) Uranium and molybdenum isotope systematics in modern euxinic basins: case studies from the central Baltic Sea and the Kyllaren fjord (Norway). *Chemical Geology* 396, 182–195.

Och, L.M., Cremonese, L., Shields-Zhou, G.A., Poulton, S.W., Struck, U., Ling, H., Li, D., Chen, X., Manning, C.A., Thirlwall, M., Strauss, H., Zhu, M. (2016) Paleoceanographic controls on spatial redox distribution over the Yangtze Platform during the Ediacaran-Cambrian transition. *Sedimentology* 63, 378–410.

Olson, S.L., Kump, L.R., Kasting, J.F. (2013) Quantifying the areal extent and dissolved oxygen concentrations of Archean oxygen oases. *Chemical Geology* 362, 35–43.

Olson, S.L., Ostrander, C.M., Gregory, D.D., Roy, M., Anbar, A.D., Lyons, T.W. (2019) Volcanically modulated pyrite burial and ocean-atmosphere oxidation. *Earth and Planetary Sciences* 506, 417–427.

Olson, S.L., Jansen, M.F., Abbot, D.S. (2020) Oceanographic Constraints on Exoplanet Life. American Physical Society (arXiv: 1909.02928 [astro-ph.EP]).(Submitted for publication).

Ossa Ossa, F., Hofmann, A., Wille, M., Spangenberg, J.E., Bekker, A., Poulton, S.W., Eickmann, B., Schoenberg, R. (2018a) Aerobic iron and manganese cycling in a redox-stratified Mesoarchean epicontinental sea. *Earth and Planetary Science Letters* 500, 28-40.

Ossa Ossa, F., Eickmann, B., Hofmann, A., Planavsky, N.J., Asael, D., Pambo, F., Bekker, A. (2018b) Two-step deoxygenation at the end of the Paleoproterozoic Lomagundi Event. *Earth and Planetary Science Letters* 486, 70-83.

Ostrander, C.M., Owens, J.D., Nielsen, S.G. (2017) Constraining the rate of oceanic deoxygenation leading up to a Cretaceous oceanic anoxic event (OAE-2: ~94 Ma). *Science Advances* 3, e1701020.

Ostrander, C.M., Nielsen, S.G., Owens, J.D., Kendall, B., Gordon, G.W., Romaniello, S.J., Anbar, A.D. (2019a) Fully oxygenated water columns over continental shelves before the Great Oxidation Event. *Nature Geoscience* 12, 186–191.

Ostrander, C.M., Sahoo, S.K., Kendall, B., Jiang, G., Planavsky, N.J., Lyons, T.W., Nielsen, S.G., Owens, J.D., Gordon, G.W., Romaniello, S.J., Anbar, A.D. (2019b) Multiple negative molybdenum isotope excursions in the Doushantuo Formation (South China) fingerprint complex redox-related processes in the Ediacaran Nanhua Basin. *Geochimica et Cosmochimica Acta* 261, 191–209.

Ostrander, C.M., Kendall, B., Olson, S.L., Gordon, G.W., Romaniello, S.J., Lyons, T.W., Zheng, W., Roy, M., Reinhard, C.T., Anbar, A.D. (2020) An expanded shale δ^{98}Mo record permits recurrent shallow marine oxygenation during the Neoarchean. *Chemical Geology* 532, 119391.

Owens, J.D., Lyons, T.W., Li, X., Macleod, K.G., Gordon, G., Kuypers, M.M.M., Anbar, A.D., Kuhnt, W., Severmann, S. (2012) Iron isotope and trace metal records of iron cycling in the proto-North Atlantic during the Cenomanian-Turonian oceanic anoxic event (OAE-2). *Paleoceanography* 27, PA3223.

Owens, J.D., Gill, B.C., Jenkyns, H.C., Bates, S.M., Severmann, S., Kuypers, M.M.M., Woodfine, R.G., Lyons, T.W. (2013) Sulfur isotopes track the global extent and dynamics of euxinia during Cretaceous Oceanic Anoxic Event 2. *Proceedings of the National Academy of Sciences U.S.A*. 110, 18407–18412.

Owens, J.D., Reinhard, C.T., Rohrssen, M., Love, G.D., Lyons, T.W. (2016) Empirical links between trace metal cycling and marine microbial ecology during a large perturbation to Earth's carbon cycle. *Earth and Planetary Science Letters* 449, 407–417.

Owens, J.D., Nielsen, S.G., Horner, T.J., Ostrander, C.M., Peterson, L.C. (2017a) Thallium-isotopic compositions of euxinic sediments as a proxy for global manganese-oxide burial. *Geochimica et Cosmochimica Acta* 213, 291-307.

Owens, J.D., Lyons, T.W., Hardisty, D.W., Lowery, C.M., Lu, Z., Lee, B., Jenkyns, H.C. (2017b) Patterns of local and global redox variability during the Cenomanian-Turonian Boundary Event (Oceanic Anoxic Event 2) recorded in carbonates and shales from central Italy. *Sedimentology* 64, 168–185.

Owens, J.D., Lyons, T.W., Lowery, C.M. (2018) Quantifying the missing sink for global organic carbon burial during a Cretaceous oceanic anoxic event. *Earth and Planetary Science Letters* 499, 83–94.

Partin, C.A., Bekker, A., Planavsky, N.J., Scott, C.T., Gill, B.C., Li, C., Podkovyrov, V., Maslov, A., Konhauser, K.O., Lalonde, S.V., Love, G.D., Poulton, S.W., Lyons, T.W. (2013) Large- scale fluctuations in Precambrian atmospheric and oceanic oxygen levels from the record of U in shales. *Earth and Planetary Science Letters* 369–370, 284–293.

Partin, C.A., Bekker, A., Planavsky, N.J., Lyons, T.W. (2015) Euxinic conditions recorded in the ca. 1.93 Ga Bravo Lake Formation, Nunavut (Canada): Implications for oceanic redox evolution. *Chemical Geology* 417, 148-162.

Pavlov, A.A., Kasting, J.F. (2002) Mass-independent fractionation of sulfur isotopes in Archean sediments: strong evidence for an anoxic Archean atmosphere. *Astrobiology* 2, 27–41.

Peacock, C.L., Moon, E.M. (2012) Oxidative scavenging of thallium by birnessite: explanation for thallium enrichment and stable isotope fractionation in marine ferromanganese precipitates. *Geochimica et Cosmochimica Acta* 84, 297–313.

Pearce, C.R., Cohen, A.S., Coe, A.L., Burton, K.W. (2008) Molybdenum isotope evidence for global ocean anoxia coupled with perturbations to the carbon cycle during the Early Jurassic. *Geology* 36, 231-234.

Pearce, C.R., Coe, A.L., Cohen, A.S. (2010) Seawater redox variations during deposition of the Kimmeridge Clay Formation, United Kingdom (Upper Jurassic): Evidence from molybdenum isotopes and trace metal ratios. *Paleoceanography* 25, PA4213.

Philippot, P., Ávila, J.N., Killingsworth, B.A., Tessalina, S., Baton, F., Caquineau, T., Muller, E., Pecoits, E., Cartigny, P., Lalonde, S.V., Ireland, T., Thomazo, C., Kranendonk, M.J., Busigny, V. (2018) Globally asynchronous sulphur isotope signals require re-definition of the Great Oxidation Event. *Nature Communications* 9, 2245.

Planavsky, N.J., Asael, D., Hofmann, A., Reinhard, C.T., Lalonde, S.V., Knudsen, A., Wang, X., Ossa Ossa, F., Pecoits, E., Smith, A.J.B., Beukes, N.J., Bekker, A., Johnson, T.M., Konhauser, K.O., Lyons, T.W., Rouxel, O.J. (2014) Evidence for oxygenic photosynthesis half a billion years before the Great Oxidation Event. *Nature Geoscience* 7, 283-286.

Planavsky, N.J., Slack, J.F., Cannon, W.F., O'Connell, B., Isson, T.T., Asael, D., Jackson, J.C., Hardisty, D.S., Lyons, T.W., Bekker, A. (2018) Evidence for episodic oxygenation in a weakly redox-buffered deep mid-Proterozoic ocean. *Chemical Geology* 483, 581-594.

Poulson, R.L., Siebert, C., McManus, J., Berelson, W.M. (2006) Authigenic molybdenum isotope signatures in marine sediments. *Geology* 34, 617–620.

Poulson Brucker, R.L., McManus, J., Severmann, S., Berelson, W.M. (2009) Molybdenum behavior during early diagenesis: insights from Mo isotopes. *Geochemistry Geophysics Geosystems* 10, Q06010.

Poulton, S.W., Canfield, D.E. (2011) Ferruginous conditions: a dominant feature of the ocean through Earth's history. *Elements* 7, 107–112.

Proemse, B.C., Grasby, S.E., Wieser, M.E., Mayer, B., Beauchamp, B. (2013) Molybdenum isotopic evidence for oxic marine conditions during the latest Permian extinction. *Geology* 41, 967-970.

Raiswell, R., Hardisty, D.S., Lyons, T.W., Canfield, D.E., Owens, J.D., Planavsky, N.J., Poulton, S.W., Reinhard, C.T. (2018) The iron paleoredox proxies: a guide to pitfalls, problems and proper practice. *American Journal of Science* 318, 491–526.

Rehkämper, M., Halliday, A.N. (1999) The precise measurement of Tl isotopic compositions by MC-ICPMS: Applications to the analysis of geological materials and meteorites. *Geochimica et Cosmochimica Acta* 63, 935-944.

Rehkämper, M., Frank, M., Hein, J.R., Porcelli, D., Halliday, A.N., Ingri, J., Liebetrau, V. (2002) Thallium isotope variations in seawater and hydrogenetic, diagenetic, and hydrothermal ferromanganese deposits. *Earth and Planetary Science Letters* 197, 65–81.

Rehkämper, M., Frank, M., Hein, J.R., Halliday, A. (2004) Cenozoic marine geochemistry of thallium deduced from isotopic studies of ferromanganese crusts and pelagic sediments. *Earth and Planetary Science Letters* 219, 77-91.

Reinhard, C.T., Raiswell, R., Scott, C., Anbar, A.D., Lyons, T.W. (2009) A late Archean sulfidic sea stimulated by early oxidative weathering of the continents. *Science* 326, 713–716.

Reinhard, C.T., Planavsky, N.J., Robbins, L.J., Partin, C.A., Gill, B.C., Lalonde, S.V., Bekker, A., Konhauser, K.O., Lyons, T.W. (2013) Proterozoic ocean redox and biogeochemical stasis. *Proceedings of the National Academy of Sciences USA* 111, 5357–5362.

Reinhard, C.T., Planavsky, N.J., Olson, S.L., Lyons, T.W. (2016) Earth's oxygen cycle and the evolution of animal life. *Proceedings of the National Academy of Sciences USA* 113, 8933–8938.

Riding, R., Fralick, P., Liang, L. (2014) Identification of an Archean marine oxygen oasis. *Precambrian Research* 251, 232-237.

Romaniello, S.J., Herrmann, A.D., Anbar, A.D. (2013) Uranium concentrations and $^{238}U/^{235}U$ isotope ratios in modern carbonates from the Bahamas: assessing a novel paleoredox proxy. *Chemical Geology* 362, 305–316.

Rooney, A.D., Strauss, J.V., Brandon, A.D., Macdonald, F.A. (2015) A Cryogenian chronology: Two long-lasting synchronous Neoproterozoic glaciations. *Geology* 43, 459-462.

Rudnick, R.L., Gao, S. (2003) Composition of the continental crust. In The Crust, vol. 3 (ed. R. L. Rudnick). Elsevier, pp. 1– 64.

Rue, E.L., Smith, G.J., Cutter, G.A., Bruland, K.W. (1997) The response of trace element redox couples to suboxic conditions in the water column. *Deep-Sea Research Part I: Oceanographic Research Papers* 44, 113–134.

Sageman, B.B., Meyers, S.R., Arthur, M.A. (2006) Orbital time scale and new C-isotope record for Cenomanian-Turonian boundary stratotype. *Geology* 34, 125–128.

Sahoo, S.K., Planavsky, N.J., Kendall, B., Wang, X., Shi, X., Scott, C., Anbar, A.D., Lyons, T.W., Jiang, G. (2012) Ocean oxygenation in the wake of the Marinoan glaciation. *Nature* 489, 546–549.

Sahoo, S.K. (2015) Ediacaran ocean redox evolution. UNLV Theses. Dissertations, Professional Papers, and Capstones (Paper 2577).

Sahoo, S.K., Planavsky, N.J., Jiang, G., Kendall, B., Owens, J.D., Wang, X., Shi, X., Anbar, A.D., Lyons, T.W. (2016) Oceanic oxygenation events in the anoxic Ediacaran ocean. *Geobiology* 14, 457–468.

Satkoski, A.M., Beukes, N.J., Li, W., Beard, B.L., Johnson, C.M. (2015) A redox-stratified ocean 3.2 billion years ago. *Earth and Planetary Science Letters* 430, 43-53.

Scheller, E.L., Dickson, A.J., Canfield, D.E., Korte, C., Kristiansen, K.K., Dahl, T.W. (2018) Ocean redox conditions between the snowballs – Geochemical constraints from Arena Formation, East Greenland. *Precambrian Research* 319, 173-186.

Schlanger, S.O., Jenkyns, H.C. (1976) Cretaceous anoxic events: Causes and consequences. *Geologie en Mijnbow* 55, 179-184.

Schneider, A., Tanhua, T., Roether, W., Steinfeldt, R. (2014) Changes in ventilation of the Mediterranean Sea during the past 25 year. *Ocean Science* 10, 1–16.

Schmidtko, S., Stramma, L., Visbeck, M (2017) Decline in global oceanic oxygen content during the past five decades. *Nature* 542, 335–339.

Scholz, F., Hensen, C., Noffke, A., Rohde, A., Liebetrau, V., Wallmann, K. (2011) Early diagenesis of redox-sensitive trace metals in the Peru upwelling area – response to ENSO-related oxygen fluctuations in the water column. *Geochimica et Cosmochimica Acta* 75, 7257–7276.

Scholz, F., McManus, J., Sommer, S. (2013) The manganese and iron shuttle in a modern euxinic basin and implications for molybdenum cycling at euxinic ocean margins. *Chemical Geology* 355, 56–68.

Scholz, F., Siebert, C., Dale, A.W., Frank, M. (2017) Intense molybdenum accumulation in sediments underneath a nitrogenous water column and implications for the reconstruction of paleo-redox conditions based on molybdenum isotopes. *Geochimica et Cosmochimica Acta* 213, 400–417.

Scholz, F., Baum, M., Siebert, C., Eroglu, S., Dale, A.W., Naumann, M., Sommer, S. (2018) Sedimentary molybdenum cycling in the aftermath of seawater inflow to the intermittently euxinic Gotland Deep, Central Baltic Sea. *Chemical Geology* 491, 27–38.

Schrag, D.P., Higgins, J.A., Macdonald, F.A., Johnston, D.T. (2013) Authigenic carbonate and the history of the global carbon cycle. *Science* 339, 540-543.

Schröder, S., Lacassie, J.P., Beukes, N.J. (2006) Stratigraphic and geochemical framework of the Agouron drill cores, Transvaal Supergroup (Neoarchean-Paleoproterozoic, South Africa). *South Africa Journal of Geology* 109, 23–54.

Schwieterman, E.W., Kiang, N.Y., Parenteau, M.N., Harman, C.E., DasSarma, S., Fisher, T.M., Arney, G.N., Hartnett, H.E., Reinhard, C.T., Olson, S.L., Meadows, V.S., Cockell, C.S., Walker, S.I., Grenfell, J.L., Hege, S., Rugheimer, S., Hu, R., Lyons, T.W. (2018) Exoplanet biosignatures: A review of remotely detectable signs of life. *Astrobiology* 18, 663-708.

Scotese, C.R. (2008) Cretaceous Paleogeographic and Plate Tectonic Reconstructions, vol. 2 of The PALEOMAP Project PaleoAtlas for ArcGIS (PALEOMAP Project).

Scott, C., Lyons, T.W., Bekker, A., Shen, Y., Poulton, S.W., Chu, X., Anbar, A.D. (2008) Tracing the stepwise oxygenation of the Proterozoic ocean. *Nature* 452, 456–459.

Scott, C.T., Bekker, A., Reinhard, C.T., Schnetger, B., Krapež, B., Rumble III, D., Lyons, T.W. (2011) Late Archean euxinic conditions before the rise of atmospheric oxygen. *Geology* 39, 119–122.

Scott, C., Slack, J.F., Kelley, K.D. (2017) The hyper-enrichment of V and Zn in black shales of the Late Devonian- Early Mississippian Bakken Formation (USA). *Chemical Geology* 452, 24–33.

Sheen, A.I., Kendall, B., Reinhard, C.T., Creaser, R.A., Lyons, T.W., Bekker, A., Poulton, S.W., Anbar, A.D. (2018) A model for the oceanic mass balance of rhenium and implications for the extent of Proterozoic ocean anoxia. *Geochimica et Cosmochimica Acta* 227, 75–95.

Shipboard Scientific Party, Site 1258. *Proceedings of the Ocean Drilling Program: Initial Reports* 207, 1–117.

Siebert, C., Nägler, T.F., Kramers, J.D. (2001) Determination of the molybdenum isotope fractionation by double-spike multicollector inductively coupled plasma mass spectrometry. *Geochemistry Geophysics Geosystems* 2, 2000GC000124.

Siebert, C., McManus, J., Bice, A., Poulson, R., Berelson, W.M. (2006) Molybdenum isotope signatures in continental margin sediments. *Earth and Planetary Science Letters* 241, 723–733.

Siebert, C., Kramers, J.D., Meisel, T., Morel, P., Nägler, T.F. (2005) PGE, Re-Os, and Mo isotope systematics in Archean and early Proterozoic sedimentary systems as proxies for redox conditions of the early Earth. *Geochimica et Cosmochimica Acta* 69, 1787-1801.

Siebert, C., Pett-Ridge, J.C., Opfergelt, S., Guicharnaud, R.A., Halliday, A.N., Burton, K.W. (2015) Molybdenum isotope fractionation in soils: influence of redox conditions, organic matter, and atmospheric inputs. *Geochimica et Cosmochimica Acta* 162, 1–24.

Slotznick, S.P., Eiler, J.M., Fischer, W.W. (2018) The effects of metamorphism on iron mineralogy and the iron speciation proxy. *Geochimica et Cosmochimica Acta* 224, 96–115.

Sossi, P.A., Eggins, S.M., Nesbitt, R.W., Nebel, O., Hergt, J.M., Campbell, I.H., O'Neill, H.S.C., Van Kranendonk, M., Davies, D.R. (2016) Petrogenesis and geochemistry of Archean komatiites. *Journal of Petrology* 57, 147–184.

Sperling, E.A., Wolock, C.J., Morgan, A.S., Gill, B.C., Kunzmann, M., Halverson, G.P., Macdonald, F.A., Knoll, A.H., Johnston, D.T. (2015) Statistical analysis of iron geochemical data suggests limited late Proterozoic oxygenation. *Nature* 523, 451–454.

Sperling, E.A., Carbone, C., Strauss, J.V., Johnston, D.T., Narbonne, G.M., Macdonald, F.A. (2016) Oxygen, facies, and secular controls on the appearance of Cryogenian and Ediacaran body and trace fossils in the Mackenzie Mountains of northwestern Canada. *Geological Society of America Bulletin* 128, 558-575.

Stüeken, E.E., Buick, R., Anbar, A.D. (2015) Selenium isotopes support free O_2 in the latest Archean. *Geology* 43, 259–262.

Sumner, D.Y., Bowring, S.A. (1996) U-Pb geochronologic constraints on deposition of the Campbellrand Subgroup, Transvaal Supergroup, South Africa. *Precambrian Research* 79, 25–35.

Sumner, D.Y., Hawes, I., Mackey, T.J., Jungblut, A.D., Doran, P.T. (2015) Antarctic microbial mats: a modern analog for Archean lacustrine oxygen oases. *Geology* 43, 887–890.

Them, T.R., Gill, B.C., Caruthers, A.H., Gerhardt. A.M., Gröcke, D.R., Lyons, T.W., Marroquin, S.M., Nielsen, S.G., Trabucho Alexandre, J.P., Owens, J.D. (2018) Thallium isotopes reveal protracted anoxia during the Toarcian (Early Jurassic) associated with volcanism, carbon burial, and mass extinction. *Proceedings of the National Academy of Sciences USA* 115, 6596–6601.

Thoby, M., Konhauser, K.O., Fralick, P.W., Altermann, W., Visscher, P.T., Lalonde, S.V. (2019) Global importance of oxic molybdenum sinks prior to 2.6 Ga revealed by the Mo isotope composition of Precambrian carbonates. *Geology* 47, 559-562.

Tissot, F.L.H., Chen, C., Go, B.M., Naziemiec, M., Healy, G., Bekker, A., Swart, P.K., Dauphas, N. (2018) Controls of eustasy and diagenesis on the $^{238}U/^{235}U$ of carbonates and evolution of the seawater ($^{234}U/^{238}U$) during the last 1.4 Myr. *Geochimica et Cosmochimica Acta* 242, 233–265.

Tossell, J.A. (2005) Calculating the partitioning of the isotopes of Mo between oxidic and sulfidic species in aqueous solution. *Geochimica et Cosmochimica Acta* 69, 2981–2993.

Trendall, A.F., Nelson, D.R., De Laeter, J.R., Hassler, S.W. (1998) Precise zircon U-Pb ages from the Marra Mamba iron formation and Wittenoom Formation, Hamersley Group, Western Australia. *Australian Journal of Earth Sciences* 45, 137–142.

Trendall, A.F., Compston, W., Nelson, D.R., De Laeter, J.R., Bennett, V.C. (2004) SHRIMP zircon ages constraining the depositional chronology of the Hamersley Group, Western Australia. *Australian Journal of Earth Sciences* 51, 621–644.

Tribovillard, N., Algeo, T.J., Lyons, T.W., Riboulleau, A. (2006) Trace metals as paleoredox and paleoproductivity proxies: An update. *Chemical Geology* 232, 12–32.

Turgeon, S.C., Creaser, R.A. (2008) Cretaceous oceanic anoxic event 2 triggered by a massive magmatic episode. *Nature* 454, 323–326.

Voegelin, A.R., Nägler, T.F., Beukes, N.J., Lacassie, J.P. (2010) Molybdenum isotopes in late Archean carbonate rocks: implications for early Earth oxygenation. *Precambrian Research* 182, 70–82.

Voegelin, A.R., Pettke, T., Greber, N.D., von Niederhäusern, B., Nägler, T.F. (2014) Magma differentiation fractionates Mo isotope ratios: evidence from the Kos Plateau Tuff (Aegean Arc). *Lithos* 190–191, 440–448.

Volkov, I.I. (2000) Dissolved inorganic carbon and its isotopic composition in the waters of anoxic marine basin. *Oceanology* 40, 499–502.

Wang, L., Shi, X., Jiang, G. (2012) Pyrite morphology and redox fluctuations recorded in the Ediacaran Doushantuo Formation. *Palaeogeography, Palaeoclimatology, Palaeoecology* 333, 218–227.

Wang, X., Jiang, G., Shi, X., Xiao S. (2016) Paired carbonate and organic carbon isotope variations of the Ediacaran Doushantuo Formation from an upper slope section at Siduping, South China. *Precambrian Research* 273, 53–66.

Wasylenki, L.E., Rolfe, B.A., Weeks, C.L., Spiro, T.G., Anbar, A.D. (2008) Experimental investigation of the effects of temperature and ionic strength on Mo isotope fractionation during adsorption to manganese oxides. *Geochimica et Cosmochimica Acta* 72, 5997–6005.

Wasylenki, L.E., Weeks, C.L., Bargar, J.R., Spiro, T.G., Hein, J.R., Anbar, A.D. (2011) The molecular mechanism of Mo isotope fractionation during adsorption to birnessite. *Geochimica et Cosmochimica Acta* 75, 5019–5031.

Wedepohl, H. (1995) The composition of the continental crust. *Geochimica et Cosmochimica Acta* 59, 1217–1239.

Wen, H., Fan, H., Zhang, Y., Cloquet, C., Carignan, J. (2015) Reconstruction of early Cambrian ocean chemistry from Mo isotopes. *Geochimica et Cosmochimica Acta* 164, 1-16.

Westermann, S., Vance, D., Cameron, V., Archer, C., Robinson, S.A. (2014) Heterogeneous oxygenation states in the Atlantic and Tethys oceans during Oceanic Anoxic Event 2. *Earth and Planetary Science Letters* 404, 178-189.

Widdel, F., Schnell, S., Heising, S., Ehrenreich, A., Assmus, B., Schink, B. (1993) Ferrous iron oxidation by anoxygenic phototrophic bacteria. *Nature* 362, 834–836.

Wignall, P.B., Twitchett, R.J. (1996) Oceanic Anoxia and the End Permian Mass Extinction. *Science* 272, 1155-1158.

Willbold, M., Elliot, T. (2017) Molybdenum isotope variations in magmatic rocks. *Chemical Geology* 449, 253–268.

Wille, M., Kramers, J.D., Nägler, T.F., Beukes, N.J., Schröder, S., Meisel, T., Lacassie, J.P., Voegelin, A.R. (2007) Evidence for a gradual rise of oxygen between 2.6 and 2.5 Ga from Mo isotopes and Re-PGE signatures in shales. *Geochimica et Cosmochimica Acta* 71, 2417–2435.

Wille, M., Nägler, T.F., Lehmann, B., Schröder, S., Kramers, J.D. (2008) Hydrogen sulphide release to surface waters at the Precambrian/Cambrian boundary. *Nature* 453, 767-769.

Wille, M., Nebel, O., Van Kranendonk, M.J., Schoenberg, R., Kleinhanns, I.C., Ellwood, M.J. (2013) Mo-Cr isotope evidence fro a reducing Archean atmosphere in 3.46-2.76 Ga black shales from the Pilbara, Western Australia. *Chemical Geology* 340, 68-76.

Xiong, Y.L. (2007) Hydrothermal thallium mineralization up to 300 degrees C: A thermodynamic approach. *Ore Geology Reviews* 32, 291–313.

Xu, L., Lehmann, B., Mao, J. (2013) Seawater contribution to polymetallic Ni-Mo-PGE-Au mineralization in Early Cambrian black shales of South China: Evidence from Mo isotope, PGE, trace element, and REE geochemistry. *Ore Geology Reviews* 52, 66-84.

Zahnle, K., Claire, M., Catling, D. (2006) The loss of mass-independent fractionation in sulfur due to a Palaeoproterozoic collapse of atmospheric methane. *Geobiology* 4, 271–283.

Zerkle, A.L., Claire, M.W., Domagal-Goldman, S.D., Farquhar, J., Poulton, S.W. (2012) A bistable organic-rich atmosphere on the Neoarchaean Earth. *Nature Geoscience* 5, 359–363.

Zhang, F., Xiao, S., Romaniello, S.J., Hardisty, D., Li, C., Melezhik, V., Pokrovsky, B., Cheng, M., Shi, W., Lenton, T.M., Anbar, A.D. (2019) Global marine redox changes drove the rise and fall of the Ediacaran biota. *Geobiology* 17, 594-610.

Zheng, S., Wang, X., Wang, H., Bjerrum, C.J., Hammarlund, E.U., Mafalda Costa, M., Connelly, J.N., Zhang, B., Su, J., Canfield, D.E. (2016) Sufficient oxygen for animal respiration 1,400 million years ago. *Proceedings of the National Academy of Sciences USA* 113, 1731-1736.

Zhou, L., Wignall, P.B., Su, J., Su, J., Feng, Q., Xie, S., Zhao, L., Huang, J. (2012) U/Mo ratios and $\delta^{98/95}$Mo as local and global redox proxies during mass extinction events. *Chemical Geology* 324-325, 99-107.

APPENDIX A

SUPPLEMENTARY INFORMATION FOR CHAPTER 2

Table A.1 Supplementary Data

Drill core	Sample depth (m)	Formation	Al (wt%)	Mo (ppm)	Fe_{HR}/Fe_{T}	Fe_{PY}/Fe_{HR}	$\delta^{98}Mo$	2 SD
AIDP3	66.03	Jeerinah	8.24	2.85	0.36	0.56	0.48	0.10
AIDP3	67.17	Jeerinah	8.55	3.09	0.52	0.86	0.38	0.10
AIDP3	68.22	Jeerinah	8.40	4.12	0.60	0.94	1.02	0.10
AIDP3	68.59	Jeerinah	8.40	3.05	0.42	0.54		
AIDP3	68.92	Jeerinah	8.85	2.68	0.44	0.58	0.45	0.10
AIDP3	70.55	Jeerinah	7.38	2.06	0.62	0.74		
AIDP3	70.62	Jeerinah	7.89	2.09	0.58	0.72		
AIDP3	70.82	Jeerinah	8.26	2.03	0.51	0.73		
AIDP3	71.05	Jeerinah	8.40	2.64	0.39	0.86	0.58	0.10
AIDP3	71.12	Jeerinah	8.46	2.83	0.47	0.84		
AIDP3	71.22	Jeerinah	8.58	2.91	0.39	0.83		
AIDP3	71.44	Jeerinah	8.34	2.72	0.53	0.86		
AIDP3	71.93	Jeerinah	8.70	2.41	0.23	0.65		
AIDP3	72.44	Jeerinah	8.39	2.51	0.28	0.74	0.54	0.10
AIDP3	74.10	Jeerinah	6.94	2.41	0.21	0.36	-0.25	0.10
AIDP3	76.99	Jeerinah	7.02	1.76	0.28		0.25	0.10
AIDP3	77.52	Jeerinah	6.67	2.70	0.21	0.55		
AIDP3	78.56	Jeerinah	6.79	1.76	0.44	0.87	0.52	0.10
AIDP3	79.36	Jeerinah	8.22	2.45	0.64	0.99	0.59	0.10
AIDP3	79.78	Jeerinah	7.81	2.53	0.81	0.98		
AIDP3	80.78	Jeerinah	7.80	2.46	0.82	0.99		
AIDP3	82.19	Jeerinah	6.89	2.70	0.85	0.99		
AIDP3	83.23	Jeerinah	7.05	2.95	0.67	0.99	0.52	0.10
AIDP3	83.93	Jeerinah	7.08	2.68	0.82	1.00		
AIDP3	84.56	Jeerinah	6.19	2.61	0.78	0.99		
AIDP3	85.40	Jeerinah	6.89	2.63	0.82	0.98		
AIDP3	86.54	Jeerinah	6.86	2.77	0.72	0.99	0.44	0.10
AIDP3	87.70	Jeerinah	3.81	1.51				
AIDP3	88.22	Jeerinah	4.13	1.42	0.83	0.99		
AIDP3	88.78	Jeerinah	5.96	2.12	0.66	1.00		
AIDP3	89.93	Jeerinah	5.95	2.12	0.73	1.00	0.75	0.10
AIDP3	91.67	Jeerinah	6.11	2.00	0.84	0.97		

Drill core	Sample depth (m)	Formation	Al (wt%)	Mo (ppm)	Fe_{HR}/Fe_{T}	Fe_{PY}/Fe_{HR}	$\delta^{98}Mo$	2 SD
AIDP3	92.83	Jeerinah	5.71	2.49	0.79	0.97	0.50	0.12
AIDP3	93.88	Jeerinah	6.34	2.66	0.88	0.96		
AIDP3	95.49	Jeerinah	4.96	1.78	0.73	0.95		
AIDP3	95.92	Jeerinah	5.09	2.15	0.77	0.93		
AIDP3	97.13	Jeerinah	5.62	2.04	0.77	0.96	0.63	0.10
AIDP3	97.55	Jeerinah	4.92	4.87	0.60	0.93		
AIDP3	101.77	Jeerinah	7.07	1.62	0.62	0.92	0.25	0.10
AIDP3	104.50	Jeerinah	3.73	1.74	0.17	0.26		
AIDP3	104.92	Jeerinah	6.52	6.17	0.32	0.81	0.37	0.10
AIDP3	105.40	Jeerinah	3.95	1.71	0.26	0.40		
AIDP3	106.82	Jeerinah	9.89	4.83	0.18	0.35	0.56	0.12
AIDP3	107.18	Jeerinah	7.82	3.38	0.22	0.36		
AIDP3	108.39	Jeerinah	7.40	2.81	0.23	0.11		
AIDP3	109.06	Jeerinah	6.71	2.12	0.17	0.16		
AIDP3	109.90	Jeerinah	5.02	1.24	0.29	0.11	0.45	0.10
AIDP3	109.90	Jeerinah	5.45	1.38				
AIDP3	111.48	Jeerinah	4.34	1.34	0.24	0.07		
AIDP3	111.60	Jeerinah	4.99	1.38	0.25	0.06	0.41	0.10
AIDP3	114.59	Jeerinah	4.78	1.59	0.29	0.05		
AIDP3	115.35	Jeerinah	5.54	2.06	0.38	0.23	0.39	0.10
AIDP3	115.83	Jeerinah	5.99	1.93	0.26	0.20		
AIDP3	116.39	Jeerinah	6.14	1.64	0.28	0.14		
AIDP3	118.32	Jeerinah	7.23	2.58	0.23	0.28	0.44	0.10
AIDP3	119.05	Jeerinah						
AIDP3	120.40	Jeerinah	7.77	3.42	0.19	0.33	0.73	0.10
AIDP3	121.08	Jeerinah	8.20	3.59				
AIDP3	121.47	Jeerinah	7.98	3.55	0.22	0.15		
AIDP3	123.01	Jeerinah	6.87	2.80	0.23	0.29	0.47	0.10
AIDP3	123.22	Jeerinah	6.75	3.11	0.22	0.33		
AIDP3	124.52	Jeerinah	7.77	4.05	0.24	0.30		
AIDP3	125.54	Jeerinah						
AIDP3	125.80	Jeerinah	7.70	4.28	0.29	0.51	0.70	0.10
AIDP3	127.17	Jeerinah	7.50	4.53	0.45	0.19		
AIDP3	127.83	Jeerinah	8.04	3.99	0.26	0.15		
AIDP3	128.70	Jeerinah	7.33	4.20	0.30	0.23		

Drill core	Sample depth (m)	Formation	Al (wt%)	Mo (ppm)	Fe_{HR}/Fe_{T}	Fe_{PY}/Fe_{HR}	δ^{98}Mo	2 SD
AIDP3	129.65	Jeerinah	6.79	4.72	0.23	0.23		
AIDP3	130.17	Jeerinah	6.87	3.58	0.30	0.29	0.82	0.10
AIDP3	131.31	Jeerinah	8.18	4.49	0.29	0.28		
AIDP3	131.98	Jeerinah	8.48	3.82	0.34	0.56		
AIDP3	132.78	Jeerinah	7.38	6.09	0.40	0.55		
AIDP3	133.37	Jeerinah	7.96	4.25				
AIDP3	134.13	Jeerinah	8.46	5.44	0.26	0.26		
AIDP3	134.81	Jeerinah	8.37	6.84	0.24	0.21	0.44	0.10
AIDP3	135.86	Jeerinah	9.74	4.17				
AIDP3	137.53	Jeerinah	8.13	4.90	0.22	0.22		
AIDP3	138.53	Jeerinah	8.27	5.28	0.17	0.29	0.62	0.10
AIDP3	138.99	Jeerinah	8.36	4.74	0.19	0.26		
AIDP3	139.55	Jeerinah	8.30	5.20	0.21	0.30		
AIDP3	140.36	Jeerinah	8.25	5.64	0.24	0.38	0.75	0.10
AIDP3	141.28	Jeerinah	8.17	6.00	0.24	0.44		
AIDP3	141.75	Jeerinah	8.29	5.10	0.23	0.42		
AIDP3	142.04	Jeerinah	8.70	5.06	0.17	0.27		
AIDP3	142.11	Jeerinah	8.28	5.18	0.23	0.37	0.78	0.10
AIDP3	142.31	Jeerinah	8.31	4.89	0.22	0.34		
AIDP3	142.53	Jeerinah	8.08	4.74	0.22	0.43		
AIDP3	142.75	Jeerinah	8.34	4.92	0.23	0.39		
AIDP3	142.99	Jeerinah	8.27	5.24				
AIDP3	144.72	Jeerinah	7.94	4.64	0.22	0.41	0.66	0.10
AIDP3	145.77	Jeerinah	7.60	6.38	0.35	0.66		
AIDP3	146.29	Jeerinah	7.46	4.82	0.24	0.45	0.65	0.10
AIDP3	149.00	Jeerinah	7.62	3.70	0.33	0.62		
AIDP3	150.06	Jeerinah	7.97	4.10	0.13			
AIDP3	151.23	Jeerinah	7.89	4.09			0.58	0.10
AIDP3	151.96	Jeerinah	7.73	4.85				
AIDP3	152.84	Jeerinah	7.28	3.88	0.31	0.51		
AIDP3	153.81	Jeerinah	7.17	3.71	0.14			
AIDP3	154.46	Jeerinah	7.35	3.92				
AIDP3	154.90	Jeerinah	7.15	4.10	0.27	0.39		
AIDP3	155.75	Jeerinah	6.44	4.25	0.26			
AIDP3	156.84	Jeerinah	6.76	3.47				

Drill core	Sample depth (m)	Formation	Al (wt%)	Mo (ppm)	Fe_{HR}/ Fe_T	Fe_{PY}/Fe_{HR}	δ^{98}Mo	2 SD
AIDP3	158.26	Jeerinah	8.18	5.42	0.13			
AIDP3	159.56	Jeerinah	7.30	4.74	0.44	0.78		
AIDP3	160.33	Jeerinah	7.72	4.27				
AIDP3	160.88	Jeerinah	8.10	4.76	0.36	0.57		
AIDP3	161.62	Jeerinah	7.64	4.46				
AIDP3	164.12	Jeerinah	6.38	1.98	0.12		0.43	0.10
AIDP3	165.00	Jeerinah	6.09	3.23				
AIDP3	165.74	Jeerinah	6.71	1.87	0.17	0.43		
AIDP3	169.62	Jeerinah	7.73	1.30				
AIDP3	171.56	Jeerinah	9.01	1.61				
AIDP3	173.76	Jeerinah	9.39	1.45				
AIDP3	179.11	Jeerinah	8.93	1.98				
AIDP3	179.77	Jeerinah	8.46	1.85				
AIDP3	181.23	Jeerinah	8.21	1.19				
AIDP3	181.53	Jeerinah	8.59	1.80				
AIDP3	183.36	Jeerinah	7.91	1.16				
AIDP3	185.71	Jeerinah	8.66	1.24			0.37	0.10
AIDP3	189.55	Jeerinah	8.66	1.19				
AIDP3	193.27	Jeerinah	8.51	0.97				
AIDP3	194.39	Jeerinah	9.07	1.14				
AIDP3	198.32	Jeerinah	8.02	1.68				
AIDP3	200.58	Jeerinah	8.52	1.28				
AIDP3	204.37	Jeerinah	8.95	1.42			0.34	0.10
AIDP3	207.88	Jeerinah	9.57	1.13				
AIDP3	211.54	Jeerinah	9.28	1.07				
AIDP3	213.40	Jeerinah	9.24	1.52				
AIDP2	299.24	Jeerinah	6.88	1.40	0.24			
AIDP2	300.43	Jeerinah	6.06	1.35				
AIDP2	301.07	Jeerinah	7.00	1.75				
AIDP2	302.11	Jeerinah	7.05	2.42	0.17			
AIDP2	302.65	Jeerinah	8.07	3.90	0.13			
AIDP2	303.88	Jeerinah	7.55	2.74				
AIDP2	304.25	Jeerinah	6.50	1.56	0.41	0.44	0.42	0.10
AIDP2	305.05	Jeerinah	7.13	2.11				
AIDP2	306.05	Jeerinah	6.51	2.43				

Drill core	Sample depth (m)	Formation	Al (wt%)	Mo (ppm)	Fe_{HR}/Fe_T	Fe_{PY}/Fe_{HR}	$\delta^{98}Mo$	2 SD
AIDP2	307.17	Jeerinah	5.59	1.70				
AIDP2	307.64	Jeerinah	7.62	2.26				
AIDP2	309.12	Jeerinah	6.08	2.42	0.22	1.00		
AIDP2	309.80	Jeerinah	7.25	2.29				
AIDP2	310.51	Jeerinah	6.98	2.32	0.10			
AIDP2	311.15	Jeerinah	6.58	1.86			0.39	0.10
AIDP2	312.03	Jeerinah	5.45	1.92				
AIDP2	313.69	Jeerinah	6.21	1.45				
AIDP2	315.67	Jeerinah	5.35	1.42	0.16			
AIDP2	316.66	Jeerinah	1.78	0.17				
AIDP2	317.90	Jeerinah	7.78	2.02				
AIDP2	318.44	Jeerinah	4.69	1.00	0.55	0.76		
AIDP2	319.45	Jeerinah	5.16	1.20				
AIDP2	319.89	Jeerinah	3.90	1.80			0.37	0.10
AIDP2	321.01	Jeerinah	5.58	1.30	0.18			
AIDP2	322.31	Jeerinah	4.62	1.69			0.65	0.10
AIDP2	323.06	Jeerinah	5.26	1.33				
AIDP2	324.23	Jeerinah	7.03	2.41	0.56	0.86	0.43	0.10
AIDP2	324.85	Jeerinah	4.07	1.41				
AIDP2	325.73	Jeerinah	7.36	3.29	0.42	0.77	0.40	0.10
AIDP2	326.73	Jeerinah	3.67	1.73	0.22	1.00		
AIDP2	328.46	Jeerinah	4.54	1.11				
AIDP2	328.97	Jeerinah	4.80	2.16				
AIDP2	330.25	Jeerinah	5.25	1.27				
AIDP2	330.60	Jeerinah	5.93	1.78			0.62	0.10
AIDP2	330.90	Jeerinah	13.67	10.26				
AIDP2	332.00	Jeerinah	5.10	0.71				
AIDP2	332.52	Jeerinah	5.34	0.93				
AIDP2	333.57	Jeerinah	8.08	0.73	0.23	0.44		
AIDP2	334.13	Jeerinah	3.24	1.21			0.39	0.10
AIDP2	334.97	Jeerinah	2.07	0.41				
AIDP2	336.44	Jeerinah	7.55	0.87				
AIDP2	337.54	Jeerinah	4.46	1.19	0.21	0.59	0.58	0.10
AIDP2	338.39	Jeerinah	5.04	1.21				
AIDP2	338.85	Jeerinah	5.03	1.33				

Drill core	Sample depth (m)	Formation	Al (wt%)	Mo (ppm)	Fe_{HR}/Fe_T	Fe_{PY}/Fe_{HR}	$\delta^{98}Mo$	2 SD
AIDP2	340.03	Jeerinah	6.05	2.30				
AIDP2	341.74	Jeerinah	5.09	1.53				
AIDP2	342.74	Jeerinah	6.19	2.93	0.66	0.82		
AIDP2	343.20	Jeerinah	5.02	1.57			0.41	0.10
AIDP2	344.18	Jeerinah	6.80	2.63				
AIDP2	344.99	Jeerinah	7.91	3.01				
AIDP2	346.03	Jeerinah	6.34	3.04	0.74	0.84	0.84	0.10
AIDP2	346.03	Jeerinah	6.30	3.15				
AIDP2	346.03	Jeerinah	6.53	3.04				
AIDP2	347.00	Jeerinah	6.88	3.00	0.74	0.78		
AIDP2	347.83	Jeerinah	7.82	3.93				
AIDP2	348.55	Jeerinah	7.89	3.87				
AIDP2	349.31	Jeerinah	7.25	3.57	0.78	0.91	0.88	0.10
AIDP2	350.44	Jeerinah	6.97	2.90				
AIDP2	351.81	Jeerinah	7.71	6.55				
AIDP2	352.56	Jeerinah	7.44	5.62	0.61	0.98		
AIDP2	352.82	Jeerinah	8.12	5.11				
AIDP2	353.66	Jeerinah	7.97	4.41	0.61	0.90	0.92	0.10
AIDP2	354.66	Jeerinah	7.35	4.26	0.64	0.90		
AIDP2	355.54	Jeerinah	7.78	4.58			0.95	0.10
AIDP2	356.19	Jeerinah	8.00	4.69				
AIDP2	357.37	Jeerinah	8.03	6.90			0.98	0.10
AIDP2	358.09	Jeerinah	8.07	7.15	0.75	0.95	0.89	0.10
AIDP2	358.58	Jeerinah	7.69	5.84				
AIDP2	359.39	Jeerinah	7.67	7.15	0.64	0.95		
AIDP2	360.39	Jeerinah	8.03	6.83				
AIDP2	361.42	Jeerinah	7.96	5.73	0.79	0.95	0.97	0.10
AIDP2	362.08	Jeerinah	7.52	5.56	0.82	0.94		
AIDP2	363.04	Jeerinah	7.56	6.24				
AIDP2	364.26	Jeerinah	7.23	3.97	0.66	0.80	0.92	0.10
AIDP2	365.75	Jeerinah	7.57	4.42	0.27	1.00		
AIDP2	366.34	Jeerinah	7.36	3.68				
AIDP2	367.38	Jeerinah	7.77	3.39	0.34	0.76	0.86	0.10
AIDP2	368.14	Jeerinah	8.10	3.07				
AIDP2	369.05	Jeerinah	6.99	2.73			0.85	0.10

Drill core	Sample depth (m)	Formation	Al (wt%)	Mo (ppm)	Fe_{HR}/Fe_T	Fe_{PY}/Fe_{HR}	δ^{98}Mo	2 SD
AIDP2	369.72	Jeerinah	8.06	3.49	0.08			
AIDP2	370.34	Jeerinah	8.16	3.20				
AIDP2	370.69	Jeerinah	8.30	3.23				
AIDP2	370.98	Jeerinah	8.36	3.26				
AIDP2	371.07	Jeerinah	7.94	3.11				
AIDP2	371.54	Jeerinah	8.06	3.76	0.37	0.78		
AIDP2	371.80	Jeerinah	7.86	3.54				
AIDP2	372.86	Jeerinah	7.87	2.80				
AIDP2	374.04	Jeerinah	7.62	2.90				
AIDP2	374.67	Jeerinah	7.59	2.79	0.38	1.00	0.72	0.10
AIDP2	375.94	Jeerinah	8.51	3.16				
AIDP2	377.05	Jeerinah	8.41	3.04				
AIDP2	377.89	Jeerinah	7.98	3.10			0.69	0.10
AIDP2	380.37	Jeerinah	8.29	2.89	0.33	0.25	0.62	0.10
AIDP2	381.43	Jeerinah	8.36	2.82				
AIDP2	382.34	Jeerinah	7.47	2.61				
AIDP2	382.76	Jeerinah	8.38	2.07				
AIDP2	384.66	Jeerinah	3.86	1.75				
AIDP2	386.28	Jeerinah	5.64	1.64	0.37	0.06	0.47	0.10
AIDP2	386.82	Jeerinah	4.53	1.60				
AIDP2	388.52	Jeerinah	4.20	1.28				
AIDP2	389.03	Jeerinah	5.94	1.74				
AIDP2	390.56	Jeerinah	7.86	2.36				
AIDP2	392.33	Jeerinah	7.40	2.22	0.25	0.18		
AIDP2	392.79	Jeerinah	7.53	2.45			0.69	0.10
AIDP2	393.54	Jeerinah	7.40	2.31				
AIDP2	394.57	Jeerinah	6.41	2.04				
AIDP2	397.88	Jeerinah	6.19	2.19				
AIDP2	415.33	Jeerinah	8.19	3.07				
AIDP2	415.45	Jeerinah	7.92	3.19				
AIDP2	415.60	Jeerinah	8.05	3.30	0.21	0.10		
AIDP2	416.03	Jeerinah	7.80	3.17				
AIDP2	416.44	Jeerinah	7.82	2.35				
AIDP2	416.69	Jeerinah	8.15	2.56				
AIDP2	416.85	Jeerinah	8.17	2.66				

Drill core	Sample depth (m)	Formation	Al (wt%)	Mo (ppm)	Fe_{HR}/Fe_T	Fe_{PY}/Fe_{HR}	$\delta^{98}Mo$	2 SD
AIDP2	417.26	Jeerinah	8.05	3.08				
AIDP2	419.59	Jeerinah	5.93	2.58	0.25	0.16		
AIDP2	420.41	Jeerinah	7.41	4.00				
AIDP2	420.58	Jeerinah	8.14	3.52				
AIDP2	426.62	Jeerinah	8.28	3.52	0.22	0.15		
AIDP2	427.00	Jeerinah	8.38	3.09				
AIDP2	427.34	Jeerinah	8.56	3.47				
AIDP2	427.60	Jeerinah	7.90	3.42				
AIDP2	427.91	Jeerinah	8.31	3.14	0.24	0.11	0.66	0.10
AIDP2	428.06	Jeerinah	8.53	3.86				
AIDP2	428.16	Jeerinah	8.17	3.16	0.20			
AIDP2	430.10	Jeerinah	8.25	4.11				
AIDP2	430.19	Jeerinah	7.75	3.48				
AIDP2	430.38	Jeerinah	8.46	3.68				
ABDP9	193.39	Mt. Sylvia	5.35	2.71				
ABDP9	197.00	Mt. Sylvia	5.48	2.24	0.24	0.26	1.44	0.10
ABDP9	198.83	Mt. Sylvia	8.87	3.32				
ABDP9	199.26	Mt. Sylvia	5.77	2.02				
ABDP9	199.93	Mt. Sylvia	5.43	2.64	0.32	0.69		
ABDP9	201.68	Mt. Sylvia	5.51	4.19	0.26	0.79	0.76	0.10
ABDP9	203.98	Mt. Sylvia	5.36	2.39				
ABDP9	204.70	Mt. Sylvia	6.71	2.54	0.47	0.58	0.78	0.10
ABDP9	206.73	Mt. Sylvia	7.16	3.29	0.22	0.45		
ABDP9	207.93	Mt. Sylvia	6.51	2.53	0.19	0.62		
ABDP9	208.02	Mt. Sylvia	4.32	3.07				
ABDP9	209.67	Mt. Sylvia	6.38	3.46	0.42	0.80	0.96	0.16
ABDP9	218.91	Mt. Sylvia	6.75	4.40	0.41	0.48	1.20	0.10
ABDP9	220.55	Mt. Sylvia	5.34	2.15	0.34	0.38		
ABDP9	223.35	Mt. Sylvia	8.23	2.01				
ABDP9	223.93	Mt. Sylvia	8.89	1.81				
ABDP9	226.10	Mt. Sylvia	8.45	1.19			0.69	0.10
ABDP9	226.31	Mt. Sylvia	6.37	1.92	0.46	0.37		
ABDP9	227.43	Mt. Sylvia	6.06	1.55	0.28	0.28		
ABDP9	228.70	Mt. Sylvia	6.46	3.28	0.46	0.68	1.00	0.10
ABDP9	231.95	Wittenoom	5.26	1.81	0.50	0.41	0.75	0.14

Drill core	Sample depth (m)	Formation	Al (wt%)	Mo (ppm)	Fe_{HR}/Fe_{T}	Fe_{PY}/Fe_{HR}	$\delta^{98}Mo$	2 SD
ABDP9	234.37	Wittenoom	5.83	1.82	0.47	0.29		
ABDP9	235.71	Wittenoom	6.34	1.92	0.44	0.27	0.73	0.10
ABDP9	238.31	Wittenoom	6.64	2.75				
ABDP9	239.09	Wittenoom	7.50	2.53				
ABDP9	240.16	Wittenoom	5.73	1.78				
ABDP9	242.20	Wittenoom	7.11	2.17				
ABDP9	246.62	Wittenoom	6.36	2.37	0.23	0.48	0.76	0.10
ABDP9	247.06	Wittenoom	6.81	2.10	0.22	0.48		
ABDP9	247.35	Wittenoom	8.92	3.58				
ABDP9	249.45	Wittenoom	6.64	2.69				
ABDP9	251.93	Wittenoom	8.63	3.60	0.29	0.72		
ABDP9	253.17	Wittenoom	7.76	3.24	0.38	0.77	0.58	0.10
ABDP9	253.51	Wittenoom	7.26	2.93	0.35	0.73		
ABDP9	253.99	Wittenoom	8.41	2.61	0.31	0.63		
ABDP9	257.39	Wittenoom	7.14	2.54	0.22	0.46		
ABDP9	259.04	Wittenoom	8.51	3.85	0.17	0.35	0.86	0.10
ABDP9	263.38	Wittenoom	6.38	2.72	0.26	0.49		
ABDP9	264.29	Wittenoom	6.41	2.49	0.22	0.40		
ABDP9	266.85	Wittenoom	7.95	3.65	0.21	0.52	0.90	0.10
ABDP9	269.51	Wittenoom	5.52	4.00				
ABDP9	272.28	Wittenoom	7.40	3.35	0.21	0.42		
ABDP9	273.94	Wittenoom	8.21	3.64	0.20	0.55	0.74	0.10
ABDP9	275.15	Wittenoom	8.26	3.34	0.21	0.56		
ABDP9	275.90	Wittenoom	8.53	4.26	0.19	0.53		
ABDP9	280.50	Wittenoom	8.02	3.37	0.14	0.36	0.64	0.17
ABDP9	281.75	Wittenoom	7.99	3.84	0.18	0.31		
ABDP9	283.58	Wittenoom	6.62	3.71	0.17	0.28		
ABDP9	284.57	Wittenoom	8.09	5.20	0.14	0.24	1.03	0.10
ABDP9	287.48	Wittenoom	7.46	3.67	0.19	0.16		
ABDP9	290.52	Wittenoom	6.98	4.25	0.33	0.06		
ABDP9	291.68	Wittenoom	6.95	4.37				
ABDP9	292.74	Wittenoom	7.56	5.16	0.21	0.09	0.86	0.10
ABDP9	311.12	Wittenoom	8.76	4.08	0.13	0.31	0.69	0.10
ABDP9	311.88	Wittenoom	10.70	3.52				
ABDP9	313.24	Wittenoom	7.69	3.56	0.12	0.32	0.69	0.10

Drill core	Sample depth (m)	Formation	Al (wt%)	Mo (ppm)	Fe_{HR}/Fe_T	Fe_{PY}/Fe_{HR}	$\delta^{98}Mo$	2 SD
ABDP9	313.89	Wittenoom	8.27	3.61	0.14	0.43		
ABDP9	315.15	Wittenoom	8.14	4.06	0.16	0.57		
ABDP9	316.56	Wittenoom	8.39	4.31	0.12	0.45	0.81	0.10
ABDP9	317.53	Wittenoom	9.81	4.54				
ABDP9	318.51	Wittenoom	7.82	3.96	0.13	0.47		
ABDP9	320.93	Wittenoom	7.91	3.48				
ABDP9	322.91	Wittenoom	8.05	3.54	0.16	0.54	0.57	0.10
ABDP9	324.74	Wittenoom	7.71	3.25	0.18	0.42		
ABDP9	325.51	Wittenoom	8.93	3.69	0.15	0.28		
ABDP9	327.40	Wittenoom	6.79	3.28	0.24	0.27		
ABDP9	328.91	Wittenoom	8.26	3.57	0.20	0.46	0.61	0.10
ABDP9	335.43	Wittenoom	9.16	3.22				
ABDP9	336.33	Wittenoom	7.28	3.24	0.22	0.34	0.65	0.10
ABDP9	340.12	Wittenoom	8.19	3.93	0.15	0.46	0.67	0.10
ABDP9	341.24	Wittenoom	5.95	3.93				
ABDP9	343.08	Wittenoom	7.68	4.16	0.24	0.36		
ABDP9	344.32	Wittenoom	8.20	4.17	0.19	0.61	0.76	0.10
ABDP9	345.11	Wittenoom	10.82	5.05	0.09	0.50	0.70	0.10
ABDP9	348.42	Wittenoom	8.31	4.24	0.20	0.56		
ABDP9	350.15	Wittenoom	7.38	3.38	0.16	0.39	0.87	0.10
ABDP9	351.39	Wittenoom	8.77	4.46	0.16	0.61		
ABDP9	351.78	Wittenoom	5.97	3.76				
ABDP9	354.12	Wittenoom	7.19	3.74	0.18	0.29		
ABDP9	355.28	Wittenoom	11.11	4.59				
ABDP9	358.63	Wittenoom	7.30	3.52	0.22	0.33	0.67	0.11
ABDP9	361.29	Wittenoom	5.26	2.44				
ABDP9	364.21	Wittenoom	7.99	4.07				
ABDP9	366.50	Wittenoom	6.00	3.07				
ABDP9	371.95	Wittenoom	5.44	2.69				
ABDP9	375.02	Wittenoom	6.23	2.98				
ABDP9	379.40	Wittenoom	2.80	1.50				
ABDP9	382.52	Wittenoom	5.93	2.81				
GKP01	238.57	Klein Naute	5.60	3.44	0.39	0.04	0.82	0.10
GKP01	239.53	Klein Naute	7.21	5.14				
GKP01	240.20	Klein Naute			0.26	0.04		

Drill core	Sample depth (m)	Formation	Al (wt%)	Mo (ppm)	Fe_{HR}/Fe_T	Fe_{PY}/Fe_{HR}	$\delta^{98}Mo$	2 SD
GKP01	240.50	Klein Naute	7.32	5.89	0.36	0.02		
GKP01	241.27	Klein Naute	8.20	4.69				
GKP01	241.50	Klein Naute			0.24	0.36		
GKP01	242.60	Klein Naute			0.28	0.10		
GKP01	242.70	Klein Naute	8.24	6.83				
GKP01	243.55	Klein Naute	7.84	5.48				
GKP01	243.60	Klein Naute			0.27	0.12		
GKP01	244.45	Klein Naute	7.90	5.96	0.13	0.35	0.89	0.10
GKP01	244.98	Klein Naute			0.36	0.29		
GKP01	245.51	Klein Naute	7.38	5.21				
GKP01	245.60	Klein Naute			0.27	0.18		
GKP01	246.20	Klein Naute			0.28	0.26		
GKP01	246.45	Klein Naute	7.56	5.08	0.14	0.27	1.03	0.14
GKP01	248.00	Klein Naute			0.38	0.09		
GKP01	249.68	Klein Naute	5.04	6.43				
GKP01	249.80	Klein Naute			0.36	0.04		
GKP01	250.45	Klein Naute	1.54	1.54				
GKP01	253.35	Klein Naute	0.63	0.93				
GKP01	255.50	Klein Naute			0.70	0.00		
GKP01	257.90	Klein Naute			0.62	0.04		
GKP01	258.20	Klein Naute			0.29	0.03		
GKP01	260.00	Klein Naute			0.69	0.02		
GKP01	260.07	Klein Naute	4.16	2.88	0.42	0.03	0.89	0.10
GKP01	261.00	Klein Naute	2.74	1.80				
GKP01	261.95	Klein Naute	3.12	2.08				
GKP01	262.30	Klein Naute	2.74	1.68				
GKP01	263.85	Klein Naute	2.89	2.80				
GKP01	265.55	Klein Naute	3.12	1.57				
GKP01	266.40	Klein Naute	2.93	1.97	0.32	0.05	0.38	0.10
GKP01	267.40	Klein Naute	2.71	1.35				
GKP01	268.93	Klein Naute	3.66	1.75				
GKP01	269.25	Klein Naute	1.65	3.36	0.25	0.03		
GKP01	273.00	Klein Naute	3.05	1.39				
GKP01	273.95	Klein Naute	3.21	1.43				
GKP01	274.50	Klein Naute	3.37	1.51	0.27	0.05	0.57	0.10

Drill core	Sample depth (m)	Formation	Al (wt%)	Mo (ppm)	Fe_{HR}/ Fe_T	Fe_{PY}/Fe_{HR}	δ^{98}Mo	2 SD
GKP01	275.50	Klein Naute	3.81	2.61				
GKP01	276.10	Klein Naute	4.23	2.82				
GKP01	276.65	Klein Naute	3.47	2.26				
GKP01	277.15	Klein Naute	3.57	2.14				
GKP01	277.75	Klein Naute	2.97	6.98				
GKP01	278.60	Klein Naute	4.01	2.48	0.30	0.06	0.64	0.10
GKP01	279.35	Klein Naute	3.32	2.11				
GKP01	280.27	Klein Naute	1.90	2.32	0.44	0.06	1.17	0.13
GKP01	281.59	Klein Naute	4.02	1.41				
GKP01	283.65	Klein Naute	5.29	3.56				
GKP01	283.80	Klein Naute			0.42	0.01		
GKP01	284.25	Klein Naute	4.16	2.74				
GKP01	286.00	Klein Naute			0.42	0.01		
GKP01	286.65	Klein Naute	3.69	3.29				
GKP01	290.57	Klein Naute	2.36	1.64				
GKP01	291.20	Klein Naute			0.41	0.02		
GKP01	291.55	Klein Naute	3.53	2.42				
GKP01	292.47	Klein Naute	3.86	1.88				
GKP01	292.50	Klein Naute			0.56	0.05		
GKP01	293.38	Klein Naute	3.01	2.19				
GKP01	297.85	Klein Naute	6.55	5.78				
GKP01	299.40	Klein Naute	7.51	5.55	0.21	0.46	1.01	0.10
GKP01	300.42	Klein Naute	7.39	5.25				
GKP01	301.47	Klein Naute	8.14	5.05				
GKP01	302.50	Klein Naute	8.03	4.53	0.17	0.40	1.04	0.10
GKP01	303.50	Klein Naute	3.92	2.88				
GKP01	304.08	Klein Naute	7.48	3.92	0.23	0.30		
GKP01	305.34	Klein Naute	6.40	5.49	0.85	0.94	0.79	0.10
GKP01	306.28	Klein Naute	6.43	6.29	0.78	0.90	1.11	0.10
GKP01	307.62	Klein Naute	7.75	3.89	0.61	0.88		
GKP01	308.40	Klein Naute	4.50	1.66	0.43	0.18	0.94	0.10
GKP01	309.45	Klein Naute	6.95	5.64	0.65	0.84	1.14	0.15
GKP01	310.45	Klein Naute	4.62	4.78	0.81	0.84		
GKP01	311.48	Klein Naute	4.75	4.54	0.81	0.86	0.95	0.10
GKP01	312.73	Klein Naute	5.77	8.61	0.75	0.95	1.08	0.10

Drill core	Sample depth (m)	Formation	Al (wt%)	Mo (ppm)	Fe_{HR}/Fe_T	Fe_{PY}/Fe_{HR}	$\delta^{98}Mo$	2 SD
GKP01	314.10	Klein Naute	1.57	2.47	0.72	0.36		
GKP01	315.85	Klein Naute	6.58	6.81	0.61	0.76	1.27	0.10
GKP01	316.35	Klein Naute	6.83	5.10	0.74	0.72		
GKP01	317.55	Klein Naute	5.30	3.82	0.63	0.77	0.91	0.10
GKP01	318.72	Klein Naute	6.74	7.59	0.69	0.87	1.07	0.10
GKP01	319.75	Klein Naute	6.79	5.08	0.84	0.96	1.09	0.10
GKP01	320.00	Klein Naute			0.28	0.75		
GKP01	321.10	Klein Naute			0.92	0.81		
GKP01	321.65	Klein Naute	2.71	2.18				
GKP01	321.90	Klein Naute			0.63	0.72		
GKP01	322.23	Klein Naute	4.29	1.73				
GKP01	323.07	Klein Naute	0.75	1.19				
GKP01	324.36	Klein Naute	3.59	2.03				
GKP01	324.70	Klein Naute			0.82	0.44		
GKP01	325.40	Klein Naute	1.19	0.49				
GKP01	326.85	Klein Naute	1.18	0.43				
GKP01	328.30	Klein Naute			0.72	0.12		
GKP01	328.50	Klein Naute	1.79	0.69				
GKP01	330.00	Klein Naute	0.84	0.46				
GKP01	482.80	Nauga			0.32	0.18		
GKP01	483.60	Nauga	9.54	1.44				
GKP01	484.38	Nauga	9.50	0.49	0.29	0.27		
GKP01	484.92	Nauga	10.83	1.45				
GKP01	484.95	Nauga			0.33	0.16		
GKP01	486.07	Nauga	8.86	2.65	0.41	0.56		
GKP01	486.70	Nauga			0.53	0.08		
GKP01	486.76	Nauga	10.61	1.02				
GKP01	487.68	Nauga	10.98	0.88	0.25	0.15		
GKP01	490.00	Nauga			0.50	0.14		
GKP01	490.18	Nauga	9.92	1.10	0.38	0.15		
GKP01	490.70	Nauga			0.60	0.07		
GKP01	491.89	Nauga	9.99	0.98	0.34	0.12		
GKP01	491.95	Nauga			0.42	0.05		
GKP01	493.33	Nauga	7.90	0.90				
GKP01	494.51	Nauga	8.86	0.92	0.41	0.12		

Drill core	Sample depth (m)	Formation	Al (wt%)	Mo (ppm)	Fe_{HR}/Fe_T	Fe_{PY}/Fe_{HR}	$\delta^{98}Mo$	2 SD
GKP01	495.75	Nauga	13.09	1.38	0.44	0.50		
GKP01	637.10	Nauga			0.27	0.75		
GKP01	637.14	Nauga	9.09	1.07				
GKP01	637.72	Nauga	7.61	1.12	0.33	0.95		
GKP01	637.80	Nauga			0.16	0.84		
GKP01	638.15	Nauga	12.35	1.22				
GKP01	638.40	Nauga			0.34	0.94		
GKP01	638.56	Nauga	13.00	1.21	0.19	0.92	0.22	0.10
GKP01	639.20	Nauga			0.38	0.91		
GKP01	639.35	Nauga	12.12	1.51	0.13	0.91	0.32	0.10
GKP01	639.83	Nauga	10.79	0.94				
GKP01	640.00	Nauga			0.08	0.64		
GKP01	640.60	Nauga			0.12	0.75		
GKF01	234.20	Klein Naute	4.76	6.05				
GKF01	235.19	Klein Naute	3.99	4.84				
GKF01	235.50	Klein Naute			0.52	0.32		
GKF01	236.03	Klein Naute	3.34	4.31				
GKF01	240.00	Klein Naute			0.63	0.06		
GKF01	241.94	Klein Naute	4.56	13.30				
GKF01	263.74	Klein Naute	4.28	3.61	0.86	0.37	1.03	0.10
GKF01	264.43	Klein Naute	7.09	6.47	1.02	0.87		
GKF01	264.92	Klein Naute	9.59	5.52				
GKF01	265.67	Klein Naute	7.83	6.24	1.09	0.97	0.89	0.12
GKF01	266.60	Klein Naute	3.42	9.43	1.05	0.47	1.40	0.10
GKF01	267.46	Klein Naute	3.50	2.39	1.05	0.38	1.20	0.10
GKF01	267.93	Klein Naute	5.51	9.35				
GKF01	268.75	Klein Naute	6.38	8.60	1.09	0.95	1.11	0.10
GKF01	269.58	Klein Naute	5.20	11.73	1.08	0.90	1.17	0.10
GKF01	271.90	Klein Naute	3.31	18.89	1.10	0.95	1.39	0.10
GKF01	272.71	Klein Naute	5.63	21.85	1.05	0.92	1.43	0.10
GKF01	273.57	Klein Naute	7.19	16.35	0.96	0.91	1.50	0.10
GKF01	274.23	Klein Naute	5.73	19.02	1.09	0.84	1.54	0.11
GKF01	275.45	Klein Naute	4.23	7.12	1.01	0.63	1.41	0.10
GKF01	277.55	Klein Naute	3.85	4.42	0.97	0.43	1.38	0.10
GKF01	278.47	Klein Naute	1.58	4.84				

Drill core	Sample depth (m)	Formation	Al (wt%)	Mo (ppm)	Fe_{HR}/Fe_{T}	Fe_{PY}/Fe_{HR}	δ^{98}Mo	2 SD
GKF01	279.40	Klein Naute	1.35	1.28				
GKF01	280.02	Klein Naute	6.51	6.94	0.95	0.91	1.10	0.10
GKF01	280.20	Klein Naute			0.85	0.29		
GKF01	281.35	Klein Naute	3.55	2.30	1.01	0.50	1.17	0.10
GKF01	282.47	Klein Naute	0.62	0.58				
GKF01	283.50	Klein Naute	1.98	2.08				
GKF01	284.00	Klein Naute			0.64	0.90		
GKF01	284.68	Klein Naute	2.12	2.11				
GKF01	285.30	Klein Naute	1.15	1.35				
GKF01	286.10	Klein Naute			0.75	0.28		
GKF01	286.50	Klein Naute			0.97	0.37		
GKF01	286.81	Klein Naute	5.56	5.62				
GKF01	287.30	Klein Naute			0.75	0.22		
GKF01	287.90	Klein Naute			0.73	0.68		
GKF01	288.10	Klein Naute	8.81	15.22				
GKF01	289.05	Klein Naute	10.41	3.96				
GKF01	289.10	Klein Naute			0.92	0.43		
GKF01	290.00	Klein Naute			0.78	0.17		
GKF01	439.64	Nauga	7.82	1.58	0.41	0.51	0.38	0.10
GKF01	440.30	Nauga	10.45	2.12	0.26	0.68		
GKF01	441.67	Nauga	10.07	2.25	0.25	0.69	0.35	0.12
GKF01	442.49	Nauga	8.69	2.68	0.30	0.82	0.32	0.11
GKF01	443.51	Nauga	10.35	2.46				
GKF01	444.00	Nauga			0.23	0.47		
GKF01	444.70	Nauga	11.25	2.59				
GKF01	445.20	Nauga			0.34	0.66		
GKF01	445.88	Nauga	11.69	2.17	0.32	0.72	0.31	0.10
GKF01	446.10	Nauga			0.24	0.45		
GKF01	446.51	Nauga	11.38	2.37				
GKF01	447.19	Nauga	10.32	2.41	0.25	0.69	0.32	0.10
GKF01	447.50	Nauga			0.30	0.42		
GKF01	448.16	Nauga	9.48	2.34				
GKF01	448.50	Nauga			0.21	0.47		
GKF01	448.68	Nauga	8.99	2.44				
GKF01	449.13	Nauga	10.44	2.39	0.23	0.74	0.31	0.10

Drill core	Sample depth (m)	Formation	Al (wt%)	Mo (ppm)	Fe_{HR}/Fe_{T}	Fe_{PY}/Fe_{HR}	$\delta^{98}Mo$	2 SD
GKF01	450.40	Nauga	8.46	1.51				
GKF01	451.38	Nauga	10.29	1.54				
GKF01	452.15	Nauga	10.35	1.54	0.24	0.56	0.24	0.10
GKF01	452.90	Nauga	8.17	1.86				
GKF01	453.80	Nauga	10.01	1.50	0.34	0.59	0.24	0.10
GKF01	454.71	Nauga	9.61	1.45	0.30	0.75		
GKF01	616.11	Nauga	8.16	0.89				
GKF01	617.00	Nauga	9.77	1.16				
GKF01	618.00	Nauga	11.29	1.12				
GKF01	618.86	Nauga	10.58	0.90	0.15	0.20	0.27	
GKF01	619.81	Nauga	10.99	0.87				
GKF01	620.27	Nauga	11.49	0.82				
GKF01	620.88	Nauga	8.77	0.70	0.25	0.10		
GKF01	621.88	Nauga	11.14	0.69				
GKF01	623.07	Nauga	8.31	0.68				
GKF01	625.18	Nauga	9.98	0.86	0.24	0.16	0.09	0.10
GKF01	625.90	Nauga	10.20	0.78				
GKF01	626.54	Nauga	7.87	0.45	0.17	0.24		
GKF01	627.00	Nauga	7.54	1.14	0.25	0.23	0.24	0.10
GKF01	829.35	Nauga	8.27	0.20				
GKF01	830.46	Nauga	10.27	0.94	0.12	0.64	0.24	0.10
GKF01	830.80	Nauga			0.18	0.67		
GKF01	831.24	Nauga	9.15	1.30				
GKF01	831.58	Nauga	11.97	0.87				
GKF01	832.10	Nauga			0.19	0.66		
GKF01	832.36	Nauga	10.05	1.37				
GKF01	833.84	Nauga	10.56	0.79	0.16	0.87	0.27	0.10
GKF01	834.60	Nauga			0.18	0.65		
GKF01	835.10	Nauga	11.29	1.08				
GKF01	835.60	Nauga			0.29	0.72		
GKF01	836.30	Nauga	9.24	0.75				
GKF01	836.94	Nauga	8.90	1.07	0.20	0.87	0.19	0.11
GKF01	837.20	Nauga			0.15	0.54		
GKF01	837.70	Nauga	9.61	0.80				
GKF01	838.50	Nauga			0.52	0.47		

APPENDIX B

SUPPLEMENTARY INFORMATION FOR CHAPTER 3

Text B.1 Methods

Text B.1.1 Sample Digestion

Previously powdered samples were digested using a technique modified from previous literature (Nielsen et al. 2011). Samples were first treated with 2 M HNO_3 to separate authigenic and detrital components, and the supernatant was isolated from the silicate residue. This partial dissolution was immediately followed by 1.5 hours of digestion at ~300°C and 100 bars in a high-pressure asher to help dissolve organic compounds. Following dissolution of the silicate residue in 1:1 concentrated HNO_3 and HF, both fractions were completely dissolved in 1 M HCl in preparation for ion exchange chromatography.

Text B.1.2 Tl purification

Thallium was isolated from a sample matrix using previously described anion exchange chromatography techniques (Rehkämper and Halliday 1999; Nielsen et al. 2004). However, unlike previous studies, only one column was used during Tl purification. Testing of standards and samples showed that there was no difference in concentration or isotope composition between samples that had been processed through one or two columns (table B.2).

Text B.1.3 Sample analysis

The Tl isotope compositions were determined at the Woods Hole Oceanographic Institution (WHOI) Plasma Mass Spectrometry Facility using a Thermo Finnigan Neptune multiple collector inductively coupled plasma mass spectrometer. Isotopic compositions are reported relative to the National Institute of Standards and Technology (NIST) 997 Tl metal in epsilon notation:

$$\varepsilon^{205}\mathrm{Tl} = [(^{205/203}\mathrm{Tl}_{\mathrm{sample}})/(^{205/203}\mathrm{Tl}_{\mathrm{NIST\ 997}}) - 1] \times 10^{4}$$

Previously described techniques that used both external normalization to NIST SRM (Standard Reference Materials) 981 Pb and standard-sample bracketing were applied for mass bias correction (Rehkämper and Halliday 1999; Nielsen et al. 2004). Because of the quantitative yields of Tl from the column chemistry procedure, Tl concentrations were determined by monitoring the ^{205}Tl signal intensities of the samples during the isotopic measurements. A known quantity of NIST SRM 981 Pb was added to the sample Tl, and the measured $^{205\mathrm{Tl}/208}$Pb ratios were then converted directly into Tl abundances. The U.S. Geological Survey (USGS) shale standard SCO-1 was processed and analyzed, with each sample set to monitor long-term precision and accuracy of our Tl isotope data (average calculated ε^{205}Tl = −2.64 ± 0.24; table B.3), and was found to be better than most recent Tl isotope studies, which have 2SD uncertainties of ~0.3 to 0.5 ε^{205}Tl units (Kersten et al. 2014).

Text B.2 Demerara Rise, Site 1258

Cores from Site 1258 (holes 1258A, 1258B, and 1258C) were drilled during leg 207 of the Ocean Drilling Program (ODP) at Demerara Rise, off the coast of Suriname, South America (Shipboard Scientific Party 2004). Of the five Sites drilled at Demerara

Rise during ODP (1257-1261), 1258 was the deepest of the paleoceanographic transect (3192 m below sealevel). The composite section of nearly continuous and finely laminated, organic-rich sedimentary rocks across the Cenomanian-Turonian boundary are believed to have been deposited under ocean paleodepths > 1000m and the site is thought to have maintained uninterrupted connection to the proto-North Atlantic Ocean (Fig. B.1). As is typical of strata hosting OAE-2, the positive $\delta^{13}C$ excursion identifies the onset and termination of the event at this site (426 – 422 mcd (Erbacher et al. 2005)). Unique to site 1258, Fe speciation data supports the development of localized euxinia before, during, and after OAE-2 (Owens et al. 2016), which makes this site particularly appealing for global paleoredox reconstructions because local redox conditions do not change across the event.

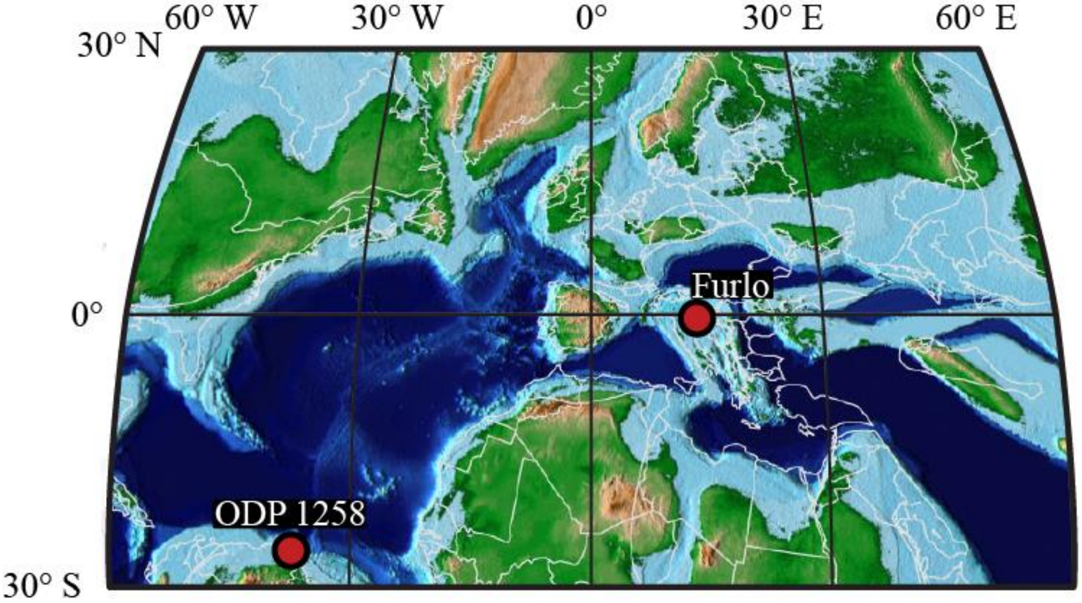

Fig. B.1 Paleogeographic locations of the sites analyzed in this study during the Cenomanian-Turonian boundary Anoxic Event (OAE-2: ~94 Ma). Areas in dark blue indicate deep-marine settings, areas in light blue indicate shallow-marine settings, and areas in green/brown represent continental land masses. Modified from previous work (Scotese 2008).

Site 1258 is believed to host a continuous record of marine sedimentation before and during OAE-2 (Shipboard Scientific Party 2004). However, based upon the abrupt decline of $\delta^{13}C$ values at Site 1258 relative to other Demerara Sites, a hiatus may exist between the uppermost depths hosting heavy C isotope values at the end of the event and the depths with isotopically lighter values immediately thereafter (i.e. ~422 mcd) (Erbacher et al. 2005). Because this study focuses primarily on what is occurring prior to OAE-2, where there is no clear evidence for a hiatus at Site 1258, our interpretations of pre-event conditions are unaffected. Similarly, because V concentrations and $\varepsilon^{205}Tl$ values do not change across this possible hiatus, our speculative interpretations of post-event conditions are also largely unaffected.

Text B.3 Furlo Site, Marche-Umbria, Italy

Low-resolution sedimentary Tl isotope values from the Furlo Site reported in this supplement are from outcrop samples used in a previous study (Owens et al. 2017b). Here, we analyzed shale samples before and during OAE-2 from this site, believed to have been deposited under pelagic conditions on the continental margin of the Tethyan Ocean across the Cenomanian-Turonian boundary (Fig. B.1). Organic-rich shale deposition at this site prior to the event is limited to extremely thin intervals within the carbonate that dominates the section. During OAE-2, however, deposition of organic-rich shale dominates. Unlike the Demerara Rise sediments, which likely were deposited beneath persistent euxinia across the Cenomanian-Turonian boundary (Owens et al. 2016), this Furlo section underwent a transition from reducing anoxic deposition prior to OAE-2 to euxinic deposition during the event (Owens et al. 2017b).

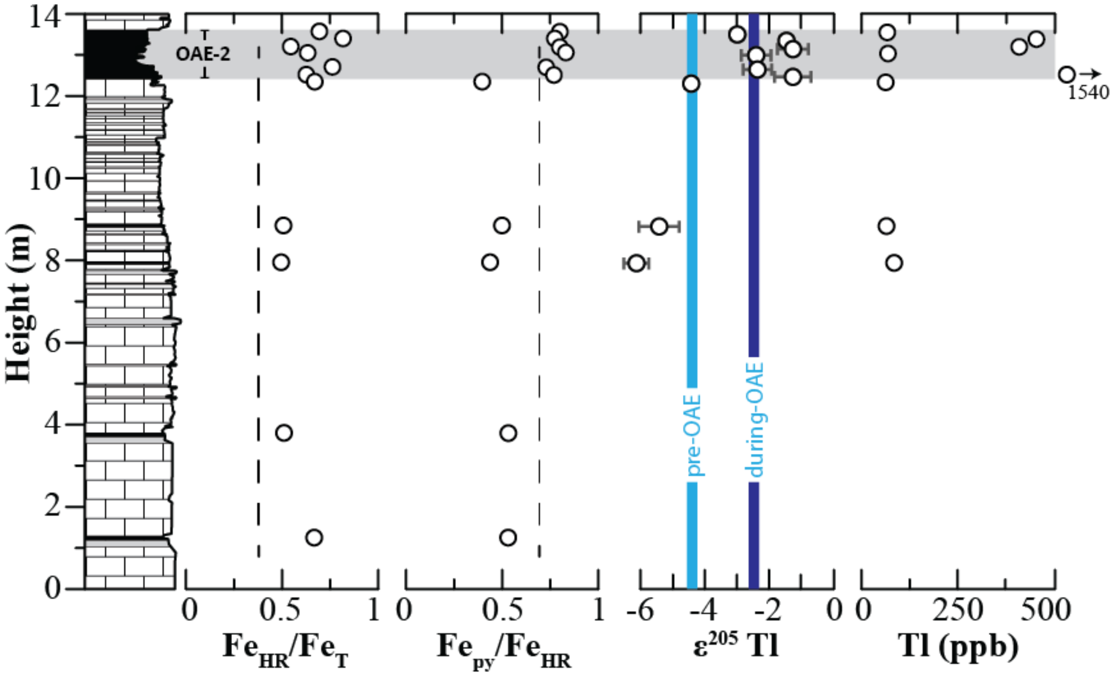

Fig. B.2 Geochemical data from interbedded shales of the Furlo section in Central Italy. The lighter-colored blue line signifies average Tl isotope compositions from Demerara Rise prior to enhanced organic carbon burial (ε^{205}Tl = ~ -4.3), while the darker- colored blue line represents those values during the event (ε^{205}Tl ~ -2.5). Importantly, samples from both Demerara Rise and this Furlo section exhibit a Tl isotope shift of similar magnitude across the Cenomanian-Turonian boundary event. Such behavior supports a global disturbance to the Tl isotope cycle during OAE-2. Due to pre-OAE lithological alterations at Furlo, the timing of the Tl isotope shift is not discernable. Uncertainties are in 2SD and represent the reproducibility of multiple sample analyses or the long-term reproducibility of SCO-1, whichever is greater.

Text B.5 Time lag between marine deoxygenation and C-isotope shift

The amount of time separating stages of marine deoxygenation and increased organic carbon burial is estimated using a linear sedimentation rate of 6.7 m/myr at Demerara Rise, which is calculated using a previously proposed duration for OAE-2 of 600 ky (Sageman et al. 2006; Meyers et al. 2012; Du Vivier et al. 2014; Du Vivier et al. 2015) and a 4 m interval of enhanced organic carbon burial at site 1258. The carbon isotope shift begins as early as 426.09, or as late as 426.04 meters MCD (Erbacher et al. 2005). Thus, we compare the Tl isotope shift (interpreted here to represent the onset of deep marine deoxygenation), which begins as early as 426.40 or as late as 426.30 meters (table B.1), to both depths that may represent the onset of increased carbon burial to get a maximum and minimum amount of time separating the two. This yields a timeframe of 54 – 32 ky, here reported as an average of 43 with a range of ± 11 ky. When the drawdown in [V] begins at site 1258 is more ambiguous, however. V concentrations are relatively stable between 426.69 and 426.5 meters, ranging from ~2000-1850 ppm, before a slight decrease to ~1700 ppm through 426.43 m, a decrease to ~1300-1000 ppm through 426.32 m, and a decrease to ~800-600 ppm through 426.23m (Hetzel et al. 2009; Owens et al. 2016). Between 426.23 m and the onset of the C-isotope excursion, V concentrations never again eclipse 600 ppm. For this study, we use a depth range of 426.5 to 426.42 m to loosely estimate the onset of V concentration drawdown because it encompasses the end of pronounced pre-OAE-2 enrichment ([V] ≥ 1900 ppm) and the onset of much lower values ([V] ≤ 1300 ppm). This yields an estimate of 69 – 50 ky, here reported as 59 ± 10 ky. Importantly, this range slightly precedes that deduced from the Tl isotope shift.

If there is indeed a hiatus at Site 1258, as previously suggested (Erbacher et al. 2005), then our estimated sedimentation rate is too slow and our calculated timing of pre-event redox changes are, as a result, placed too far before OAE-2. Furthermore, if the duration of OAE-2 was actually shorter than the 600 ky assumed here, then our estimated sedimentation rate is too slow and our calculated timing of pre-event redox changes are, again, placed too far before OAE-2. If we have underestimated the duration of OAE-2, this would have the opposite effect (i.e. our redox changes are placed too close to the onset of the event).

Text B.6 Magnitude of Mn oxide drawdown

We use a previously proposed simple isotope mass-balance model to estimate the decrease in Mn oxide burial associated with the observed Tl isotope shift (Nielsen et al. 2009):

$$\varepsilon_{SW} = \varepsilon_{IN} - \Delta_{MnOx} + (\Delta_{MnOx} - \Delta_{AOC})((F_{MnOx}/F_{AOC}) + 1) \qquad (1)$$

where ε_{SW} and ε_{IN} are the Tl isotope compositions of seawater and total input, Δ_{MnOx} and Δ_{AOC} are the isotopic differences between seawater and Mn oxides and seawater and altered oceanic crust (AOC), respectively, and F_{MnOx} and F_{AOC} are the relative fluxes of seawater Tl removal via Mn oxides and altered oceanic crust, respectively. The Tl isotope composition of marine inputs is effectively constant (Nielsen et al. 2011) and the same is likely the case for the two Tl isotope fractionation factors between seawater, Mn oxides and AOC (Nielsen et al. 2009). The relative removal rate of Tl from seawater by Mn oxides and AOC, and how this changes, ultimately governs the Tl isotope composition of seawater. However, F_{AOC} depends directly on the long-term (multi-million year) average ocean crust production rate, which can be assumed effectively constant over time scales shorter than one million years, like OAE-2. Hence, over the time scale of OAE-2, the Tl isotope composition of seawater depends almost exclusively on the rate of Tl burial associated with Mn oxides (Nielsen et al. 2009).

Various ranges of fractionation factors have been proposed between seawater and Mn oxides and seawater and altered oceanic crust (Nielsen et al. 2009). Of these, the fractionation factor between seawater and Mn oxides is the more well-constrained value (Nielsen et al. 2013). Using the most recent published steady-state flux conditions (Nielsen et al. 2017) and the most robust value of this fractionation factor (Δ_{MnOx} = 19 epsilon units observed between modern ferromanganese crusts and seawater), a Δ_{AOC} value of ~ -2.5 epsilon units is necessary to achieve steady-state for the modern ocean. It has been suggested that Δ_{MnOx} might be smaller, due to unknown effects that modify the Tl isotope fractionation factor for Mn oxides in pelagic clays (Nielsen et al. 2017). However, given that AOC is lighter than seawater (Nielsen et al. 2006) Δ_{AOC} cannot take a value higher than zero, a scenario that would occur only if effectively all the Tl in seawater that circulates through the oceanic crust was removed into low-temperature hydrothermal alteration phases. Assuming this most extreme endmember value for Tl isotope fractionation during ocean crust alteration, we obtain Δ_{MnOx} ~13.5 epsilon units. Overall, these considerations provide an updated range of fractionation factor pairs that can be used in equation (1) to calculate the possible change in Mn oxide drawdown prior to OAE-2. The updated calculations yield a range of Mn oxide burial that decreased somewhere between 40% (Δ_{MnOx} = 19, Δ_{AOC} = -2.5) and 80% (Δ_{MnOx} = 13.5, Δ_{AOC} = 0) that can account for a shift in the Tl isotope composition of seawater from ε^{205}Tl = -4.5 to -2.5 (Fig. 3.2).

It should be noted that the fractionation factors Δ_{MnOx} = 13.5, Δ_{AOC} = 0 represent a theoretical lower bound for the Tl isotope fractionation factors and most available data would suggest that the higher values (Δ_{MnOx} = 19, Δ_{AOC} = -2.5) are more likely. Hence, the decrease in Mn oxide burial of 40% appears the most consistent with current knowledge on Tl isotope fractionation in the marine environment. In addition, it should also be noted that basinal restriction before and during OAE-2 at ODP Site 1258 could contribute to the Tl isotope increase as observed for the modern Black Sea (Owens et al. 2017a). If basinal restriction contributed to the shift in Tl isotopes then the required changes in global Mn oxide burial prior to OAE-2 would be smaller than 40 – 80%. However, basinal restriction appears to have had a very minor effect of Tl isotopes at ODP Site 1258 for two reasons: 1) Tl concentrations are very high throughout the period surrounding OAE-2, which suggests that Tl was not significantly drawn down from seawater at this site (as opposed to the modern Black Sea (Owens et al. 2017a)) and 2) The Tl isotope compositions found in the Furlo section (Fig. B.2) reveal values before and during OAE-2 that are identical to ODP Site 1258, which strongly implies that both sites were sufficiently well connected with the open ocean to record global seawater Tl isotopes.

Text B.7 Rate of deoxygenation

Using our range of values for Mn oxide drawdown and estimates for the modern area of pelagic sedimentation (3.0×10^8 km^2 (Hay et al. 1988; Milliman 1993)) – where Mn oxide precipitation primarily occurs – gives an area of seafloor affected by deoxygenation of $1.2 – 2.4 \times 10^8$ km^2. This is likely a conservative estimate given high sea levels associated with the Cenomanian- Turonian boundary (Jenkyns 2010). When we combine the deoxygenated seafloor area with the time between initial bottom water deoxygenation and the onset of the carbon isotope excursion (i.e. 32 to 54 ky, reported as 43 ± 11 ky), we obtain a rate of seafloor deoxygenation of ~$2.2 – 7.5 \times 10^3$ km^2/yr.

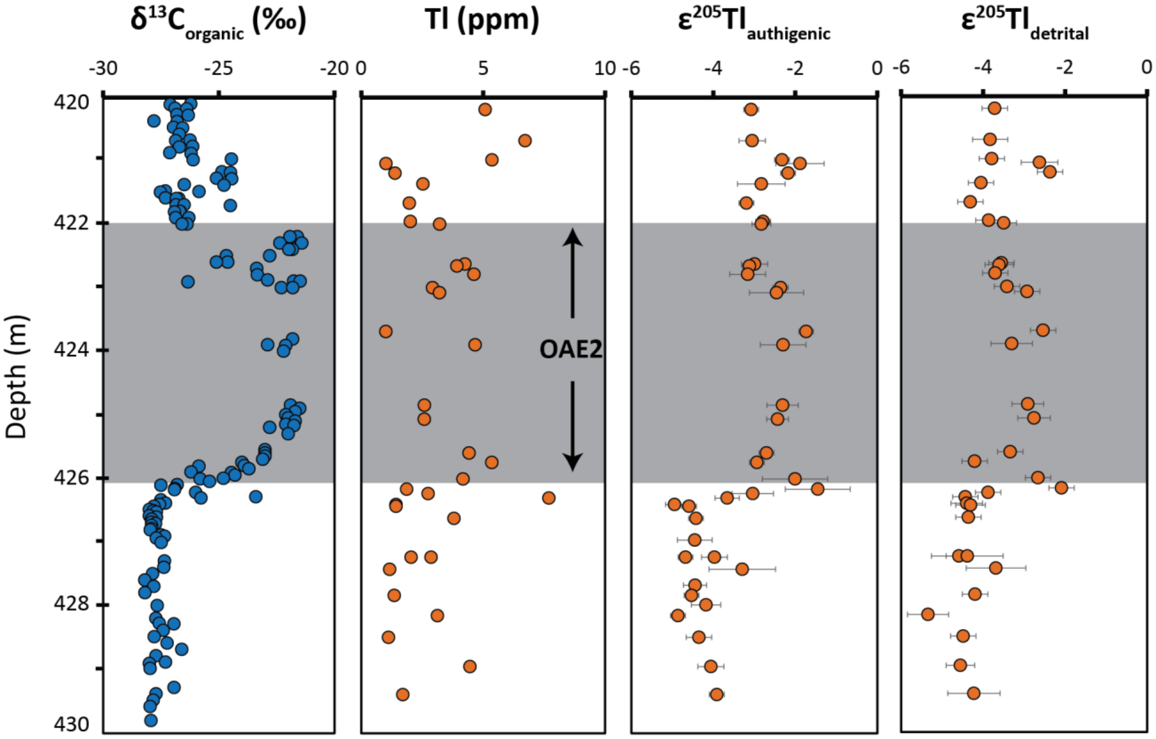

Fig. B.3 Tl isotope composition of the authigenic fraction alongside that of the detrital fraction to show similarity. In theory, the silicate fraction should have a ε^{205}Tl value similar to that of bulk continental crust (ε^{205}Tl ~-2). This appears not to be the case, however, as our measured silicate ε^{205}Tl values in several cases are lighter than the leached values. This offset between the leachate and residue either suggests that the silicate is lighter than the authigenic fraction, that the authigenic fraction contains several components with slightly different Tl isotope compositions, or that some minor Tl isotope fractionation occurred during partial dissolution of the sediments. However, given that for all the samples investigated here the authigenic fraction was 80% or more (except sample 207-1258C 17R-1 137-138) the potential effect on the authigenic fraction would be negligible. Even if the two fractions were combined such that the bulk sediment was considered more representative of the Tl isotope composition of seawater the Tl isotope excursion would be identical to the leachate-only values. Importantly, whole rock Tl concentrations do not vary significantly across OAE-2, signifying a good connection to the open ocean. Uncertainties are in 2SD and represent the reproducibility of multiple sample analyses or the long-term reproducibility of SCO-1, whichever is greater.

Table B.1 Tl isotope and concentration data. a, Sample name follows "leg-site&hole core-section interval". b, sum of authigenic and detrital fractions. c, reproducibility of multiple sample analyses or the long-term reproducibility of SCO-1, whichever is greater. d, replicate refers to multiple MC-ICPMS analyses on the same sample solution (*signifies multiple powder digestions).

[a]Sample	Depth (mcd)	[b]Tl (ppm)	$\varepsilon^{205}\mathrm{Tl}_{\mathrm{auth}}$	[c]2sd	[d]n	$\varepsilon^{205}\mathrm{Tl}_{\mathrm{detrital}}$	2sd	[d]n
207-1258B 45R-3 1-2	420.19	5.09	-3.08	0.11	4	-3.72	0.31	1
207-1258A 42-5 51-53	420.68	6.72	-3.05	0.32	3	-3.83	0.43	3
207-1258B 45-3 80-81	420.98	5.37	-2.33	0.11	2	-3.79	0.31	2
207-1258A 42-5 87-88	421.04	1.02	-1.89	0.59	*4	-2.62	0.45	*4
207-1258A 42-5 102-103	421.19	1.39	-2.18	0.11	2	-2.37	0.31	1
207-1258A 42-5 119-121	421.36	2.53	-2.83	0.58	2	-4.05	0.31	2
207-1258A 42-6 17-18	421.66	1.98	-3.19	0.17	2	-4.31	0.31	1
207-1258A 42-6 47-49	421.95	2.02	-2.79	0.17	*8	-3.86	0.32	*7
207-1258B 45R-4 40-41	421.99	3.22	-2.83	0.23	2	-3.50	0.31	1
207-1258A 42-6 113-114	422.62	4.26	-2.99	0.32	4	-3.55	0.31	1
207-1258B 45R-4 106-107	422.65	3.93	-3.12	0.11	2	-3.61	0.35	2
207-1258A 42-6 127-129	422.78	4.63	-3.16	0.44	*7	-3.71	0.31	*5
207-1258A 42-7 10-11	422.99	2.93	-2.36	0.19	2	-3.42	0.31	2
207-1258B 45R-4 148-149	423.07	3.21	-2.46	0.66	2	-2.93	0.31	1
207-1258A 42-7 79-80	423.68	1.01	-1.74	0.17	4	-2.54	0.31	1
207-1258A 42-7 100-101	423.89	4.67	-2.30	0.55	2	-3.30	0.50	2
207-1258C 17R-1 5-6	424.84	2.59	-2.31	0.38	5	-2.91	0.39	3
207-1258C 17R-1 27-28	425.06	2.59	-2.43	0.27	2	-2.76	0.40	2
207-1258C 17R-1 80-81	425.59	4.43	-2.70	0.18	2	-3.34	0.31	1
207-1258C 17R-1 95-96	425.74	5.36	-2.94	0.11	2	-4.21	0.31	2
207-1258C 17R-1 121-122	426.00	4.18	-2.01	0.80	2	-2.66	0.31	1
207-1258C 17R-1 137-138	426.16	1.87	-1.45	0.79	*4	-2.09	0.31	*4
207-1258A 42-7 114-115	426.23	2.74	-3.04	0.50	2	-3.88	0.31	1
207-1258C 17R-2 12-13	426.30	7.70	-3.66	0.29	2	-4.44	0.31	1
207-1258C 17R-2 22-23	426.40	1.43	-4.95	0.22	*5	-4.40	0.39	*5
207-1258C 17R-2 25-26	426.43	1.43	-4.59	0.11	2	-4.31	0.36	2
207-1258A 43-1 14-15	426.62	3.80	-4.42	0.11	2	-4.36	0.31	1
207-1258A 43-1 41-42	426.96	-	-4.45	0.43	2	-	-	-
207-1258A 43-1 75-76.5	427.23	2.86	-3.97	0.31	2	-4.59	0.31	2
207-1258C 17R-2 105-106	427.23	2.05	-4.68	0.11	2	-4.39	0.88	2
207-1258C 17R-3 4-5	427.42	1.17	-3.29	0.81	*4	-3.69	0.73	2
207-1258A 43-1 119-120	427.67	-	-4.45	0.28	2	-	-	-
207-1258C 17R-3 45-46	427.83	1.36	-4.53	0.11	2	-4.20	0.31	2
207-1258C 17R-CC 2-3	427.98	-	-4.18	0.36	2	-	-	-
207-1258A 43-2 39-41	428.15	3.13	-4.86	0.11	2	-5.34	0.50	3
207-1258A 43-2 73-75	428.49	1.12	-4.35	0.31	*3	-4.48	0.31	*3
207-1258A 43-2 119-121	428.95	4.46	-4.06	0.32	*5	-4.55	0.35	*5
207-1258A 43-3 37-39	429.39	1.71	-3.92	0.18	*5	-4.22	0.64	*5

Table B.2 Reproducibility of Tl isotope composition with one vs. two columns. Samples put through only one micro-column yielded similar results as those that went through the typical two-column procedure. Therefore, all samples in this study were only passed through one micro-column.

Sample Name	Leach		Silicate		Columns
	ε^{205}Tl	Tl (ppb)	ε^{205}Tl	Tl (ppb)	
SCO-1	-2.94	169	-2.52	339	1
SCO-1	-2.98	204	-2.43	220	2
207 1258A 42-6 47-49	-2.74	2297	-3.87	227	1
207 1258A 42-6 47-49	-2.77	2368	-4.02	219	2
207-1258C 17R-2 22-23	-5.02	1253	-4.30	179	1
207-1258C 17R-2 22-23	-4.82	1422	-4.64	173	2
207-1258A 42-5 51-53	-2.92	6102	-4.05	957	1
207-1258A 42-5 51-53	-3.23	6107	-3.80	980	2
207-1258C 17R-1 5-6	-2.12	2561	-2.91	550	1
207-1258C 17R-1 5-6	-2.55	2419	-3.10	554	2
Average difference **(*abs value*)**	**0.20**	**85**	**0.21**	**29**	

Table B.3 Reproducibility of USGS shale standard SCO-1. SCO-1 was leached, digested, purified, and analyzed with each sample set to monitor long-term precision and accuracy of our Tl isotope data. Our reproducibility was better than previous Tl isotope studies, which report 2SD uncertainties of ~0.3 – 0.5 epsilon units (Kersten et al. 2014), and our values for both the silicate and authigenic (leached) fractions are in general agreement with measurements from a recent study using the same methodology (Owens et al. 2017a).

	Silicate fraction	Authigenic fraction	whole rock (calculated)
	-2.27	-2.82	-2.47
	-2.43	-2.98	-2.69
	-2.39	-2.86	-2.54
	-2.52	-2.94	-2.66
	-2.42	-2.90	-2.61
	-2.73	-2.96	-2.81
	-2.29	-2.91	-2.50
	-2.63	-2.91	-2.71
	-2.67	-2.97	-2.78
average	*-2.48 ± 0.31*	*-2.92 ± 0.11*	*-2.64 ± 0.24*

APPENDIX C

SUPPLEMENTARY INFORMATION FOR CHAPTER 4

Text C.1. Methods

Text C.1.1 Tl isotopes

Tl sample preparation and purification were performed in the NIRVANA Laboratory at Woods Hole Oceanographic Institution (WHOI), as well as in J. Owens' Laboratory at Florida State University within the National High Magnetic Field Laboratory (NHMFL). Powdered samples from ABDP9 were leached using a method from the literature (Nielsen et al. 2011; Ostrander et al. 2017), which has been shown to effectively separate authigenic Tl (that is Tl bound to pyrite) from detrital Tl. Each fraction was subsequently digested following procedures discussed in that literature. Ion exchange chromatography was completed using previously described techniques (Rehkämper and Halliday 1999; Nielsen et al. 2004). Similar to recent work (Ostrander et al. 2017), samples were only subjected to one column pass because Tl concentrations were high and thus very little sample mass was processed.

Tl isotopic analyses were conducted at the WHOI Plasma Mass Spectrometry Facility and at the NHMFL in Tallahassee. At both locations a Thermo Neptune multi-collector inductively coupled plasma mass spectrometer (MC-ICPMS) was used with an Aridus II desolvating nebulizer sample introduction system. Measurements were made in low-resolution mode utilizing sample-standard bracketing relative to NIST 997 Tl in epsilon notation. External normalization to NIST SRM 981 Pb was utilized to monitor instrumental mass bias, similar to previous studies (Rehkämper and Halliday 1999; Nielsen et al. 2004). As a known quantity of NIST SRM 981 Pb was added to each sample, Tl concentrations could be calculated during MC-ICPMS analysis using the measured ^{205}Tl/^{208}Pb ratios. Tl isotope values are reported in epsilon notation relative to NIST 997

Tl metal. One USGS shale SCO-1 standard was leached, purified, and analysed with each sample set to monitor accuracy and showed good reproducibility ($\varepsilon^{205}\mathrm{Tl}_{\mathrm{authigenic}} = -2.80 \pm 0.13$, 2 s.d., n = 8) compared to a recent study (−2.92 ± 0.11; Ostrander et al. 2017).

Text C.1.2 Mo isotopes

All Mo sample digestion, isotope purification and analysis was completed at the W.M. Keck Foundation Laboratory for Environmental Biogeochemistry at Arizona State University. Quarter cores were cut from ABDP9, powdered, ashed and digested; concentrations were then analysed using the same techniques employed in previous work (Anbar et al. 2007). A large enough sample was then taken from the same digested stock solutions to provide 125 ng Mo that was spiked with an optimal amount of calibrated synthetic Mo isotope double-spike (^{97}Mo and ^{100}Mo) before purification via ion exchange chromatography, again utilizing methods from previous studies (Siebert et al. 2001, Barling et al. 2001). The double spike is used for chromatography and instrumental mass fractionation correction.

Isotope ratio measurements were performed on a Thermo Neptune MC-ICPMS in low-resolution mode with an Elemental Scientific Inc. Apex inlet system and using sample-standard bracketing (Kendall et al. 2009; Duan et al. 2010). All measurements were made using the Johnson Matthey Specpure Mo plasma standard (Lot no. 802309E; Roch-Mo2) as the bracketing standard, and then re-calculated relative to the new international NIST SRM 3134 standard = + 0.25‰ (Nägler et al. 2014). Samples and standards were analysed at a concentration of 25 μg g−1 Mo, which yielded about 3 V of signal on mass 98. Samples were analysed in triplicate (at least), with the average 2 s.d. sample reproducibility being

0.06‰, and the maximum being 0.11‰. Over the 12-month period of Mo isotope analysis for this study, USGS rock reference material SDO-1 was simultaneously processed with each batch of samples to monitor accuracy and showed good reproducibility (δ^{98}Mo = 1.00 ± 0.09‰ (2 s.d.) compared with 1.05 ± 0.14‰ from a previous study; Goldberg et al. 2013), as did various analytical replicates (Table C.1). Lastly, for each analytical run, a series of standards with varying spike/sample ratios was measured. All samples were within the validated spike/sample range for accurate and precise δ^{98}Mo values.

Table C.1 Standard solution δ^{98}Mo values from this study vs. previous work

Standard	*This study*[a]	*n*	*Normalized to NIST + 0.25‰*[b]	*Goldberg et al. (2013)*
Roch-Mo2	Bracketing std.		-0.09‰	-0.09 ± 0.05‰
ICL-Mo	0.16 ± 0.03‰	38	0.07 ± 0.03‰	0.09 ± 0.05‰
Kyoto-Mo	-0.04 ± 0.05‰	39	-0.13 ± 0.05‰	-0.12 ± 0.06‰
NIST SRM 3134	0.33 ± 0.06‰	45	0.24 ± 0.06‰	0.25‰ (reporting std.)
SDO-1	1.12 ± 0.05‰	45	1.03 ± 0.05‰	1.05 ± 0.14‰

a. Measured relative to Roch-Mo2

b. Normalized using $\delta^{98}\text{Mo}_{\text{Roch-Mo2}}$ = -0.09‰ relative to $\delta^{98}\text{Mo}_{\text{NIST+0.25‰}}$ (Goldberg et al. 2013)

*all reported errors are 2SD of the standard reproducibility

Text C.2. The Mt. McRae Shale in drill core ABDP9

The core sampled in this study was drilled in the Pilbara Craton of Western Australia during the summer of 2004 as a part of the Archean Biosphere Drilling Project (ABDP (Anbar et al. 2007; Kaufman et al. 2007)). Drilling took place at 21°59’29.5” S, 117°25’13.6”E, and the hole azimuth was 186° with a dip of 89°. One-half of the core is housed and curated at the School of Earth and Space Exploration at Arizona State

University (ASU). The archived half is housed at the Geological Survey of Western Australia's Perth Core Library.

Sedimentary rocks preserved in the ABDP9 core have experienced only mild regional metamorphism (prehnite-pumpellyite facies; <300°C) and minimal deformation (gentle folding dips <5°) since original deposition (Brocks et al. 2003). Geochemical signatures preserved in these rocks are thought to be primary, with no indication of a secondary and metasomatic origin (Anbar et al. 2007; Stüeken et al. 2015; Kendall et al. 2015). Both the upper and lower shale members were deposited below wave base in a marine environment (Krapež et al. 2003; Kaufman et al. 2007). Black shales from the upper shale member previously yielded depositional ages of 2495 ± 14 Ma (145.22-148.32 m depth) and 2495 ± 20 Ma (128.71-129.85 m) using Re-Os geochronometry (Anbar et al. 2007; Kendall et al. 2015). The lower Mt. McRae Shale in ABDP9 (189.65 – 173 m) contains pyritic black shales, with carbonate/marl interbeds. The first ~2m of the upper Mt. McRae Shale (153.3 – 125.5 m) contains interbedded black shale and siderite. This is followed by ~19m of black shales with frequent pyrite laminae and abundant pyrite nodules, with a few short occurrences of carbonate. Massive pyrite nodules occur in black shales from 134 – 131m. Above this, and until the end of the analyzed section, black shales without massive pyrite nodules again dominate. To best estimate primary depositional chemistry, and not post-depositional diagenetic effects, we avoided pyrite nodules and laminae when possible.

Text C.3 Tl concentration data

Measured $Tl_{authigenic}$ abundances are invariant in the lower shale member (avg. = 1.3 µg/g ± 0.2 SE) and increase at the same depths as whole-rock Mo concentrations in the upper member (Fig. C.2). Peak values (6 µg/g), however, are sustained over a greater range of depths (~145 to 135 m compared to ~147 to 143 m for Mo).

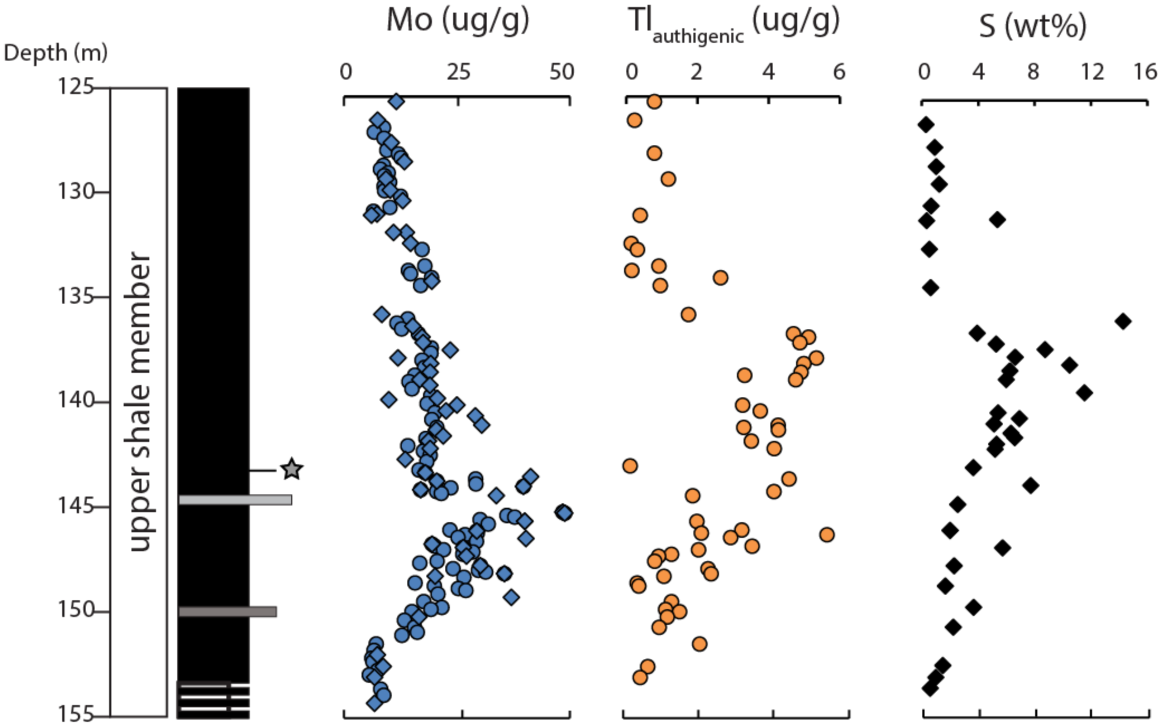

Figure C.1 Mo and Tl concentration data from this study from the upper Mt. McRae Shale member, plotted alongside data from previous work. Concentration measurements from this study are signified by circles. Data from previous work (Anbar et al. 2007; Kaufman et al. 2007) are plotted as diamonds. See Fig. 4.1 of the main text for a lithological key.

Tl concentration trends mirror those of S from previous work (Kaufman et al. 2007), highlighting the slight affinity Tl possesses for sulfides (Xiong 2007; Nielsen et al. 2011) (Fig. C.1). This trend is different from that of Mo most likely because of the redox-sensitivity of Mo not shared by Tl. Increases in the rate of oxidative weathering will enhance dissolution of continental molybdenite (MoS_2) and pyrite, and thus delivery of Mo to the ocean (Miller et al. 2011). Tl is only a trace constituent in continental minerals (Nielsen et al. 2017), and thus it is unlikely that the delivery rate of Tl to the ocean would be greatly affected under increased oxidative weathering. Instead, the rate of Tl delivery to the ocean would be more sensitive to changes in subaerial volcanism, the primary oceanic Tl source today (Nielsen et al. 2017). Similarly, changes in global marine redox can have a profound effect on the dissolved marine Mo reservoir, but are unlikely to affect the dissolved marine Tl reservoir to the same extent. Changes in the area of sulfidic seafloor – the strongest marine sink of Mo – are largely responsible for driving variations in the size of the global marine Mo reservoir (Reinhard et al. 2013). Sulfidic environments are not a strong sink for Tl in the ocean (Owens et al. 2017a), where removal from seawater is instead dominated by low-temperature hydrothermal alteration of oceanic crust and during adsorption to Mn oxides (Nielsen et al. 2017).

Text C.4 Mo concentration data

Measured Mo abundances in the upper Mt. McRae Shale mirror the trends from previous lower-resolution work in the same core and are perhaps the most substantial evidence for a “whiff” of oxygen at 2.5 Ga (Anbar et al. 2007) (Fig. C.1). Concentrations rise gradually from ~150 to 145 m, where they reach a peak value of 50 μg/g.

Whole-rock sample digestion liberates Mo from the two primary sources of Mo in shales: authigenic incorporation and detrital minerals, both of which have unique δ^{98}Mo values. Therefore, there is a potential for whole-rock δ^{98}Mo to be diluted by the detrital value (~0.35 – 0.60‰; Willbold and Elliot 2017) if the sample contains an appreciable amount of detrital-sourced Mo. The following equation can be used to calculate authigenic δ^{98}Mo ($\delta^{98}Mo_{auth}$) by correcting for detrital dilution:

$$\delta^{98}Mo_{auth} = (\delta^{98}Mo_{sample} - \delta^{98}Mo_{detrital} * Mo/X_{detrital} * [X]_{sample} \div [Mo]_{sample}) \div (1 - Mo/X_{detrital} * [X]_{sample} \div [Mo]_{sample})$$

where $\delta^{98}Mo_{detrital}$ is the Mo isotope composition of continental detritus and $Mo/X_{detrital}$ is the ratio of Mo (in μg/g) to a non-redox sensitive element (X). By normalizing to a non-redox sensitive element, we assume any surplus in the Mo/X ratio of our samples relative to continental Mo/X is due to enrichment from authigenic Mo. Here, we use aluminum (Al) as our non-redox sensitive element and assume a $Mo/Al_{detrital}$ of 0.13 (Al being in wt%; Rudnick and Gao 2003). Results are presented in Supplementary Fig. C.2 and show that calculated $\delta^{98}Mo_{auth}$ closely matches whole-rock values throughout the upper Mt. McRae Shale member regardless of the assumed $\delta^{98}Mo_{detrital}$ value.

Text C.5 Isotope trends in the lower Mt. McRae Shale

In contrast to the upper member, deposition of the lower Mt. McRae Shale took place under primarily non-euxinic conditions (i.e. $Fe_{HR}/Fe_T < 0.70$; Reinhard et al. 2009) and makes it difficult to extrapolate seawater trends from sedimentary isotope compositions. Measured δ^{98}Mo are heavier than bulk continental crust (avg. δ^{98}Mo = 0.97‰ (Duan et al. 2010); see Fig. 4.2 of the Main Text) but may still fall short of the coeval seawater signature because deposition under non-euxinic conditions results in a

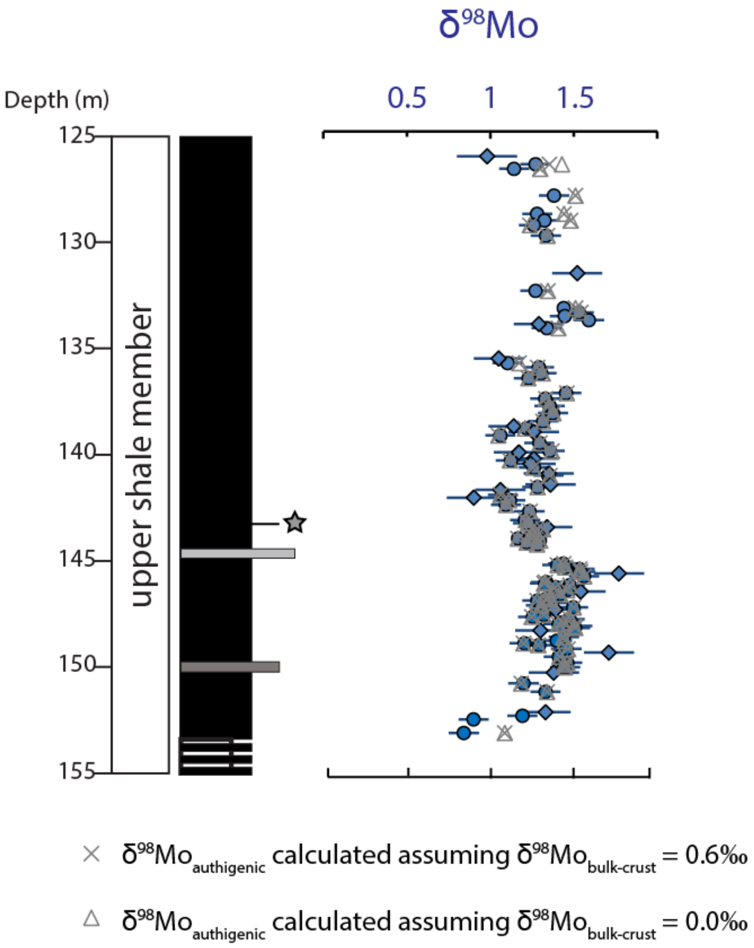

Figure C.2 Measured bulk-rock δ^{98}Mo plotted alongside calculated authigenic δ^{98}Mo estimates. The dominant Mo isotope trend observed in the upper Mt. McRae Shale is preserved even after correction for detrital dilution using extreme endmembers for the possible detrital Mo isotope value. This includes a very light detrital δ^{98}Mo composition, similar to estimates of bulk-Earth (~ 0.0‰; Greber et al. 2015), and a heavy δ^{98}Mo similar to that used as an upper estimate for bulk continental crust (0.6‰; Willbold and Elliot 2017). See Fig. 4.1 of the main text for a lithological key. All error bars represent the 2SD reproducibility of that sample or the external long-term reproducibility of natural reference materials, whichever is greater.

sedimentary δ^{98}Mo value lighter than seawater (Neubert et al. 2008). The actual seawater value is impossible to estimate, but the mere fact that it must have been heavier than continental crust implies some mechanism was removing isotopically light Mo (either adsorption to Mn oxides (Wasylenki et al. 2011), oxidation during riverine and continental weathering (Archer and Vance 2008; Siebert et al. 2015), Fe oxides (Goldberg et al. 2009), and/or weakly sulfidic sediments (Neubert et al. 2008)). The ε^{205}Tl in the lower Mt. McRae Shale are near crustal (~ -2 epsilon units (Nielsen et al. 2005); see Fig. 4.2 of the Main Text) and may indicate little to no fractionation of Tl by Mn oxides in the ocean. Little is known about Tl removal under ferruginous conditions, however, and thus any interpretation of the near-crustal Tl isotope values in the lower Mt. McRae Shale is highly speculative.

Text C.6 Isotope mass-balance modeling

Thallium

The following Tl isotope mass-balance equation was used in this study:

$$\varepsilon^{205}\mathrm{Tl}_{\mathrm{Inputs}} = \varepsilon^{205}\mathrm{Tl}_{\mathrm{AOC}}(f_{\mathrm{AOC}}) + \varepsilon^{205}\mathrm{Tl}_{\mathrm{oxic}}(f_{\mathrm{Tl\text{-}oxic}}) + \varepsilon^{205}\mathrm{Tl}_{\mathrm{other}}(f_{\mathrm{other}})$$

where $\varepsilon^{205}\mathrm{Tl}_{\mathrm{X}}$ represents the isotopic composition of average oceanic inputs and the dominant marine outputs, and $f_{\mathrm{Tl\text{-}X}}$ their relative removal flux. We designate low-T alteration of oceanic crust (AOC), oxic sediments (oxic), and "other" as three dominant outputs, where "other" signifies Tl removal with no associated isotopic fractionation. ε^{205}Tl of each output can be calculated if a seawater ε^{205}Tl estimate is made, and the isotopic offset of that output is assumed: $\varepsilon^{205}\mathrm{Tl}_{\mathrm{output}} = \varepsilon^{205}\mathrm{Tl}_{\mathrm{seawater}} - \Delta^{205}\mathrm{Tl}_{\mathrm{solution\text{-}output}}$.

Low-T alteration of oceanic crust preferentially removes isotopically light Tl from solution (Nielsen et al. 2006), with the most recent estimate for Δ^{205}Tl being 0 to 2.5 (Ostrander et al. 2017). Importantly, the lower estimate (i.e. zero-fractionation) would signify complete uptake of seawater Tl into AOC and is likely unrealistic. Here, as in the most recent estimate (Nielsen et al. 2017), we utilize the larger offset of 2.5 epsilon units.

Mn oxides impart the greatest magnitude of Tl isotope offset from solution, preferentially retaining heavier-mass isotopes (Nielsen et al. 2013). The most recent estimate for $\Delta^{205}Tl_{seawater\text{-}MnOx}$ is -13.5 to – 19 (Ostrander et al. 2017). Here, we utilize the larger offset of -19 epsilon units so as to satisfy mass-balance.

The Tl isotope composition of oceanic inputs is shown to not differ within analytical uncertainty from bulk Earth and continental crust (Nielsen et al. 2005) and is therefore assigned a $\varepsilon^{205}Tl$ of -2.

Our Tl isotope mass-balance differs from previous work in that it departs from the typical two-sink model that applies to modern oceans [only AOC and MnOx (Nielsen et al. 2009; Ostrander et al. 2017)] by adding a third, non- fractionating sink. Euxinic settings minimally fractionate Tl isotopes and are not thought to be a dominant Tl removal mechanism from seawater today (Owens et al. 2017a). However, this may not have been the case in Earth's past. Moreover, in the absence of a strong Mn oxide sink, Tl isotope fractionation in the marine environment would be taking place primarily at the flanks of mid-ocean ridges during low-T alteration of basalt, which continues until hydrothermal circulation is arrested by a sufficient sediment blanket. This means the bulk of the seafloor would not be fractionating Tl isotopes, and must, due to its sheer size, be viewed as a contributor to the seawater $\varepsilon^{205}Tl$.

Sensitivity calculations for Tl isotope mass-balance show that, regardless of the fractionation factors used, Mn oxide-rich oxic sediments are required to drive the measured light ε^{205}Tl compositions (Supplementary Table C.1). The minimum $f_{\mathrm{Tl\text{-}oxic}}$ is always non-zero, but the maximum can vary between 0.06 and 0.28.

Table C.2

Results of sensitivity calculations for Tl isotope mass-balance

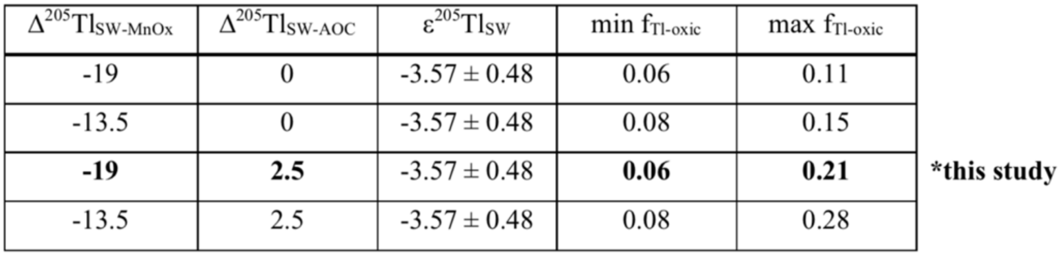

$\Delta^{205}\mathrm{Tl}_{\mathrm{SW\text{-}MnOx}}$	$\Delta^{205}\mathrm{Tl}_{\mathrm{SW\text{-}AOC}}$	$\varepsilon^{205}\mathrm{Tl}_{\mathrm{SW}}$	min $f_{\mathrm{Tl\text{-}oxic}}$	max $f_{\mathrm{Tl\text{-}oxic}}$	
-19	0	-3.57 ± 0.48	0.06	0.11	
-13.5	0	-3.57 ± 0.48	0.08	0.15	
-19	**2.5**	-3.57 ± 0.48	**0.06**	**0.21**	***this study**
-13.5	2.5	-3.57 ± 0.48	0.08	0.28	

Molybdenum

The following Mo isotope mass-balance equation was used in this study:

$$\delta^{98}\mathrm{Mo}_{\mathrm{Inputs}} = \delta^{98}\mathrm{Mo}_{\mathrm{euxinic}}(f_{\mathrm{euxinic}}) + \delta^{98}\mathrm{Mo}_{\mathrm{oxic}}(f_{\mathrm{Mo\text{-}oxic}}) + \delta^{98}\mathrm{Mo}_{\mathrm{SAD}}(f_{\mathrm{SAD}})$$

where, similar to Tl, $\delta^{98}\mathrm{Mo}_{\mathrm{X}}$ represents the isotopic composition of average oceanic inputs and the dominant marine outputs, and $f_{\mathrm{Mo\text{-}X}}$ their relative removal flux. We designate euxinic sediments, Mn oxide-rich oxic sediments (oxic), and sediments that are sulfidic at depth (SAD; where sulfide is limited to sediment pore waters) as the three dominant outputs. These are the three marine sinks used in recent Mo isotope mass-balance calculations (Chen et al. 2015; Kendall et al. 2017). Estimates for our $\delta^{98}\mathrm{Mo}_{\mathrm{X}}$ values are calculated similar to those for Tl and are identical to these references (i.e. Chen et al. 2015; Kendall et al. 2017).

Mn oxides present in well oxygenated marine sediments are the strongest Mo isotope fractionation mechanism found to date, and multiple estimates agree on a $\Delta^{98}Mo_{solution\text{-}MnOx}$ of ~3.0‰ (Wasylenki et al. 2011). For this study, we use a $\delta^{98}Mo_{oxic}$ value of $\delta^{98}Mo_{seawater}$ – 3.0‰ (e.g. using the seawater δ^{98}Mo estimate from data in this study: 1.56‰ – 3.0‰ = -1.46‰, where 1.56‰ represents a minimum value for seawater δ^{98}Mo based on the highest δ^{98}Mo measured for the Mt. McRae Shale in this study).

For $\delta^{98}Mo_{euxinic}$, we use an isotopic offset from seawater of 0.5‰ so as to lump together weakly and strongly euxinic environments, both of which are strong sinks for Mo (i.e. where H_2S is present in the water column and pore waters; Chen et al. 2015). Hence, $\delta^{98}Mo_{euxinic}$ would be equal to 1.06‰ if seawater δ^{98}Mo was 1.56‰.

For $\delta^{98}Mo_{SAD}$, we use an isotopic offset from seawater of 0.7‰ because this is the value most often observed in modern settings where H_2S is limited to sediment pore waters (Arnold et al. 2004; Poulson et al. 2006; Poulson Brucker et al. 2009; Nägler et al. 2011). A substantial amount of Mo is removed from the ocean today into these environments (Reinhard et al. 2013). Applying this isotopic offset would result in a $\delta^{98}Mo_{SAD}$ composition of 0.86‰ if seawater δ^{98}Mo was 1.56‰.

For our Mo isotope mass-balance calculation δ^{98}MoInputs is assumed to be 0.3‰, within the range of currents estimates for the continental crust (modern continental crust δ^{98}Mo = 0.48 ± 0.12‰[Willbold and Elliot 2017]) and molybdenite ($\delta^{98}Mo_{molybdenite}$ = 0.29 ± 1.04‰[Breillat et al. 2016]), which is the predominant Mo host in the continental crust. A recent study shows that, while Mo isotope fractionation can occur during transport of Mo to the ocean (Archer and Vance 2008; Sibert et al. 2015), the vast majority of this Mo comes to the ocean unfractionated (King and Pett-Ridge 2018). As such, the isotopic composition of Mo delivered to the ocean should replicate that of the upper continental crust.

The results of sensitivity calculations for Mo isotope mass-balance are reported below (Supplementary Table C.2). These calculations were performed to test the influence of changing two modeling parameters: 1) a $\delta^{98}Mo_{Inputs}$ value equal to 0.7‰, which was until recently (King and Pett-Ridge 2018) thought to be the modern value (Archer and Vance 2008). And 2) a $\delta^{98}Mo_{euxinic}$ composition equal to that of seawater, which does happen in some basins today (Neubert et al. 2008). Again, regardless of the changes, Mn oxide-rich oxic sediments are required to drive the measured Tl isotope compositions. The minimum $f_{Mo\text{-}oxic}$ is always non-zero, but the maximum can vary between 0.18 and 0.45.

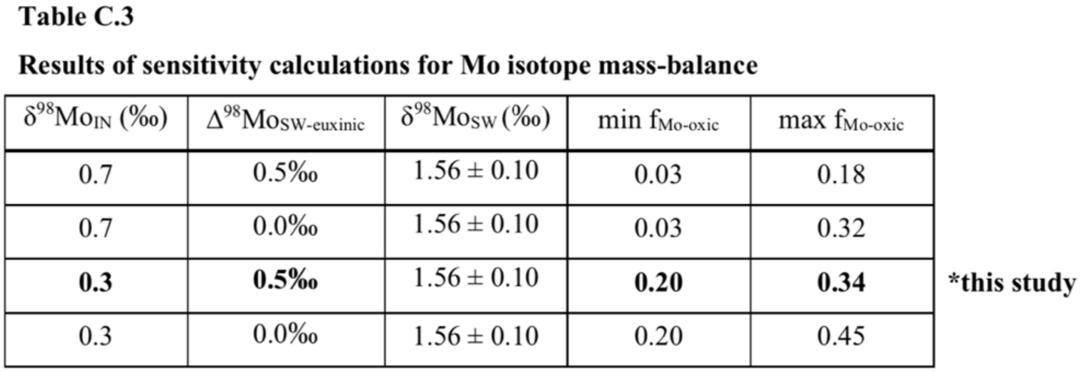

Table C.3

Results of sensitivity calculations for Mo isotope mass-balance

$\delta^{98}Mo_{IN}$ (‰)	$\Delta^{98}Mo_{SW\text{-}euxinic}$	$\delta^{98}Mo_{SW}$ (‰)	min $f_{Mo\text{-}oxic}$	max $f_{Mo\text{-}oxic}$	
0.7	0.5‰	1.56 ± 0.10	0.03	0.18	
0.7	0.0‰	1.56 ± 0.10	0.03	0.32	
0.3	**0.5‰**	1.56 ± 0.10	**0.20**	**0.34**	***this study**
0.3	0.0‰	1.56 ± 0.10	0.20	0.45	

Table C.4 Supplementary Data

ABDP9 Depth	Al[a]	Mo[a]	δ^{98}Mo[b]	reported error[c]	$\text{Tl}_{\text{authigenic}}$	$\varepsilon^{205}\text{Tl}_{\text{authigenic}}$	reported error[d]
(m)	(wt%)	(µg/g)	(‰)		(µg/g)		
126.15	6.9	7.4	0.98	0.18	0.23	-2.63	0.13
126.52	7.1	8.7	1.27	0.09			
126.74	5.9	6.6	1.14	0.09			
127.03	7.2	8.8					
127.61	7.1	9.4					
127.75					0.80	-2.90	0.23
127.79	8.5	12.0					
127.98	8.0	12.6	1.38	0.09			
128.34	7.2	8.7					
128.54	7.3	8.0					
128.71	7.6	9.8					
128.84	7.4	8.9	1.28	0.09			
129.01	8.1	9.2			1.19	-2.38	0.13
129.15	7.8	10.0	1.32	0.09			
129.36	7.6	8.8	1.26	0.09			
129.58	7.5	8.9					
129.85	8.1	12.5	1.33	0.09			
130.39	7.2	10.1					
130.57	6.8	6.5					
130.76	6.3	6.0			0.39	-3.00	0.39
131.60	8.0	13.8	1.52	0.15			
132.13	6.8	14.7			0.15	-0.75	0.17
132.43	7.1	17.2	1.27	0.09	0.31	-2.85	0.53
133.23	6.1	17.9	1.44		0.92	-2.65	0.39
133.44	6.5	14.2	1.53	0.09	0.16	-2.59	0.26
133.60	6.1	14.7	1.45	0.09	0.48	-3.25	0.13
133.79	5.0	19.3	1.59	0.09	2.65	-3.02	0.39
133.97	7.8	19.4	1.29	0.15			
134.17	6.2	16.9	1.34	0.09	0.96	-2.34	0.63
135.58	4.2	8.3	1.05	0.15	1.75	-1.81	0.20
135.80	6.2	14.1	1.10	0.09			
136.00	5.1	11.7	1.29	0.09			
136.28	5.5	12.7	1.30	0.09			
136.51	5.8	16.4	1.23	0.09	4.70	-2.46	0.21
136.67	6.8	17.3			5.12	-1.92	0.38
136.94	5.3	17.5			4.88	-3.01	0.13
137.20	4.8	19.3	1.45	0.09			
137.46	4.5	19.2	1.33	0.09			

ABDP9 Depth	Al[a]	Mo[a]	δ^{98}Mo[b]	reported error[c]	$Tl_{authigenic}$	$\varepsilon^{205}Tl_{authigenic}$	reported error[d]
(m)	(wt%)	(µg/g)	(‰)		(µg/g)		
137.68	4.6	11.9			5.34	-2.03	0.13
137.80	4.9	17.2	1.35	0.09			
137.96	5.7	19.1			4.99	-2.41	0.23
138.14	6.1	17.8	1.38	0.09			
138.38	6.0	19.0			4.91	-2.36	0.13
138.52	4.9	15.6	1.32	0.09	3.33	-2.55	0.34
138.74	5.9	16.8	1.14	0.15	4.76	-2.23	0.33
138.84	6.0	14.3	1.22	0.09			
139.01	5.0	19.0	1.26	0.15	3.97	-2.55	0.13
139.18	4.9	15.0	1.06	0.09			
139.52	4.9	19.1	1.29	0.09			
139.90	6.0	18.4	1.35	0.09			
139.97	6.6	25.0	1.17	0.15	3.27	-2.11	0.13
140.25	6.0	22.6	1.26	0.15	3.77	-2.25	0.13
140.34	5.2	20.1	1.12	0.09			
140.50	6.2	29.1	1.24	0.15			
140.67	5.0	19.4	1.26	0.09			
140.95	6.0	30.5	1.35	0.15	4.27	-2.17	0.25
141.05	5.5	20.5	1.35	0.09	3.30	-2.75	0.19
141.17	6.3	20.4			4.28	-2.31	0.13
141.47	6.4	21.9	1.36	0.15			
141.59	5.0	18.1	1.28	0.09			
141.72	6.7	18.6	1.06	0.15	3.52	-2.26	0.13
141.94	5.3	14.1	1.08	0.09			
142.08	6.5	19.1	0.90	0.16	4.16	-2.28	0.44
142.20	4.8	17.6	1.12	0.09			
142.41	4.6	19.1	1.09	0.09			
142.71	4.9	18.3	1.23	0.09			
142.92					0.11	-2.95	0.22
143.12	4.1	16.5	1.21	0.09			
143.26	3.6	18.0	1.23	0.09			
143.45	3.7	41.4	1.34	0.15			
143.55	2.8	29.1	1.31	0.09	4.02	-2.86	0.70
143.66	3.7	20.5	1.26	0.09			
143.80	4.0	29.2	1.25	0.09			
143.92	4.2	39.8	1.23	0.09			
143.98	3.2	23.6	1.17	0.09			
144.08	4.1	16.9	1.30	0.09			
144.16	4.2	20.5	1.22	0.09	4.15	-2.46	0.49
144.26	5.9	21.5	1.28	0.09			

ABDP9 Depth	Al[a]	Mo[a]	δ^{98}Mo[b]	reported error[c]	Tl$_{\text{authigenic}}$	ε^{205}Tl$_{\text{authigenic}}$	reported error[d]
(m)	(wt%)	(µg/g)	(‰)		(µg/g)		
144.36	4.4	33.7			1.87	-1.85	0.13
145.16	5.9	48.4	1.44	0.09			
145.22	5.2	48.9	1.40	0.09			
145.32	5.4	36.1	1.45	0.09			
145.41	5.8	37.8	1.53	0.09			
145.53	5.5	30.1	1.54	0.09			
145.61	6.1	40.1	1.77	0.15	1.99	-2.64	0.27
145.74	5.6	31.9	1.56	0.09			
146.02	4.8	23.4	1.33	0.09	3.25	-2.63	0.36
146.08	5.2	29.4	1.33	0.09			
146.17	4.5	29.5	1.47	0.09	2.11	-3.16	0.39
146.26	3.1	26.8	1.39	0.09	5.64	-2.99	0.13
146.39	4.8	25.2	1.46	0.09	2.94	-2.26	0.13
146.45	5.1	40.3	1.54	0.15			
146.58	4.1	29.3	1.42	0.09			
146.72	4.1	19.5	1.36	0.09			
146.81	4.1	20.0	1.33	0.09	3.54	-2.58	0.68
146.88	3.7	26.4	1.28	0.09			
146.99	4.4	22.0	1.37	0.11	2.03	-3.12	0.22
147.10	5.2	28.5	1.30	0.09			
147.20	4.5	26.3	1.50	0.09	1.27	-2.35	0.13
147.30	5.8	27.1	1.39	0.15	0.91	-3.41	0.13
147.54	5.0	20.6	1.32	0.09	0.80	-2.76	0.29
147.64	4.2	16.7	1.26	0.09			
147.75	4.8	30.2	1.48	0.09			
147.90	4.9	24.1	1.43	0.09	2.30	-2.59	0.68
147.98	5.3	29.7	1.41	0.09		-2.71	0.54
148.07	5.0	31.4	1.50	0.09	1.27	-3.06	0.68
148.15	4.9	35.5	1.51	0.09	2.39	-3.36	0.71
148.27	5.5	20.2	1.30	0.15	1.06	-2.51	0.13
148.32	4.7	26.5					
148.59	5.1	15.7	1.44	0.09	0.31	-3.07	0.52
148.75	4.9	20.0	1.40	0.09	0.35	-3.57	0.48
148.87	5.7	25.3	1.21	0.09			
148.96	6.3	27.0	1.29	0.09	1.00	-3.16	0.24
149.14	6.4	20.8	1.45	0.09			
149.30	7.1	37.1	1.71	0.15			
149.50	5.2	17.6	1.41	0.09	1.28	-2.99	0.28
149.78	5.2	21.6	1.46	0.09			
149.88	5.3	19.2	1.44	0.09	1.11	-2.63	0.43

ABDP9 Depth	Al^{a}	Mo^{a}	$\delta^{98}\mathrm{Mo}^{b}$	reported error^{c}	$\mathrm{Tl}_{\mathrm{authigenic}}$	$\varepsilon^{205}\mathrm{Tl}_{\mathrm{authigenic}}$	reported error^{d}
(m)	(wt%)	(µg/g)	(‰)		(µg/g)		
149.99	4.6	15.0	1.45	0.09	1.50	-3.06	0.50
150.24	6.1	16.5	1.38	0.15	1.16	-2.50	0.13
150.40	7.1	13.3					
150.74	6.1	15.5	1.20	0.09	0.93	-2.71	0.13
150.99	6.2	16.2					
151.14	5.6	12.8	1.33	0.09			
151.56	4.6	7.1			2.06	-2.95	0.39
151.86	4.7	6.6			0.52	-1.87	0.47
152.08	5.7	7.3	1.33	0.15			
152.25	5.4	6.1	1.19	0.09			
152.42	5.2	6.3	0.90	0.09			
152.65	5.4	8.7			0.60	-1.87	0.13
152.84	7.0	7.4					
153.06	9.3	5.6	0.84	0.09		-1.59	0.13
153.18	6.4	6.7			0.39	-1.77	0.14
157.80	7.2	8.0	1.16	0.18			
163.95	5.6	5.1	1.00	0.15			
168.36	3.1	3.3	0.91	0.17			
175.51	5.9	3.3	0.90	0.15			
177.10	6.5	3.1	0.91	0.15	1.48	-2.29	0.13
178.61	6.3	3.2			1.96	-2.50	0.13
178.83	6.2	3.4	0.98	0.17			
180.33	5.2	2.9	1.03	0.15	1.01	-4.28	0.13
181.2	4.8	2.0			1.96	-2.00	0.13
182.50	5.4	2.5	1.10	0.15			
183.65	4.8	2.4			0.83	-2.12	0.20
185.43	3.4	1.8			0.52	-2.14	0.13
187.46	6.0	3.2	0.90	0.15			
188.01	5.5	4.6			1.37	-1.79	0.14
188.87	4.9	7.7			0.91	-2.15	0.13

a. Some of this trace metal data is previously published in Anbar et al. 2007

b. Some of this isotope data is previously published in Duan et al. 2010

c. 2SD sample reproducibility or long-term reproducibility of SDO-1, whichever is greater

d. 2SD sample reproducibility or long-term reproducibility of SCO-1, whichever is greater

APPENDIX D

SUPPLEMENTARY INFORMATION FOR CHAPTER 5

Table D.1 Supplementary Data

Sample No.	Member	Strat. Height	Fe_{HR}/Fe_T	Fe_{Py}/Fe_{HR}	Mo	$\delta^{98/95}$Mo	2SD
		(m)			(ppm)	(‰)	
Rongxi section, Hunan Province, China							
RX09-4.5	II	4.5	0.38	0.30	9	0.30	0.10
RX09-4.8	II	4.8	0.82	0.92	20	0.76	0.10
RX09-5.0	II	5.0	1.03	0.99	19	0.12	0.10
RX09-5.2	II	5.2	0.51	1.00	10	0.47	0.10
RX09-7.3	II	7.3	0.37	0.33	3	-0.32	0.22
RX09-9.4	II	9.4	0.62	0.08	3	0.38	0.13
RX09-56.5	IV	56.5	0.65	0.52	44	-1.00	0.10
RX09-57.6	IV	57.6	0.73	0.75	95	0.01	0.10
RX09-58.0	IV	58.0	0.63	0.52	37	0.01	0.10
RX09-58.8	IV	58.8	0.85	0.82	69	-0.02	0.10
RX09-59.5	IV	59.5	0.79	0.34	81	1.19	0.10
RX09-60.2	IV	60.2	0.84	0.74	35	1.32	0.15
RX09-61.2	IV	61.2	1.00	0.72	47	1.09	0.10
RX09-62.5	IV	62.5	1.15	0.30	12	0.43	0.10
Taoying section, Guizou Province, China							
TY09-7.6	II	7.6	0.27	0.12	3		
TY09-7.9	II	7.9	0.30	0.71	4	-2.24	0.10
TY09-8.0	II	8.0	0.23	0.22	1		
TY09-8.3	II	8.3	0.13	0.07	3		
TY09-8.6	II	8.6	0.11	0.22	25		
TY09-8.8	II	8.8	0.26	0.48	6		
TY09-9.0	II	9.0	0.15	0.43	4		
TY09-9.4	II	9.4	0.13	0.42	5	-1.87	0.10
TY09-9.8	II	9.8	0.19	0.19	3		
TY09-10.0	II	10.0	0.12	0.23	3		
TY09-10.2	II	10.2	0.17	1.00	29	-1.47	0.10
TY09-10.4	II	10.4	0.31	0.40	39	-1.19	0.10
TY09-10.7	II	10.7	0.15	0.41	11		
TY09-11.0	II	11.0	1.00	1.00	30	-1.11	0.10
TY09-11.3	II	11.3	0.30	0.50	11		
TY09-11.5	II	11.5	0.32	0.66	11		
TY09-11.8	II	11.8	0.22	0.46	11		
TY09-12.0	II	12.0	0.12	0.23	6		
TY09-13.3	II	13.3	0.53	0.85	1		
TY09-13.8	II	13.8	0.59	1.00	3	-1.98	0.10
TY09-14.0	II	14.0	0.29	0.68	15		
TY09-15.1	II	15.1	0.31	0.93	38	-1.30	0.10
TY09-15.5	II	15.5	0.71	0.89	165	-1.21	0.10
TY09-16.3	II	16.3	1.00	0.81	48	-1.01	0.10

Sample No.	Member	Strat. Height	Fe_{HR}/Fe_{T}	Fe_{Py}/Fe_{HR}	Mo	$\delta^{98/95}Mo$	2SD
		(m)			(ppm)	(‰)	
TY09-16.5	II	16.5	0.70	0.96	114	-0.84	0.10
TY09-17.5	II	17.5	0.56	0.47	13	0.48	0.10
TY09-18.8	II	18.8	0.69	0.70	9		
TY09-19.7	II	19.7	0.59	0.77	11		
TY09-21.3	II	21.3	1.00	0.94	12		
TY09-22.3	II	22.3	1.00	1.00	0		
TY09-30.4	III	30.4	0.79	0.26	43		
TY09-34.8	III	34.8	0.49	0.35	41	-1.25	0.10
TY09-35.4	III	35.4	0.36	1.00	29	0.59	0.10
TY09-35.9	III	35.9	0.38	1.00	19	0.44	0.10
TY09-36.3	III	36.3	0.47	1.00	76	0.78	0.10
TY09-38.5	III	38.5	0.48	0.78	4		
TY09-38.8	III	38.8	0.39	1.00	1		
TY09-39.0	III	39.0	0.61	0.56	4		
TY09-40.0	III	40.0	0.43	1.00	5	-1.59	0.10
TY09-47.0	IV	47.0	0.52	0.78	2		
TY09-48.0	IV	48.0	0.62	0.30	17		
TY09-49.0	IV	49.0	0.36	0.24	2		
TY09-50.0	IV	50.0	1.00	0.07	9		
TY09-51.0	IV	51.0	0.33	0.59	4		
TY09-52.0	IV	52.0	1.00	0.10	2		
TY09-53.0	IV	53.0	0.31	0.71	3		
TY09-55.0	IV	55.0	0.53	0.24	5	1.00	0.10
TY09-57.0	IV	57.0	0.27	0.14	5		
TY09-59.0	IV	59.0	0.63	0.23	2		
Wuhe section, Guizou Province, China							
WH09-2.4	II	2.4	0.17	0.41	1		
WH09-2.7	II	2.7	0.29	0.29	9		
WH09-3	II	3.0	0.39	0.73	4		
WH09-3.2	II	3.2	0.49	0.97	38	-0.51	0.10
WH09-3.5	II	3.5	0.40	0.23	2		
WH09-3.7	II	3.7	0.63	0.87	62	-0.89	0.10
WH09-4	II	4.0	0.38	0.85	8	-0.81	0.10
WH09-4.3	II	4.3	0.54	0.91	172	-0.30	0.10
WH09-4.6	II	4.6	0.62	0.57	11	-0.30	0.10
WH09-4.8	II	4.8	0.30	0.72	13	-0.10	0.10
WH09-5.0	II	5.0	0.70	0.34	40	-0.50	0.10
WH09-5.4	II	5.4	0.64	0.79	41		
WH09-5.6	II	5.6	0.63	0.58	42	-0.42	0.10
WH09-5.8	II	5.8	0.69	0.64	22		
WH09-6.0	II	6.0	0.69	1.00	30	-0.30	0.10
WH09-6.3	II	6.3	0.70	0.99	27		
WH09-6.5	II	6.5	0.29	0.05	58		

Sample No.	Member	Strat. Height	Fe_{HR}/Fe_T	Fe_{Py}/Fe_{HR}	Mo	$\delta^{98/95}$Mo	2SD
		(m)			(ppm)	(‰)	
WH09-6.8	II	6.8	0.48	0.97	38	0.06	0.10
WH09-7.0	II	7.0	0.62	0.91	26	0.31	0.11
WH09-7.3	II	7.3	0.62	0.83	13		
WH09-8.6	II	8.6	0.67	0.87	24	0.72	0.10
WH09-9.4	II	9.4	0.68	0.86	8	0.60	0.10
WH09-9.7	II	9.7	0.71	0.91	12		
WH09-11.6	II	11.6	0.67	0.95	12	0.68	0.10
WH09-13.7	II	13.7	0.91	0.70	4	1.47	0.10
WH09-21.5	II	21.5	0.64	0.87	1		
WH09-24.1	II	24.1	0.71	0.93	1	0.86	0.10
WH09-26.0	II	26.0	0.81	0.93	1	0.69	0.10
WH09-29.0	II	29.0	0.76	0.95	1	0.16	0.10
WH09-32.4	II	32.4	0.88	0.95	1		
WH09-35.1	II	35.1	0.88	0.97	1		
WH09-38.5	II	38.5	0.62	0.95	3	0.32	0.10
WH09-41.1	II	41.1	0.88	0.97	2	0.49	0.10
WH09-44.3	II	44.3	0.90	0.86	2	0.48	0.10
WH09-47.5	II	47.5	1.00	0.95	7	0.74	0.10
WH09-50.1	II	50.1	0.94	0.94	4	0.73	0.10
WH09-53.4	II	53.4	0.82	0.97	4	0.77	0.10
WH09-54.9	II	54.9	1.00	0.96	2		
WH09-56.3	II	56.3	1.00	0.97	1		
WH09-57.3	II	57.3	0.61	0.98	1		
WH09-60.7	III	60.7	0.79	0.77	7	0.94	0.10
WH09-61.1	III	61.1	0.85	0.41	5		
WH09-62.4	III	62.4	0.88	0.14	2		
WH09-63.1	III	63.1	0.77	0.81	2	-1.42	0.10
WH09-63.7	III	63.7	0.38	0.79	14		
WH09-63.9	III	63.9	0.68	0.71	9	-1.08	0.10
WH09-64.5	III	64.5	0.70	0.99	15	-1.50	0.10
WH09-65.5	III	65.5	0.61	0.81	3		
WH09-66.3	III	66.3	0.56	0.09	11	-1.72	0.10
WH09-66.8	III	66.8	0.58	0.30	14	-1.58	0.10
WH09-67.1	III	67.1	0.49	0.02	9		
WH09-67.4	III	67.4	0.54	0.02	6		
WH09-81.9	III	81.9	0.56	0.90	1	0.44	0.10
WH09-82.8	III	82.8	0.84	0.88	1		
WH09-83.7	III	83.7	0.52	0.93	2	0.59	0.10
WH09-84.5	III	84.5	0.98	0.89	1		
WH09-85.7	III	85.7	0.82	0.96	4	0.44	0.10
WH09-86.6	III	86.6	0.85	0.91	2	0.47	0.10
WH09-87.1	III	87.1	0.89	0.85	1		
WH09-88.3	III	88.3	0.88	0.70	5	0.44	0.10

Sample No.	Member	Strat. Height	Fe_{HR}/Fe_T	Fe_{Py}/Fe_{HR}	Mo	$\delta^{98/95}Mo$	2SD
		(m)			(ppm)	(‰)	
WH09-89.2	III	89.2	0.88	0.97	3	0.40	0.10
WH09-90.7	III	90.7	0.86	0.97	2	0.29	0.10
WH09-91.5	III	91.5	0.81	0.97	1		
WH09-93.0	III	93.0	0.77	0.95	1	0.39	0.10
WH09-94.0	III	94.0	0.76	0.71	1		
WH09-95.6	III	95.6	0.83	0.97	3		
WH09-96.3	III	96.3	0.85	0.97	2	0.44	0.10
WH09-97.9	III	97.9	0.94	0.97	2		
WH09-99.6	III	99.6	0.81	0.96	1	0.39	0.10
WH09-100.4	III	100.4	0.72	0.96	1	0.51	0.10
WH09-101.2	III	101.2	0.89	0.87	3	0.51	0.10
WH09-102.4	III	102.4	0.93	0.97	7	0.68	0.10
WH09-103.3	III	103.3	0.88	0.87	6	0.74	0.10
WH09-104.1	III	104.1	0.79	0.96	6	0.76	0.10
WH09-105.3	III	105.3	0.72	0.90	5	0.83	0.10
WH09-106.4	III	106.4	0.74	0.99	3		
WH09-107.4	III	107.4	0.81	0.98	4	0.93	0.10
WH09-108.3	III	108.3	0.80	0.93	2		
WH09-110.7	III	110.7	1.00	0.76	19	2.24	0.10
WH09-114.5	IV	114.5	0.70	0.98	2		
WH09-115.3	IV	115.3	0.60	0.95	68	-1.37	0.10
WH09-115.5	IV	115.5	0.74	0.90	76	-0.80	0.10
WH09-115.9	IV	115.9	0.72	0.90	126	-0.93	0.10
WH09-116.3	IV	116.3	0.65	0.84	66		
WH09-116.8	IV	116.8	0.73	0.88	79	0.48	0.10
WH09-117.4	IV	117.4	0.83	0.92	95		
WH09-117.8	IV	117.8	0.67	0.94	61		
WH09-118.3	IV	118.3	0.84	0.90	34		
WH09-118.9	IV	118.9	0.92	0.87	35		
WH09-119.5	IV	119.5	0.88	0.85	33		
WH09-120.0	IV	120.0	0.67	0.86	22	0.20	0.10
Yuanjia section, Hunan Province, China							
WHH-5.6	II	5.6	0.65	0.89	13	-1.49	0.10
WHH-5.7	II	5.7	0.72	0.94	64	-1.35	0.10
WHH-6.3	II	6.3	0.72	0.88	136	-0.74	0.10
WHH-6.4	II	6.4	0.73	0.93	148	0.52	0.10
WHH-6.8	II	6.8	0.84	0.92	97	-0.18	0.10
WHH-6.9	II	6.9	0.69	0.95	25	-0.48	0.10
WHH-7.2	II	7.2	0.86	0.96	37	0.28	0.10
WHH-7.4	II	7.4	0.81	0.97	37	0.54	0.10
WHH-7.6	II	7.6	0.26	0.67	11	-0.04	0.10
WHH-9.1	II	9.1	0.11	0.20	0		
WHH-9.5	II	9.5	0.16	0.42	0		

APPENDIX E

SUPPLEMENTARY INFORMATION FOR CHAPTER 6

Table E.1 Supplementary Data

section	sample meterage	Fe_{HR}/Fe_T	Fe_{Py}/Fe_{HR}	$\varepsilon^{205}Tl_{authigenic}$	measured 2SD	$\varepsilon^{205}Tl_{detrital}$
Wernecke Mtns., NW Canada						
Blueflower Fm.	262.00	0.46	0.00			
Blueflower Fm.	263.50	0.36	0.00			
Blueflower Fm.	266.00	0.44	0.00	-1.78	0.07	
Blueflower Fm.	272.50	0.52	0.12	-2.21	0.10	
Blueflower Fm.	273.00	0.56	0.07			
Blueflower Fm.	273					
Blueflower Fm.	275					
Blueflower Fm.	276.00	0.42	0.03			
Blueflower Fm.	276					
Blueflower Fm.	281					
Blueflower Fm.	282.00	0.73	0.05	-2.25	0.01	
Blueflower Fm.	282					
Blueflower Fm.	283.5					
Blueflower Fm.	283.5					
Blueflower Fm.	285					
Blueflower Fm.	287.00	0.33	0.00			
Blueflower Fm.	291					
Blueflower Fm.	298.00	0.26	0.10	-2.50	0.07	
Blueflower Fm.	301					
Blueflower Fm.	302.5					
Blueflower Fm.	309.50	0.27	0.05	-2.72	0.04	
Blueflower Fm.	311.00	0.54	0.08			
Blueflower Fm.	312.00	0.60	0.02	-2.63	0.21	
Blueflower Fm.	320.5					
Blueflower Fm.	332.50	0.36	0.00	-1.93	0.07	
Blueflower Fm.	334					
Blueflower Fm.	335.00	0.86	0.02			
Blueflower Fm.	337.00	0.71	0.07	-2.34	0.28	
Blueflower Fm.	340					
Blueflower Fm.	344					
Blueflower Fm.	344.80	0.38	0.00	-2.80	0.03	

section	sample meterage	Fe_{HR}/Fe_T	Fe_{Py}/Fe_{HR}	$\varepsilon^{205}Tl_{authigenic}$	measured 2SD	$\varepsilon^{205}Tl_{detrital}$
Sheepbed Fm.	10					
Sheepbed Fm.	10.8					
Sheepbed Fm.	15.8					
Sheepbed Fm.	16					
Sheepbed Fm.	16.00	0.71	0.00			
Sheepbed Fm.	16.3					
Sheepbed Fm.	16.5					
Sheepbed Fm.	17.1					
Sheepbed Fm.	17.4					
Sheepbed Fm.	17.8					
Sheepbed Fm.	18					
Sheepbed Fm.	18.00	0.72	0.00			
Sheepbed Fm.	19					
Sheepbed Fm.	20.00	0.29	0.05	-1.91	0.18	
Sheepbed Fm.	20.00	0.78	0.02			
Sheepbed Fm.	20.7					
Sheepbed Fm.	21					
Sheepbed Fm.	21.3					
Sheepbed Fm.	21.7					
Sheepbed Fm.	22.00	0.77	0.04	-2.45	0.13	
Sheepbed Fm.	22.7					
Sheepbed Fm.	23					
Sheepbed Fm.	23.3					
Sheepbed Fm.	23.8					
Sheepbed Fm.	24					
Sheepbed Fm.	24.00	0.76	0.01			
Sheepbed Fm.	24.5					
Sheepbed Fm.	25					
Sheepbed Fm.	26					
Sheepbed Fm.	26.00	0.74	0.09			
Sheepbed Fm.	28					
Sheepbed Fm.	28.00	0.59	0.06			
Sheepbed Fm.	28.5					
Sheepbed Fm.	28.8					
Sheepbed Fm.	29.30	0.66	0.09	-2.76	0.23	
Sheepbed Fm.	30					

section	sample meterage	Fe_{HR}/Fe_T	Fe_{Py}/Fe_{HR}	$\varepsilon^{205}Tl_{authigenic}$	measured 2SD	$\varepsilon^{205}Tl_{detrital}$
Sheepbed Fm.	30.20	0.52	0.02			
Sheepbed Fm.	31					
Sheepbed Fm.	32.00	0.39	0.09			
Sheepbed Fm.	34.00	0.72	0.09			
Sheepbed Fm.	36.00	0.34	0.04			
Sheepbed Fm.	40.00	0.35	0.15	-3.42	0.27	
Sheepbed Fm.	40.00	0.55	0.09			
Sheepbed Fm.	42					
Sheepbed Fm.	42.5					
Sheepbed Fm.	43					
Sheepbed Fm.	43.80	0.32	0.05			
Sheepbed Fm.	44.4					
Sheepbed Fm.	45.6					
Sheepbed Fm.	46					
Sheepbed Fm.	46.00	0.44	0.12			
Sheepbed Fm.	48.20	0.46	0.07			
Sheepbed Fm.	49					
Sheepbed Fm.	50.00	0.51	0.07	-4.35	0.00	
Sheepbed Fm.	54.00	0.46	0.05	-3.74	0.25	
Sheepbed Fm.	56					
Sheepbed Fm.	56.00	0.35	0.21			
Sheepbed Fm.	58.00	0.35	0.08			
Sheepbed Fm.	60.00	0.57	0.06			
Sheepbed Fm.	60.5					
Sheepbed Fm.	61					
Sheepbed Fm.	62.50	0.35	0.13	-3.78	0.54	
Sheepbed Fm.	64.00	0.34	0.05			
Sheepbed Fm.	66					
Sheepbed Fm.	66.00	0.38	0.02			
Sheepbed Fm.	68.00	0.34	0.11			
Sheepbed Fm.	70.00	0.31	0.25			
Sheepbed Fm.	71					
Sheepbed Fm.	72.00	0.47	0.15			
Sheepbed Fm.	75.00	0.25	0.05			
Sheepbed Fm.	77.00	0.25	0.12			
Sheepbed Fm.	79.00	0.23	0.08	-3.07	0.04	

section	sample meterage	Fe_{HR}/Fe_T	Fe_{Py}/Fe_{HR}	$\varepsilon^{205}Tl_{authigenic}$	measured 2SD	$\varepsilon^{205}Tl_{detrital}$
Sheepbed Fm.	82.00	0.31	0.11			
Sheepbed Fm.	85.00	0.43	0.11			
Sheepbed Fm.	86					
Sheepbed Fm.	87.00	0.49	0.04	-3.37	0.01	
Sheepbed Fm.	90.00	0.34	0.13			
Sheepbed Fm.	91					
Sheepbed Fm.	91.00	0.34	0.08			
Sheepbed Fm.	93.00	0.39	0.08			
Sheepbed Fm.	95.00	0.36	0.11			
Sheepbed Fm.	97.00	0.43	0.05			
Sheepbed Fm.	99.00	0.67	0.15	-2.82	0.23	
Sheepbed Fm.	100.5					
Sheepbed Fm.	101.00	0.56	0.07			
Sheepbed Fm.	103.00	0.41	0.09			
Sheepbed Fm.	105.00	0.45	0.05			
Sheepbed Fm.	107.00	0.49	0.06			
Sheepbed Fm.	109.00	0.51	0.08			
Sheepbed Fm.	112.00	0.56	0.08			
Sheepbed Fm.	113.00	0.38	0.07			
Sheepbed Fm.	119.00	0.33	0.11			
Sheepbed Fm.	120.5					
Sheepbed Fm.	121.00	0.31	0.14			
Sheepbed Fm.	122					
Sheepbed Fm.	123.00	0.32	0.10			
Sheepbed Fm.	125.00	0.49	0.14	-2.84	0.54	
Sheepbed Fm.	127.00	0.35	0.13			
Sheepbed Fm.	128					
Sheepbed Fm.	129.00	0.24	0.17			
Sheepbed Fm.	131.00	0.44	0.09			
Sheepbed Fm.	131.8					
Sheepbed Fm.	134					
Sheepbed Fm.	134.8					
Sheepbed Fm.	135.00	0.45	0.06	-2.81	0.16	
Sheepbed Fm.	139.00	0.34	0.10			
Sheepbed Fm.	141.00	0.34	0.05			
Sheepbed Fm.	143.00	0.41	0.08	-2.72	0.14	

section	sample meterage	Fe_{HR}/Fe_T	Fe_{Py}/Fe_{HR}	$\varepsilon^{205}Tl_{authigenic}$	measured 2SD	$\varepsilon^{205}Tl_{detrital}$
Sheepbed Fm.	145.00	0.38	0.08			
Sheepbed Fm.	147.00	0.46	0.02			
Sheepbed Fm.	149.00	0.35	0.02			
Sheepbed Fm.	151.00	0.33	0.07			
Sheepbed Fm.	153.00	0.28	0.10	-2.55	0.03	
Sheepbed Fm.	155.00	0.47	0.14			
Sheepbed Fm.	157.00	0.47	0.05			
Sheepbed Fm.	159.00	0.38	0.03			
Sheepbed Fm.	161.00	0.50	0.00			
Sheepbed Fm.	163.00	0.33	0.08	-2.32	0.08	
Sheepbed Fm.	165.00	0.53	0.05			
Sheepbed Fm.	167.00	0.36	0.06			
Sheepbed Fm.	168.00	0.33	0.01			
Sheepbed Fm.	176.00	0.62	0.01			
Sheepbed Fm.	178					
Sheepbed Fm.	179					
Sheepbed Fm.	180					
Sheepbed Fm.	182.00	0.48	0.08			
Sheepbed Fm.	184.00	0.47	0.09			
Sheepbed Fm.	187.00	0.47	0.06			
Sheepbed Fm.	188.50	0.48	0.06			
Sheepbed Fm.	191.00	0.41	0.05			
Sheepbed Fm.	193.50	0.37	0.03			
Sheepbed Fm.	195.00	0.73	0.06			
Sheepbed Fm.	197.00	0.45	0.02	-2.62	0.33	
Sheepbed Fm.	199.00	0.39	0.00			
Sheepbed Fm.	201.00	0.41	0.02			
Sheepbed Fm.	203.00	0.53	0.04			
Sheepbed Fm.	205.20	0.21	0.11			
Sheepbed Fm.	207.00	0.32	0.02	-2.37	0.08	
Sheepbed Fm.	208.50	0.38	0.03			
Sheepbed Fm.	213.00	0.31	0.01	-2.07	0.00	
Sheepbed Fm.	215.00	0.36	0.02			
Sheepbed Fm.	219.00	0.36	0.03			
Sheepbed Fm.	221.00	0.42	0.11			
Sheepbed Fm.	223.00	0.43	0.02			

section	sample meterage	Fe_{HR}/Fe_{T}	Fe_{Py}/Fe_{HR}	$\varepsilon^{205}Tl_{authigenic}$	measured 2SD	$\varepsilon^{205}Tl_{detrital}$
Sheepbed Fm.	225.00	0.91	0.02			
Sheepbed Fm.	227.00	0.41	0.03			
Sheepbed Fm.	229.00	0.38	0.04	-2.09	0.10	
Sheepbed Fm.	234.00	0.40	0.07			
Sheepbed Fm.	236.00	0.44	0.02	-2.02	0.03	
Sheepbed Fm.	238.00	0.31	0.05			
Sheepbed Fm.	240.00	0.55	0.01			
Sheepbed Fm.	242.00	0.41	0.01			
Sheepbed Fm.	244.00	0.34	0.01			
Sheepbed Fm.	248.00	0.26	0.00	-2.22	0.16	
Sheepbed Fm.	252.00	0.41	0.06			
Sheepbed Fm.	253.00	0.48	0.04			
Sheepbed Fm.	254.00	0.40	0.02			
Sheepbed Fm.	256.00	0.28	0.02			
Sheepbed Fm.	258.00	0.51	0.03			
Sheepbed Fm.	260.00	0.25	0.03			
Sheepbed Fm.	262.00	0.32	0.03	-2.07	0.03	
Sheepbed Fm.	264.00	0.26	0.02			
Sheepbed Fm.	264.00	0.42	0.01			
Sheepbed Fm.	266.00	0.63	0.02			
Sheepbed Fm.	268.00	0.45	0.01			
Sheepbed Fm.	270.00	0.44	0.01			
Sheepbed Fm.	272.00	0.38	0.01			
Sheepbed Fm.	274.00	0.45	0.02			
Sheepbed Fm.	276.00	0.40	0.00			
Sheepbed Fm.	278.00	0.33	0.01	-2.75	0.08	
Sheepbed Fm.	280.00	0.36	0.02			
Sheepbed Fm.	282.00	0.43	0.02			
Sheepbed Fm.	284.00	0.22	0.05	-2.62	0.21	
Sheepbed Fm.	284.00	0.25	0.03			
Sheepbed Fm.	286.00	0.18	0.02			
Sheepbed Fm.	288.00	0.42	0.06			
Sheepbed Fm.	290.00	0.21	0.13			
Sheepbed Fm.	292.00	0.22	0.07			
Sheepbed Fm.	294.00	0.30	0.04	-2.65	0.08	
Sheepbed Fm.	298.00	0.24	0.01			

section	sample meterage	Fe_{HR}/Fe_T	Fe_{Py}/Fe_{HR}	$\varepsilon^{205}Tl_{authigenic}$	measured 2SD	$\varepsilon^{205}Tl_{detrital}$
Sheepbed Fm.	300.00	0.32	0.00			
Sheepbed Fm.	302.00	0.48	0.00			
Sheepbed Fm.	304					
Sheepbed Fm.	304.00	0.18	0.05	-2.86	0.14	
Sheepbed Fm.	305					
Sheepbed Fm.	306.00	0.30	0.07			
Sheepbed Fm.	312					
Sheepbed Fm.	312.5					
Sheepbed Fm.	313					
Sheepbed Fm.	313.5					
Sheepbed Fm.	315					
Sheepbed Fm.	315.7					
Sheepbed Fm.	316.00	0.37	0.01			
Sheepbed Fm.	318.00	0.34	0.00			
Sheepbed Fm.	320.00	0.45	0.00	-2.42	0.24	
Sheepbed Fm.	323					
Sheepbed Fm.	324.00	0.29	0.01			
Sheepbed Fm.	326.00	0.28	0.01			
Sheepbed Fm.	328.00	0.26	0.00			
Sheepbed Fm.	331.00	0.26	0.13			
Sheepbed Fm.	332.00	0.29	0.02			
Sheepbed Fm.	334.00	0.20	0.01	-1.92	0.17	
Sheepbed Fm.	336.00	0.11	0.00			
Sheepbed Fm.	338.00	0.20	0.08			
Sheepbed Fm.	340					
Sheepbed Fm.	340.00	0.22	0.09			
Sheepbed Fm.	342.00	0.29	0.00			
Sheepbed Fm.	344.00	0.27	0.08			
Sheepbed Fm.	346.00	0.37	0.03			
Sheepbed Fm.	348					
Sheepbed Fm.	348.50	0.23	0.12			
Sheepbed Fm.	350.00					
Sheepbed Fm.	350.5					
Sheepbed Fm.	351.5					
Sheepbed Fm.	351.5					
Sheepbed Fm.	352.00	0.14	0.06			

section	sample meterage	Fe_{HR}/Fe_T	Fe_{Py}/Fe_{HR}	$\varepsilon^{205}Tl_{authigenic}$	measured 2SD	$\varepsilon^{205}Tl_{detrital}$
Sheepbed Fm.	354.00	0.21	0.03			
Sheepbed Fm.	356.00	0.31	0.15			
Sheepbed Fm.	356.5					
Sheepbed Fm.	358.00	0.33	0.20			
Sheepbed Fm.	358.5					
Sheepbed Fm.	360					
Sheepbed Fm.	360.00	0.35	0.03			
Sheepbed Fm.	360.00	0.48	0.01			
Sheepbed Fm.	361					
Sheepbed Fm.	362.00	0.46	0.01			
Sheepbed Fm.	364.00	0.46	0.07	-2.45	0.21	
Sheepbed Fm.	366.00	0.77	0.10			
Sheepbed Fm.	368.00	0.64	0.08			
Sheepbed Fm.	371					
Sheepbed Fm.	372					
Sheepbed Fm.	373					
Sheepbed Fm.	375					
Sheepbed Fm.	376					
Sheepbed Fm.	377					
Sheepbed Fm.	378					
Sheepbed Fm.	379					
Sheepbed Fm.	380					
Sheepbed Fm.	381					
Sheepbed Fm.	382					
Sheepbed Fm.	383					
Sheepbed Fm.	384					
Sheepbed Fm.	385					
Sheepbed Fm.	386					
Sheepbed Fm.	387					
Sheepbed Fm.	388					
Sheepbed Fm.	389					
Sheepbed Fm.	390					
Sheepbed Fm.	391					
Mackenzie Mtns., NW Canada						

section	sample meterage	Fe_{HR}/Fe_{T}	Fe_{Py}/Fe_{HR}	$\varepsilon^{205}Tl_{authigenic}$	measured 2SD	$\varepsilon^{205}Tl_{detrital}$
June Beds	28.5	0.57	0.25	-1.43	0.76	
June Beds	31.2	0.67	0.11			
June Beds	33.76	0.47	0.07	-1.12	0.68	
June Beds	38.6	0.37	0.14	-0.97	0.81	
June Beds	53.3	0.44	0.10	-1.85	0.28	
June Beds	66.5	0.58	0.08			
June Beds	70	0.63	0.07			
June Beds	76.9	0.54	0.01			
June Beds	86	0.55	0.05	-2.01	0.67	
June Beds	92	0.36	0.02	-1.01	0.44	
June Beds	103.5	0.73	0.08			
June Beds	116.5	0.57	0.05			
June Beds	126.8	0.56	0.01	-0.52	0.18	
June Beds	141.3	0.09	0.01	-1.17	0.00	
June Beds	159	0.13	0.11	-1.31	0.29	
June Beds	181.9	0.11	0.04	-1.04	0.56	
June Beds	196.2	0.48	0.04	-1.99	0.53	
June Beds	209.2	0.49	0.02	-1.41	0.59	
June Beds	217.5	0.51	0.04	-1.27	0.47	
June Beds	223	0.60	0.04			
June Beds	232.5	0.58	0.11	-1.35	0.31	
June Beds	253	0.58	0.03	-0.55	0.50	
June Beds	278	0.59	0.05	-1.54	0.50	
June Beds	289.5	0.65	0.04	-1.53	0.08	
June Beds	303.4	0.81	0.06	-0.88	0.59	
June Beds	51.3	0.84	0.06	-1.44	0.26	
June Beds	56	0.63	0.14	-1.18	0.36	
June Beds	122.5	0.90	0.03			
June Beds	135	0.75	0.08	-1.40	0.19	
June Beds	145	0.83	0.07			
June Beds	165.2	0.84	0.04	-1.76	0.62	
June Beds	176.5	0.78	0.02			
June Beds	179.5	0.89	0.05	-2.43	0.10	
June Beds	194	0.68	0.02	-2.31	0.40	
June Beds	203.4	0.38	0.03	-1.37	0.29	
June Beds	212	0.11	0.36	-1.15	0.12	

section	sample meterage	Fe_{HR}/Fe_T	Fe_{Py}/Fe_{HR}	$\varepsilon^{205}Tl_{authigenic}$	measured 2SD	$\varepsilon^{205}Tl_{detrital}$
June Beds	226	0.65	0.03	-0.58	0.31	
June Beds	250.5	0.94	0.07	-3.44	0.55	
June Beds	419	0.94	0.00			
Blueflower Fm.	445.7	0.90	0.03			
Blueflower Fm.	496.4	0.91	0.02			
Blueflower Fm.	542.3	0.78	0.00			
Blueflower Fm.	542.7	0.59	0.00			
Blueflower Fm.	547.4	0.63	0.01			
Blueflower Fm.	547.8	0.38	0.01			
Blueflower Fm.	22.5	0.78	0.05	-2.59	0.41	
Blueflower Fm.	28.6	0.84	0.17			
Blueflower Fm.	46.4	0.40	0.13	-2.16	0.47	
Blueflower Fm.	50.3	0.81	0.12			
Blueflower Fm.	61.3	0.69	0.11			
Blueflower Fm.	71	0.32	0.30	-1.43	0.10	
Blueflower Fm.	80	0.67	0.08			
Blueflower Fm.	90.7	0.31	0.01			
Blueflower Fm.	103.5	0.18	0.04	-0.66	0.14	
Blueflower Fm.	113	0.67	0.01			
Blueflower Fm.	128.2	0.49	0.01			
Blueflower Fm.	134.6	0.67	0.02	-2.18	0.69	
Blueflower Fm.	147.1	0.76	0.04			
Blueflower Fm.	8.9	0.48	0.01	-2.59	0.14	
Blueflower Fm.	20	0.40	0.06			
Blueflower Fm.	20.01	0.33	0.03	-2.07	0.52	
Blueflower Fm.	31.5	0.73	0.01			
Blueflower Fm.	40.1	0.73	0.01			
Blueflower Fm.	49.1	0.81	0.00			
Blueflower Fm.	64	0.58	0.01	-1.53	0.01	
Blueflower Fm.	75.9	0.47	0.02			
Blueflower Fm.	84.2	0.64	0.13	-1.40	0.22	
Blueflower Fm.	93.1	0.76	0.01			
Wuhe Section, S China						
Member II	0.1	0.17	0.41	-2.53	0.03	
Member II	0.4	0.29	0.29			

section	sample meterage	Fe_{HR}/Fe_T	Fe_{Py}/Fe_{HR}	$\varepsilon^{205}Tl_{authigenic}$	measured 2SD	$\varepsilon^{205}Tl_{detrital}$
Member II	0.7	0.39	0.73			
Member II	0.9	0.49	0.97			
Member II	1.2	0.40	0.23			
Member II	1.4	0.63	0.87			
Member II	1.7	0.38	0.85	-3.01	0.59	-2.46
Member II	2	0.54	0.91			
Member II	2.3	0.62	0.57			
Member II	2.5	0.30	0.72	-1.98	0.50	
Member II	2.7	0.70	0.34			
Member II	3.1	0.64	0.79	-2.87	0.33	
Member II	3.3	0.63	0.58			
Member II	3.5	0.69	0.64			
Member II	3.7	0.69	1.00	-2.29	0.22	
Member II	4	0.70	0.99			
Member II	4.2	0.29	0.05			
Member II	4.5	0.48	0.97			
Member II	4.7	0.62	0.91	-2.63	0.06	
Member II	5	0.62	0.83	-3.79	0.01	
Member II	6.3	0.67	0.87	-3.57	0.12	
Member II	7.1	0.68	0.86	-3.14	0.29	
Member II	7.4	0.71	0.91	-4.24	0.08	
Member II	9.3	0.67	0.95			
Member II	11.4	0.91	0.70	-3.47	0.17	
Member II	19.2	0.64	0.87	-4.26	0.26	
Member II	21.8	0.71	0.93	-4.38	0.19	-3.52
Member II	23.7	0.81	0.93	-5.45	0.19	
Member II	26.7	0.76	0.95	-4.51	0.25	
Member II	30.1	0.88	0.95	-6.78	0.06	-3.06
Member II	32.8	0.88	0.97			
Member II	36.2	0.62	0.95	-9.08	0.07	
Member II	38.8	0.88	0.97	-10.39	0.06	-4.82
Member II	42	0.90	0.86	-9.85	0.84	-5.23
Member II	45.2	1.00	0.95	-7.93	0.56	
Member II	47.8	0.94	0.94	-3.99	0.16	
Member II	51.1	0.82	0.97	-4.32	0.16	
Member II	52.6	1.00	0.96			

section	sample meterage	Fe_{HR}/Fe_T	Fe_{Py}/Fe_{HR}	$\varepsilon^{205}Tl_{authigenic}$	measured 2SD	$\varepsilon^{205}Tl_{detrital}$
Member II	54	1.00	0.97	-2.23	0.27	-2.33
Member II	55	0.61	0.98			
Member III	58.4	0.79	0.77	-3.98	0.12	
Member III	58.8	0.85	0.41			
Member III	60.1	0.88	0.14			
Member III	60.8	0.77	0.81	-4.30	0.38	
Member III	61.4	0.38	0.79			
Member III	61.6	0.68	0.71	-5.35	0.30	
Member III	62.2	0.70	0.99	-5.19	0.06	-3.12
Member III	63.2	0.61	0.81	-3.37	0.63	
Member III	64	0.56	0.09			
Member III	64.5	0.58	0.30			
Member III	64.8	0.49	0.02			
Member III	65.1	0.54	0.02			
Member III	79.6	0.56	0.90	-3.90	0.24	-3.42
Member III	80.5	0.84	0.88	-3.55	0.00	
Member III	81.4	0.52	0.93	-4.42	0.11	
Member III	82.2	0.98	0.89	-4.79	0.31	
Member III	83.4	0.82	0.96	-8.39	0.09	
Member III	84.3	0.85	0.91	-6.24	0.13	-4.11
Member III	84.8	0.89	0.85			
Member III	86	0.88	0.70	-8.75	0.36	
Member III	86.9	0.88	0.97	-7.66	0.02	
Member III	88.4	0.86	0.97	-5.82	0.04	
Member III	89.2	0.81	0.97			
Member III	90.7	0.77	0.95	-6.75	0.47	
Member III	91.7	0.76	0.71	-5.26	0.12	
Member III	93.3	0.83	0.97			
Member III	94	0.85	0.97	-8.45	0.24	-3.91
Member III	95.6	0.94	0.97			
Member III	97.3	0.81	0.96	-9.10	0.11	-4.63
Member III	98.1	0.72	0.96	-6.19	0.14	
Member III	98.9	0.89	0.87	-7.84	0.43	
Member III	100.1	0.93	0.97	-8.52	0.20	
Member III	101	0.88	0.87	-7.31	0.10	-3.78
Member III	101.8	0.79	0.96	-5.35	0.38	

section	sample meterage	Fe_{HR}/Fe_T	Fe_{Py}/Fe_{HR}	$\varepsilon^{205}Tl_{authigenic}$	measured 2SD	$\varepsilon^{205}Tl_{detrital}$
Member III	103	0.72	0.90	-3.85	0.78	
Member III	104.1	0.74	0.99	-5.88	0.07	
Member III	105.1	0.81	0.98	-4.44	0.28	
Member III	106	0.80	0.93	-2.22	0.04	
Member III	108.4	1.00	0.76	-6.01	0.26	
Member IV	112.2	0.70	0.98	-2.95	0.13	
Member IV	113	0.60	0.95			
Member IV	113.2	0.74	0.90	-0.96	0.04	-2.18
Member IV	113.6	0.72	0.90	-1.82	0.52	
Member IV	114	0.65	0.84	-3.29	0.18	
Member IV	114.5	0.73	0.88	-2.86	0.08	
Member IV	115.1	0.83	0.92	-1.04	0.04	
Member IV	115.5	0.67	0.94	-1.22	0.27	
Member IV	116	0.84	0.90			
Member IV	116.6	0.92	0.87			
Member IV	117.2	0.88	0.85	0.35	0.66	
Member IV	117.7	0.67	0.86	-3.51	0.17	